THE OXIDATION RESISTANCE OF NITRIDED IRON ALLOYS

A dissertation submitted for the degree of

Doctor of Philosophy

of the University of Newcastle upon Tyne

by

David John Coates

Crystallography Laboratory

Department of Metallurgy and Engineering Materials

University of Newcastle upon Tyne

October 1980

To TRICIA

for her patience and support

PREFACE

This dissertation describes original work which has not been submitted for a degree at any other University.

The investigations were carried out in the Crystallography Laboratory, Department of Metallurgy and Engineering Materials of the University of Newcastle upon Tyne during the period October 1977 to September 1980 under the supervision of Professor K.H. Jack and Dr. A. Hendry.

The thesis describes a study of the oxidation of nitrided mild steel and of nitrided iron-chromium, iron-titanium and iron-molybdenum alloys.

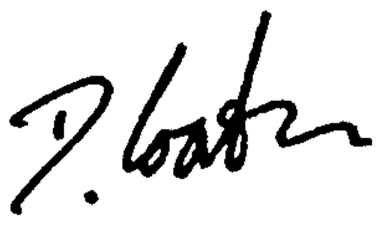

October 1980

ACKNOWLEDGEMENTS

I would like to express my sincere thanks to Dr. A. Hendry for his supervision, advice and interest during this work.

I would also like to express my gratitude to Professor K.H. Jack for his advice and for provision of facilities in the Crystallography Laboratory.

Thanks are also due to:
The Central Electricity Generating Board for provision of funds for the work;

Dr. D.J. Lees of the Scientific Services Department, Midlands Region, C.E.G.B. for his assistance as technical correspondent, and for providing facilities for oxidation kinetics studies;

Mr. G. Rickards of the Berkeley Nuclear Laboratories, C.E.G.B. for his assistance with the High Voltage Electron Microscopy;

Mrs. P. Carrick and Mr. G. Staines for their technical assistance with the scanning electron microscopy;

Many colleagues, past and present, in the Crystallography Laboratory for their stimulating company over the past three years;

The technical staff of the Crystallography Laboratory for their assistance;

Mrs. A. Rule for typing the script.

October 1980

ABSTRACT

Using gas-metal equilibration, a nitrogen martensite case can be produced on iron and mild steel and tempering of this nitrogen martensite produces a fine dispersion of iron nitrides in a ferrite matrix. Under oxidising conditions the finely distributed nitrides provide sites for oxide nucleation and also act as vacancy sinks for inwardly diffusing cation vacancies during the subsequent growth of the oxide scale, thus giving improved metal-oxide adherence. The fine-grained oxide layer produced on nitrided iron and mild steel inhibits the outward diffusion of cations along dislocations and enhances the inward diffusion of anions along oxide grain boundaries. An oxide forming reaction thus takes place at the metal/oxide interface as well as at the oxide/gas interface, further enhancing metal-oxide adherence.

Nitriding of binary Fe-X alloys (where X is a strong nitride forming substitutional alloying element) occurs by the formation of metastable substitutional-interstitial clusters which subsequently transform to stable nitrides. The dispersion of stable nitrides formed on Fe-Cr, Fe-Ti and Fe-Mo alloys behaves similarly to the iron nitrides in nitrided iron and mild steel in affecting the subsequent formation and growth of oxide. Coherent clusters are less effective in improving oxide adherence.

There is no significant increase in oxidation

resistance of nitrided alloys in isothermal oxidation (450°-500°C) in air for exposures up to 500h. The oxidation rates of nitrided alloys thermally cycled in air for similar times can be greater than those of un-nitrided alloys.

CONTENTS

Chapter I

INTRODUCTION

Mild steel is used extensively for furnace wall evaporator tubes in coal-fired power-station boilers. The high-temperature performance of this material varies from plant to plant such that fireside corrosion creates only minor problems in some instances, but is a major cause of tube failure in others necessitating unscheduled shutdown of plant with consequent expensive loss of power generation.

The inherent disadvantage of mild steel in terms of oxidation resistance at high temperatures lies in the non-protective nature of the scale. The latter spalls from the metal as a result of relatively minor changes in environmental conditions, thus exposing fresh metal to attack by gaseous oxidants. The coherency of the oxide layer on ferritic alloys not containing elements such as chromium can be improved only by modifying the physical and mechanical properties of the oxide which can be influenced by the microstructure of the underlying metal substrate. Thus, the oxidation resistance of mild steel may be improved by a suitable surface treatment which leaves the microstructure and properties of the bulk material unaffected.

Solutions to the problem of oxidation of furnace wall tubing have been sought through the use of steels

of higher alloy content (such as low chromium-molybdenum steels) or by coating mild steel tubes with an oxidation resistant material. Metallic coatings in the form of flame-sprayed alloys or co-extruded tubing are generally expensive. Ceramic coatings such as silica and silicon carbide have proved unsuccessful because they are not sufficiently adherent to withstand the stresses imposed during fabrication and service. The main disadvantage of both types of coating is their susceptibility to spalling at the coating/metal interface, particularly during thermal cycling, as a result of differences in thermal expansion. In addition, ceramic coatings have a high degree of porosity which increases the possibility of gas access to the metal surface and consequent "jacking-off" of the coating.

A novel method of improving the oxidation resistance of mild steel by nitriding has been demonstrated by Hendry (1978). A surface nitrided layer is formed by constant-activity aging in an NH_3:H_2 gas mixture to form austenite at the nitriding temperature and this transforms to martensite with retained austenite when air-cooled. The oxidation resistance of the nitrided steel is markedly superior to that of the un-nitrided material when tested under similar conditions. The improvement is attributed partly to the fine grain size of the oxide formed on the nitrided metal, due to the large number of suitable surface nucleation sites, and partly to a modification of the condensation processes for cation vacancies.

This technique for improving oxidation resistance has additional advantages. The nitriding

treatment, which can be carried out using existing heat treatment technology at little additional cost, produces a hard, strong surface layer which is an integral part of the tube and is thus resistant to handling and fabrication damage. The high strength of internally nitrided layers (Jack, 1975) also allows a reduction in the tube wall thickness, thus representing a saving in material.

The present work investigates further the oxidation of nitrided mild steel. Techniques employed include oxidation weight-gain measurements, electron microscopy (scanning and transmission) and X-ray diffraction. The work on nitrided iron alloys is extended to include a number of Fe-X alloys where X (Cr, Ti and Mo) is a substitutional solute that forms coherent X-N clusters or incoherent nitride precipitates.

Chapter II

NITRIDING OF IRON AND IRON ALLOYS

II.1. The Iron-Nitrogen Phase Diagram

Figure II.1 shows the iron-nitrogen phase diagram. There are five major phases formed with increasing nitrogen potential: α-nitrogen ferrite, γ-nitrogen austenite, γ'-Fe_4N, ε-$Fe_{3-2}N$ and ζ-Fe_2N. There are two additional phases: α'-nitrogen martensite obtained by quenching γ-nitrogen austenite; and α''-$Fe_{16}N_2$, formed during the tempering of nitrogen martensite or the aging of nitrogen ferrite. Nitrogen austenite can exist down to 590°C at which temperature it contains 9.4 a/o nitrogen. The maximum solubility of nitrogen in ferrite is about 0.4 a/o at this temperature. γ'-Fe_4N has a face-centred cubic arrangement of iron atoms, like austenite, but the nitrogen atoms occupy one-quarter of the number of available octahedral interstices in a completely ordered manner (see Figure II.2).

Tetragonal α''-$Fe_{16}N_2$ can be regarded as a fully-ordered supersaturated solid solution of nitrogen in body-centred cubic iron, i.e. a fully ordered martensite. Alternatively, it is a distorted "Fe_4N" in which alternate nitrogen atoms are missing and which has a Bain orientation relationship with the ferrite matrix (Jack, 1951a). α''-$Fe_{16}N_2$ is therefore

Figure II.1

The iron-nitrogen phase diagram

(after Jack, 1951).

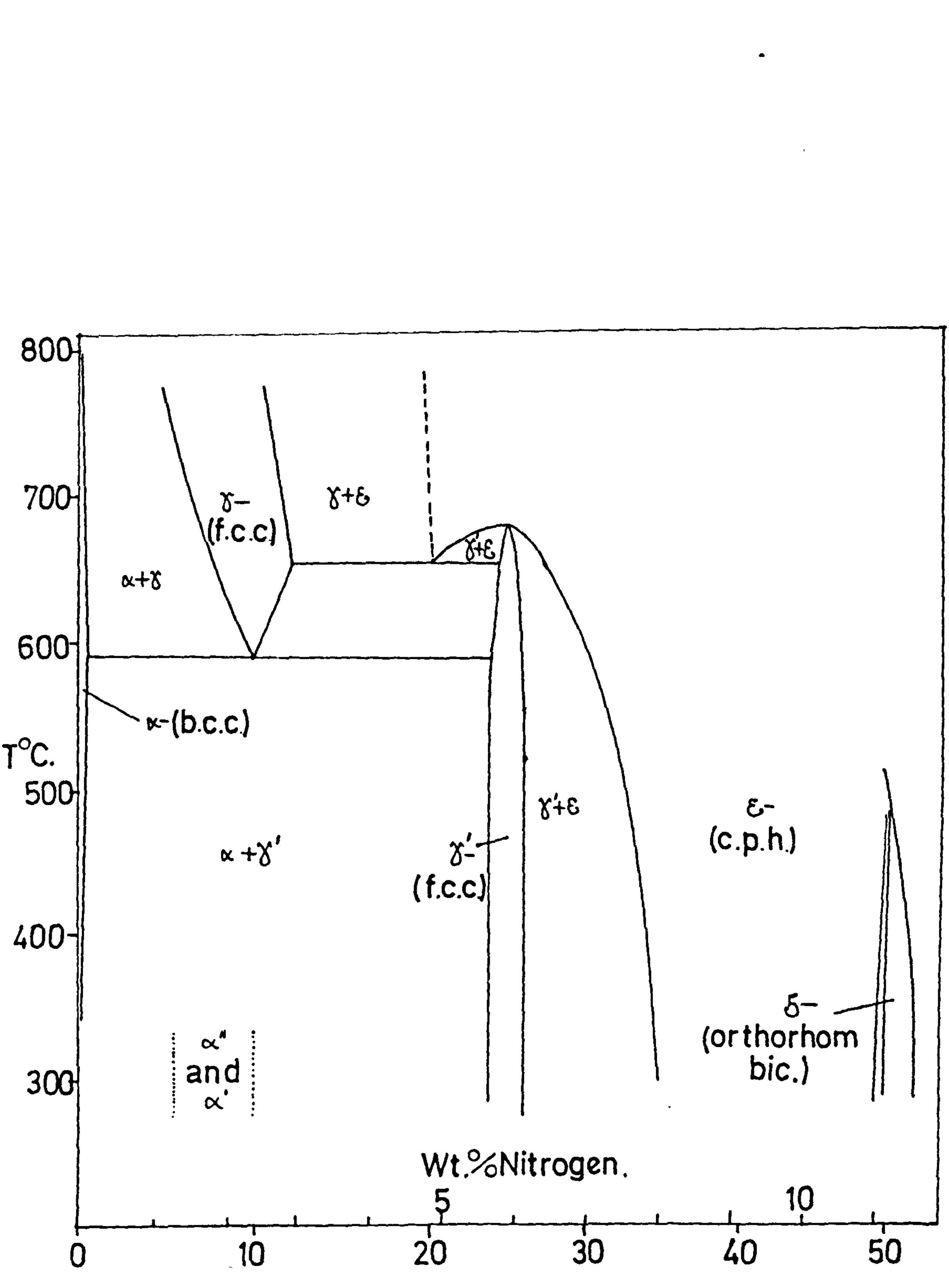

Nitrogen atoms per 100 Iron atoms.

Figure II.2

Structures of nitrogen austenite

and γ'-Fe_4N.

γ

nitrogen
austenite

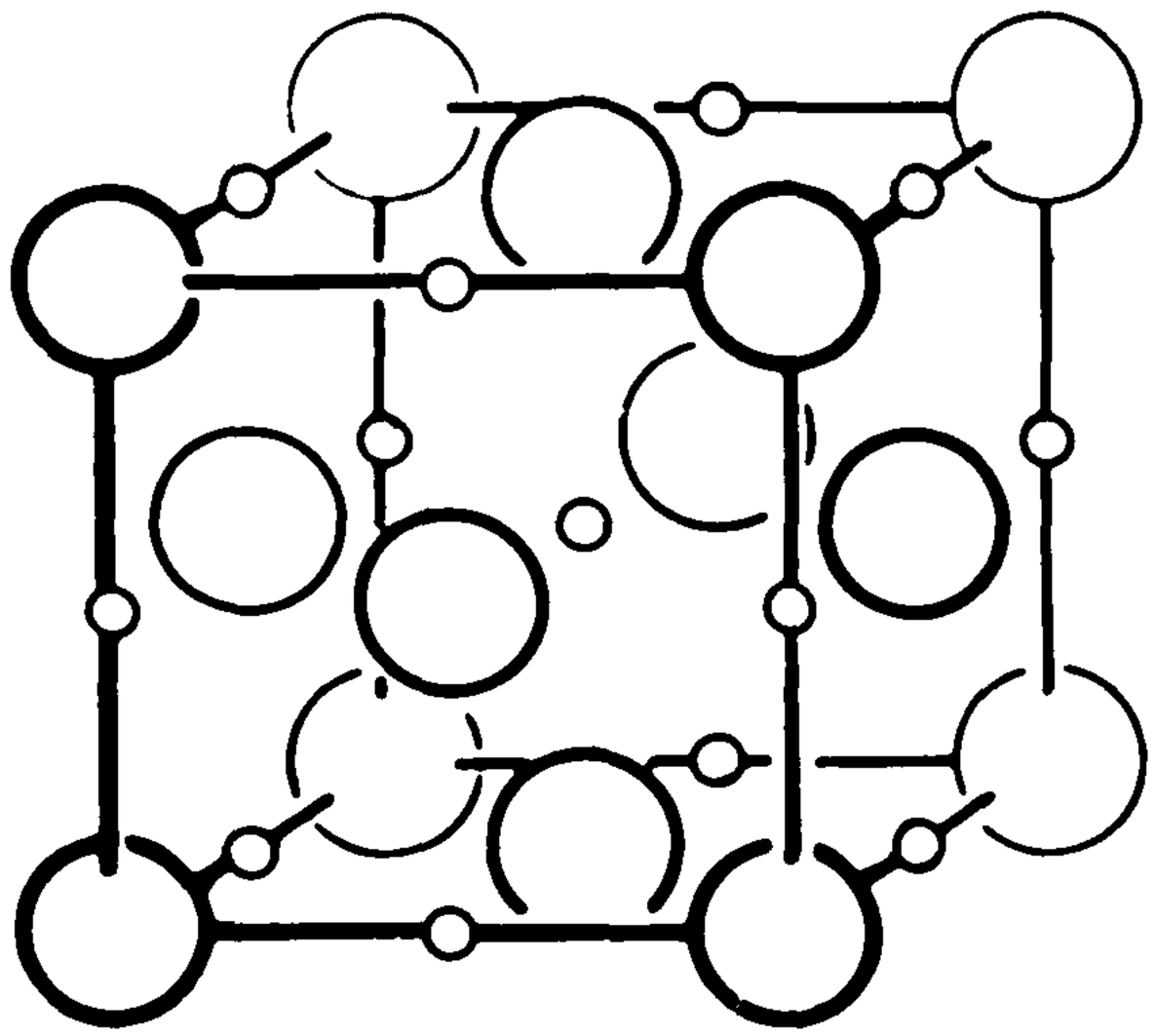

γ′

Fe_4N

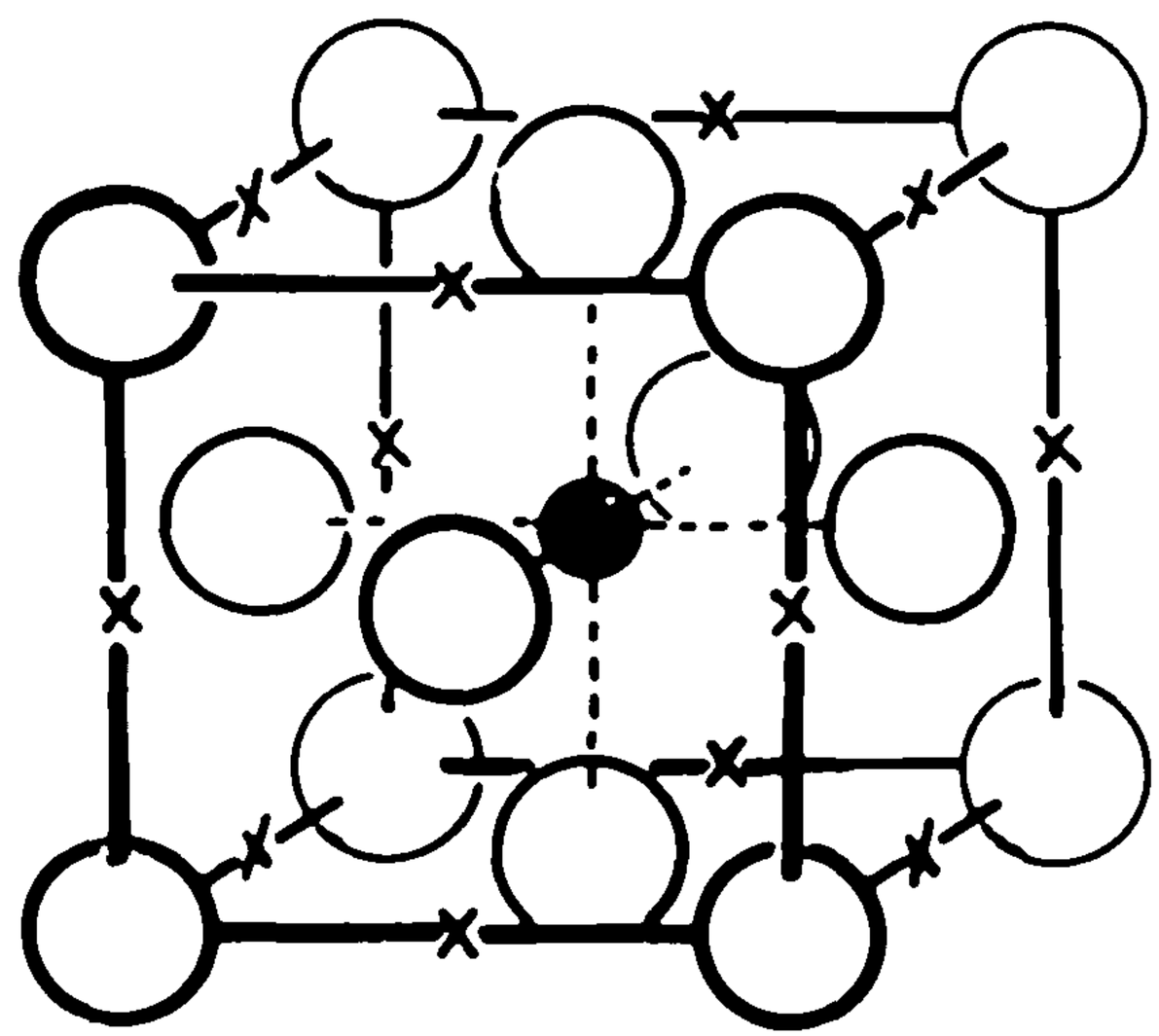

○ Fe atoms

× unoccupied interstices

o octahedral interstices
1 in 10 randomly filled

● N atom

intermediate both in structure and in composition between b.c.c. N-ferrite and f.c.c. γ' -Fe_4N.

II.2. The Tempering of Nitrogen Martensite

Nitrogen martensites have a morphology similar to that of carbon martensites and above about 0.3 w/o N lath martensite begins to be replaced by internally twinned martensite. Above 200°C nitrogen martensites decompose into ferrite plus γ' -Fe_4N , but below this temperature the intermediate precipitate, α'' -$Fe_{16}N_2$, occurs.

Metallographic and crystallographic examination of the Fe_4N which is produced during tempering of nitrogen martensites shows that the phase has a habit plane, an orientation relationship and an internal structure characteristic of a reverse martensitic transformation (Pitsch, 1961). This is, however, diffusion controlled so that local regions with close to the required composition must exist before the transformation occurs. A nitrogen concentration above that of the martensite average already exists in $Fe_{16}N_2$ and local fluctuations are more likely to initiate the martensite reaction within, or at the interface of the α'' transition phase than elsewhere. Once nucleated, Fe_4N grows by transfer of nitrogen from the dissolving $Fe_{16}N_2$ particles around it.

II.3. Kinetics of the Nitriding of Iron

Nitriding of iron is a diffusion controlled

process. The depth of penetration during nitriding may be obtained from the solution of Fick's Second Law of Diffusion:

$$dC/dt = D(\partial^2 C/\partial x^2) \qquad \ldots\ldots \text{II.1}$$

where C is the concentration of the diffusing species at a depth X after time t and D is the diffusion coefficient.

The solution of equation II.1 for the diffusion of nitrogen is

$$\frac{C}{C_s} = 1 - \frac{2}{\sqrt{\pi}} \int_0^{X/2\sqrt{Dt}} e^{-\lambda^2} \cdot d\lambda \qquad \ldots\ldots \text{II.2}$$

where C_s is the concentration of nitrogen at the surface ($X = 0$) and λ is an integration variable. Numerical solutions of this equation are tabulated by Darken & Gurry (1953).

II.4. Fe-X-N Systems

(a) Introduction

The substitutional-interstitial solute interactions occurring in nitrogen ferrites can be classified as taking place in three ranges of temperature, high, medium and low, defined by the relative mobilities of the substitutional and interstitial solutes. At high

temperatures, substitutional solutes such as Ti, V, Cr, Mn, Mo, Ta, and W move readily through the ferrite matrix to precipitate alloy nitrides by reaction with nitrogen. At low temperatures, where these solutes are unable to move, they still affect the precipitation of iron nitrides because they change the activity coefficients of interstitial elements (Pipkin, 1968; Speirs, 1969; Mortimer et al., 1972). At intermediate temperatures, where substitutional solute atoms move over only short distances in the same time that nitrogen moves over large ones, mixed solute-atom clustering is observed (Speirs et al., 1970). The clustered non-random solid solution is a pre-precipitation stage in a continuous series of transformations and is accompanied by a very high specific strengthening. The successive stages of homogeneous precipitation are analogous to those observed in the classical work on aluminium-copper alloys (e.g. Silcock et al., 1953-54).

During quench aging of Fe-X-N alloys the concentration of nitrogen, and hence the driving force for the reaction, decreases as the precipitation or clustering reaction proceeds and this leads to conditions under which different phases are stable at different stages of the treatment. Constant-activity aging eliminates this complication. Precipitation or clustering takes place at a rate controlled by the slowly diffusing substitutional solute, whilst nitrogen is replenished almost instantaneously from the gas phase and its activity maintained virtually constant throughout the specimen because of its very high diffusivity.

(b) Zone formation in Fe-X-N systems

Using constant-activity aging, Speirs (1969) produced mixed substitutional-interstitial solute-atom clusters, i.e. Guinier-Preston zones, in Fe-5w/oMo nitrided in $6NH_3:94H_2$ at 590°C. High hardnesses and microstructures almost identical to those of Al-4w/oCu aged at 160°C for 5h were reported. Similar results are obtained for Fe-V, Fe-Mn, Fe-Nb, and Fe-Ti alloys (Speirs et al., 1970) and the microstructures are also similar to those preceding the formation of α''-$Fe_{16}N_2$ in aged nitrogen ferrite (Roberts, 1970).

Since the GP zones observed in these alloys are very small and only a few atom-layers thick it might be argued that they are, in fact, very small coherent precipitates. However, the evidence that they are true GP zones formed by solute-atom clustering is based on the following observations:

(i) the abnormal nitrogen/substitutional solute atom-ratios (N/X) in the alloys are higher than can be accounted for by equilibrium nitride precipitates (Jack, 1975);

(ii) very high nitrogen potentials are required to form the zones compared with those necessary to precipitate the equilibrium nitride;

(iii) a zone solvus which is different from the solvus for the equilibrium nitride is observed (Roberts, 1970; Stephenson, 1973);

(iv) continuous streaking of matrix reflections with no maxima characteristic of the precipitate structure occurs on electron diffraction patterns of nitrided Fe-X alloys;

(v) the microstructures observed by transmission

electron microscopy (TEM) are similar to those for classical GP zones (e.g. in Al-4w/oCu);

(vi) there is a similarity with the initial stages of quench aging of nitrogen ferrite at room temperature where transformation occurs by diffusion and ordering of nitrogen atoms without major movement of iron atoms;

(vii) the interstitial content of clusters in nitrided Fe-5w/oMo can be continuously changed and reduced to zero by aging in hydrogen at 580°C to leave Mo atom clusters on {100} matrix planes (Driver et al., 1972). Mo clusters cannot be produced in Fe-5w/oMo without introduction of nitrogen nor can they be obtained by decomposition of the equilibrium nitride precipitate.

Further and more direct evidence is provided from measurement of the unit-cell dimensions of these alloys. Krawitz & Sinclair (1975) show that the unit-cell dimensions of a solid solution are essentially invariant with respect to the distribution and arrangement of its solute atoms. A matrix containing GP zones is a solid solution in which non-random local atomic arrangements exist, but its unit-cell dimensions are identical to a random solid solution having the same solute concentration. The unit-cell dimensions change to those of the solvent when complete precipitation occurs. The unit-cell dimensions of constant-activity nitrided Fe-Mo and Fe-V alloys are in close agreement with those expected for iron containing the same amount of solute in random solution (Pope et al., 1975), but electron microscopy, field ion microscopy and electron diffraction patterns indicate that the solute-atom distribution cannot be random. The solute atoms must therefore be clustered in a non-random solid solution.

(c) Conditions for zone formation

The general conditions for zone formation in Fe-X-N alloys can be summarised as:

(i) the nitrogen potential must exceed that of the zone solvus;

(ii) there must be a strong interaction between the substitutional solute and nitrogen. The most effective solutes are those which decrease the activity coefficient, $\left\{ {}^{X}_{N} \right.$, of nitrogen in iron (see Figure II.3), that is, they increase the solubility of nitrogen in equilibrium with a given gas atmosphere prior to precipitation;

(iii) the substitutional solute must have a high affinity for nitrogen (see Figure II.4);

(iv) the temperature should be high enough for movement of substitutional atoms over short distances, but not so high as to allow large-scale metal-atom movement and thus the ready nucleation and growth of the equilibrium alloy nitride.

(d) The precipitation sequence in nitrided Fe-X alloys

GP zones formed in Fe-X-N alloys age in a similar manner to those formed in Al-4w/oCu alloys and the precipitation sequence is similar to the stages of homogeneous precipitation which occur in pure Fe-N alloys on quench aging at 0^{o}-200^{o}C. On nitriding b.c.c. Fe-X alloys homogeneous precipitation occurs by continuous clustering of both interstitial and substitutional solutes and their subsequent ordering within the clusters. The precipitation sequence can be represented as

Figure II.3

The effect of alloying elements on the activity coefficient of nitrogen in liquid iron.

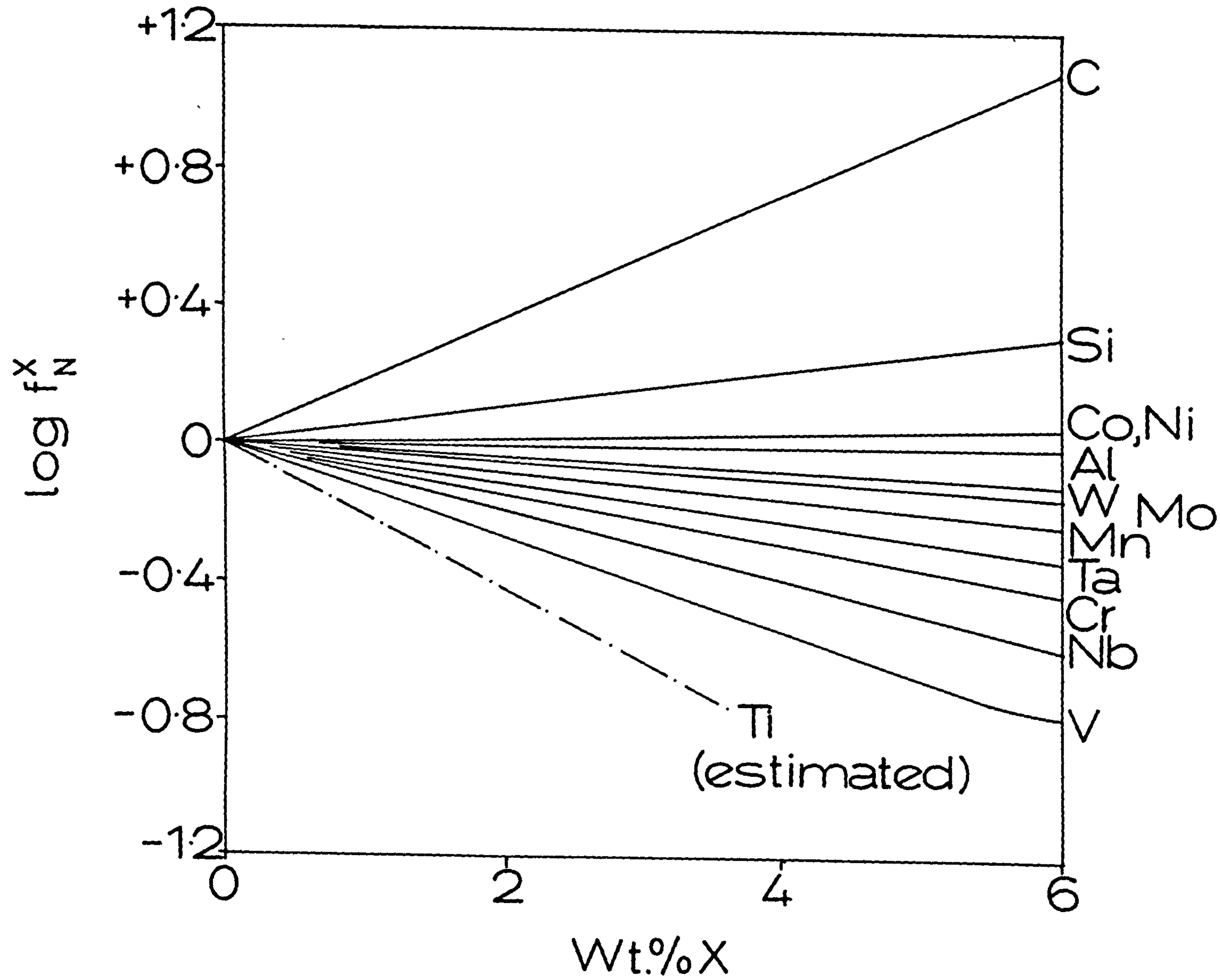
+1·2
+0·8
+0·4
0
-0·4
-0·8
-1·2
log f_N^x
0
2
4
6
Wt.%X
C
Si
Co,Ni
Al
W
Mo
Mn
Ta
Cr
Nb
V
Ti
(estimated)

Figure II.4

The standard free energies of formation of some nitrides.

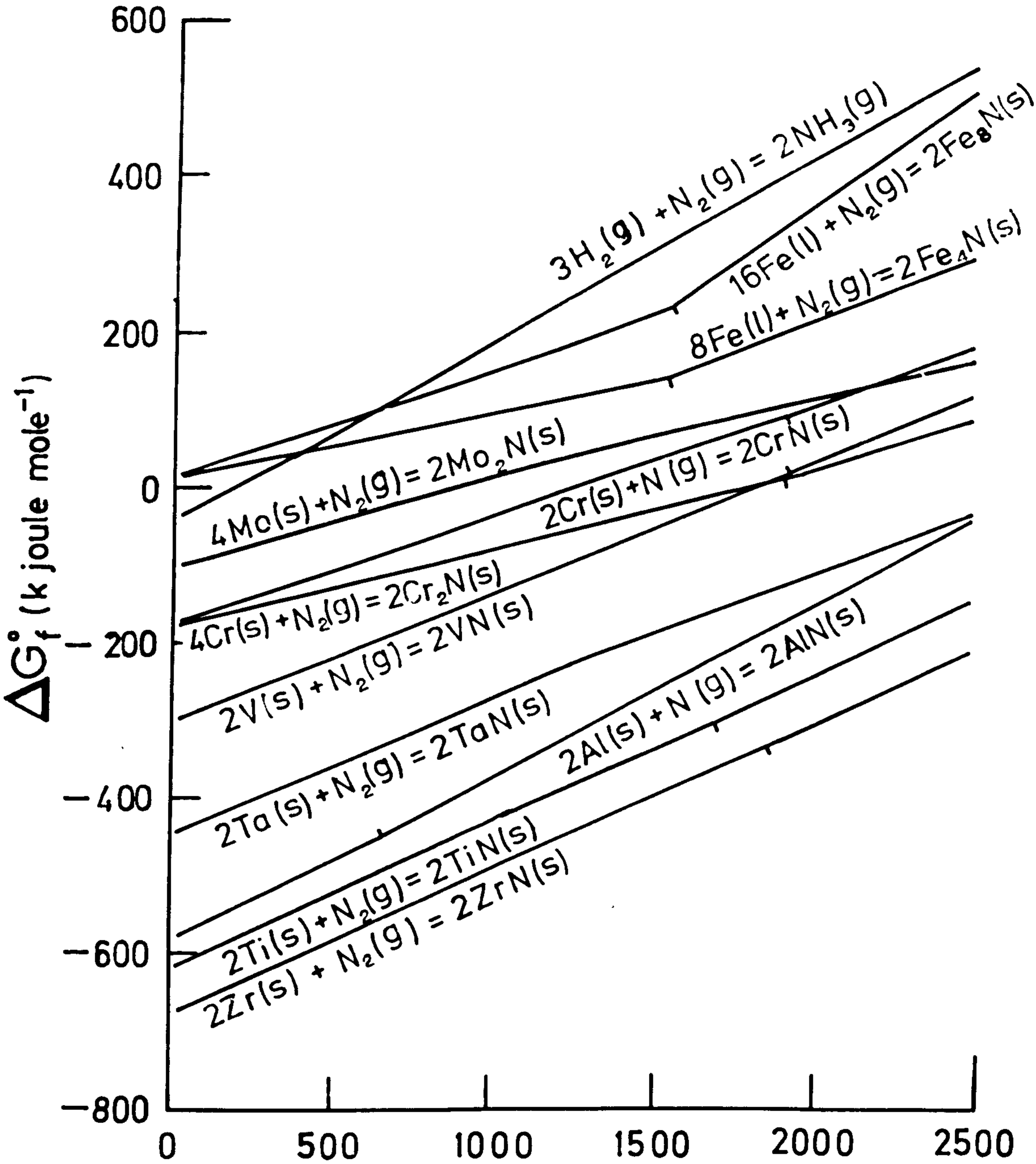

The reference states are pure phases which are stable at one atmosphere pressure and the designated temperature

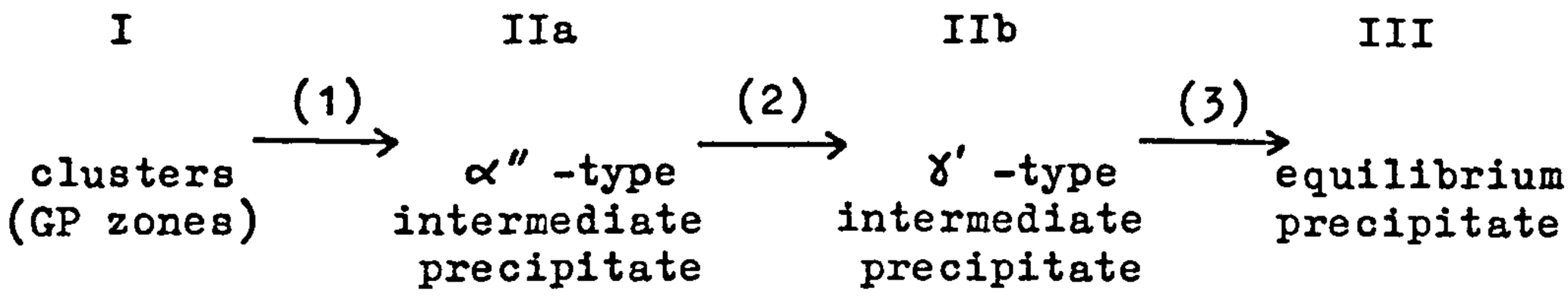

The designations α'' and γ' are not meant to imply rigid structure types but suggest respectively distorted b.c.c. and f.c.c. metal-atom arrangements accommodating nitrogen with or without ordering of either the substitutional or the interstitial solute atoms. Each particular system is different in detail. In Fe-Mo-N each of the above stages is fairly clearly recognised; in Fe-W-N , transformation (1) is rapid compared with (3) and so stage I is not observed (Stephenson, 1973), stage II being the first to be recognised.

II.5. The Nitriding Kinetics of Fe-X Alloys

The nitriding of Fe-Ti, Fe-V and high-chromium Fe-Cr alloys occurs by the formation of a hard, sharply defined subscale which advances progressively into the bulk of the material. The kinetics of subscale advance are consistent with the internal nitriding equation derived from the analogous internal oxidation equation of Hepworth et al. (1966):

$$x^2 = \frac{2}{r} \cdot \frac{[N]}{[X]} \cdot Dt \qquad \ldots\ldots \text{II.3}$$

where X = the subscale depth at time t

r = atom ratio (N/X) in the "compound" formed

D = the diffusivity of nitrogen in iron at the reaction temperature

$[N]$ = nitrogen concentration at the surface (a/o)

$[X]$ = concentration of alloying element X (a/o)

Departure from this behaviour occurs in Fe-Mo alloys (Jack et al., 1971) and at low substitutional solute concentrations in Fe-V (Pope, 1972) and Fe-Cr alloys (Mortimer, 1971).

There is a critical substitutional-interstitial activity product $(a_X . a_N)$ and a critical nucleus size, both of which must be exceeded for precipitation or solute-atom clustering to occur (Hayes, 1973). The precipitation or clustering process therefore depends on the flux of the substitutional element as well as the flux of nitrogen. Thus, in low substitutional content alloys, at high temperatures or where the substitutional solute has a low affinity for nitrogen, high nitrogen activities are required for the nucleation of clusters or precipitates.

In Fe-5w/oMo alloys, Jack et al. (1971) observed a gradual build up in hardness across the whole specimen during nitriding at 570°C until a peak hardness was reached. The hardness profiles across partially nitrided specimens were slightly dish shaped. This type of hardening occurs if the effective nitrogen activity across the thickness of the specimen is uniform. This may be achieved by the reduction of the rate of the surface reaction so that the flux of nitrogen atoms is slow compared with the diffusion of nitrogen in the solid. Hayes (1973) shows that this

behaviour is probably due to a thin oxide layer on the surface of the specimen and that with careful specimen preparation and pretreatment in pure hydrogen at the nitriding temperature, nitriding occurs by subscale advance. The subscale is not sharply defined, but this is attributed to the relatively low affinity of molybdenum for nitrogen (see Figure II.4). The rate of subscale advance under these conditions is closely approximated by the internal nitriding equation (equation II.3).

II.6. The Iron-Chromium-Nitrogen System

The nitriding kinetics of Fe-Cr alloys containing greater than 2w/oCr are consistent with the internal nitriding equation II.3 (see Mortimer et al., 1972). Mortimer's work suggested that in the Fe-Cr-N system stages (1) and (2) of the precipitation sequence (see section II.4(d)) were very rapid and only the equilibrium precipitate CrN was observed, even at nitriding temperatures as low as 475°C and at very short nitriding times. However, this work was completed before it was realised that the presence of equilibrium precipitates or pre-precipitation zones can be differentiated by measuring the X-ray lattice parameter of the matrix; see Krawitz & Sinclair (1975). Subsequently, the alloys used by Mortimer were re-examined by Pipkin & Middleton (1973) using X-ray methods. The results suggested that the majority of the nitrogen in nitrided Fe-Cr alloys is precipitated as CrN in alloys with relatively high chromium content (5.6w/o) at all nitriding temperatures and in the lower chromium alloys (1.2w/o and 2.3w/o) when

nitrided at 575°C for relatively long times. At lower nitriding temperatures or shorter nitriding times the low chromium alloys have high lattice parameters, indicating that the nitrogen is present in clusters. However, in all cases the total nitrogen estimated from weight gains is higher than the concentration found from lattice parameter measurements, showing that some CrN precipitation occurs.

II.7. The Iron-Titanium-Nitrogen System

The nitriding kinetics of Fe-Ti alloys containing 0.35-2.3a/oTi are consistent with the internal nitriding equation II.3 (Jack et al., 1971). The high hardnesses of the subscales of nitrided alloys are proportional to the square root of the titanium contents (Jack et al., 1971; Kirkwood et al., 1974).

The zones occurring in nitrided Fe-Ti-N alloys are very thin plates (Henderson, 1976) with a N:Ti atom ratio varying between 3 and 1 during nitriding and subsequent hydrogen reduction treatments respectively. The formation of metastable zones in Fe-Ti-N alloys is the first stage of a precipitation sequence that produces f.c.c. TiN. Aging the clustered alloy at high temperatures (800° and 850°C) gives stable TiN precipitates that show characteristic electron diffraction patterns but the X-ray lattice parameter of the matrix unexpectedly remains much higher than that of ferrite. It seems probable that some of the very small TiN precipitates remain coherent with the matrix and, although large enough to diffract short

wavelength electrons, continue to diffract longer wavelength X-rays as if they were merely strained regions of the matrix. As might be expected on this model, the X-ray reflections show marked strain-broadening.

II.8. The Iron-Molybdenum-Nitrogen System

The formation of mixed substitutional-interstitial clusters in nitrided iron-molybdenum alloys is accompanied by large increases in hardness. The microstructure consists of an array of thin plate-like zones lying on $\{100\}$ matrix planes (Speirs, 1969). Field-ion microscopy confirms that these are coherent disc-shaped clusters and not γ -Mo_2N precipitates (Driver & Papazian, 1973).

Driver (1972) suggests that the precipitation sequence which occurs during aging at 800°C of an Fe-5w/oMo alloy, nitrided in $7NH_3:93H_2$ at 580°C, is

$$\text{GP1 zones (clusters)} \longrightarrow \text{Ordered zones (cf. } \alpha'' \text{)} \longrightarrow \text{GP2} \longrightarrow \gamma\text{-}Mo_2N \text{ (cf. } \gamma' \text{)} \longrightarrow \eta\text{-}Fe_3Mo_3N$$

which is consistent with the sequence generally found in nitrided Fe-X alloys; see Section II.4(d).

Chapter III

OXIDATION OF METALS AND ALLOYS

III.1. Oxidation of Iron

Iron forms three stable oxides: wustite, FeO; magnetite, Fe_3O_4; and haematite, Fe_2O_3. The equilibrium diagram is shown in Figure III.1 (from Kubaschewski & Hopkins, 1962). Wustite has a NaCl-type structure but it can never be prepared with the "ideal" composition FeO; it always contains "excess oxygen". The oxygen anion arrangement is face-centred cubic and at the "ideal" composition ferrous ions would occupy all the octahedral interstices. Some ferric ions, however, are always present, i.e. a small number of ferrous ions are replaced by two-thirds of their number of ferric ions (to maintain electrical neutrality), therefore certain cation sites are left vacant. Wustite is consequently a p-type semi-conductor, diffusion being essentially via cation sites.

Magnetite has a spinel structure. Spinels have the general formula AB_2X_4, where A is usually a divalent cation and B a trivalent cation. The unit cell contains 32 anions in a f.c.c. array made up of eight smaller face-centred cubes, each with four anions at the corners and face-centres. For "normal" spinels the A ions occupy one-eighth (8) of the tetrahedral holes in an ordered manner and B ions

Figure III.1

The equilibrium diagram for iron-oxygen

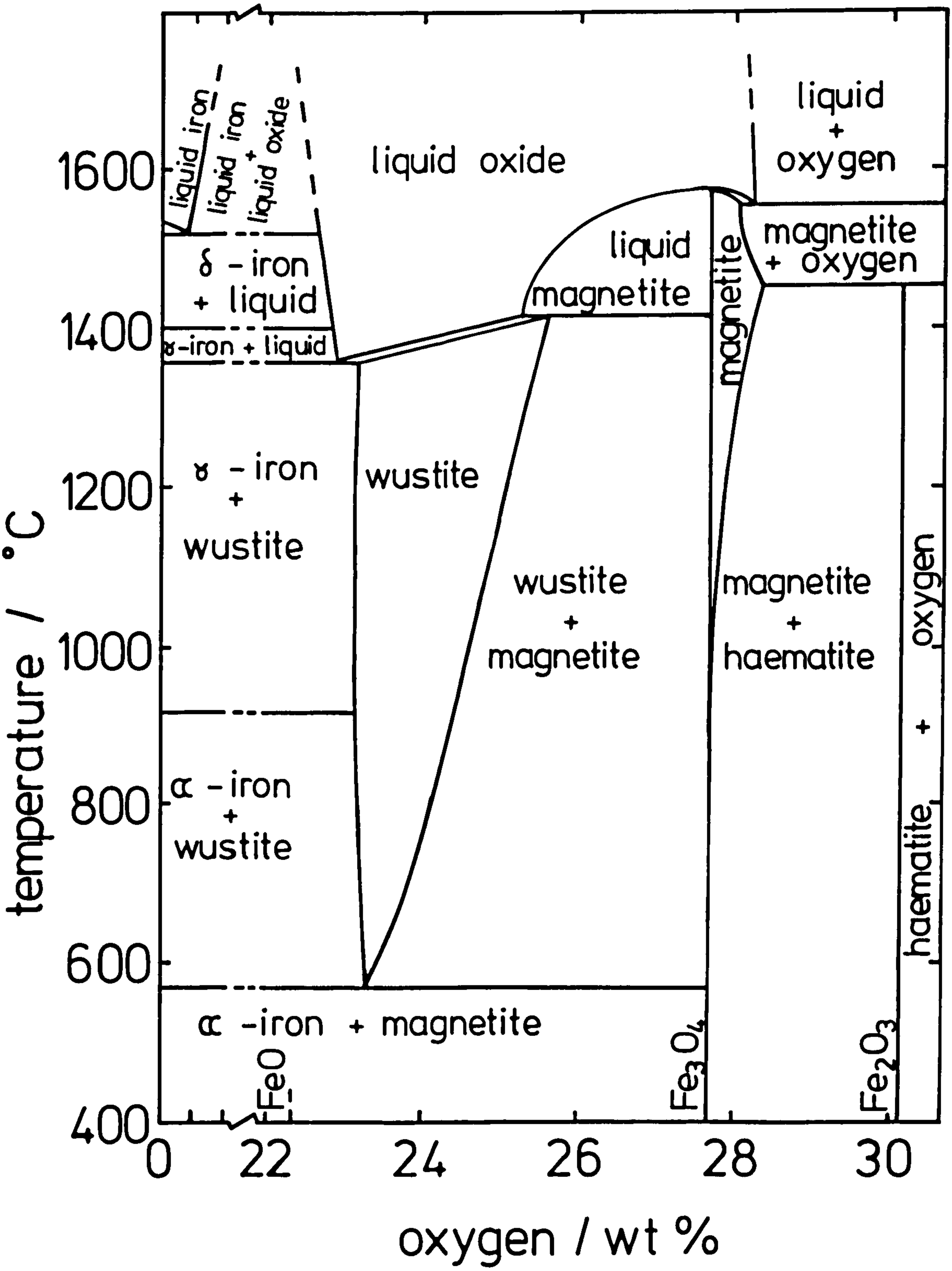
liquid iron
liquid iron + liquid oxide
liquid oxide
liquid + oxygen
δ - iron + liquid
liquid magnetite
magnetite
magnetite + oxygen
γ-iron + liquid
γ - iron + wustite
wustite
wustite + magnetite
magnetite + haematite
oxygen + haematite
α - iron + wustite
α - iron + magnetite
1600
1400
1200
1000
800
600
400
temperature / °C
0
22
24
26
28
30
FeO
Fe3O4
Fe2O3
oxygen / wt %

occupy one-half (16) of the octahedral interstices also in an ordered way. Some oxides of this composition, including magnetite, have an alternative "inverse" structure in which the pattern of sites and distribution of the oxygen ions is exactly as in the normal spinels but where the arrangement of the cations is different. One-half of the B ions occupy tetrahedral interstices and the other half, together with the A ions, are randomly distributed among 16 of the 32 octahedral sites. Magnetite is also a p-type semi-conductor, diffusion again being mainly cationic.

Haematite, α -Fe_2O_3, has a structure which may be described as a hexagonal close-packed array of oxygen atoms with metal atoms in two-thirds of the octahedrally co-ordinated interstices. It is an n-type semi-conductor with predominant anion diffusion.

Above 250°C and at normal pressures of air or oxygen, the oxidation rate of iron is parabolic (see Pilling et al., 1923; Winterbottom, 1950; Davies et al., 1951; Stanley et al., 1951). Figure III.2 shows the dependence of the parabolic rate constant on temperature.

III.2. Oxidation of Iron Alloys

(a) Iron-Chromium

Steels containing chromium are among the most oxidation resistant commercial alloys. Whilst low-chromium steels show an oxidation resistance little better than iron, concentrations of more than 12% Cr

Figure III.2

The dependence of parabolic rate constant (k_p) with temperature for iron (after Kubaschewski & Hopkins, 1962).

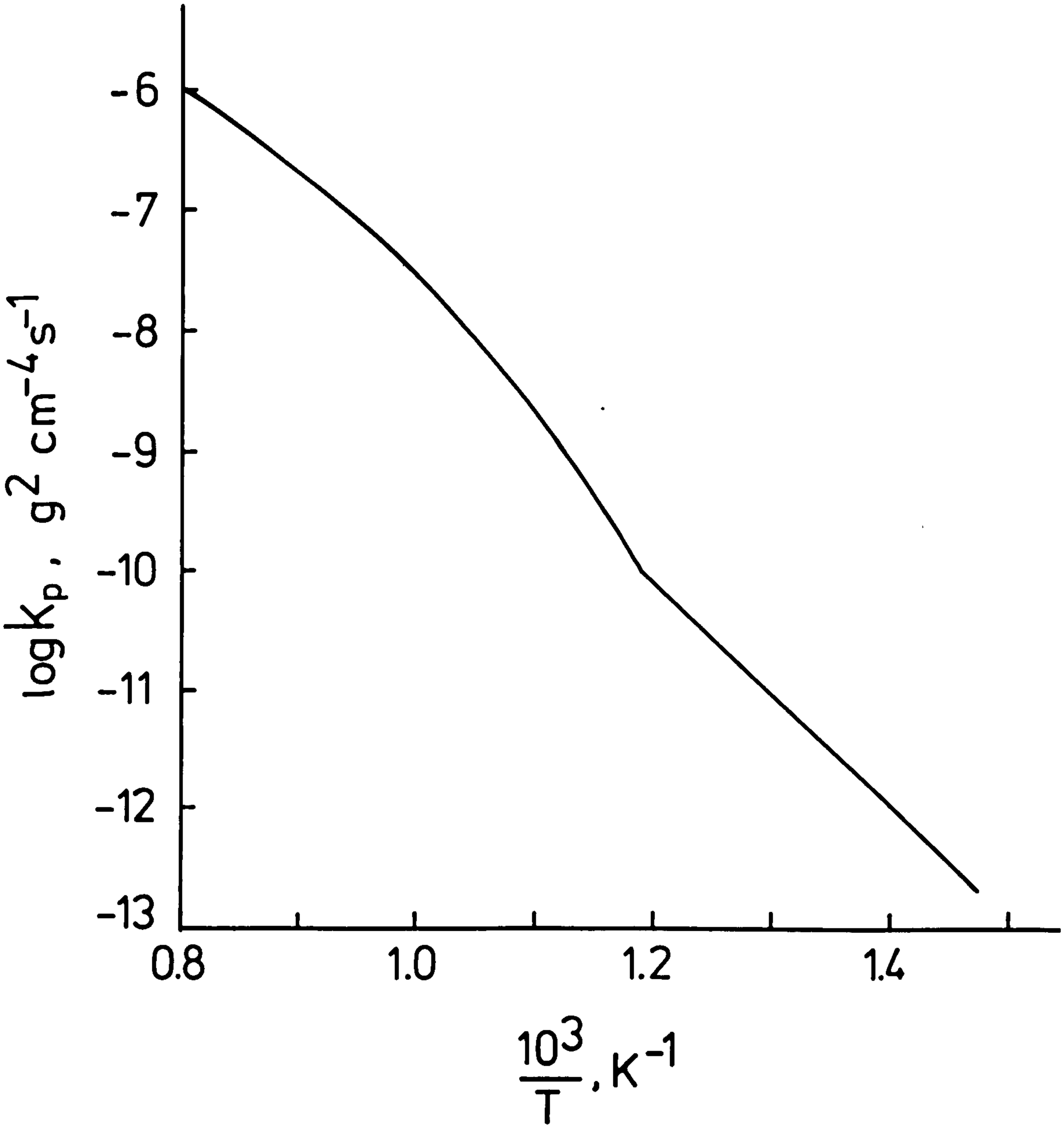
-6
-7
-8
-9
-10
-11
-12
-13
$g^2\,cm^{-4}s^{-1}$
$\log K_p$,
0.8
1.0
1.2
1.4
$\frac{10^3}{T}$, K^{-1}

below 1000°C, and more than 17% above 1000°C increase the oxidation resistance by about two orders of magnitude. The effect is shown in Figure III.3, where the factor, F, represents the ratio between the oxidation rate of alloyed material and that of pure iron.

In the first stages of oxidation of iron-chromium alloys, the rate of reaction is fairly rapid. Only when a layer of Cr_2O_3, or spinels such as $FeCr_2O_4$, is formed at the metal/scale interface is a protective effect accomplished (Yearian et al., 1956) and at least 3% chromium is required.

Cracking of the scales on iron-chromium alloys has been observed by a number of researchers (see Caplan & Cohen, 1952; Lai et al., 1961; Wood et al., 1970; Lloyd et al., 1977). There is a strong tendency for chromium-containing scales to spall on cooling which renders them less protective under thermal cycling conditions.

(b) Iron-Titanium

In percentages of 0.7-6, titanium slightly increases the oxidation resistance of iron, as indicated in Figure III.3. Oxidised titanium compounds are found near the metal/oxide interface and the formation of $FeO.TiO_2$ is suggested (Scheil et al., 1936).

(c) Iron-Molybdenum

As shown in Figure III.3, small concentrations of

Figure III.3

Effect of some alloying elements on the oxidation of iron (after Kubaschewski & Hopkins, 1962).

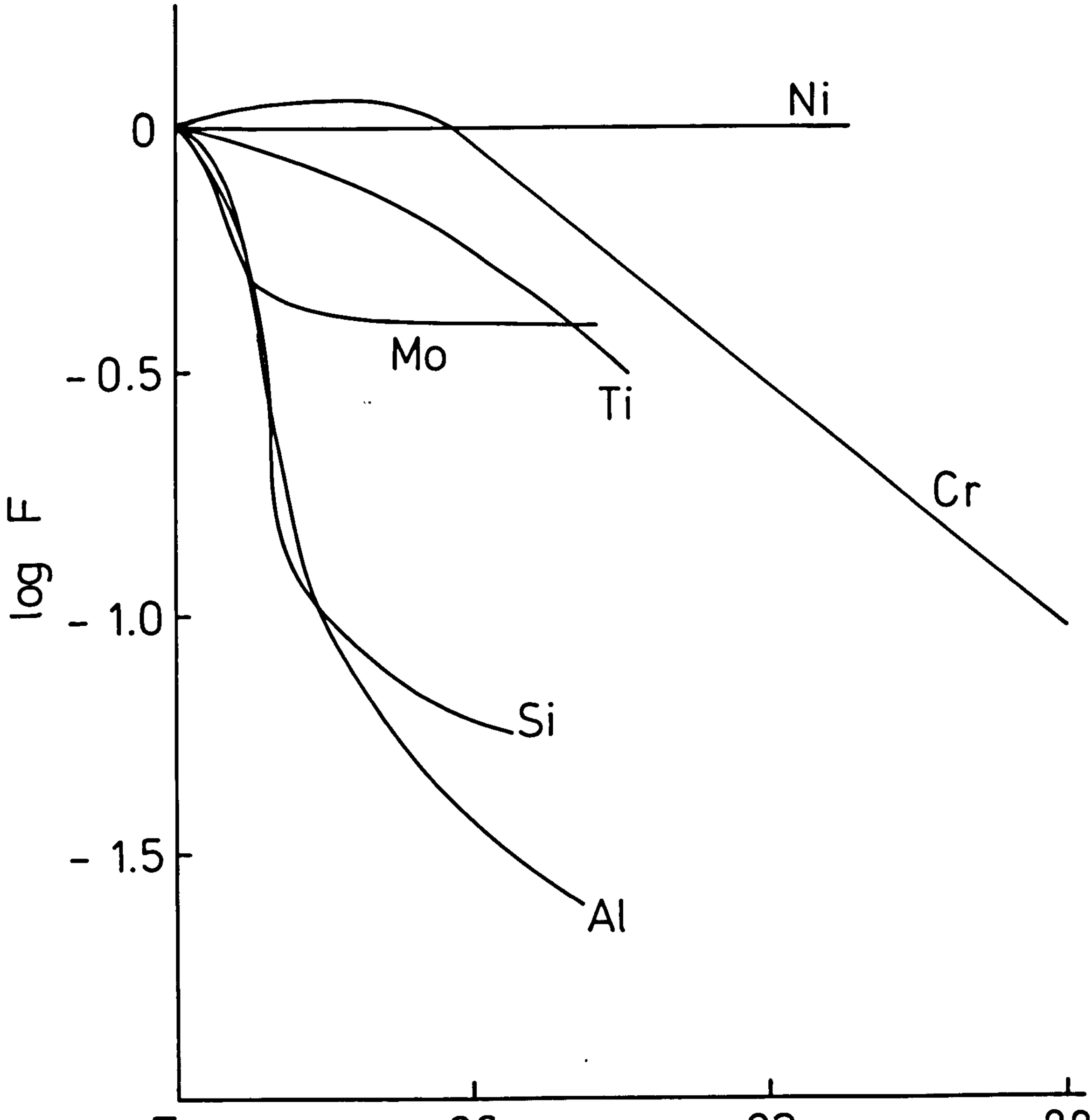
Ni
0
Mo
- 0.5
Ti
Cr
log F
- 1.0
Si
- 1.5
Al
Fe
96
92
88
wt% Fe

molybdenum somewhat improve the oxidation resistance of iron at 600°-1000°C (Rahmel et al., 1959; Scheil et al., 1936). This is due to the formation of oxides (Fe_2MoO_4 or, below 620°C, $Fe_4Mo_6O_{16}$) in which diffusion rates may be less than in Fe_3O_4.

In his detailed studies of Fe-Mo alloys at 800°-1000°C, Brenner (1955) found that up to 20% Mo decreases the oxidation rate of iron in oxygen at atmospheric pressure, the most marked decrease occurring with the first 2% Mo. The scale consists of three distinct layers, the outermost being Fe_2O_3, the middle Fe_3O_4, and the innermost MoO_2 together with an unidentified double oxide Fe_xMo_yO. Most of the molybdenum in the scale is found in the innermost layer.

III.3. Oxidation Kinetics

It is well-known that many metals absorb oxygen according to the parabolic rate law:

$$w^2 = k_p.t \qquad \text{.... III.1}$$

where w is the weight of oxygen absorbed at time t, and k_p is the parabolic rate constant (Tamman, 1920; Pilling & Bedworth, 1923). This empirical result was predicted by Wagner (1933), but a number of other oxidation rate relationships have been observed and described in terms of empirical equations.

The products of oxidation may consist of a number of different phases. In the classical model, the

oxidation surface was regarded as an infinite plane, and consequently the flow of reactants could be considered as taking place entirely normal to this surface. For a pure metal the phase rule demands that a two-phase layer cannot be formed in these circumstances, so that the reaction products consist of single-phase layers with essentially plane interfaces parallel to the metal surface. The sequence of phases is such that the oxygen activity falls progressively as the metal surface is approached. In each phase there is an oxygen activity gradient sufficient to provide the necessary reactant flux through the layer.

Pilling & Bedworth (1923) made the point that if the rate-controlling step is the transport of material across one of the layers, then, since the layer becomes proportionately thicker, the rate of transport and hence the overall reaction rate decreases with time. If it is assumed that the transport process is the same throughout the material, and does not change with time, then the rate of transport is inversely proportional to the thickness of the layer, X :

$$dm/dt = 1/X \qquad \text{.... III.2}$$

where dm/dt is the rate of transport of the reactants across the layer. This condition implies that

$$X = \text{const.}m \qquad \text{.... III.3}$$

Hence,

$$X^2 = k_p.t + k_o \qquad \text{.... III.4}$$

where, m is the amount of reactant transported across the layer in time t, and k_p and k_o are reaction constants.

III.4. Oxidation of Alloys

Wood (1970) has reviewed the high-temperature oxidation of alloys and proposes the following classification for binary alloys AB in which A is more noble and B less noble:

Class I: Only one of the elements (B) oxidises.

(a) The element B is the minor constituent and oxidises -
   (1) internally, giving BO particles in a matrix of A, e.g. Ag-Si alloys containing small concentrations of Si produce SiO_2 particles in a silver matrix,
   (2) externally, giving a single layer of BO above an alloy matrix depleted in B; Ag-Si alloys richer in Si produce an external SiO_2 layer.

(b) The element B is the major constituent and oxidises exclusively -
   (1) leaving the non-oxidizable metal A dispersed in BO; e.g. Cu-Au alloys rich in Cu,
   (2) leaving the non-oxidizable metal A in an A-enriched zone behind the BO scale, e.g. Ni-Pt alloys and Fe-Cr alloys

which are rich in Cr.

Class II: In this class both A and B oxidise to give AO and BO, the oxygen pressure in the atmosphere being greater than the equilibrium dissociation pressure of either oxide.

(a) AO and BO combine to give -

(1) a single solid solution; Ni-Co alloys behave in this way,

(2) a double oxide, often a spinel, which may produce a complete surface layer of variable composition; this happens in certain Fe-Cr alloys. There may be particles incorporated in a matrix of AO as in the case of some Ni-Cr alloys.

(b) AO and BO are virtually insoluble in one another and

(1) the less noble metal B is the minor component, and an internal oxide of BO lies beneath a mixed layer of AO and BO; this occurs in particular Cu-Ni, Cu-Zn, and Cu-Al alloys,

(2) the less noble metal B is the major component, so that no internal oxidation is now observed. In practice, BO may not be present in the outer regions of scale because AO may grow rapidly to produce a layer exclusively of this oxide. Sometimes the outer regions are oxidised to higher oxides, e.g. on Cu-Si alloys CuO is found outside the Cu_2O layer.

III.5. Origin of Stresses in Oxide Scales

The main factors that influence the stresses developed during isothermal oxidation are:

(a) The influence of the volume ratio of the oxide and the metal from which it is produced.

Pilling & Bedworth (1923) postulated that the ratio of the volume of oxide to the volume of metal from which it was formed (the Pilling-Bedworth ratio) was an important parameter in determining the protective nature of oxide scales. In general, metals that oxidise by inward diffusion of oxygen will produce stresses in the oxide unless the volume ratio is unity. If the Pilling-Bedworth ratio is greater than unity, the oxide will form in compression, if less than unity, the oxide will form in tension. If the metal oxidises by outward movement of metal ions, then the oxide should be unstressed because it is formed at a free surface.

(b) The epitaxial relationships between the metal and its surface oxide.

The lattices of metals and surface oxides are usually dissimilar. Hence the nucleation and growth of oxides on metal substrates may be accompanied by the development of epitaxial stresses. Once an oxide scale grows, however, the epitaxial constraints diminish so that stresses induced by epitaxy will be important mainly for thin films at low temperatures.

(c) The influence of compositional changes that occur in the metal and the surface oxide during

oxidation.

Howes & Richardson (1969) consider that compositional changes are responsible for the tensile deflection obtained initially in the oxidation of iron-chromium alloys. In the growth of multilayer oxide scales, the sequence of interfaces and the difference in growth rate of the different layers may have deleterious effects on the adherence of the oxide scale and on its protective properties (Kofstad, 1966).

(d) The influence of vacancies generated during oxidation.

Metals that oxidise by cation diffusion through the oxide film generate vacancies at the oxide/oxidant interface and these vacancies may accumulate at the metal/oxide interface as shown in iron-chromium alloys by Howes (1970). These interface voids will lead to lack of adhesion and scale spalling.

Holmes & Pascoe (1972) list the parameters which affect the spalling resistance during thermal cycling as:

(i) The difference between the thermal expansion coefficients of the metal and oxide, or between two oxide layers;

(ii) volume changes during phase or composition changes;

(iii) the magnitude and direction of the thermal cycle (ΔT);

(iv) the rate of change of temperature (dT/dt);

(v) the oxide thickness;

(vi) the yield stress and creep behaviour of the

metal oxide at strain rates determined by dT/dt and over the temperature range ΔT;

(vii) modifications to the structure of the metal or oxide close to the interface by factors such as internal oxidation, oxide porosity and interface voids;

(viii) specimen geometry;

(ix) changes of heat flux.

III.6. Scale Adhesion and Morphology

Stringer (1966) considers the most important property of a metal-oxide system to be the adhesion between the metal and the oxide layer and the closely associated properties involving the plastic flow of the oxides in the immediate vicinity of the interface. In practice, a slow rate of oxidation is usually associated with a process in which the rate-controlling step is the transport of the reactant through the scale layer. However, the scale layer eventually fails and so the useful life of an alloy in an oxidising atmosphere is frequently limited by the lifetime of the protective scale layer.

Often, the layer fails when it exceeds a critical thickness, X_c, and the time to failure can be increased either by slowing the transport rate through the scale or by increasing X_c. The latter may be achieved by increasing either the fracture strength of the scale or the adhesion at the metal/scale interface.

For a scale to be protective, i.e. to restrict

the access of the reactants to each other, it is not necessary for it to be in intimate contact with the metal. However, if it is not in contact, transfer of metal ions into the scale must take place through the vapour phase. Furthermore, since the scale is not supported by the metal, it will have poor resistance to shock and abrasion. Otherwise, the scale and the metal must be in such close proximity that direct atom transfer from the metal to the scale can take place.

It is possible that the stresses generated during oxidation may be relieved by plastic deformation of the oxide scales. Of the mechanisms of oxide deformation (Stringer, 1970; Douglass, 1971) the most common high-temperature processes are grain-boundary sliding, Herring-Nabarro creep and dislocation climb.

There is little direct evidence of boundary sliding at temperatures which surface oxides on metal substrates are likely to encounter. Nabarro (1948) proposed a mechanism involving self-diffusion that permits grains of a polycrystalline material to deform under a shear stress. This requires a flow of matter away from boundaries where there is a normal pressure and towards those having a normal tension. Herring (1950) derived a tensile strain rate given by

$$\dot{\epsilon} = \frac{13 \cdot 3\, D_L \Omega}{kTd^2} \cdot \sigma \qquad \ldots\ \text{III.5}$$

whereas Coble (1963) assumed grain-boundary diffusion as a rate-controlling creep step and obtained the

expression

$$\dot{\epsilon} = \frac{47\ D_b W \Omega}{kTd^3} \cdot \sigma \qquad \ldots\ldots \text{III.6}$$

where D_L = bulk self-diffusion coefficient (for the slowest moving species);

d = average grain diameter;

Ω = volume of the diffusing species;

σ = stress;

k = Boltzmann's constant;

T = temperature, ^{o}K;

D_b = grain-boundary diffusivity of the slowest moving species;

W = width of the grain boundary.

The expressions III.5 and III.6 show that the strain rate is proportional to the reciprocal of the square or the cube of the grain-size respectively, and thus a high strain rate is favoured by a very small grain size. Hancock & Hurst (1974) state that whilst diffusion creep has been reported in a number of oxides it is always at very high temperatures and hence, whilst not discounting it, consider Herring-Nabarro creep an unlikely mechanism for relief of surface oxide stresses on metal substrates. However, Holmes & Pascoe (1972) state that the observed creep rates of most fine-grained oxides are consistent with deformation by the Herring-Nabarro mechanism, and give results in support of this for creep in haematite at 1000^{o}C over a limited range of stress.

Dislocation climb processes have generally been regarded as important in creep processes in oxides.

Material transport is involved in the non-conservative motion of dislocations and since the overall stoichiometry must be maintained in oxides, it is expected that the slower moving ionic species will control the overall diffusion rate and hence the climb rate. However, Ilschner et al. (1964) show that the creep rate of wustite increases with x, the departure from stoichiometry of the composition $Fe_{(1-x)}O$, even though the oxygen ion diffusivity should not increase as x increases.

In general, diffusional creep operates under low applied stresses in fine grained materials while dislocation creep mechanisms operate at larger grain sizes and applied stresses.

In addition to the problems associated with the existence, magnitude and relief of growth stresses, adhesion in oxides requires that crack propagation along the interface should be difficult and that the mechanism of the reaction should not lead to metal-oxide separation. Crack propagation is regarded as limiting because it is felt that in most oxidation processes it is not possible to avoid the nucleation of cracks, or virtual cracks, particularly if in practice the oxidation includes a number of heating and cooling cycles. A variety of factors can result in crack propagation becoming more difficult. For example, if the oxide contains pores, although these may act as crack nuclei they may also serve to blunt, and hence stop, the running crack. Ductile metallic inclusions may also be helpful in this respect and may not lead to as many bad effects as pores. Conversely, crack propagation may become easier if the scale contains small amounts of a more brittle oxide, which

may act both as stress-raisers and as crack-initiators. The mechanism of the oxidation reaction might lead to a loss of scale adhesion if, for example, impurities in the metal are not incorporated in the scale but accumulate at the metal/scale interface. Also vacancies may accumulate and condense at the metal/scale interface to form large fissures and in this case alternative nucleation sites for vacancy condensation must be provided.

The oxidation of iron is an example of a reaction in which the removal of vacancies from the metal/oxide interface presents a problem. When iron is oxidised the scale eventually ruptures from the metal surface. Dunnington et al. (1952) demonstrated that for a thick iron specimen the scale ruptured from both sides, but for a thin specimen from one side only. They speculated that the rupture was due to condensation of vacancies as voids at the scale/metal interface. In the case of the thin sheet, a void nucleates on one side by chance and then acts as a sink for vacancies from both sides, thus preventing the nucleation of a void on the other side. For a thick sheet, the diffusion distance is too great and voids nucleate on both sides. This hypothesis was tested by Tylecote & Mitchell (1960) who oxidised iron sheets. Holes were drilled down the centres of some of the sheets parallel to the surface. The scale separated from the sheets without the holes but remained adherent much longer to the sheets with holes. In addition, the holes increased in diameter, confirming that they had acted as vacancy sinks.

An investigation into the effect of cold work on the oxidation of iron (Caplan & Cohen, 1966) showed

that at temperatures below those required to form FeO, the rate of oxidation of iron can differ by up to two orders of magnitude, cold worked material oxidising at a faster rate than annealed material. It was proposed that cold worked material provides vacancy sinks at dislocations or lattice steps on the surface of the iron. The oxide thus remains in good contact with the metal and forms a non-porous layer at a rapid rate. The porous, separated scales that develop on annealed iron result in a slower rate of transference of metal cations across the Fe/Fe_3O_4 interface, and hence in a slower oxidation rate.

III.7. Oxidation of Nitrided Alloys

In the work of Hendry (1978) which stimulated the present research, the oxidation resistance of nitrided mild steel in simulated flue gases was investigated. Mild steel, nitrided to give a N-martensite/austenite case was oxidised (i) isothermally, (ii) under thermal cycling, and (iii) with oxygen potential cycling. Figure III.4 shows that nitrided mild steel has improved oxidation resistance over the un-nitrided material, the effect being more apparent with thermal cycling and with oxygen potential cycling than under isothermal conditions.

The refinement of the oxide grain size and the modifications of the condensation process for vacancies were thought to explain the increased resistance to oxide exfoliation. Thus, the fine microstructure of the nitrided layer provided a large number of sites suitable for oxide nucleation and

Figure III.4

Oxidation curves of steels in simulated flue gas (after Hendry, 1978).

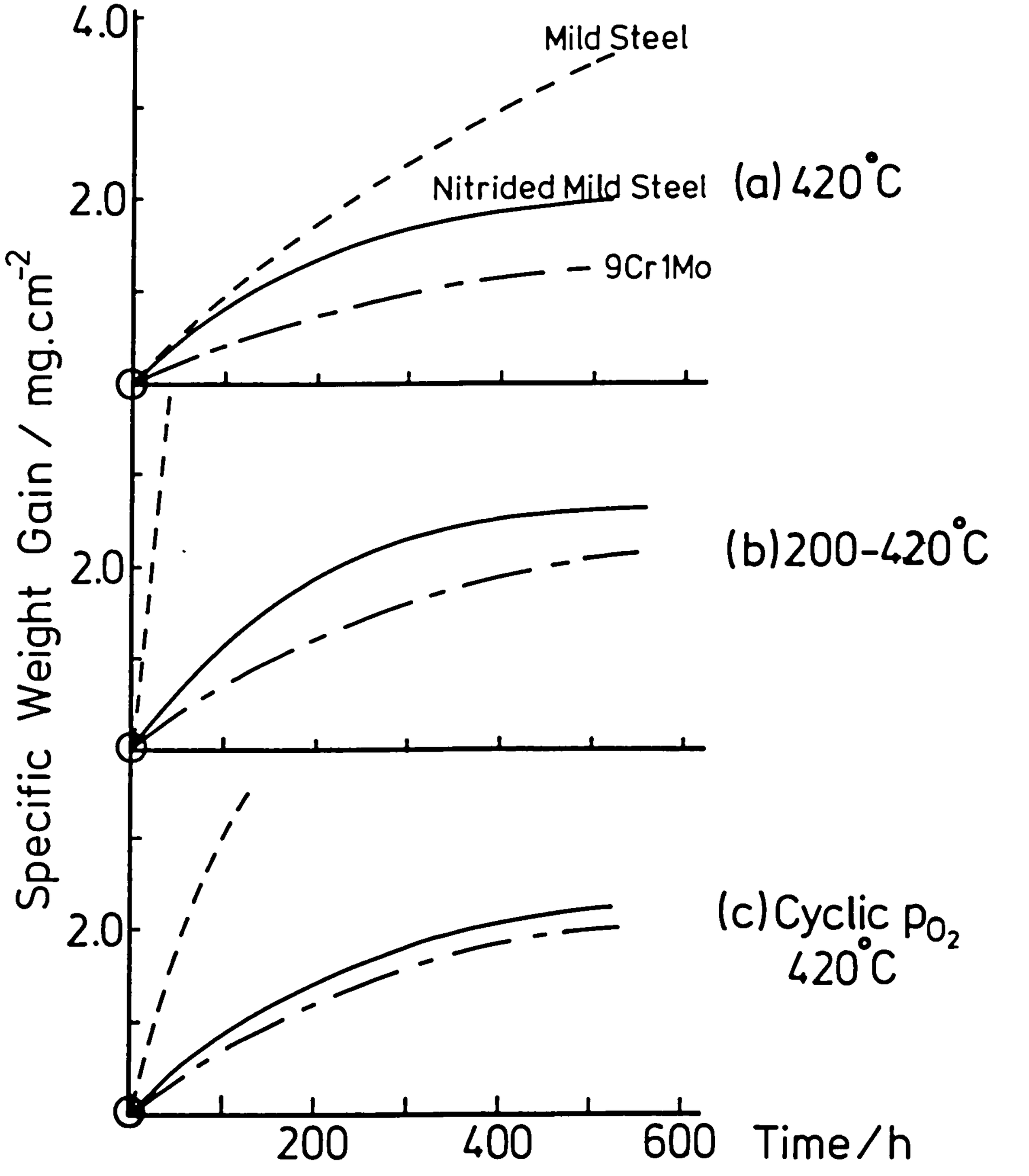
4.0
2.0
2.0
2.0
Specific Weight Gain / mg.cm-2
Mild Steel
Nitrided Mild Steel
9Cr1Mo
(a) 420°C
(b) 200-420°C
(c) Cyclic P_{O_2} 420°C
200
400
600
Time/h

consequently a finer grain size oxide than for the un-nitrided steel. It was also considered that voids were not formed at the metal/oxide interface, as normally observed, but occur at triple point cracks within the metal that are formed during stress relaxation at the oxidation temperature and which then act as vacancy sinks.

Further work by Hendry which is reported by Coates & Hendry (1979; see Appendix) investigated the oxidation of an Fe-0.15w/oTi alloy nitrided to produce a stable distribution of TiN particles in the surface layer. A fine-grained oxide formed on the nitrided material when oxidised at 420°C in air showed a greater adherence to the metal substrate than the oxide on an un-nitrided alloy; see Figure III.5.

III.8. Oxidation of Superalloys Containing Dispersed Particles

Recently there has been a great deal of interest in the oxidation of superalloys containing dispersions of oxides or of rare earth elements. The effects of finely distributed stable oxides on the oxidation behaviour of alloys based on Ni-Cr, Co-Cr, or Fe-Cr have been well documented (Wallwork et al., 1971; Giggins & Pettit, 1971; Davis et al., 1971; Stringer et al., 1972; Stringer & Wright, 1972; Wright & Wilcox, 1974; Whittle et al., 1977). The following effects summarise the role of the dispersed oxide:

(1) a continuous, protective Cr_2O_3 scale is established at chromium levels considerably

Figure III.5

Scanning electron micrographs of oxide on Fe-0.15w/oTi oxidised at 420°C for 500h in air.

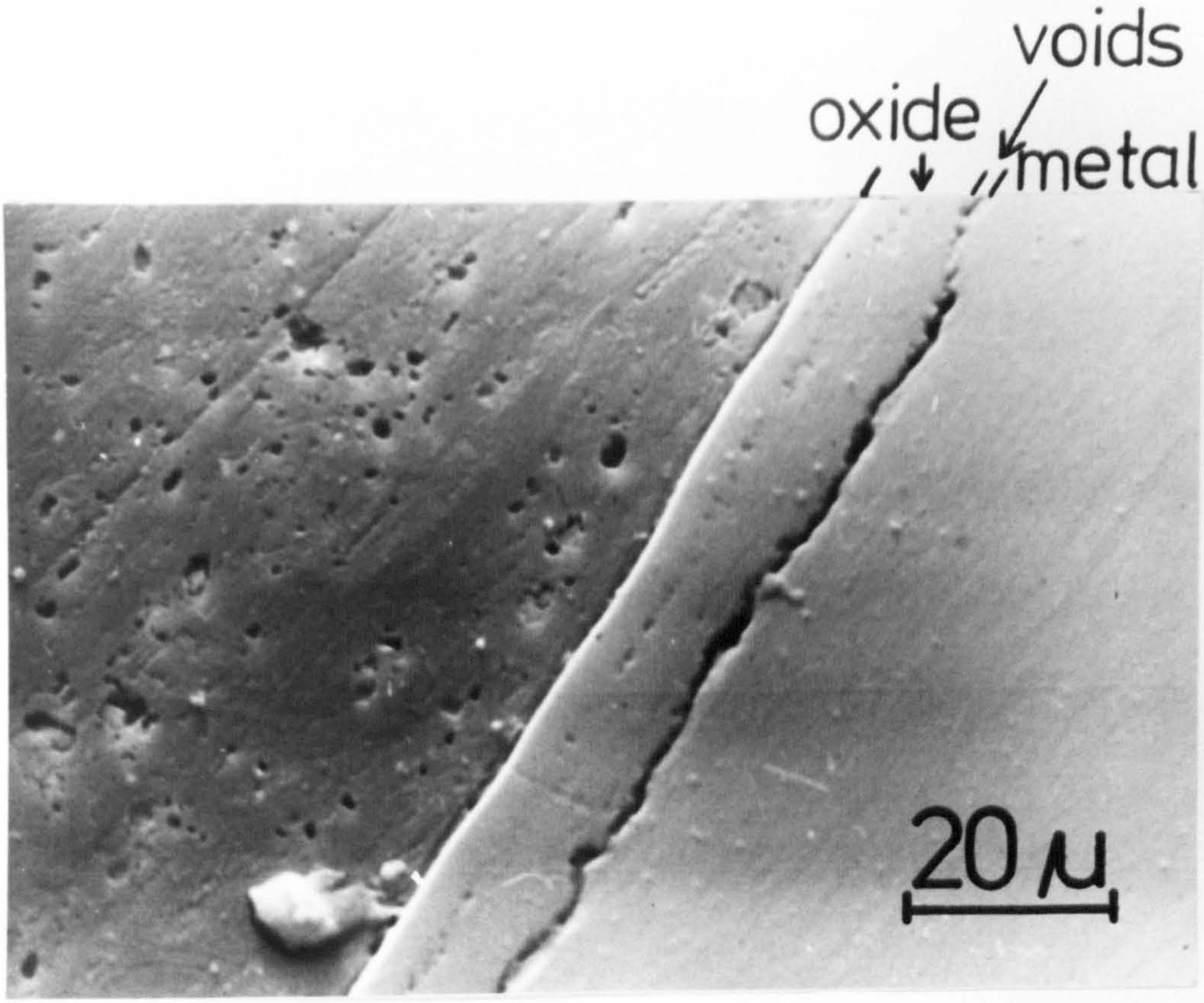

(a) Un-nitrided

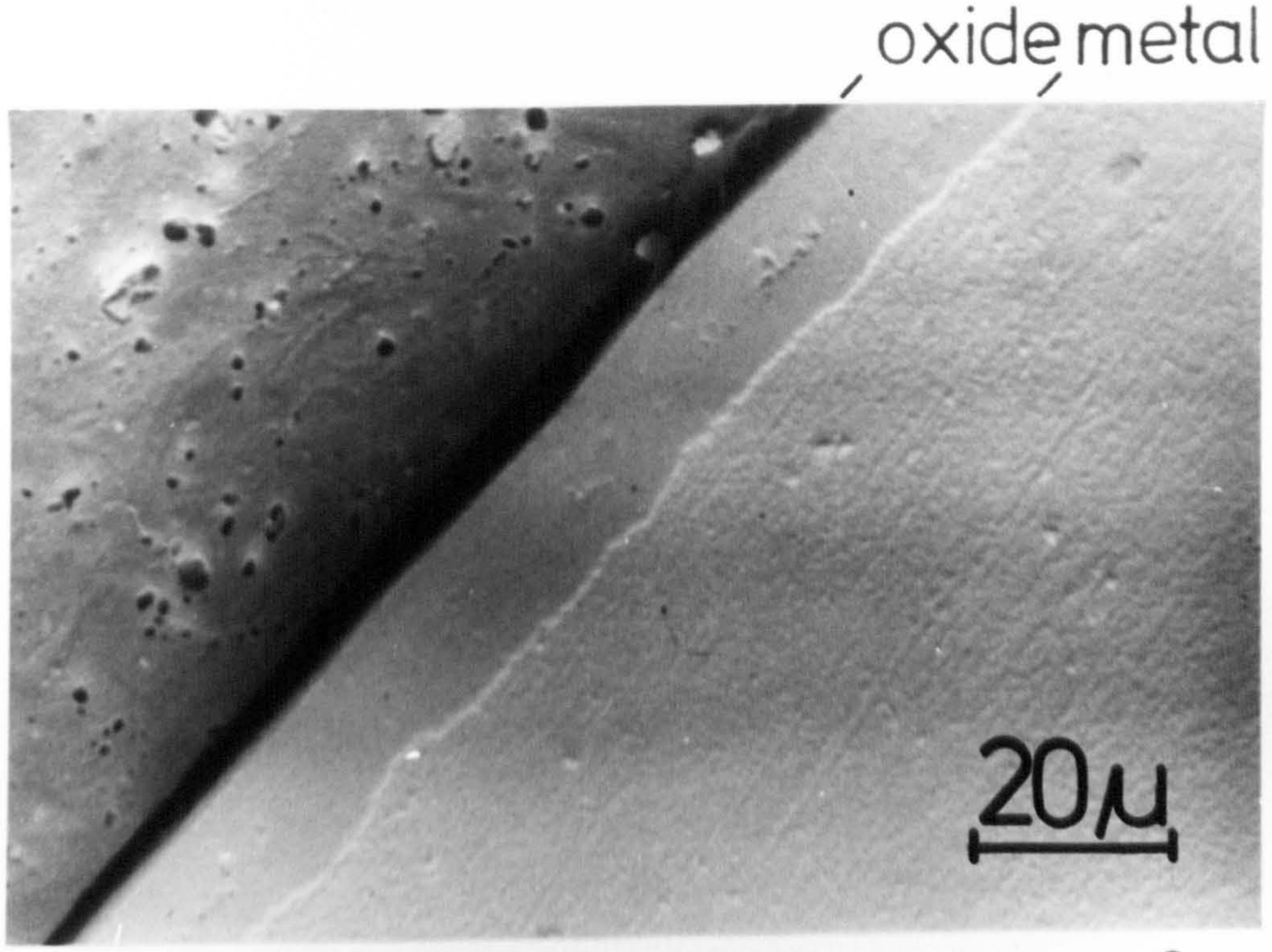

(b) Nitrided ($4NH_3$:$96H_2$, 580 °C)

below those required in the absence of a dispersoid;

(2) a reduction in the growth rate of the Cr_2O_3 compared to particle free alloys is observed, particularly at high temperatures;

(3) there is an improvement in the adhesion of the protective scale to the substrate during cyclic oxidation tests;

(4) in some cases an apparent alteration in the mode of growth of the scale is reported. The scale-forming reaction is at the scale/atmosphere interface in dispersion-free alloys, but at the scale/alloy interface with alloys containing a dispersion.

The effects are independent of the matrix and of the particular dispersoid used.

Similar work has been carried out on alloys which oxidise to give protective aluminium containing scales. The effects of dispersed rare earth elements and oxides on the oxidation behaviour of Ni-Al alloys (Kuenzly & Douglass, 1974), Fe-Cr-Al alloys (Francis & Jutson, 1968; Tien & Pettit, 1972; Stott et al., 1979) and Ni-Cr-Al alloys (Seltzer et al., 1972; Kvernes, 1973; Kumar et al., 1974) are similar to those found in Cr-containing alloys.

The most significant theories to account for the improved behaviour are:

(a) The dispersoid particles act as mechanical pegs which provide a physical keying of the oxide to the substrate - the "key-on" mechanism (Tien & Pettit, 1972);

(b) The particles of the stable oxides act as

sites for the condensation of the vacancies injected by the oxidation process, preventing their condensation at the scale/metal interface as voids - the "vacancy-sink" mechanism (Stringer, 1966);

(c) The particles of the stable oxides accumulate at the metal/oxide interface restricting the flow of reacting species - the "blocking" mechanism (Giggins & Pettit, 1971);

(d) A compound oxide is formed between the metal and the scale. This has a coefficient of thermal expansion intermediate between that of the metal and that of the scale and thus acts in the same way as a "graded seal" in the joining of glass (Pfeiffer, 1957);

(e) The scale plasticity is improved either by a chemical change in the defect concentration or (more likely) by included particles of oxide acting as dislocation sources in the scale (Francis & Jutson, 1968);

(f) The balance between the inwardly diffusing anions and outwardly diffusing cations is altered so that the oxide formation reaction takes place at the metal/oxide interface, eliminating any voidage (Stringer et al., 1972).

The "key-on" effect is thought to be relevant to a number of systems (Kvernes, 1973; Wright & Wilcox, 1974), but does not explain the elimination of interfacial voids found in some dispersion containing alloys. The "vacancy-sink" concept (Stringer, 1966) is relevant where no change of mechanism occurs and where the oxide forms by an outward diffusion of cations with an associated inward diffusion of cation vacancies. The

dispersoid particles allow the inwardly flowing vacancies to condense on the particles rather than at the metal/scale interface. This mechanism is thought to be responsible for the increased adherence of oxide formed on Ni_3Al containing yttrium (Kuenzly & Douglass, 1974) where the yttrium forms dispersed intermetallic particles and internally oxidised particles, the vacancy-sink mechanism being independent of the chemical nature of the particles.

Giggins & Pettit (1971) attribute the reduction in oxidation rate of Ni-Cr alloys containing thoria dispersions to a "blocking" effect in the inner layer of the scale. Initially the Cr_2O_3 scale grows by chromium cation diffusion outwards resulting in an accumulation of the dispersoid at the alloy surface. Eventually the outward movement of chromium is so restricted that dissociation at the inner interface of the scale occurs and the released oxygen can now pass around the inert oxide particles to form a new, inner layer of Cr_2O_3 incorporating the dispersoid. The outer scale volatilizes off at high temperature and the scale continues to grow at the alloy/oxide interface, thus improving its adhesion to the substrate. Pegging of the scale by the oxide dispersion also contributes to the improved scale adhesion. Elegant as this model is, it does not readily explain the formation of Cr_2O_3 scale at chromium levels lower than with dispersion-free alloys.

The amount of dispersoid needed to give pronounced effects is very low (less than 2 v/o) so that the accumulation of a continuous compound oxide layer at the alloy surface, incorporating the chemical constituents of the dispersoid, would take a relatively

long time. The effects appear at times much shorter than are required to form a continuous layer and so the "graded seal" mechanism is not thought to be applicable for such alloys.

No direct evidence of an improvement in scale plasticity on dispersion-containing alloys has been reported and the opposite effect is sometimes thought to occur. Kumar et al. (1974) found that yttria additions to Ni-Cr-Al alloys produced oxide particles in the grain boundaries of the surface α-Al_2O_3 and so inhibited any high-temperature plastic deformation of the scale that might occur by a grain-boundary sliding mechanism. The doping of α-Al_2O_3 by yttrium also increases the strength of the alumina and thus reduces its plasticity.

A widely applied mechanism by which dispersed oxides modify the oxidation behaviour was first proposed by Stringer et al. (1972) who suggested that the dispersoid particles act as nucleation sites for oxide formation thereby increasing the number of oxide nuclei and hence accelerating the approach to the steady state scaling condition of Cr_2O_3 formation. The consequent reduction in oxide grain size compared to that in dispersion-free alloys reduces the number of short-circuit diffusion paths for chromium (e.g. dislocations) and increases those for oxygen transport (oxide grain boundaries). Thus, the scale forming reaction occurs at the alloy/scale interface and not at the gas/scale interface, thereby eliminating void formation due to the condensation of cation vacancies.

The effect of rare earth additions on the relative diffusivities of ions through scale layers

has also been considered by Stott et al. (1979). For Fe-Cr-Al alloys containing no additions, the formation of α-Al_2O_3 is due predominantly to inward diffusion of oxygen anions down the oxide grain boundaries, together with some outward diffusion of aluminium cations in the oxide grains. Reaction in the vicinity of oxide grain boundaries between the inward and outward diffusing species forms additional oxide within the existing oxide layer and rapidly develops compressive stresses which lead to the local detachment of the oxide from the alloy and to a convoluted oxide morphology. The oxides formed on the alloys with yttrium additions do not develop this convoluted configuration and contact between the scale and the alloy surface is maintained. It is suggested that the yttrium becomes incorporated into the scale and reduces or prevents the outward diffusion of aluminium cations; this stops the formation of oxide within the oxide layer.

It is apparent, therefore, that no single mechanism can be applied to the general case of the oxidation of a dispersoid-containing alloy, and each system must be considered separately. However, the effects of dispersoids with regard to oxide adherence and oxidation rates are generally beneficial.

Chapter IV

THE SCOPE OF THE PRESENT INVESTIGATION

Previous work by Hendry (1978) shows that the oxidation resistance of mild steel in a simulated boiler flue gas atmosphere is significantly enhanced by surface nitriding to produce a N-martensite case. The present work investigates further the oxidation of nitrided mild steel and also the oxidation of nitrided binary Fe-X alloys. A number of techniques including oxidation weight gains, X-ray diffraction and electron microscopy (scanning and transmission) are used to study the oxidation mechanisms of the alloys and are described in Chapter V.

In Chapter VI the oxidation of nitrided mild steel and iron in air is considered. The N-martensite case formed on the alloys is found to age rapidly at oxidation temperatures, resulting in a distribution of γ'-Fe_4N in ferrite. The subsequent oxide growth mechanisms on the substrate are considered to be fundamentally changed by nucleation on the dispersed nitrides. These nitrides act as vacancy sinks, eliminating voidage at the metal/scale interface and the oxidation mechanism is altered so that magnetite is formed by the inward diffusion of oxygen with reaction at the metal/scale interface as well as by the outward diffusion of iron cations and

reaction at the magnetite/haematite interface.

Chapters VII, VIII and IX describe studies of the oxidation of nitrided Fe-Cr, Fe-Ti and Fe-Mo alloys respectively. The oxide growth mechanisms in these systems are thought to be analogous to those in nitrided mild steel.

Chapter X describes the oxidation of mild steel in gas mixtures containing sulphur dioxide. Nitriding does not improve the oxidation rates, contradicting Hendry's results, and reasons for the disagreement are discussed.

Chapter V

EXPERIMENTAL METHODS

V.1. Ammonia-Hydrogen Nitriding

Specimens were nitrided in ammonia-hydrogen gas mixtures at temperatures between 400° and 700°C. The nitriding reaction is

$$NH_3(g) \rightleftharpoons \underline{N} + 3/2\ H_2(g) \qquad \ldots\ V.1$$

for which, at T°K, the equilibrium constant is

$$K_T = a_{\underline{N}} \cdot p_{H_2}^{3/2} / p_{NH_3} \qquad \ldots\ V.2$$

where $a_{\underline{N}}$ is the activity of nitrogen in the nitride phase or solid solution and p_{NH_3} and p_{H_2} are the partial pressures of ammonia and hydrogen respectively. Thus, the nitrogen activity is determined by the ammonia:hydrogen ratio:

$$a_{\underline{N}} = K_T \cdot p_{NH_3} / p_{H_2}^{3/2} \qquad \ldots\ V.3$$

A system can therefore be brought to equilibrium with a given nitrogen activity by controlling the proportions

of ammonia and hydrogen in the nitriding gas atmosphere. Figure V.1 illustrates the phases in the iron-nitrogen system in equilibrium with various ammonia-hydrogen gas mixtures over a range of temperatures (Lehrer, 1930).

V.2. Nitriding Apparatus

A schematic diagram of the nitriding apparatus is shown in Figure V.2 with a vertical reaction tube (25mm i.d.) of recrystallised alumina. Commercial hydrogen, nitrogen and ammonia were purified by standard methods (Schwerdtfeger & Turkdogan, 1970) as illustrated in Figure V.3. The activated copper was pre-reduced in hydrogen for several days at 160°C and maintained at 120°C during use. Gas flows were measured by capillary flow meters (see Figure V.4) calibrated by a bubble displacement technique (Darken & Gurry, 1945). Total gas flow rates of 200ml min^{-1} were used during nitriding runs.

The temperature of the furnace hot zone was controlled to $\pm$ 5°C by an "Ether" controller using a Pt/Pt-13%Rh thermocouple positioned between the reaction tube and the furnace winding. The specimen temperature was monitored by a chromel/alumel thermocouple in an alumina sheath adjacent to the specimen.

The total gas pressure was maintained at slightly greater than atmospheric by 10-20mm of oil in an exit bubbler.

Figure V.1

Equilibrium between NH_3-H_2 mixtures (1atm)
and solid phases of the iron-nitrogen system
(after Lehrer, 1930)

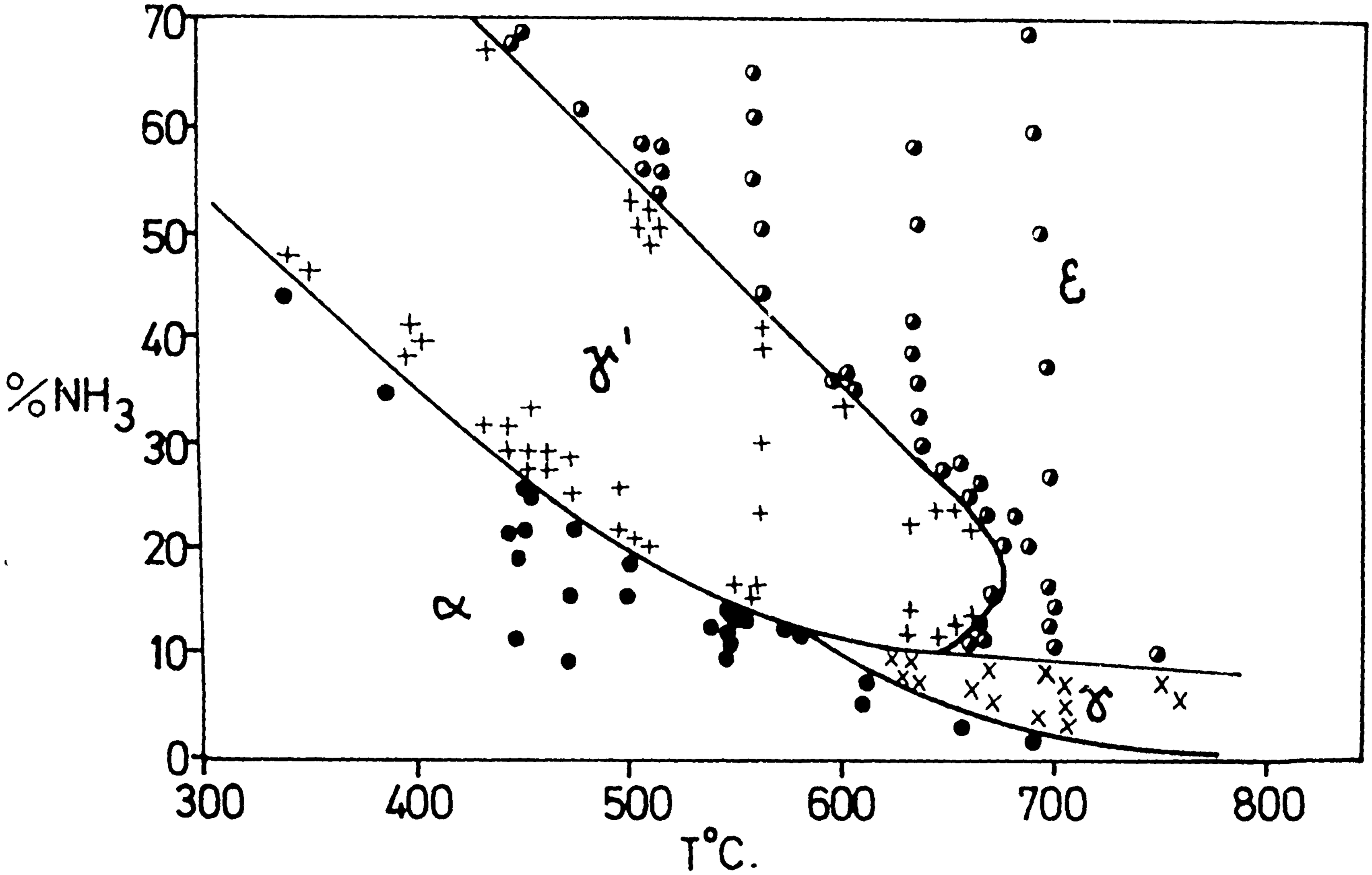
70
60
50
40
30
20
10
0
%NH3
300
400
500
600
700
800
T°C.
α
γ'
ε
γ

Figure V.2

Ammonia-hydrogen gas equilibration apparatus.

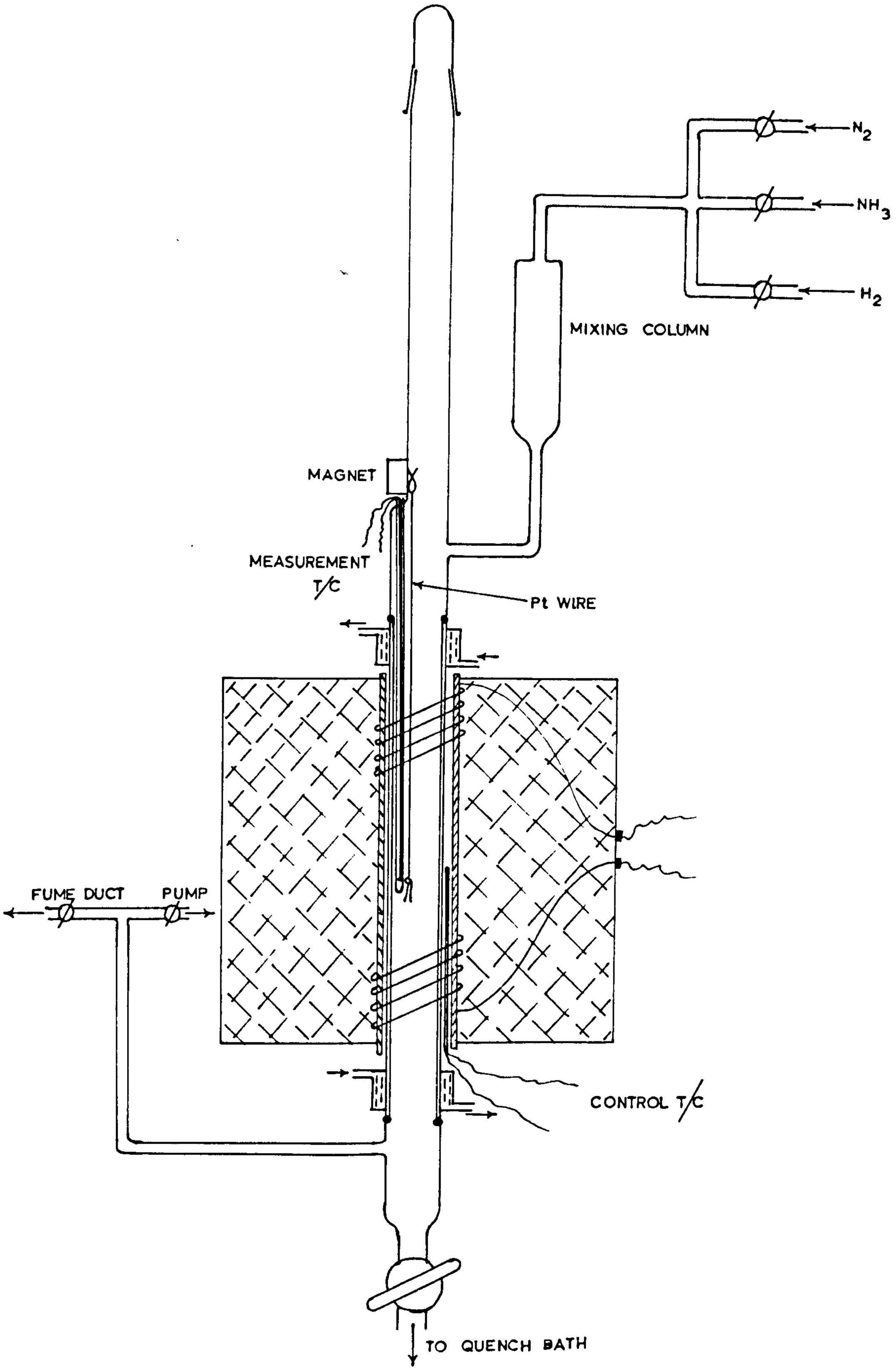
N_2
NH_3
H_2
MIXING COLUMN
MAGNET
MEASUREMENT
T/C
Pt WIRE
FUME DUCT
PUMP
CONTROL T/C
TO QUENCH BATH

Figure V.3

Gas flow system for ammonia-hydrogen gas equilibrations.

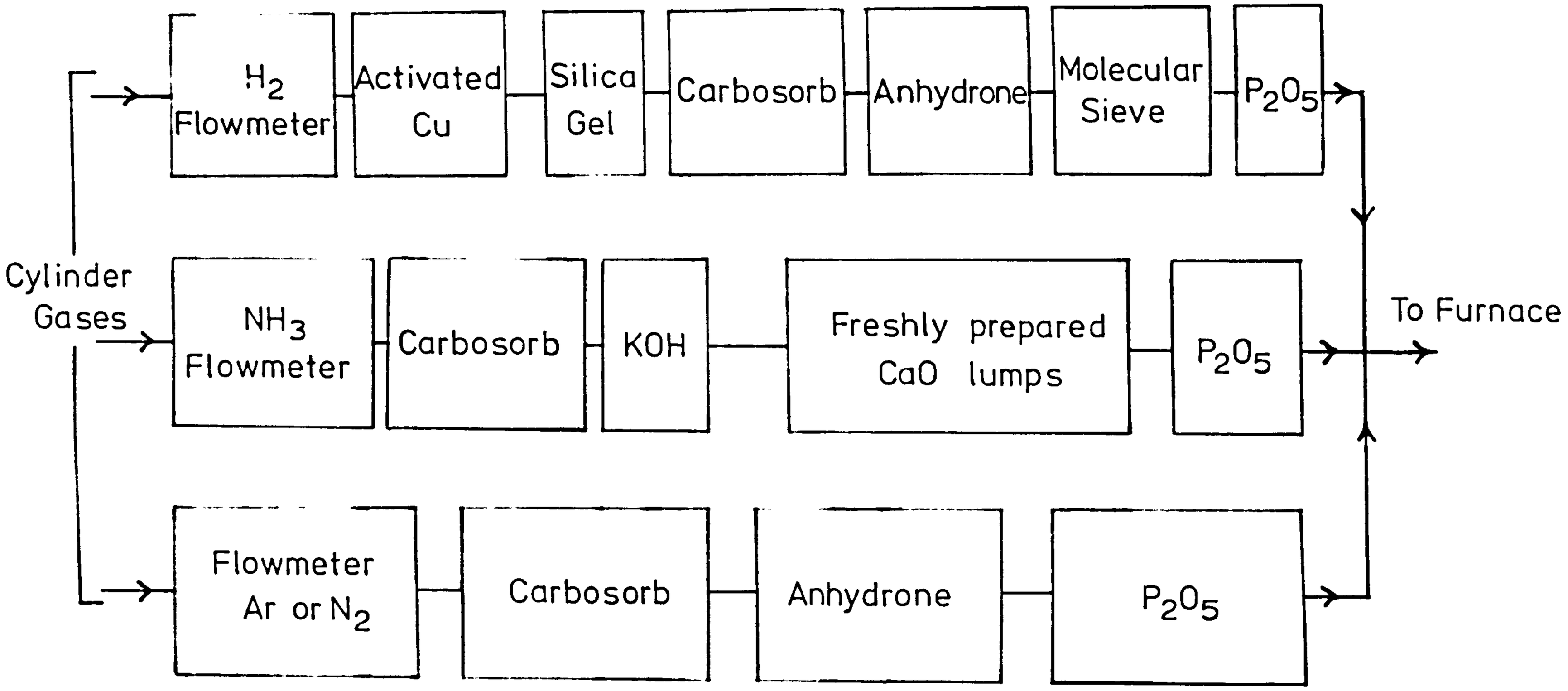
H_2 Flowmeter
Activated Cu
Silica Gel
Carbosorb
Anhydrone
Molecular Sieve
P_2O_5
Cylinder Gases
NH_3 Flowmeter
Carbosorb
KOH
Freshly prepared CaO lumps
P_2O_5
To Furnace
Flowmeter Ar or N_2
Carbosorb
Anhydrone
P_2O_5

Figure V.4

A capillary flowmeter (schematic).

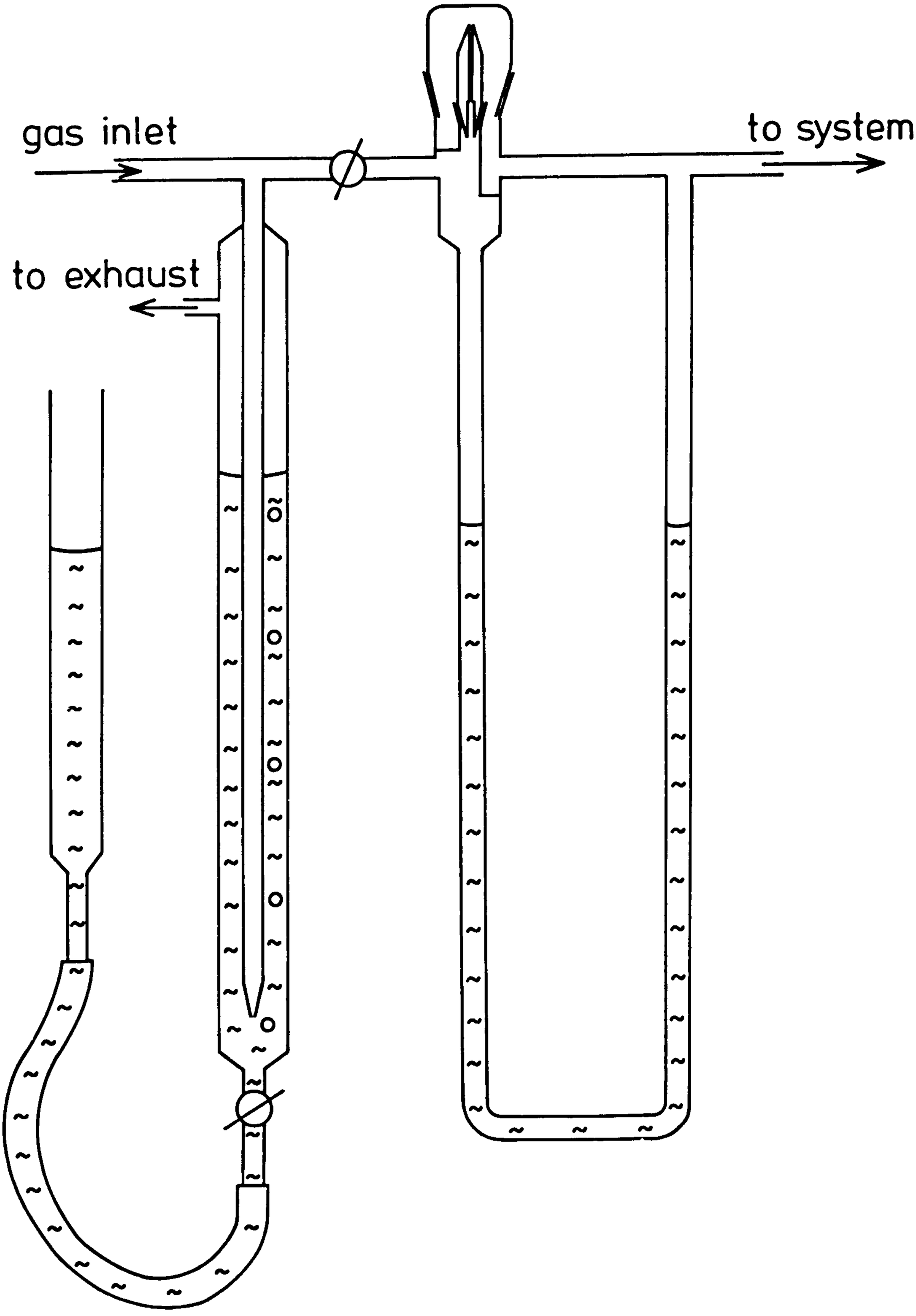
gas inlet
to system
to exhaust

V.3. Annealing the Starting Alloys

The as-rolled strip or as-drawn wire specimens were abraded, cleaned and degreased. Transparent vitreous silica capsules containing the samples were evacuated to less than 10^{-3}Pa (10^{-8}atm) then filled with argon at about $3x10^{4}$Pa (0.3atm) and sealed before annealing in a horizontal tube furnace. Annealing times and temperatures varied for the different alloys.

V.4. Nitriding Procedure

Annealed specimens were abraded and given a light electropolish. After weighing they were degreased in chemiclene, suspended on a platinum wire, inserted into the cold (upper) end of the furnace and supported there by attachment to a soft iron bob held by a magnet. The top of the reaction tube was then sealed, the system evacuated, checked for leaks and flushed with nitrogen. The appropriate ammonia-hydrogen gas mixtures were then passed through the furnace for about one hour before lowering the specimen into the furnace hot zone.

After nitriding, the specimens were removed from the hot zone by one of two methods depending on the severity of quench required. The first method involved raising the specimens quickly out of the hot zone so that they were cooled in the incoming gas stream in the cold zone of the furnace. They were left there for 15min before the furnace was evacuated, flushed with nitrogen, and the specimens removed and weighed. The second method involved opening the

quench tap at the bottom of the furnace and dropping the specimens rapidly from the hot zone into a quench bath of de-gassed, iced brine. The specimens were then removed, washed and dried. Specimens were weighed before and after nitriding to $\pm$ 0.0001g on an analytical balance, taking an average of at least three readings.

V.5. Oxidation Apparatus

(a) Isothermal oxidation experiments were carried out on a 'Stanton-Redcroft' decimilligram thermobalance, shown schematically in Figure V.5. Specimens measuring about 10x10x1.5mm were abraded down to 800 grit SiC paper, weighed, measured with a micrometer screwgauge, degreased in chemiclene and suspended by platinum wire in a silica boat, to catch any spalled oxide. The boat was placed on the silica support rod and counterbalance weights added to the suspended pans. The furnace, which could be raised and lowered, was switched on in its raised position and allowed to equilibrate at the desired test temperature. The furnace was then lowered over the specimen and the weight change was recorded continuously on the chart recorder. After a few hours the recording programme was changed such that the weight was recorded for only 5 min in every 0.5h. At the end of each run the chart was removed and the data replotted as specific weight gain against time, taking data points at 10h intervals.

(b) Further oxidation runs were conducted using horizontal tube furnaces. The specimens,

Figure V.5

Direct reading thermobalance (schematic).

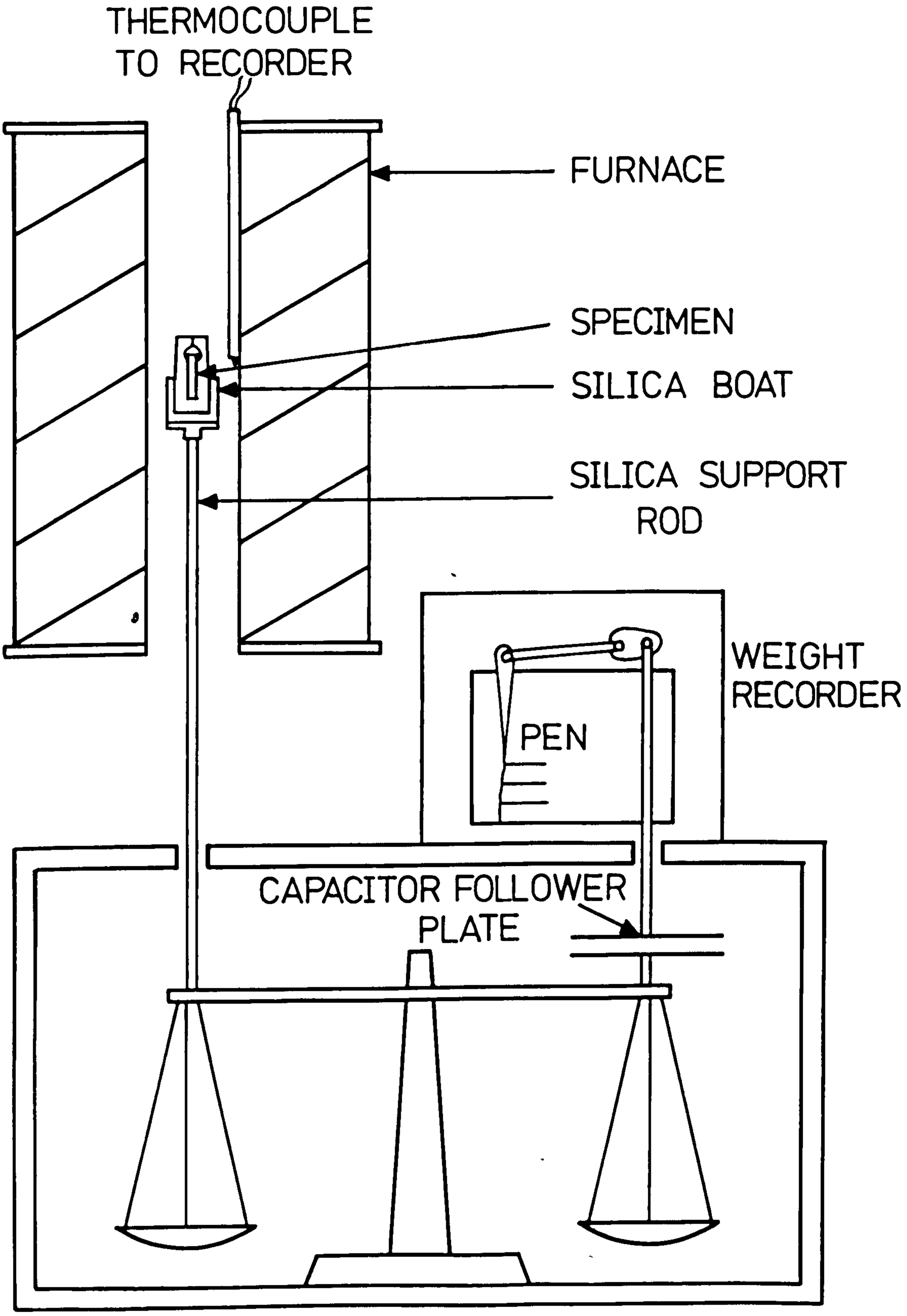
THERMOCOUPLE
TO RECORDER
FURNACE
SPECIMEN
SILICA BOAT
SILICA SUPPORT
ROD
WEIGHT
RECORDER
PEN
CAPACITOR FOLLOWER
PLATE

of similar dimensions to those described above, were suspended by platinum wire in a silica boat after abrading, cleaning, and measuring. The boat and specimen were then weighed before being introduced into the hot zone of the furnace. Periodically the specimen and boat were removed, allowed to cool, weighed, then re-introduced to the hot zone. The results from these runs were again plotted as specific weight gain versus time.

(c) Thermal-cycling runs were carried out at the Central Electricity Generating Board, Midlands Region, Scientific Services Department, Ratcliffe-on-Soar. The oxidation runs were carried out on Stanton-Redcroft decimilligram thermobalances equipped with linear variable temperature controllers and programmers. The thermal-cycling schedule used for all runs was:

(i) heat at $8^{o}Cmin^{-1}$ to the upper temperature;
(ii) hold at the upper temperature for 1h;
(iii) cool at $8^{o}Cmin^{-1}$ to the lower temperature;
(iv) immediately return to the heating stage (i).

The specimen dimensions and preparation were as described previously and the results taken from the chart recorders were replotted as specific weight gain versus the time at the upper hold temperature.

V.6. Nickel Plating

Oxidised specimens were nickel plated prior to mounting in order to reduce oxide loss due to spalling during subsequent handling, and to reduce bevelling of the oxide during metallographic polishing. The

nickel was plated from an electrolytic solution consisting of 55gl^{-1} nickel chloride: 10gl^{-1} sodium hypophosphite: 50gl^{-1} ammonium chloride, plus ammonia solution to give a pH of 8-10. The solution was heated to 90-95^{o}C and the plating reaction was started by applying a 2V potential between the specimen, acting as a cathode, and a nickel anode. After a few minutes plating the electric current was switched off, the anode removed, and the specimen left in the electrolyte as plating continued autocatalytically. Periodically, ammonia lost by evaporation was replenished by adding fresh ammonia solution to maintain a constant pH. In this way, nickel was plated at a rate of 8μm h^{-1} for 2-3h and the specimen was then removed and washed.

V.7. Optical Metallography and Micro-hardness

Specimens for optical metallography were mounted either in bakelite or in Serrifix cold mounting resin. Serrifix was used for the oxidised specimens to reduce deformation of the oxides by the pressures needed for bakelite mounting. In order to ensure intimate contact between the mounting resin and the oxide, the specimen immersed in the uncured resin was evacuated in a vacuum-dessicator to remove gas from pores in the oxide and was then re-pressurised to force resin into the pores.

Mounted specimens were abraded through various grades of silicon carbide paper down to 800 grit and then polished with diamond paste down to 1μm size on polishing wheels using a "Selvyt" cloth lap.

Metal specimens were etched in 2% Nital for about 10s. Oxides were etched in hydrochloric acid vapour over heated, concentrated HCl for 5-10s.

Optical microscopy was carried out on an upright Vickers microscope and a Reichart projection microscope - used also for photomicrography.

Hardness measurements were made on metallographic specimens using a standard micro-hardness tester fitted to the Reichart microscope with a load of 50g on the diamond indenter.

V.8. Preparation of Specimens for Transmission Electron Microscopy

Thin foils of nitrided alloy specimens were prepared from strip material, less than 0.5mm thick. The material was thinned to about 0.1mm by chemically polishing in a mixture of parts by volume 50 water: 50 hydrogen peroxide:2-10 hydrofluoric acid. Thin foils were then prepared by electropolishing using a standard "window" technique and a "Shandon" potentiostat at 18V and 0°C in a solution of 68v/o glacial acetic acid:16v/o perchloric acid: 16v/o 2-butoxyethanol.

Thin oxide films were stripped from their metal substrates using a solution of 12w/o iodine in methanol. The time needed for successful stripping varied from a few hours to a few days depending on the substrate composition and heat-treatment.

Thin-foil specimens were oxidised at reduced pressures to investigate the nucleation of oxides. These were placed in a silica boat in the cold zone of a sealed horizontal furnace, the furnace was evacuated to about 10^{-3}Pa, and the specimen was introduced into the hot zone by a silica push rod attached to a soft iron bob that could be manipulated with a magnet. The specimen was left in the hot zone for 2-30 min, removed to the cold zone, and then allowed to cool before re-pressurising the furnace and removing the foil for examination.

V.9. Electron Microscopy

Transmission electron microscopy was carried out on Philips EM 300 and JEOL 100-U instruments.

Scanning electron microscopy was carried out on metallographically prepared specimens, and on stripped oxides using a Cambridge Stereoscan S600.

Elemental distributions in oxide layers were determined using the X-ray energy dispersive analysis facilities of a Cambridge Stereoscan S2 microscope.

In-situ oxidation experiments were carried out using the Hitachi high voltage electron microscope (at 600 kV) at the Berkeley Nuclear Laboratories of the Central Electricity Generating Board. Thin foil specimens were placed in the microscope and examined to find a suitable area. The foils were then heated in a calibrated heating stage to 450°-500°C before injecting oxygen from a reservoir tank into the

microscope column via a bleed-valve. The partial pressure of oxygen used was about $1x10^{-4}$Pa (10^{-9}atm) above a total residual background pressure of $2x10^{-4}$Pa ($2x10^{-9}$atm). The specimen was examined periodically during oxidation for about 40 min, the beam being deflected from the area of interest between examinations to reduce any beam effects.

V.10. X-ray Diffraction

Metal specimens examined by X-ray powder photography were prepared from wire (0.3-0.6mm diameter) or narrow strip cut from foils. The specimens were electropolished and washed in methanol prior to exposure.

X-ray powder photographs for determination of ferrite lattice parameters were obtained using Unicam 190mm diameter cameras with iron-filtered Co-Kα radiation or graphite crystal monochromated Cr-Kα radiation. Lattice parameters were determined by Nelson-Riley extrapolation (Nelson & Riley, 1945). Unicam 90mm diameter cameras with either LiF crystal monochromated Fe-Kα radiation or graphite crystal monochromated Cr-Kα radiation were used for the determination of second phases.

Identification of oxide layers on metal substrates and investigation of the aging of nitrogen-martensite cases were carried out using a Philips diffractometer with graphite crystal monochromated Cu-Kα radiation.

Identification of stripped or spalled oxide layers was made using the 90mm diameter Unicam camera with crystal monochromated Cr-Kα radiation and gum tragacanth powder specimens or by using a Hägg-Guinier focussing camera with monochromatic Cu-Kα radiation.

Chapter VI

THE OXIDATION OF NITRIDED MILD STEEL AND IRON

VI.1. Introduction

The oxidation resistance of mild steel in simulated flue gas is improved by nitriding, as demonstrated by Hendry (1978); see Chapter I. The present work was carried out using laboratory air as the oxidant but it was thought probable that features of the oxidation of nitrided and un-nitrided mild steel similar to those found using simulated flue gas would be evident.

VI.2. Starting Materials

The mild steel was supplied from furnace wall tubing material by the Central Electricity Generating Board, Scientific Services Department, Midland Region, Ratcliffe-on-Soar and its analysis is given in Table VI.1.

The surface of the as-received material was cleaned by abrasion before being cold rolled and sectioned to either 8x8x2mm coupons or 15x10x0.15mm foil specimens. The specimens were subsequently annealed at 950°C for 2h. The analysis of the pure iron (B.I.S.R.A. cast K2770) is also given in Table VI.1.

Table VI.1

Chemical analysis of mild steel and iron (w/o)

	C	Si	Mn	Ni	Cu	O	S
Mild steel	0.23	0.15	0.45	0.07	0.07	-	-
Iron	0.002	-	-	-	-	0.075	0.006

Coupons measuring 8x8x2mm were cut from cold-rolled material and annealed at 870°C for 1h.

VI.3. Nitriding of Mild Steel

Nitriding of mild steel specimens was generally carried out in $5NH_3:95H_2$ at 700°C, within the austenite phase field of the Lehrer diagram (see Figure V.1). Runs were for 20h which gives a case depth of about 80 μm on the 2mm thick coupons and is sufficient to through-nitride the foil specimens that were used for weight gain measurements and subsequent electron microscopy.

Weight gain measurements gave a nitrogen pick-up of 0.90 ± 0.10w/o and X-ray lattice parameter measurements of the N-martensite product confirmed these results. X-ray diffractometry was also used to measure the relative amounts of α'-martensite and γ-austenite in the nitrided case. For the nitriding conditions used, the ratio $\alpha' : \gamma$ is about 6:1 . The microstructure of the as-nitrided alloy consists of twinned martensite needles surrounded by retained austenite; see Figure VI.1(a). The martensite packets are typically 0.5μm in width containing individual twin laths approximately 15 nm wide, and surrounded by austenite grains with a high density of dislocations adjacent to the martensite packets.

Figure VI.1

Transmission electron micrographs of

mild steel,

(a) nitrided, in $5NH_3$:$95H_2$ at 700°C, air-cooled,

(b) nitrided, as (a); aged 500°C for 64h.

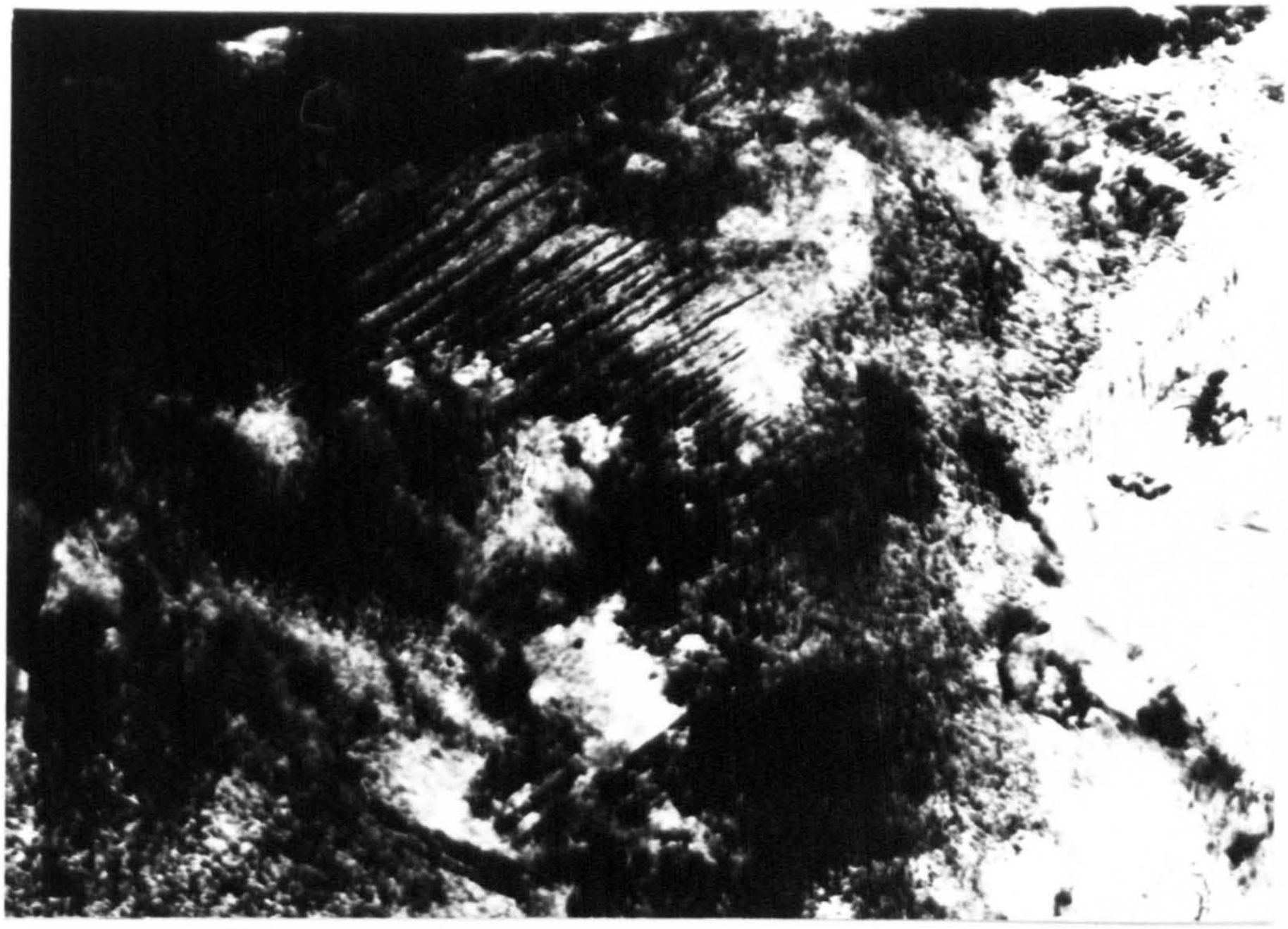

(a)

0.2 μm

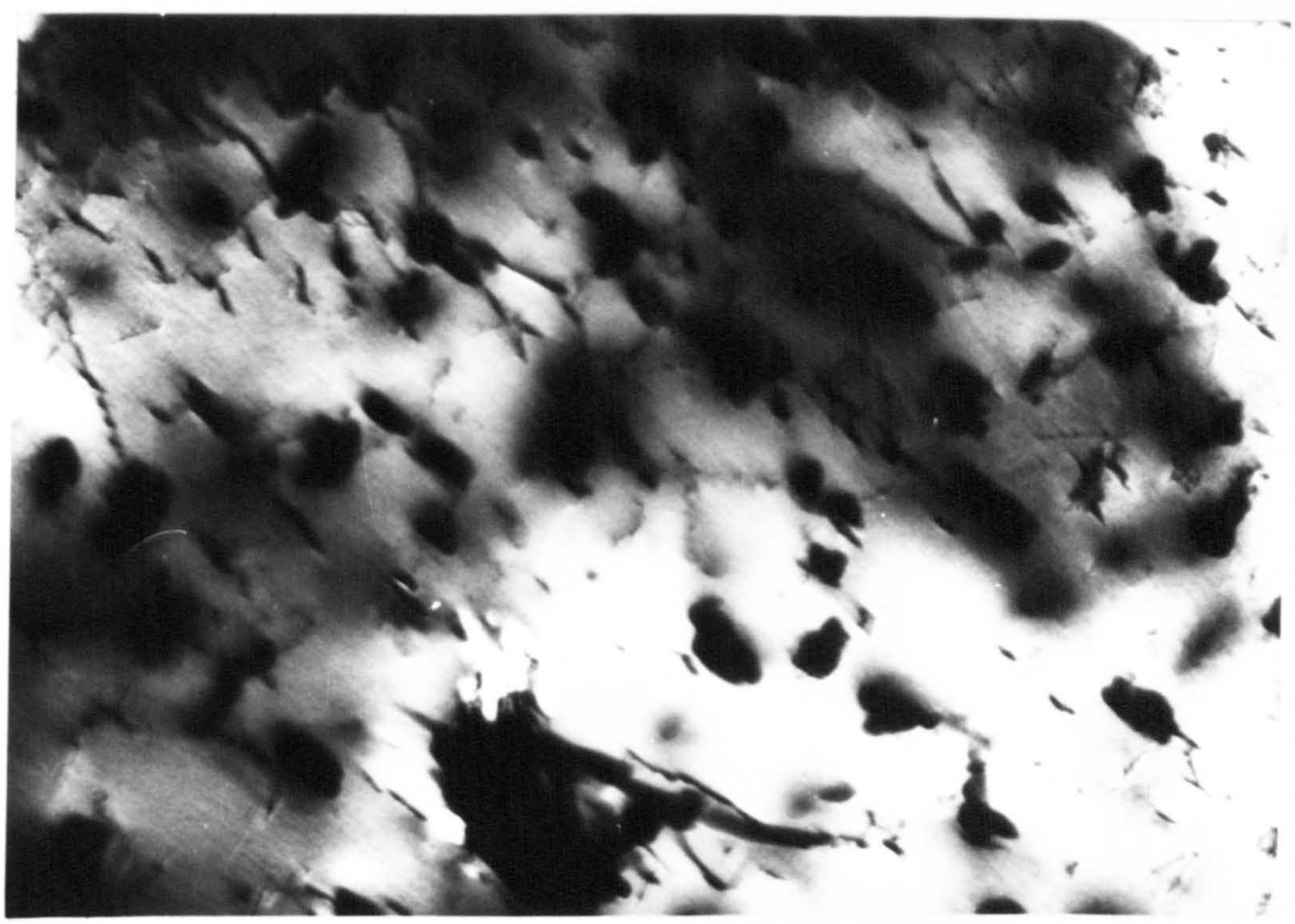

(b)

$[0\bar{1}1]$

$[1\bar{3}0]$

(311)

0.2 μm

VI.4. Kinetics of Nitriding of Mild Steel

Nitriding of iron is a diffusion controlled process (see section II.3) and the depth of penetration of nitrogen in iron can be determined by solution of equation II.2. It is not always easy to determine the total depth of penetration of a diffusing species. but if the penetration depth, x, is defined as the depth at which the concentration of the species is a fixed proportion of the difference between the surface concentration and the initial uniform concentration, this depth may be more easily measured. The concentration of the diffusing species need not be measured directly because, if some parameter which is proportional to the concentration of the diffusing species is measurable, the appropriate values of this parameter may be used in place of C and C_s in equation II.2.

It was assumed that the micro-hardness of the austenite-martensite matrix is proportional to the nitrogen content. Micro-hardness curves were determined across the cases of mild steel specimens nitrided for increasing lengths of time. The case depth, x, was defined as the depth at which the hardness was midway between the surface hardness and the core hardness, i.e. where $C/C_s = 0.5$. From tabulated solutions of equation II.2 (Darken & Gurry, 1953) this corresponds to the point where

$$x/\sqrt{Dt} = 0.9538.$$

As the nitriding case grows into the alloy at the nitriding temperature (700°C), the rate of growth is controlled by the diffusion of nitrogen through the nitrided (austenitic) layer to the un-nitrided core.

The diffusivity of nitrogen in austenite at 700°C is 8.3×10^{-10} cm^2 s^{-1} (Grieveson & Turkdogan, 1964). Therefore,

$$x = 0.9538 \sqrt{8.3 \times 10^{-10} \times t} \quad \ldots\ldots \text{VI.1}$$

Figure VI.2 shows the increase in case depth of both cold worked and annealed mild steel with nitriding time. The solid curve shows the theoretical case depths as determined from equation VI.1.

The closeness of fit of the measured and theoretical case depths shows that:

(a) the rate of growth of the nitrided case on mild steel at 700°C is indeed controlled by the diffusivity of nitrogen through austenite;

(b) the assumption that micro-hardness of the nitrided case is proportional to nitrogen content is justified;

(c) prior annealing of the mild steel has no effect on the rate of growth of the nitrided case.

VI.5. Isothermal Oxidation of Nitrided Mild Steel

The oxidation weight gain curves of nitrided and un-nitrided mild steel oxidised isothermally (see section V.5(a)) at 480°C in air are shown in Figure VI.3. Parabolic rate constants (k_p) determined from linear regression analysis of the data expressed as the square of the specific weight gain versus time

Figure VI.2

Case depth of mild steel nitrided at 700°C

in $5NH_3:95H_2$.

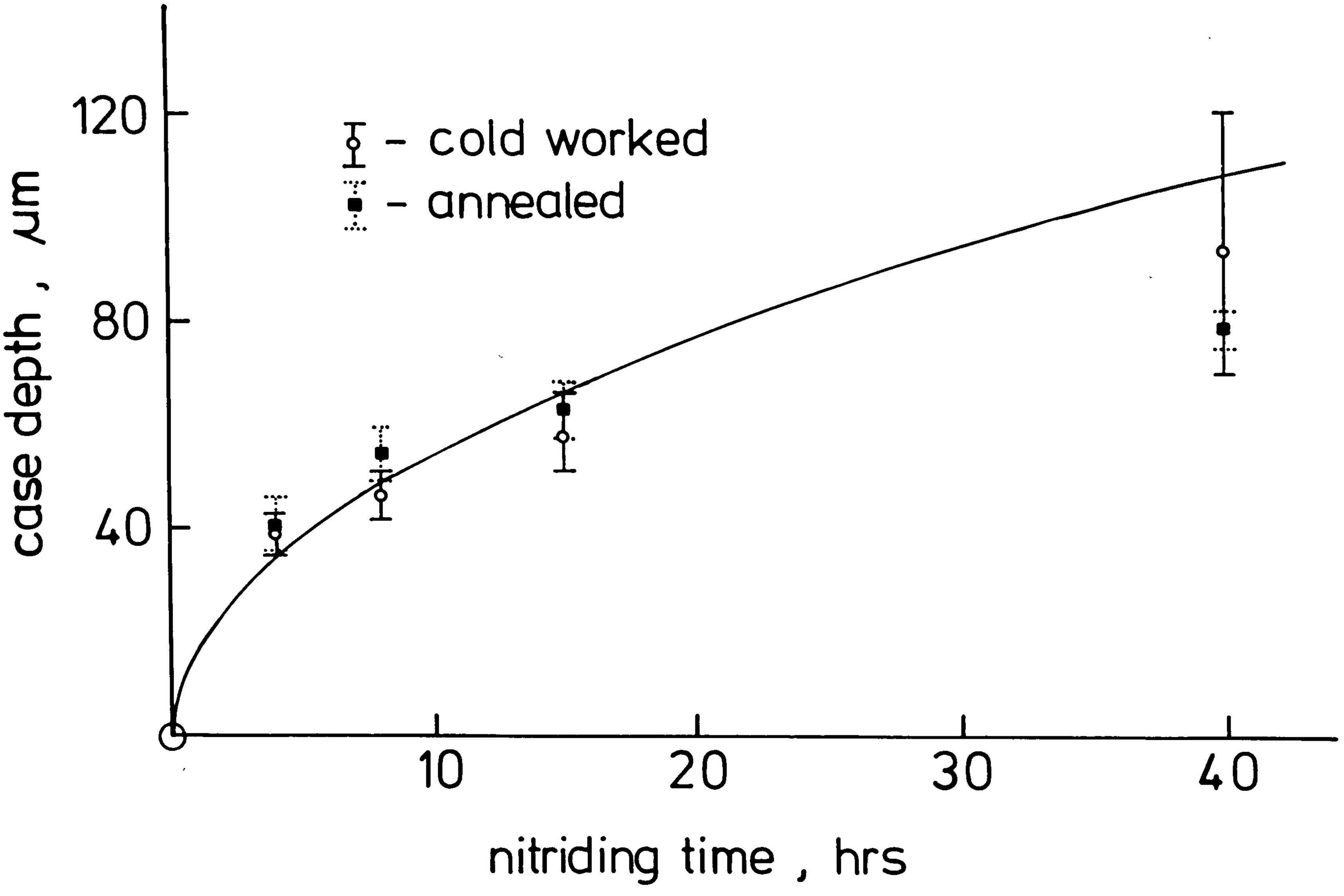
120
80
40
case depth , µm
– cold worked
– annealed
10
20
30
40
nitriding time , hrs

Figure VI.3

Oxidation curves of un-nitrided and nitrided (in $5NH_3$:$95H_2$ at 700°C) mild steel oxidised in air at 480°C.

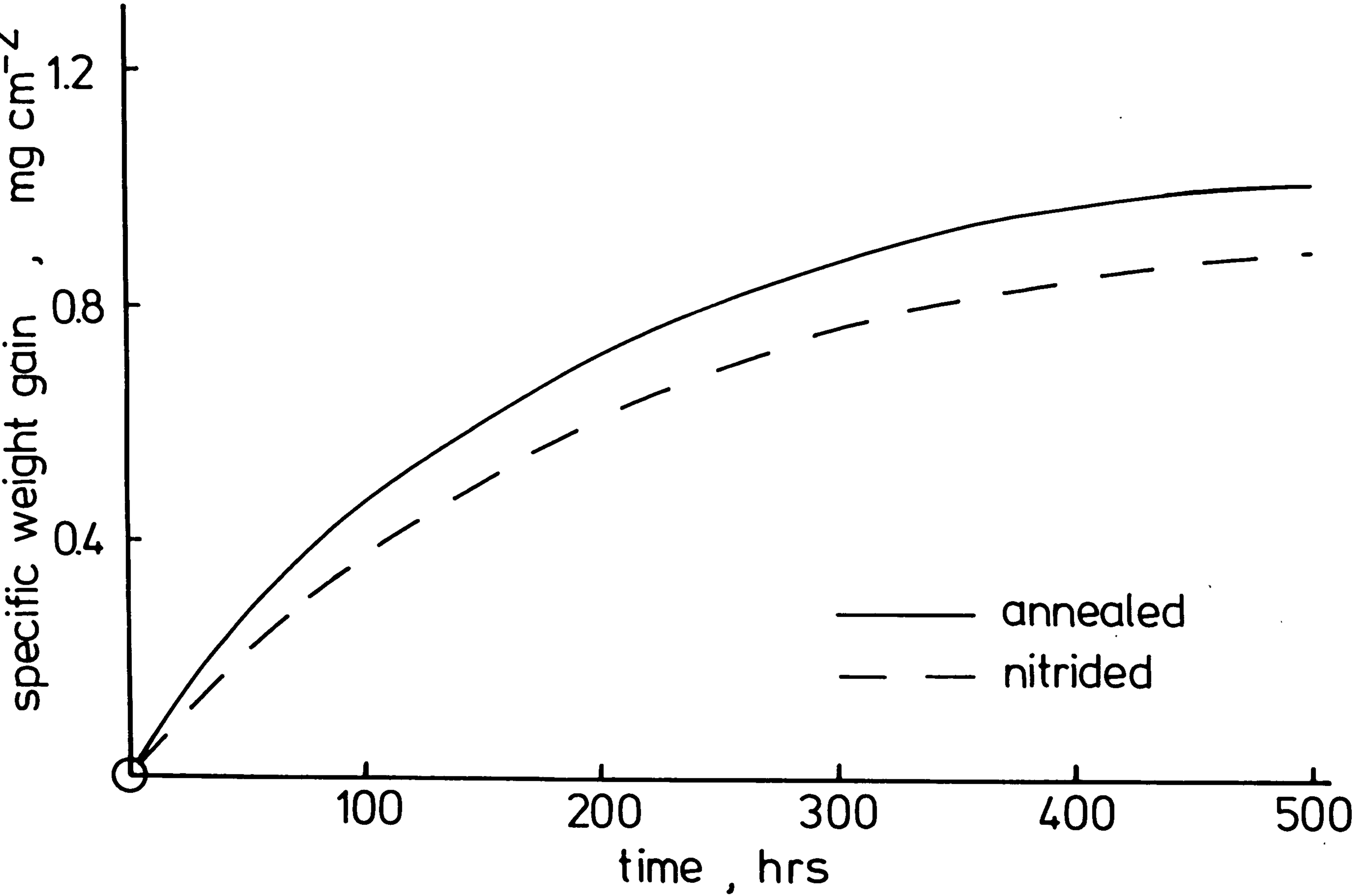
specific weight gain , mg cm^{-2}
1.2
0.8
0.4
100
200
300
400
500
time , hrs
annealed
nitrided

are given in Table VI.2

Estimated errors indicate that there is no significant difference between the oxidation rates. The value of k_p for iron at 480°C is 2.37×10^{-11} $g^2 cm^{-4} s^{-1}$ (see Figure III.2) which is two orders of magnitude higher than k_p for nitrided and un-nitrided mild steel at the same temperature.

Metallographic examinations of the oxides formed on un-nitrided and nitrided mild steel, Figure VI.4, show distinct differences however. The oxide on the un-nitrided material is completely separated from the substrate, whereas that on the nitrided steel is adherent. Some cracking of the oxide on nitrided mild steel, due to stresses imposed during cooling and/or mounting of the specimens, occurs within the oxide layer parallel to the metal/oxide interface. The total thickness of oxide is similar in both cases. The high porosity of the oxide on the nitrided specimen is probably due to oxide "pullout" during metallographic preparation.

Figure VI.5 shows micrographs of un-nitrided and nitrided specimens after isothermal oxidation at 500°C in air for 900h. The oxide scales have been etched in HCl vapour. The magnetite layer on un-nitrided mild steel (a) is coarse-grained with no variation in grain size across the layer. The magnetite on nitrided mild steel (b) is, however, relatively fine-grained with a layer about one-third of the total oxide thickness, next to the metal/oxide interface, appearing extremely fine-grained. The oxide also appears to contain fine pores but because the as-polished structure appears very compact this may

Table VI.2

Parabolic rate constants and linear regression coefficients (r) for mild steel oxidised isothermally at 480°C for 500h.

Specimen	Parabolic rate constant, k_p ($g^2\ cm^{-4} s^{-1}$)	r
Un-nitrided	6.50×10^{-13}	0.92
Nitrided in $5NH_3:95H_2$ at 700°C	5.22×10^{-13}	0.95

Figure VI.4

Scanning electron micrographs of

(a) un-nitrided mild steel,

(b) nitrided mild steel (in $5NH_3:95H_2$ at $700^{\circ}C$)

oxidised in air at $500^{\circ}C$ for 500h.

Etched in nital.

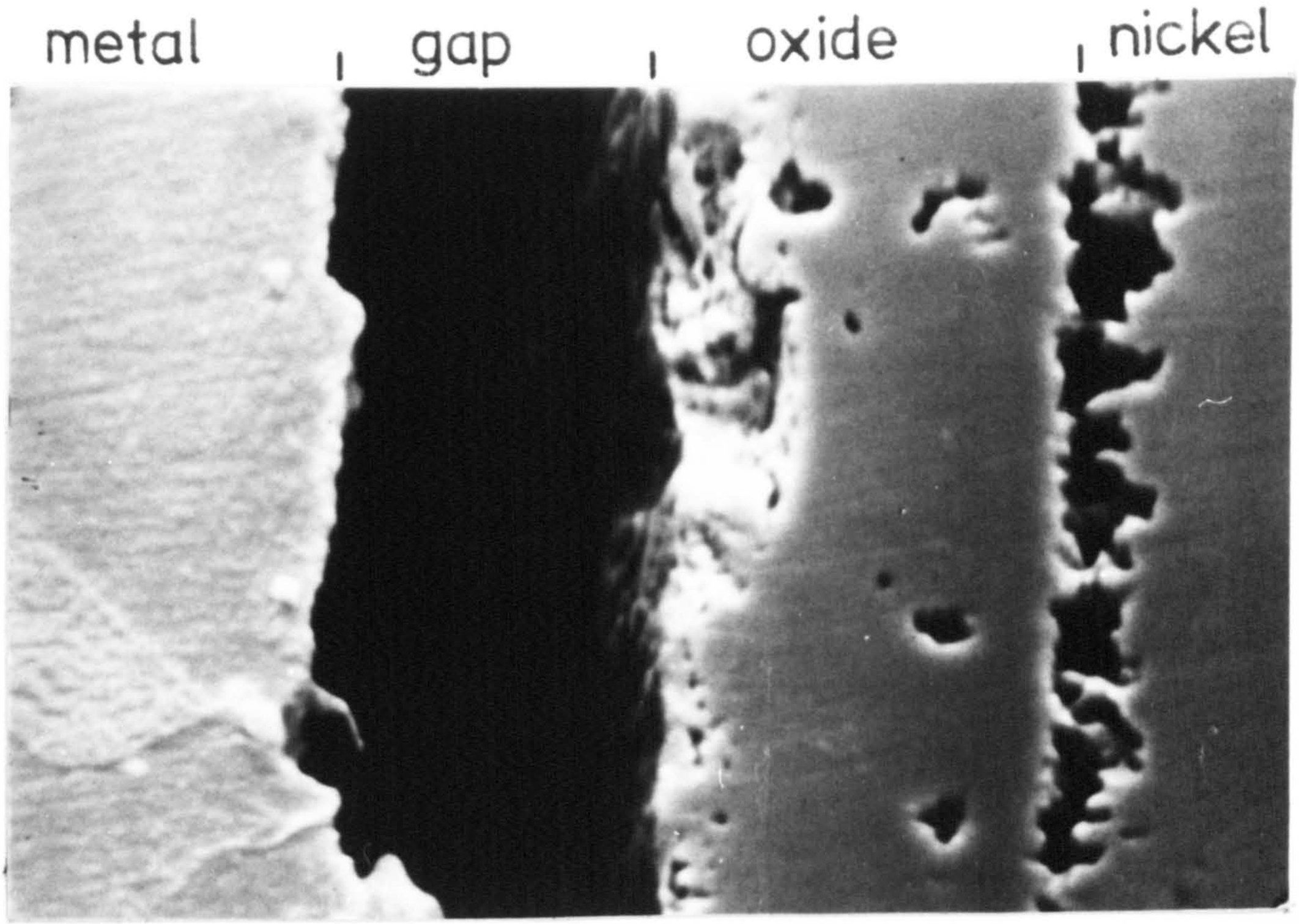

(a)

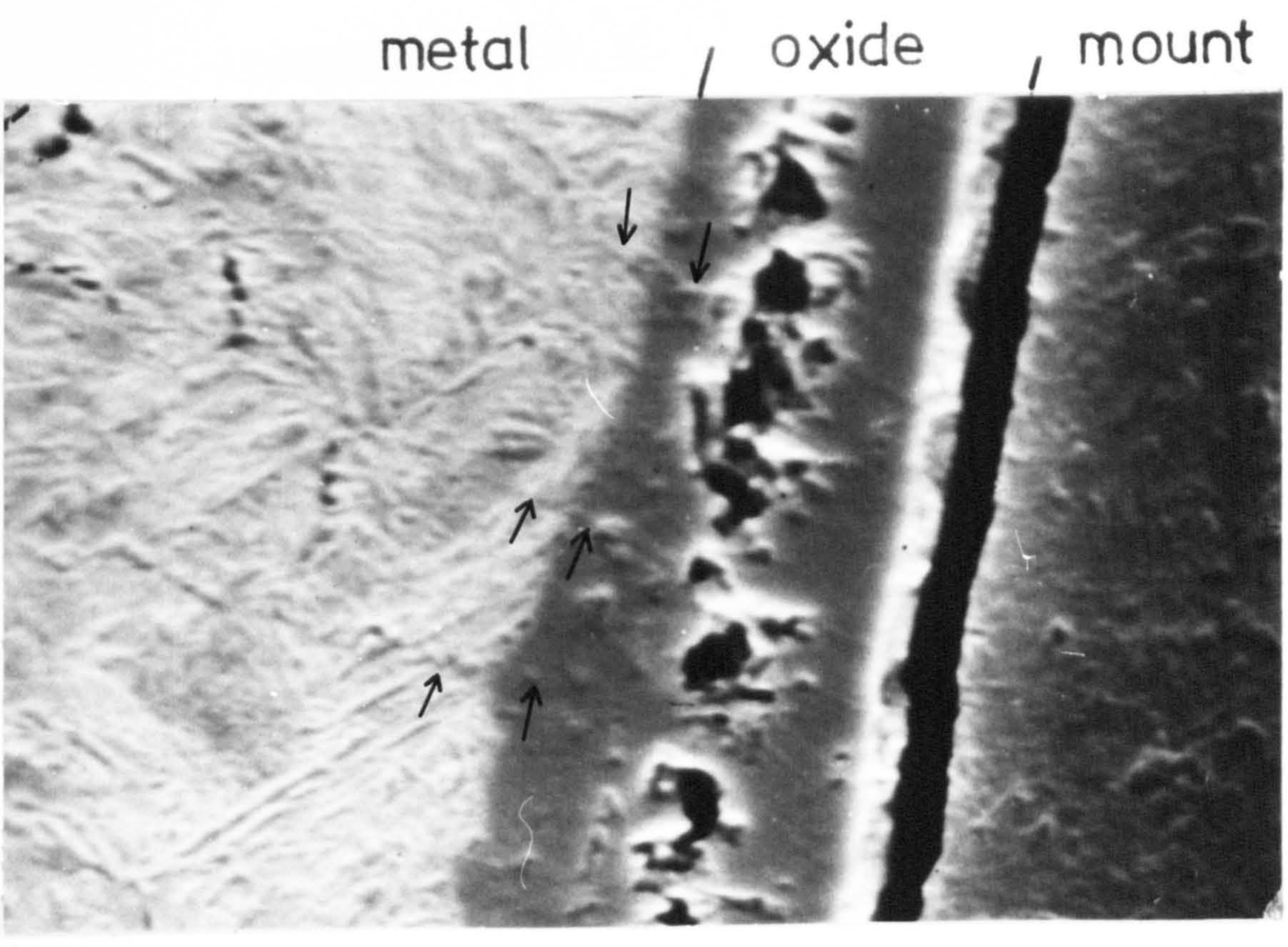

(b)

Figure VI.5

Scanning electron micrographs of

(a) un-nitrided mild steel,

(b) nitrided mild steel (in $5NH_3$:$95H_2$ at 700°C)

oxidised in air at 500°C for 900h.

Etched in HCl.

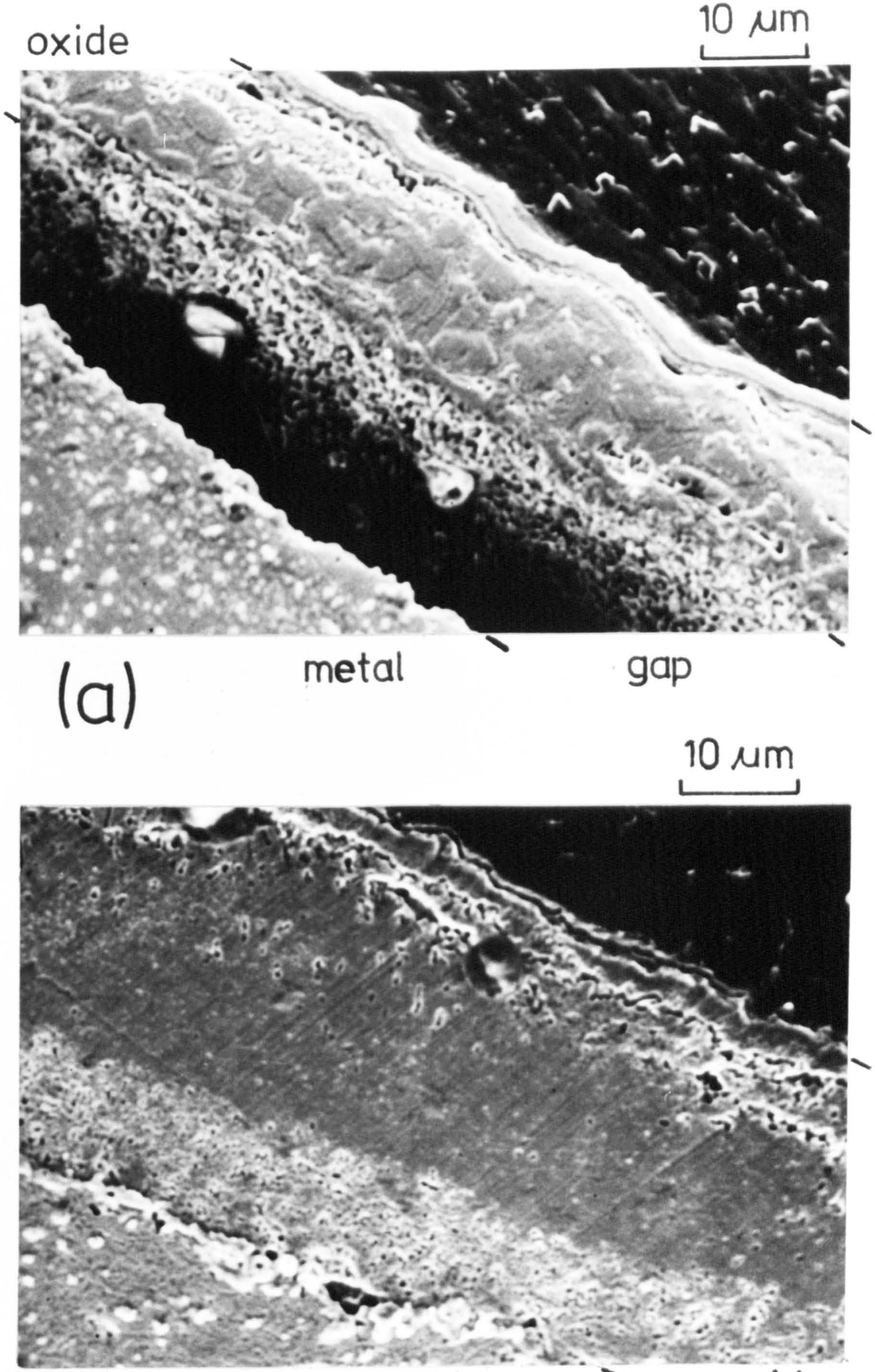
oxide
10 μm
metal
gap
(a)
10 μm
metal
oxide
(b)

be an etching effect.

Table VI.3 shows the thickness of the fine-grained inner oxide layer and the total oxide thickness of nitrided mild steel oxidised in air at 500°C for various times. The results are the mean of at least five measurements. The relative thickness of the inner oxide remains fairly constant with time and therefore must grow continuously during oxidation.

It is generally agreed that magnetite is a p-type semi-conductor, diffusion being mainly cationic and that formation of new oxide takes place at its outer boundary. However, the growth of the inner, fine-grained layer with time implies formation of new oxide either within the oxide scale or at the metal/oxide interface. If a substantial amount of oxygen diffusion takes place (either through the magnetite lattice or along oxide grain-boundaries, or by oxygen gas penetration) an oxide forming reaction could occur either at the metal/oxide interface or within the oxide scale. If oxide is formed at the metal/oxide interface, growth stresses will normally occur within the oxide which will be compressive since the Pilling-Bedworth ratio is greater than unity; see section III.5. Providing the stresses are not so large as to cause fracture of the oxide, the result will be a compact oxide layer with good metal-oxide adherence. If oxide is formed by reaction of inwardly diffusing anions (or gas molecules) and outwardly diffusing cations within the oxide layer, similar growth stresses will be set up in the oxide.

Examination of the morphology of the inner oxide layer on the nitrided specimens suggests that

Table VI.3

Thickness of oxide layers on nitrided mild steel oxidised in air at 500°C

Oxidation time, h	Total oxide thickness, T μm	Inner oxide layer thickness, t μm	t/T
50	13	3.25	0.25
115	17.5	4.5	0.26
720	35.5	11.2	0.32

microstructural features of the substrate, such as grain boundaries, are continuous into the oxide layer (see arrowed features on Figure VI.4(b)). This would imply that the inner layer grows inwards by reaction at the metal/oxide interface, the outer layer growing by the normal cation diffusion mechanism.

The initial formation and growth of the oxide scale on nitrided mild steel was studied by sequential oxidation experiments at 420°C in air. Figure VI.6 is a sequence of SEM micrographs showing the development of the oxide. For very short times (up to 5 min) the oxide layer replicates the surface of the metal substrate, clearly showing the scratch marks formed by abrasion of the specimen; see Figure VI.6(a). For longer times, as the oxide layer thickens, the impression of the metal surface morphology becomes less well defined, but a series of grooves appear in the oxide which outline a large grain structure as shown in (b). The grooves follow the prior-austenite grain boundaries of the substrate. For times in excess of 1h, the impression of the abraded metal surface is less apparent. The grooving of the oxide along the prior-austenite grain boundaries is still present but the smooth oxide surface is largely covered with a layer of oxide needles (c). After 4h the initial smooth oxide is completely covered in oxide platelets (d) and the grain boundary grooving is not as evident as for shorter exposure times. The observations show that the oxidation of nitrided mild steel occurs first by the growth of a compact oxide scale which, at longer times, is covered by a less dense, more porous layer.

Diffractometer traces were made of a series of

Figure VI.6

Scanning electron micrographs of nitrided mild steel oxidised in air at 420°C,

(a) 5 min,

(b) 12 min,

(c) 2 h,

(d) 4 h.

(a)

20 μm

(b)

10 μm

(c)

20 μm

(d)

20 μm

nitrided and oxidised specimens to identify the oxide layers and typical results are shown in Figure VI.7. For times up to 1h only magnetite occurs on the surface and haematite peaks only became evident after longer times. When related to the metallographic observations of Figure VI.6, the diffractometer results indicate that the first-formed compact oxide layer is magnetite and the less dense layer which develops at longer times is haematite.

The most striking feature of these X-ray observations, however, is that the nitrided case transforms from an α'-martensite plus γ-austenite structure to α-ferrite plus γ'-Fe_4N when oxidised at 420°C in air for very short times. The α'-martensite/ γ-austenite transforms in less than 2 min and the initial γ'-Fe_4N peaks are very broad, indicating a very fine dispersion of the nitride. The peaks become narrower with increasing oxidation time as the precipitates grow.

VI.6. Transmission Electron Microscopy of Oxides

Figure VI.8 shows the morphology of the oxide films formed on nitrided and un-nitrided mild steel oxidised in air at 420°C for 5 min. The oxide in both cases is identified from electron diffraction patterns as magnetite. The grain size of the film on the nitrided mild steel is very fine and the diameter of the individual ringed grains in (a) is about 500 Å. The grain size of the oxide film from the un-nitrided material is generally much coarser, with a grain size in excess of 1000 Å (b). Therefore,

Figure VI.7

Diffractometer traces (CuKα radiation) of nitrided mild steel oxidised in air at 420^{o}C.

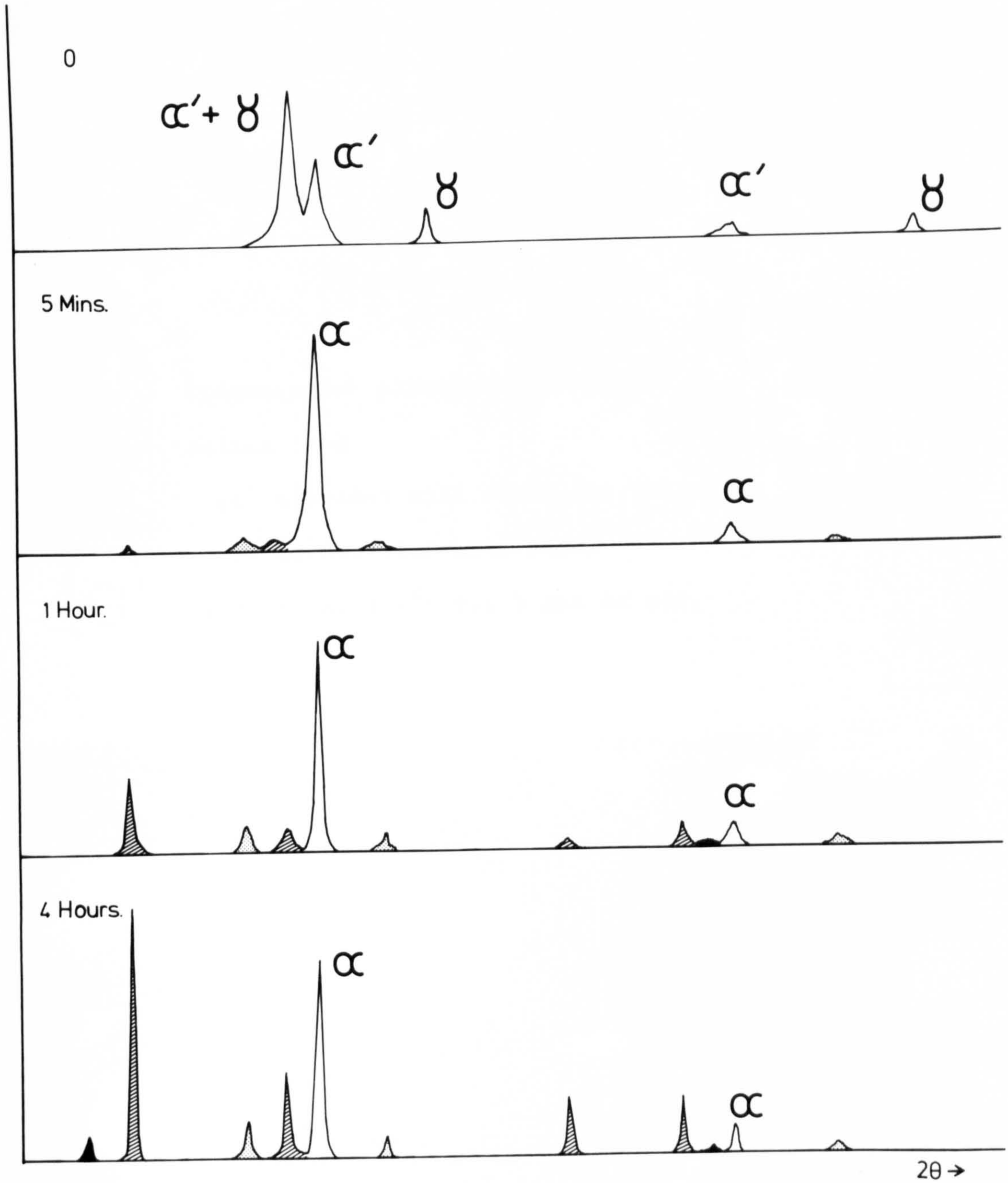
0
α′+ γ
α′
γ
α′
γ
5 Mins.
α
α
1 Hour.
α
α
4 Hours.
α
α
2θ →
Fe4N
Fe3O4
Fe2O3

Figure VI.8

Transmission electron micrographs of

oxides from

(a) nitrided mild steel (in $5NH_3$:$95H_2$ at 700°C),

(b) un-nitrided mild steel

oxidised at 420°C for 5 min in air.

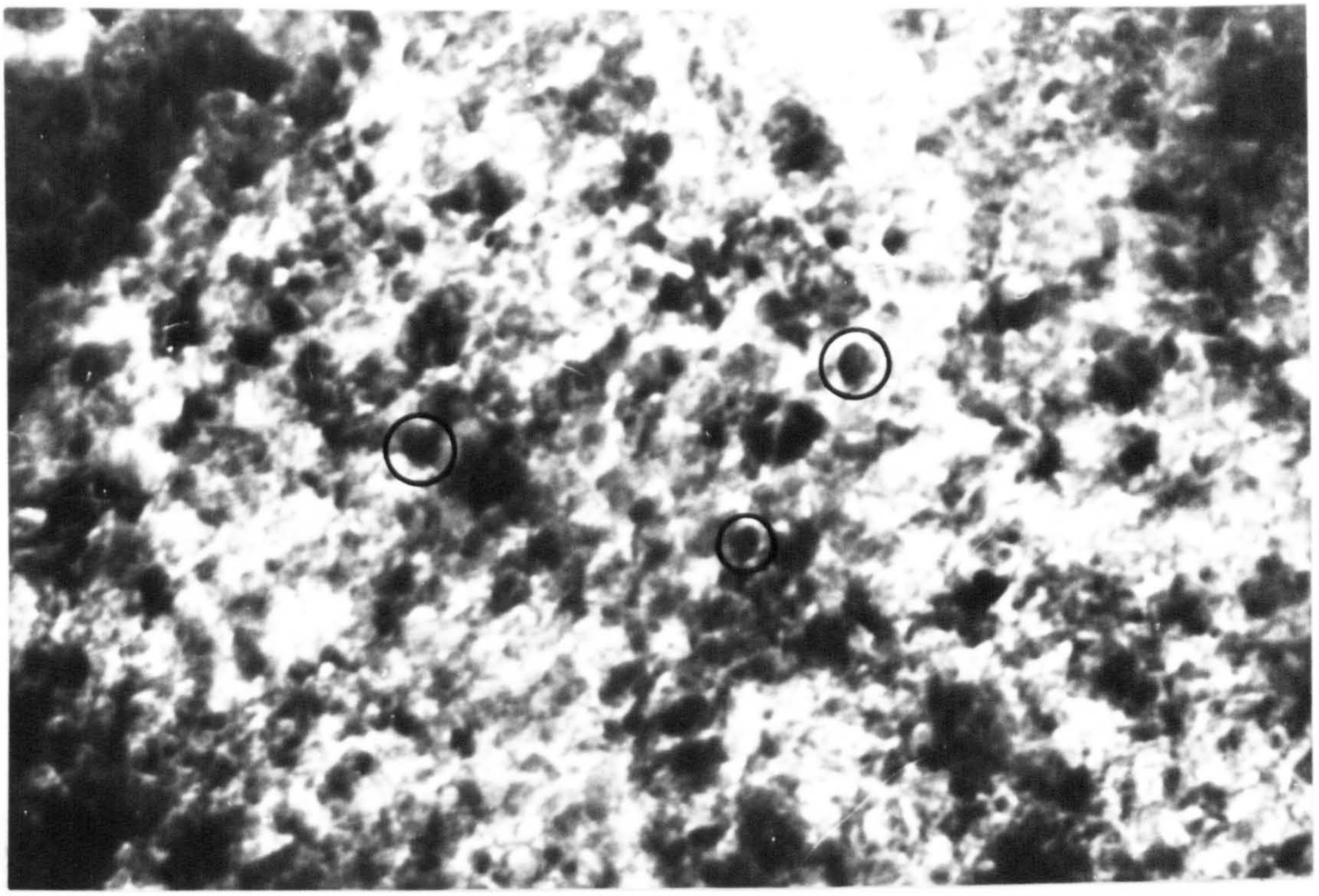

(a)

0.1 μm

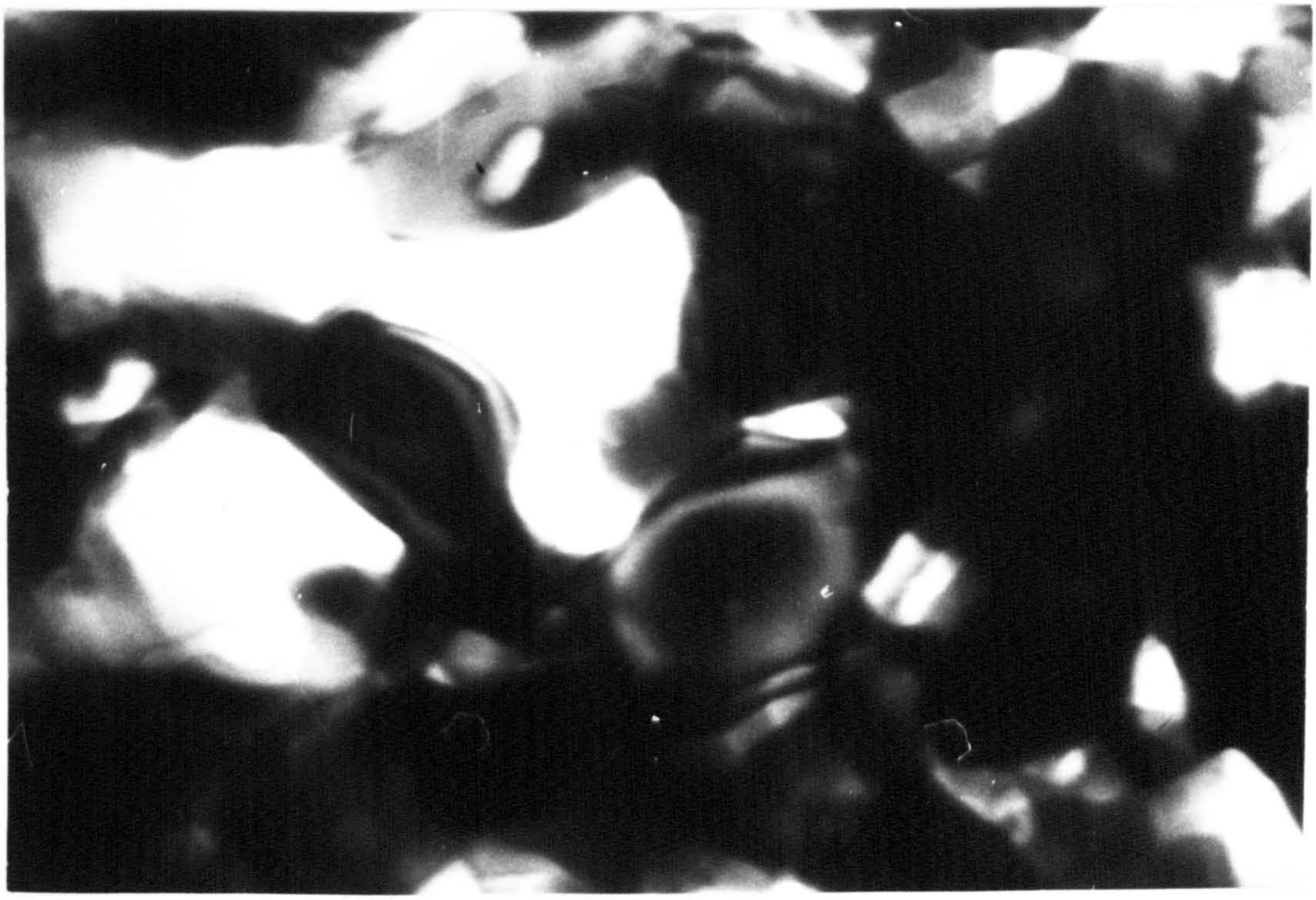

(b)

the grain size of the first-formed oxide on the steel surface is influenced by the microstructure of the nitrided layer.

Oxidation of mild steel at 420°C in one atmosphere pressure of air is too rapid for discrete oxide nuclei to be observed on the metal surface at even very short exposure times. The rate of oxidation will be reduced at low pressures and providing they are not below the dissociation pressure of the oxide, the oxidation processes will be analogous to those at normal pressures (for Fe_3O_4 at 500°C, $P_{O_2} = 10^{-31}$ Pa (10^{-36} atm)). Hussey & Cohen (1971) studied the oxidation of iron in the range 450°-550°C at pressures of 10^{-4}-10^{-2} Pa (10^{-9}-10^{-7} atm) and found that at an oxygen pressure of 10^{-3} Pa (10^{-8} atm) at 500°C, discrete oxide grains were observed on the surface of iron up to 2.5h, after which the oxide grains grew together to form a continuous film.

Aging of the nitrided α'-martensite/ γ-austenite at 500°C produces a ferritic structure with γ'-Fe_4N crystallites that stabilise at a diameter of about 1000 Å after aging for long times. Figure VI.1(b) shows the microstructure of nitrided mild steel after 64h at 500°C in an argon atmosphere; Figure VI.1(a) shows the as-nitrided structure. Since the tempering at the surface of the as-nitrided steel is extremely rapid, the initial oxide nucleation and growth processes on an as-nitrided structure must be very similar to those on an aged specimen. Figure VI.9 shows the microstructure of a nitrided mild steel thin-foil specimen after oxidation at a total

Figure VI.9

Transmission electron micrographs of mild steel nitrided in $5NH_3{:}95H_2$ at 700°C; aged at 500°C for 64h; oxidised at 500°C, $2x10^{-3}$Pa for 30 min.

(a) bright field,

(b) darkffield, δ'-Fe_4N reflection.

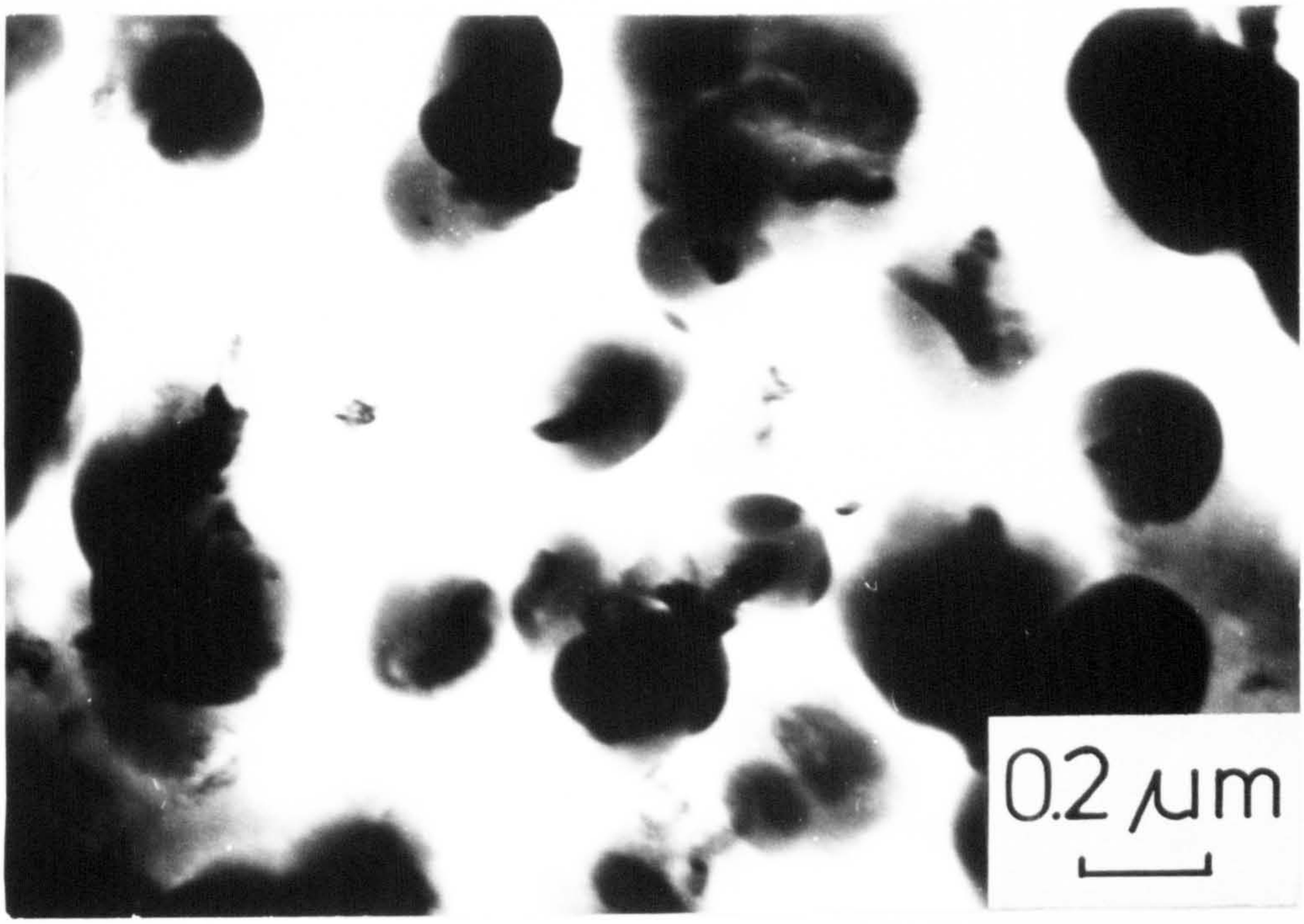

(a)

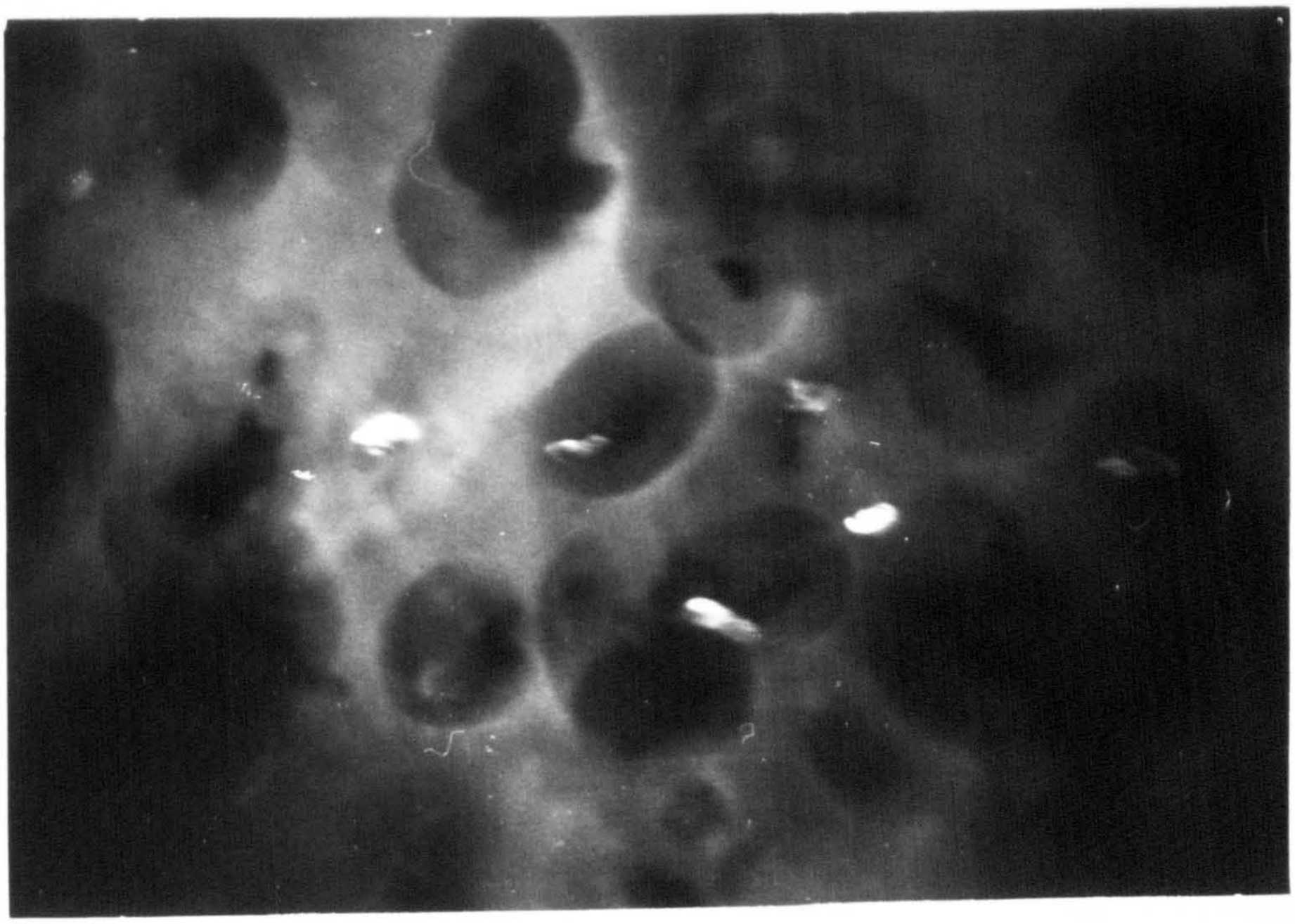

(b)

residual pressure of about $2x10^{-3}$Pa ($2x10^{-8}$atm; i.e. $p_{O_2} \sim 4x10^{-4}$Pa ($4x10^{-9}$atm)) at 500°C for 30 min.[2] Figure VI.9(a) is a bright field transmission electron micrograph showing discrete oxide nuclei having a rounded shape and which are mostly associated with smaller angular particles. Figure VI.9(b) is a dark field micrograph of the same area taken with a γ'-Fe_4N reflection showing that the angular particles are γ'-Fe_4N. These metallographic observations therefore provide direct evidence that nucleation of oxide occurs on γ'-Fe_4N precipitates. Similar observations on annealed iron specimens show that fewer oxide nuclei form on the surface and there is more rapid growth of the individual oxide grains.

VI.7. Aging of Nitrided Martensitic Case

The rapid tempering of the nitrided surface during oxidation noted in section VI.5 is at variance with measurements on bulk samples of nitrogen-martensite (Hendry, 1978). However, elastic constraints within the bulk of the specimen might be expected to be relaxed near the free surface resulting in a more rapid tempering rate.

A nitrided mild steel specimen ($5NH_3$:$95H_2$ at 700°C) was aged at 420°C for 5 min. X-ray diffractometer traces were taken of the specimen surface, using Cu-Kα radiation, after repeated removal of the surface layers by electropolishing. The absorption of the CuKα X-radiation by iron is relatively high and a large proportion of the intensity of the diffracted X-rays are from a layer only about 4 μm

thick at the surface of the specimen. The information recorded on the diffractometer trace is thus related to a thin layer close to the surface of the specimen and, by successive removal of the surface layers, any changes of the relative amounts of different phases with depth can be established. The relative intensities of the $\{111\}$ reflections of γ-austenite and γ'-Fe_4N are plotted as a function of depth below the original surface in Figure VI.10. Precipitation of γ'-Fe_4N is enhanced within 25 μm of the surface, but at greater depths a high proportion of austenite remains in the matrix. However, the $\{111\}$ austenite peak overlaps with the $\{101\}$ martensite peak so that the actual amounts of austenite will be less than those indicated.

A more quantitative method of determining the relative amounts of the phases present from diffractometer traces, based on the technique of Averbach & Cohen (1948), has been used to study the aging of the nitrided case on mild steel. The expression for the intensity diffracted by a single-phase powder specimen in a diffractometer using monochromatic X-rays is

$$I = K.R/2\mu \quad \ldots\ldots \text{VI.3}$$

where K is a constant characteristic of the incident radiation, R is a constant which includes those factors affecting the diffracted radiation for a particular reflection (see Averbach & Cohen, 1948) and μ is the linear absorption coefficient.

If the matrix contains two phases, e.g. austenite (γ) and martensite (α'), for a particular line of each phase

Figure VI.10

Variation of proportions of γ-austenite and γ'-Fe_4N with depth in surface layer of nitrided mild steel aged at 420°C for 5 min.

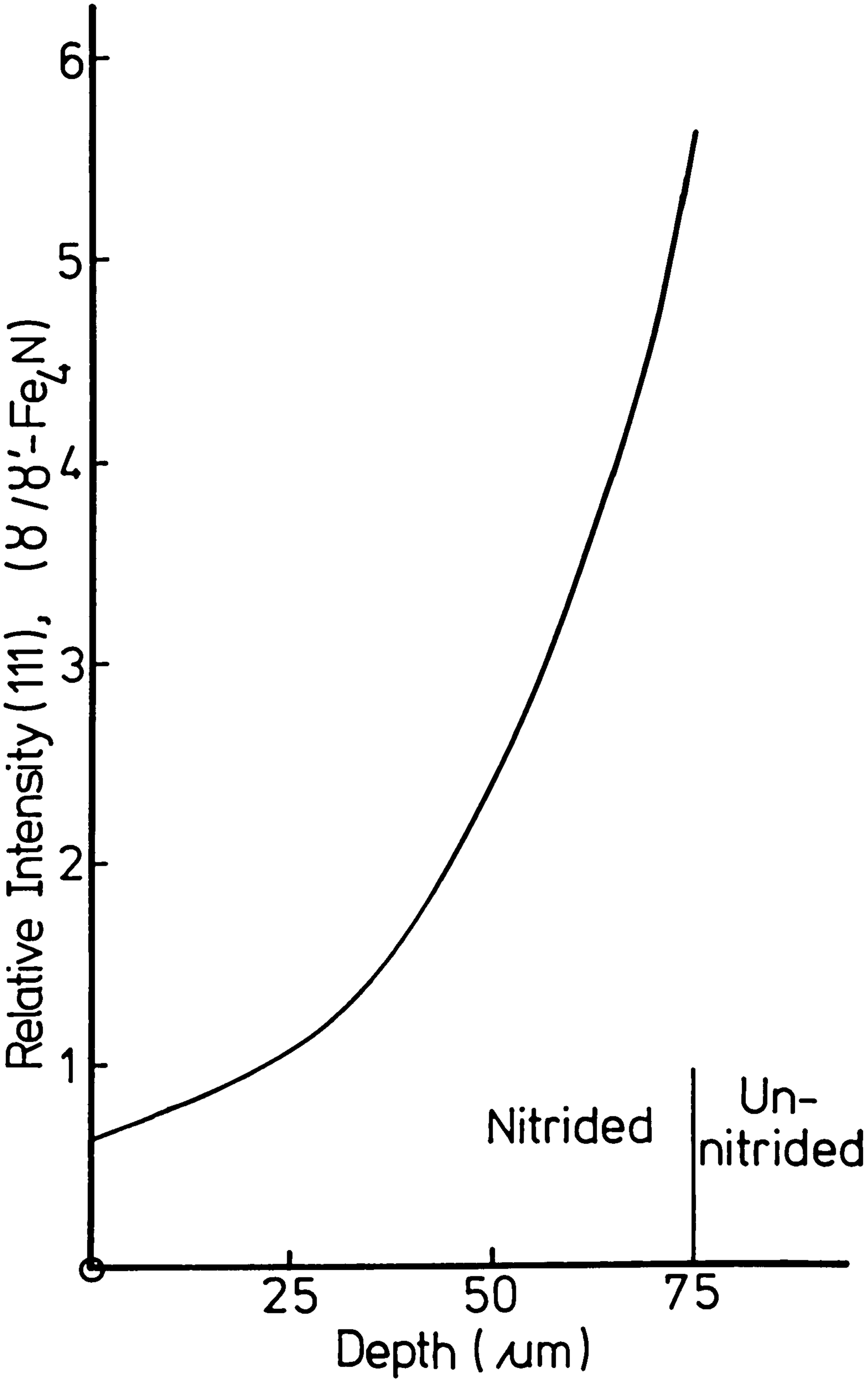
Relative Intensity (γ(111), (γ/γ'-Fe4N)
6
5
4
3
2
1
Nitrided
Un-nitrided
25
50
75
Depth (μm)

$$I_{\gamma} = K.R_{\gamma}.C_{\gamma}/2\mu_M \quad \ldots\ldots \text{VI.4}$$

$$I_{\alpha'} = K.R_{\alpha'}.C_{\alpha'}/2\mu_M \quad \ldots\ldots \text{VI.5}$$

where C is the volume fraction of the phase and μ_M is the mean linear absorption coefficient of the matrix. Division of the equations VI.4 and VI.5 gives

$$\frac{I_{\gamma}}{I_{\alpha'}} = \frac{R_{\gamma}.C_{\gamma}}{R_{\alpha'}.C_{\alpha'}} \quad \ldots\ldots \text{VI.6}$$

Therefore, $C_{\gamma}/C_{\alpha'}$ can be obtained from a measurement of $I_{\gamma}/I_{\alpha'}$ and a calculation of R_{γ} and $R_{\alpha'}$. The value of C_{γ} can be obtained from the additional relationship $C_{\alpha'} + C_{\gamma} = 1$.

If the steel contains a third phase, e.g. γ' -Fe_4N, then $C_{\gamma'}$ can be determined by measuring $I_{\gamma'}$ and calculating $R_{\gamma'}$ from which an equation similar to VI.6 can be set up and $C_{\gamma}/C_{\gamma'}$ obtained. The value of $C_{\gamma'}$ is then found from the relationship $C_{\gamma} + C_{\alpha} + C_{\gamma'} = 1$.

Figure VI.11 shows the variation with time of the volume fraction of γ -austenite and γ'-Fe_4N, as determined by the above method, in mild steel specimens nitrided in $5NH_3:95H_2$ at $700^{\circ}C$ for 23h and then aged for various times at $500^{\circ}C$. X-ray diffractometer traces were taken of the surface of the specimens and also after removing a 30μ m layer by abrasion. Discrete diffraction peaks having no overlaps were used for the calculations.

At the surface of the nitrided case the volume

Figure VI.11

Effect of aging at 500°C on volume fraction of γ-austenite and γ'-Fe_4N in nitrided case on mild steel nitrided in $5NH_3$:$95H_2$ at 700°C.

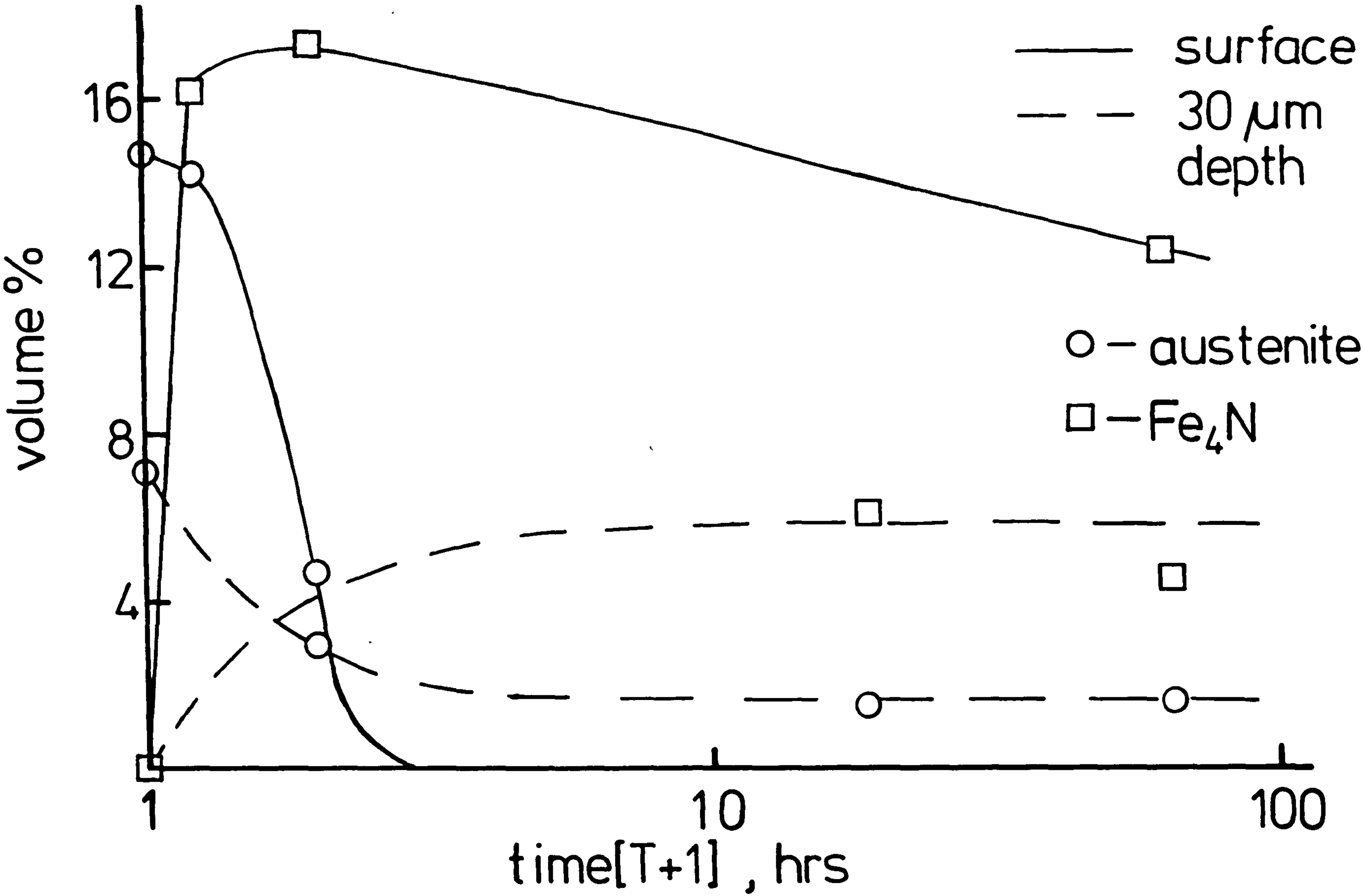
surface
30 μm depth
o – austenite
□ – Fe_4N
volume %
16
12
8
4
1
10
100
time[T+1] , hrs

fraction of γ'-Fe_4N increases rapidly with aging time from an initial value of zero to its maximum value (about 17%), but then decreases again after longer aging times. The solubility of γ'-Fe_4N in α-ferrite increases with temperature, so that during aging, dissociation of Fe_4N in the case will act as an internal source of nitrogen for further diffusion into the core of the specimens. Hence, the concentration of Fe_4N at the surface will decrease. The volume fraction of untransformed γ-austenite falls with aging time from an initial value of about 15% to zero within two hours. The increase in the volume fraction of γ'-Fe_4N at a depth of 30 μm is much less rapid than at the surface and reaches a maximum of only about 5%. The volume fraction of retained austenite is initially about 7% and its rate of transformation is slower than that found at the surface with about 1.5% remaining after 64h. These results clearly demonstrate the rapid rate of transformation of $\alpha' + \gamma$ to $\alpha + \gamma'$ at the surface compared with that at only 30 μm below the surface during aging of the nitrided case.

VI.8. Thermal Cycling of Mild Steel

Thermal cycling of metal-oxide composites develops stresses in the oxide due to differences in thermal expansion. These can be large enough to cause scale fracture allowing gas access to the metal/oxide interface and hence to an increased oxidation rate.

Figure VI.12 shows the results obtained for the thermally cycled oxidation (see section V.5(c)) of mild steel in air at 240^{o}-$480^{o}C$ with specimens:

(a) as annealed;

(b) nitrided in $8NH_3:92H_2$ at $580^{o}C$ and brine-quenched;

(c) nitrided in $5NH_3:95H_2$ at $700^{o}C$ and air-cooled.

The nitriding conditions for (b) are within the α-ferrite region (see Figure V.1) giving 0.24a/oN and on quenching, the nitrogen will remain in solid solution. At temperatures above $170^{o}C$, the super-saturated N-ferrite ages to give a distribution of γ'-Fe_4N in ferrite. The α'-martensite plus γ-austenite matrix formed by the nitriding treatment (c) also ages at high temperatures to give γ'-Fe_4N dispersed in ferrite, but the nitrogen content is much higher than in the super-saturated ferrite of (b) and so gives a greater volume fraction of γ'-Fe_4N. Table VI.4 shows the parabolic rate constants together with the r-coefficients which are relatively low for all three specimens due to the large deviation from smooth weight gain curves and hence from true parabolic rates.

Figure VI.13 shows the morphology of the oxides formed on the specimens. The oxide formed on un-nitrided mild steel is laminated and separated from the metal substrate. The oxide formed on the super-saturated N-ferrite substrate is also separated from the substrate but is more compact. A line of porosity parallel to the metal/oxide interface is found within the 12 μm thick oxide at a depth of 9 μm i.e. the ratio of oxide beneath the line of porosity to the total oxide thickness (0.25) is similar to the ratio

Figure VI.12

Oxidation curves of mild steel specimens oxidised in air at 240°-480°C.

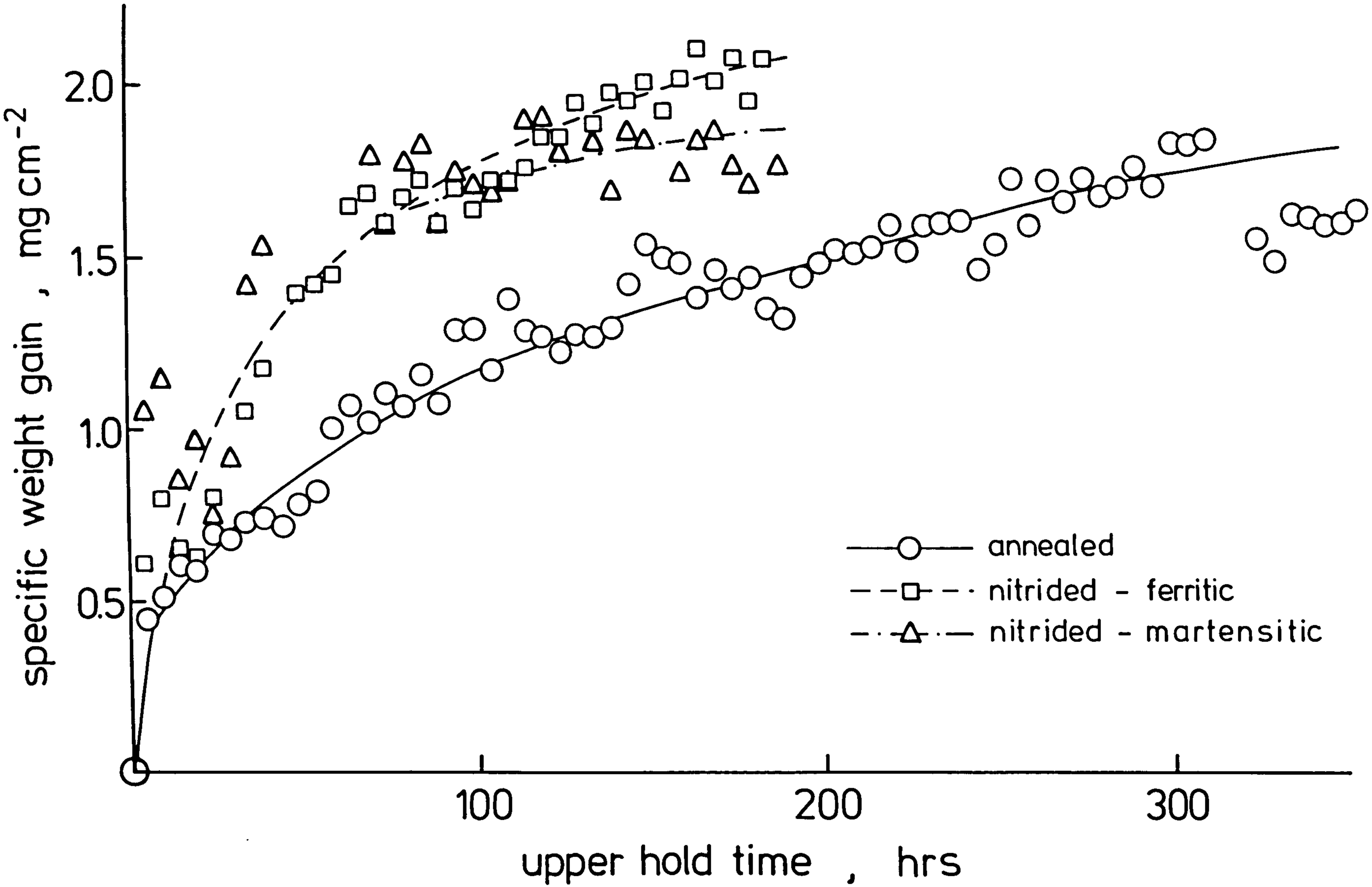
specific weight gain , mg cm-2
2.0
1.5
1.0
0.5
100
200
300
upper hold time , hrs
annealed
nitrided - ferritic
nitrided - martensitic

Figure VI.13

Scanning electron micrographs of oxides formed on mild steel oxidised at 240°-480°C in air

(a) un-nitrided,

(b) nitrided in $8NH_3{:}92H_2$ at 580°C,

(c) nitrided in $5NH_3{:}95H_2$ at 700°C.

(a)

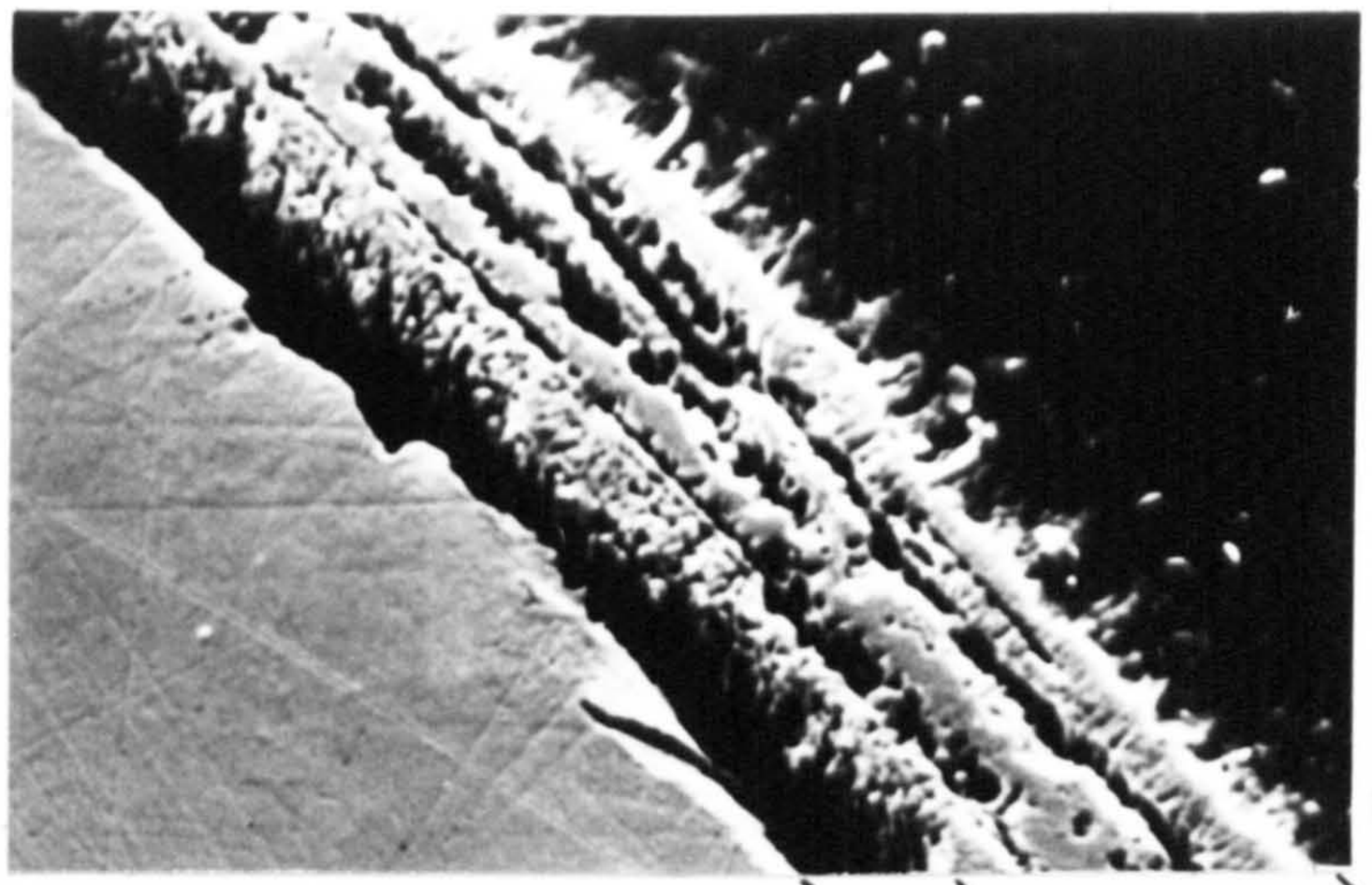

10 μm

(b)

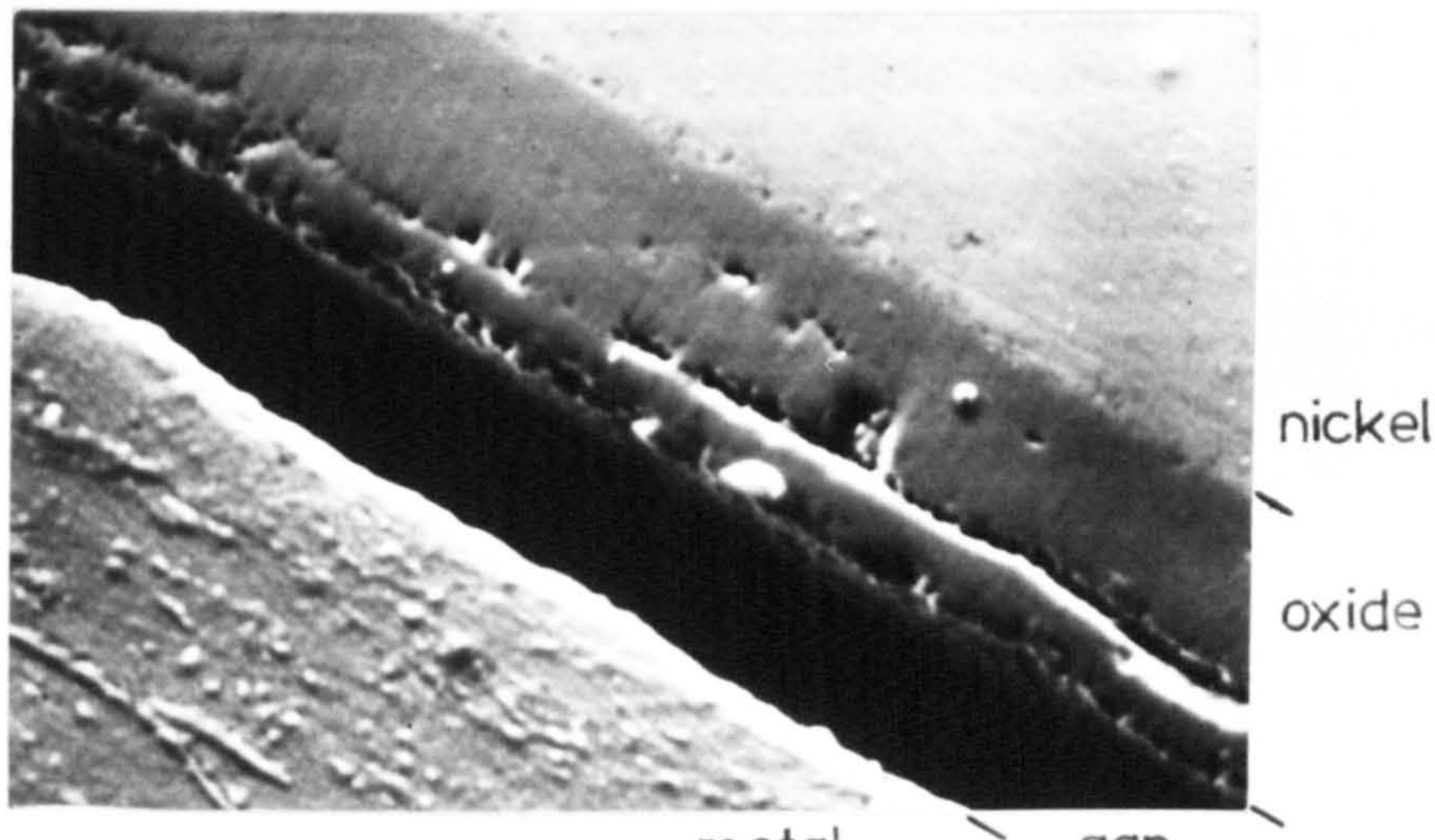

10 μm

(c)

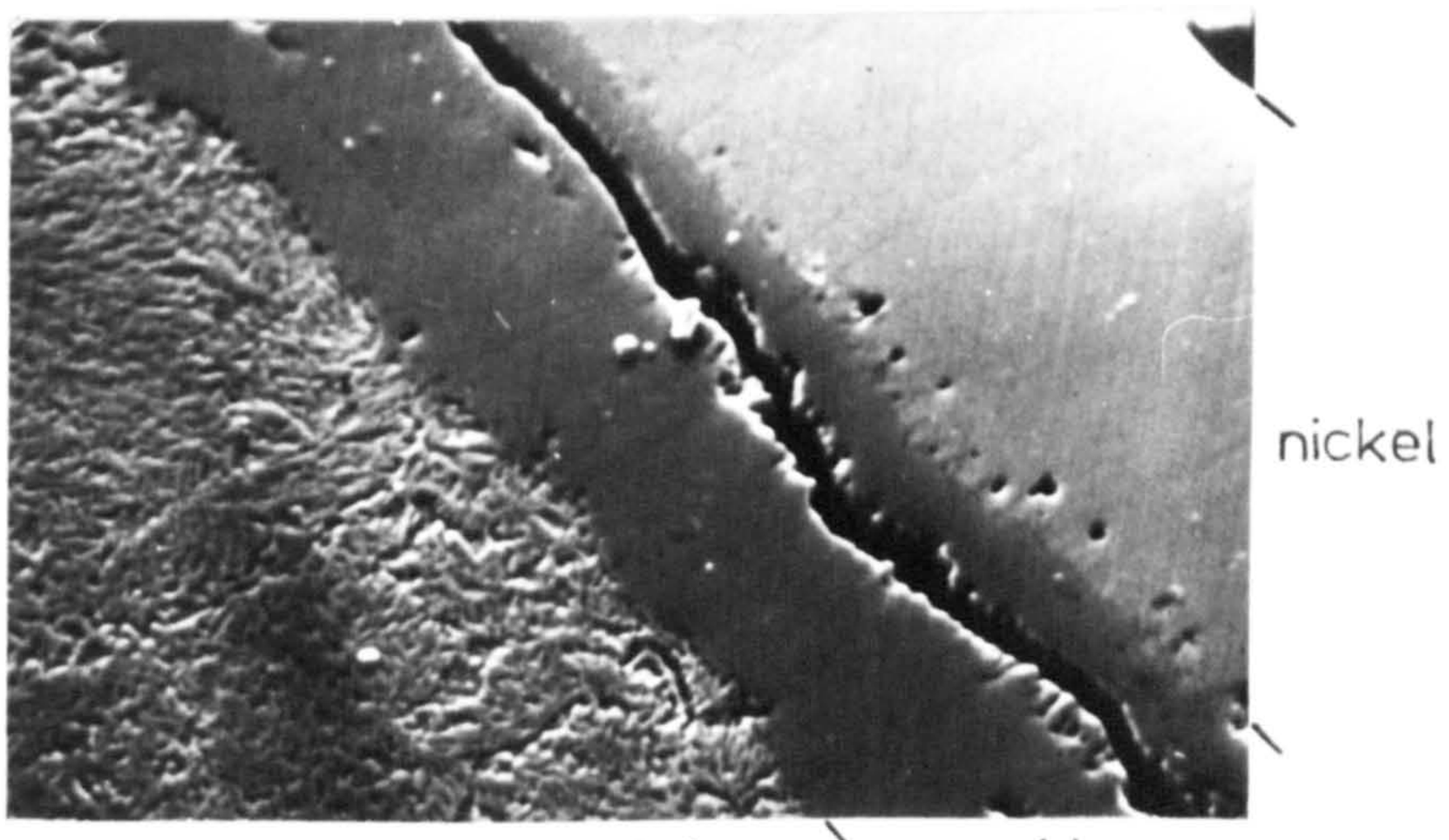

10 μm

Table VI.4

Parabolic rate constants (k_p) and linear regression coefficients (r) for mild steel thermally cycled at 240°-480°C in air.

Specimen	Parabolic rate constant, k_p $g^2\ cm^{-4} s^{-1}$	r	Upper hold time h
Un-nitrided	2.03×10^{-12}	0.87	360
Nitrided in $5NH_3:95H_2$ at 700°C	5.81×10^{-12}	0.83	190
Nitrided in $8NH_3:92H_2$ at 580°C	3.97×10^{-12}	0.82	190

of the inner fine grained layer to the total oxide thickness found on mild steel nitrided to give a martensitic case and oxidised isothermally at 500°C; see Table VI.3. The oxide formed on the N-martensite matrix is compact, adherent to the substrate and is less porous. Some cracking within the oxide is apparent and probably occurs during final cooling and/or subsequent mounting of the specimen, which causes de-adherence at the metal/oxide interface in the other specimens. Thus, nitriding of mild steel to give either a martensite-austenite structure, or a super-saturated N-ferrite structure (both of which age to give an α-ferrite matrix with γ'-Fe_4N precipitates) results in the formation of a duplex oxide which is adherent to the metal substrate during oxidation. The oxide-metal adherence is less strong on the N-ferrite than on the martensite-austenite substrate.

The reduced rate of oxidation weight gain of un-nitrided mild steel during thermal cycling is due to vacancy condensation at the metal/oxide interface causing a reduction in the contact area and hence a lower flux of cations from the metal to the oxide. Incoherent Fe_4N particles in mild steel are thought to eliminate the formation of interfacial voids by acting as vacancy sinks, similar to the effects of dislocations in cold worked mild steel (Caplan & Cohen, 1966; see section III.6).

...

The metallographic evidence of the improved adherence of the oxide on nitrided mild steel is at variance with the oxidation rate measurements. However, the rate measurements were made for relatively short times compared with the in-service

lifetimes of furnace wall tubing and the results of short-term investigations cannot be applied directly to long-term practice.

VI.9. Effect of Nitriding Heat Treatment on the Oxidation of Mild Steel

The morphology of the oxide formed on mild steel nitrided in $8NH_3:92H_2$ at $580^{\circ}C$ to give a super-saturated N-ferrite and oxidised isothermally at $500^{\circ}C$ for 900h is shown in Figure VI.14(a). The features are similar to those found on the thermally cycled specimen nitrided under similar conditions (see section VI.8). The oxide shows a duplex structure with a fine-grained inner layer and a coarse-grained outer layer with some evidence of de-adhesion and porosity at the interface of the two layers.

Figure VI.14(b) shows the morphology of the oxide formed on mild steel nitrided in $5NH_3:95H_2$ at $700^{\circ}C$ to give α'-martensite plus γ-austenite, and aged at $500^{\circ}C$ for 220h before subsequent oxidation at $500^{\circ}C$ for 530h in air. The total weight gain of the specimen was 4.1mg cm^{-2}. The magnetite again shows a duplex layer, fine-grained inside, and coarse-grained outside, the inner layer being about one-third of the total thickness. Again there is evidence of voidage along the interface of the two layers. The metal/oxide interface is coherent and features of the substrate (e.g. grain boundaries) extend into the inner oxide layer.

Figure VI.14

Scanning electron micrographs of mild steel

(a) nitrided in $8NH_3$:$92H_2$ at 580^{o}C; oxidised at 500^{o}C for 900h in air,

(b) nitrided in $5NH_3$:$95H_2$ at 700^{o}C; aged at 500^{o}C for 220h; oxidised at 500^{o}C for 530h in air.

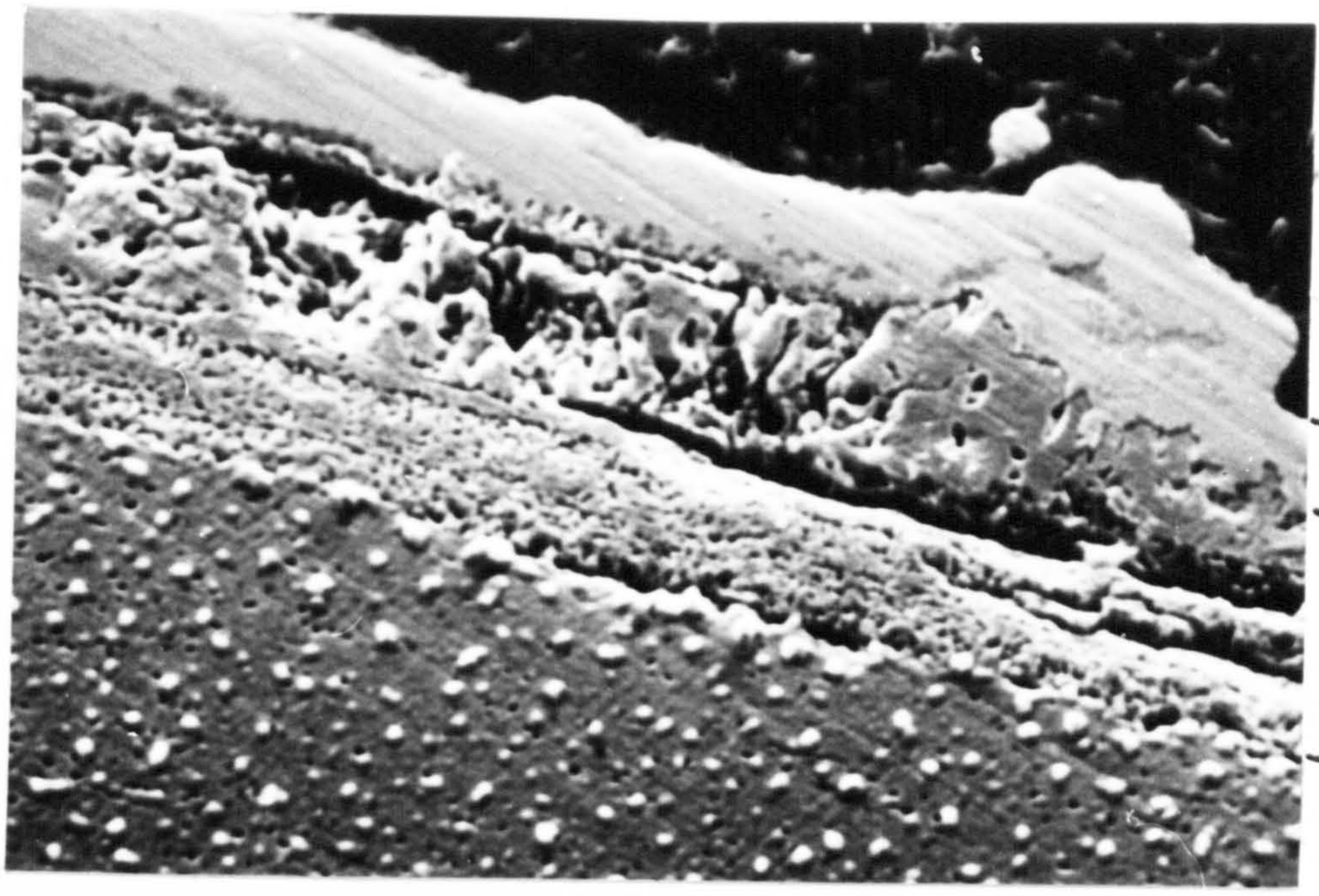

(a)

10 μm

(b)

10 μm

Figure VI.15(a) shows the morphology of the oxide formed on mild steel nitrided in $4NH_3:96H_2$ at 700^oC to give an α'-martensite: γ-austenite ratio of about 8:1 and oxidised in air at 500^oC for 530h. The total weight gain during oxidation was 3.5mg cm^{-2}. Figure VI.15(b) shows the morphology of the oxide formed on mild steel nitrided in $8.5NH_3:91.5H_2$ at 700^oC to give an α'-martensite: γ-austenite ratio of about 4:5 and then oxidised in air at 500^oC for 530h. The total weight gain during oxidation was 3.0mg cm^{-2}. Both specimens show a duplex magnetite morphology with a fine-grained inner layer, a coarse-grained outer layer and voidage at their interface. The specimen nitrided at the higher nitrogen potential shows triple-point cracking in the metal substrate (arrowed in Figure VI.15(b)); this is also present in un-oxidised specimens and results from the stresses imposed during the quenching of the high-nitrogen γ-austenite.

A significant feature of the oxide formed on this substrate is that similar triple-point cracks are observed within the inner fine-grained magnetite layer and one such crack straddles the metal oxide interface in Figure VI.15(b). The triple-point cracks can be regarded as inert markers in the substrate. If oxide formation is by metal cation diffusion across the oxide and reaction at the outer oxide interface, the cracks will become planar along the metal/oxide interface as the metal around them is consumed. If, however, oxygen diffuses inwards and reaction occurs at the metal oxide interface, the cracks do not alter their morphology and are simply incorporated into the oxide layer. Figure VI.15(b) shows that the second of these two alternatives must operate.

Figure VI.15

Scanning electron micrographs of mild steel

(a) nitrided in $4NH_3:96H_2$ at 700°C,

(b) nitrided in $8.5NH_3:91.5H_2$ at 700°C,

oxidised in air at 500°C for 530h.

Etched in HCl.

(a)

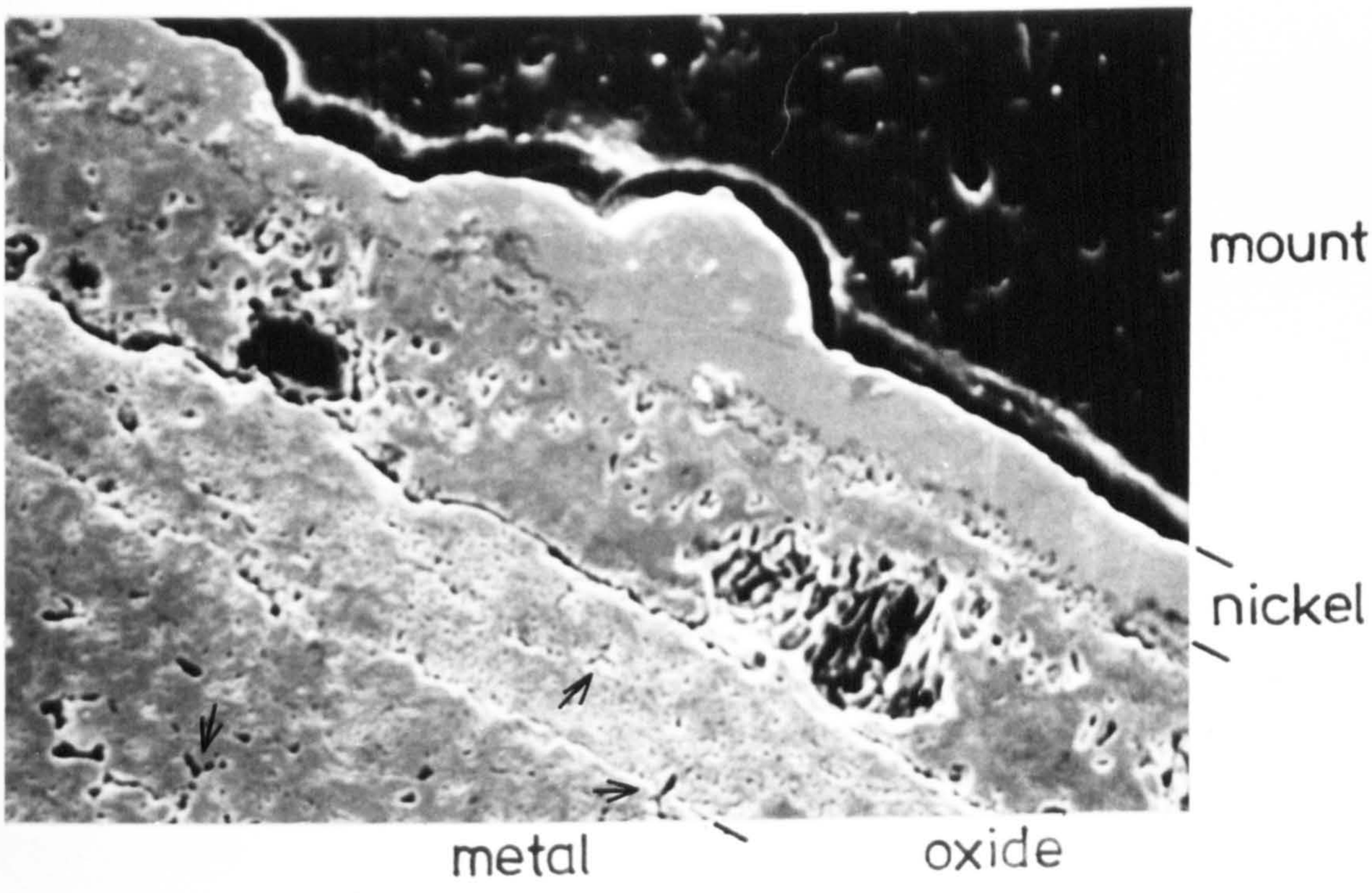

(b)

It should be noted that with the specimen nitrided at $8.5NH_3:91.5H_2$ not only is the total oxide thickness and the total weight gain less than those on specimens nitrided at lower nitrogen potentials, but also triple-point cracking occurs and is likely to have adverse effects on the high-temperature creep strength of the nitrided case. Thus the original nitriding conditions used ($5NH_3:95H_2$ at $700^{o}C$) represent a compromise between low oxidation rate and the absence of cracks in the nitrided matrix.

VI.10. Oxidation of Nitrided Mild Steel at $600^{o}C$

Wustite is stable above $570^{o}C$ and comprises the greater proportion of the scaling layer on iron oxidised above this temperature with only a thin outer layer consisting of Fe_3O_4 and Fe_2O_3 (Davies et al., 1951).

Figure VI.16 shows the morphology of the oxide formed on mild steel after oxidation at $600^{o}C$ for 650h in air. The oxide scale remains attached to the metal specimen during cooling but can easily be detached mechanically. Figure VI.16(a) shows the oxide scale and metal substrate after removal of some of the oxide. The compact oxide is separated from the substrate and is uniform in thickness. Figure VI.16(b) shows the surface of the oxide layer completely covered in oxide needles. Figures VI.16(c) and VI.16(d) show the underside of the oxide and the surface of the metal respectively which have mound and dimple structures that are complementary

Figure VI.16

Scanning electron micrographs of oxide from mild steel un-nitrided, oxidised at 600°C for 650h,

(a) oxide and metal,

(b) surface of oxide,

(c) underside of oxide,

(d) surface of metal.

(a)

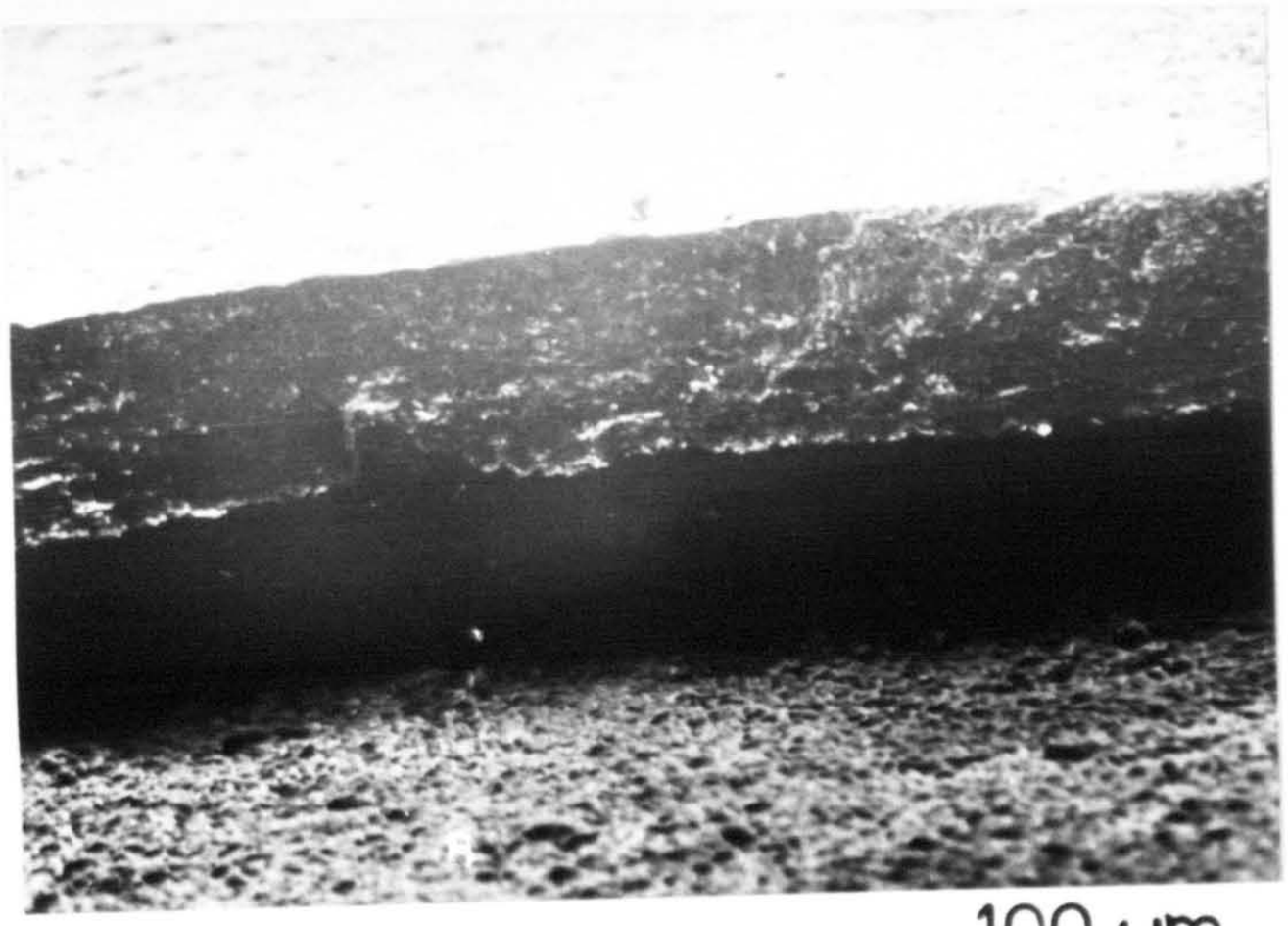

100 μm

(b)

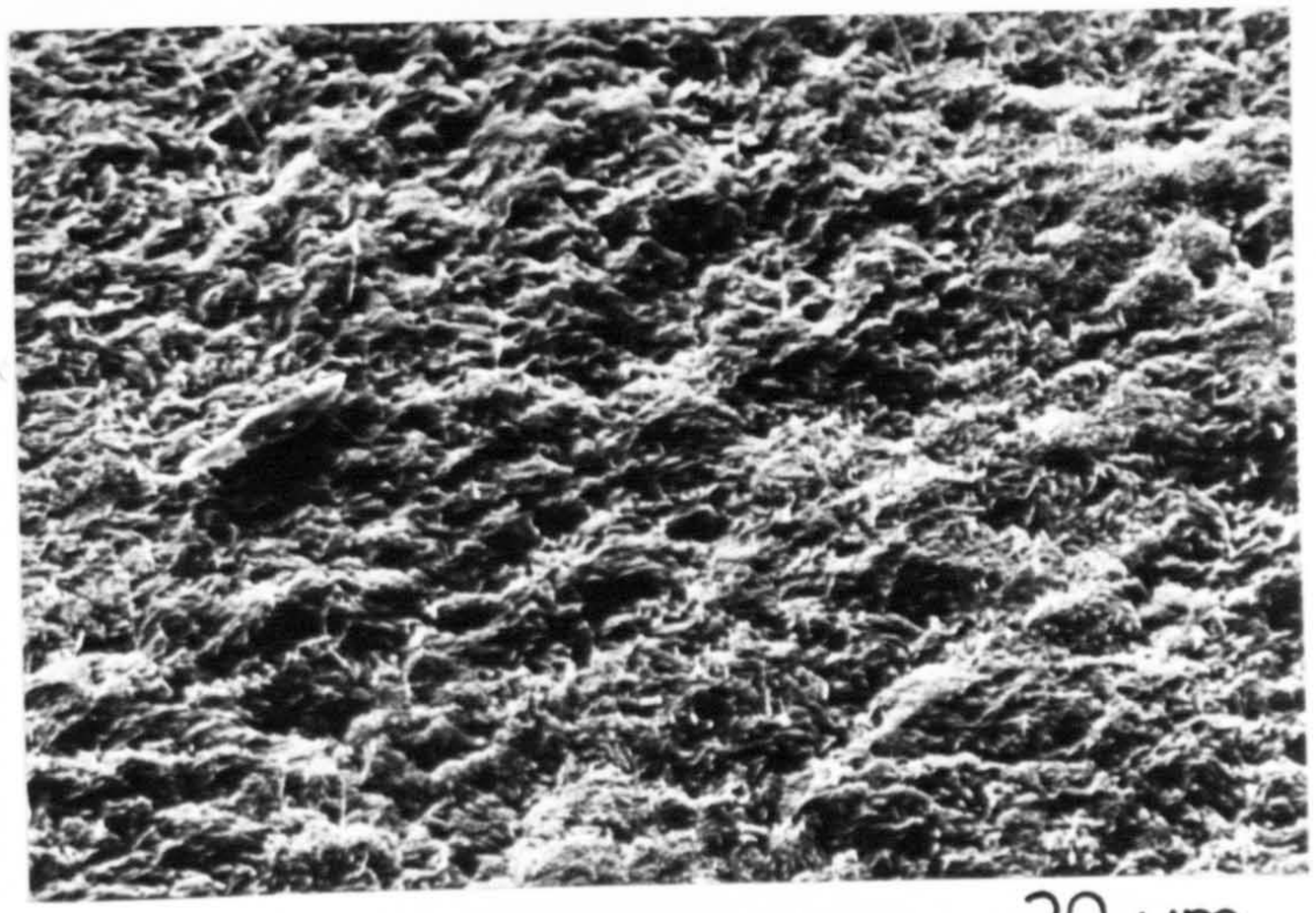

20 μm

(c)

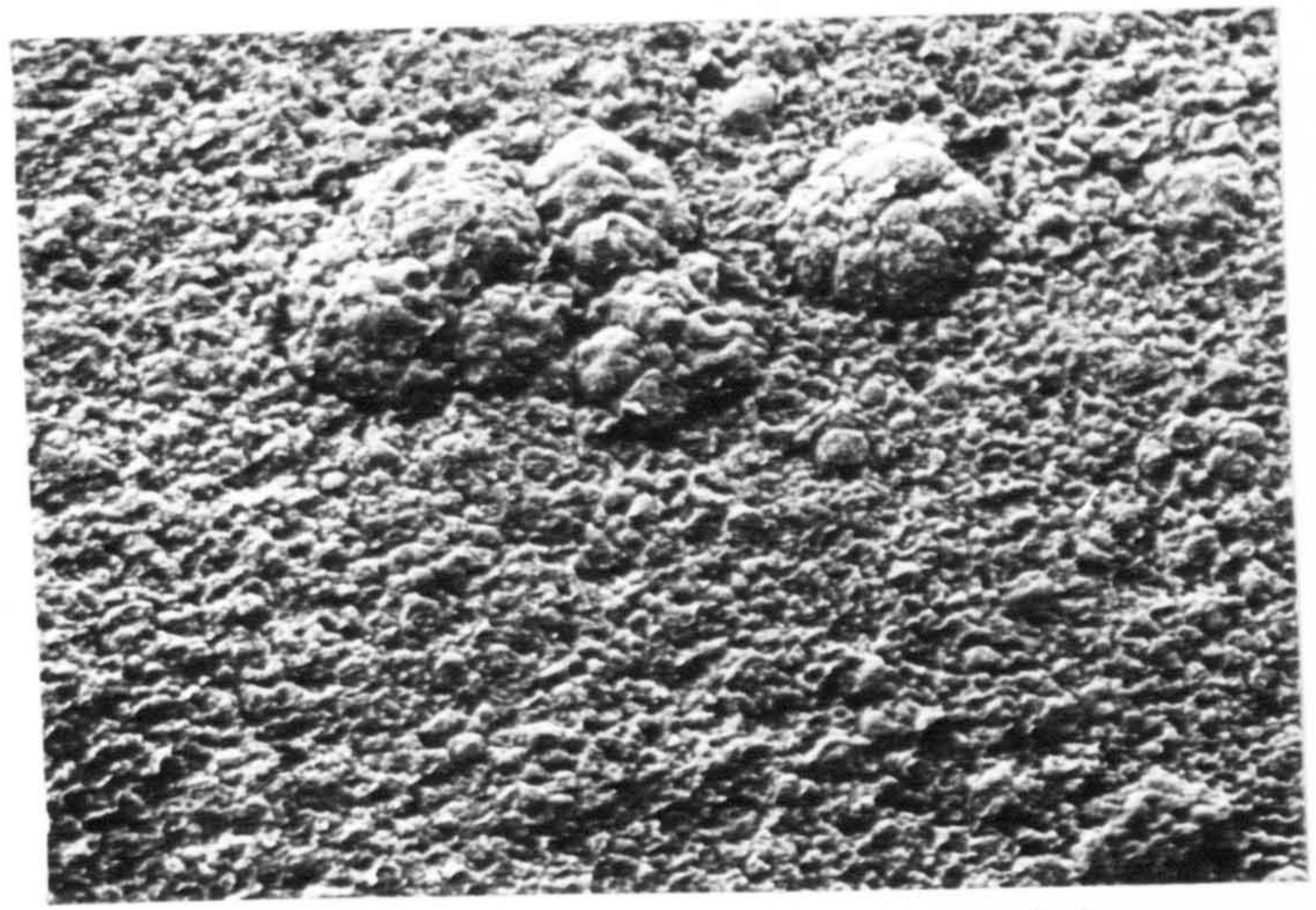

100 μm

(d)

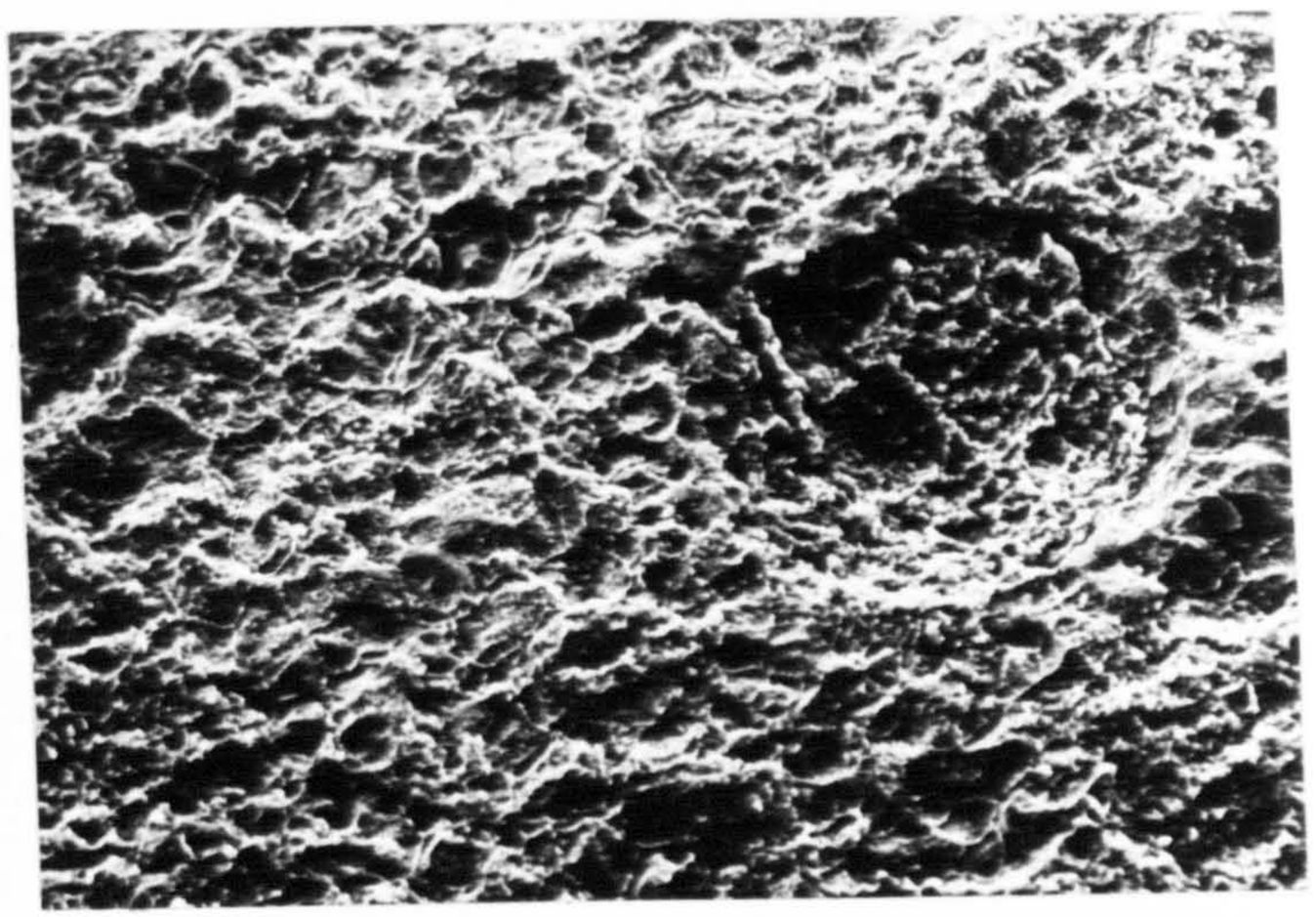

40 μm

to one another. Any voidage caused by vacancy condensation at the metal/oxide interface is eliminated by plastic deformation of the oxide (Caplan & Cohen, 1966) and is probably the cause of the dimpled nature of the metal/scale interface. The metal and oxide will thus remain in close contact at oxidation temperatures giving a high transfer area for movement of cations from the metal to the oxide. Separation of the oxide from the substrate occurs during the cooling of the specimen.

At temperatures below 570°C wustite is unstable and only magnetite and haematite form on iron. These oxides are less able to deform plastically than wustite and vacancy condensation at the metal/oxide interface results in the growth of voids. However, for the reasons given above, any benefits from the provision of vacancy sinks on the elimination of void formation are not expected to be important at temperatures above which wustite is formed. Figures VI.17 and VI.18 are scanning electron micrographs of the oxide from a mild steel specimen, nitrided in $5NH_3:95H_2$ at 700°C and oxidised in air at 600°C for 650h. The oxide spalled completely from the specimen during air-cooling and Figure VI.17(a) shows the outer oxide surface. It is extensively blistered, the oxide forming the blisters being only a small fraction of its total thickness. Figure VI.17(b) shows the underside of the inner layer of oxide with a highly convoluted morphology and small angular particles in the "valleys". The distance between the peaks of the ridges is generally 200-300 μm. Figure VI.17(c) shows the surface of the metal substrate from which the oxide has spalled. Patches of oxide remain attached to the metal, the surface of which

Figure VI.17

Scanning electron micrographs of oxide spalled from mild steel nitrided in $5NH_3:95H_2$ at 700°C; oxidised at 600°C for 650h in air,

(a) surface of oxide,

(b) underside of oxide,

(c) surface of metal.

(a)

100 μm

(b)

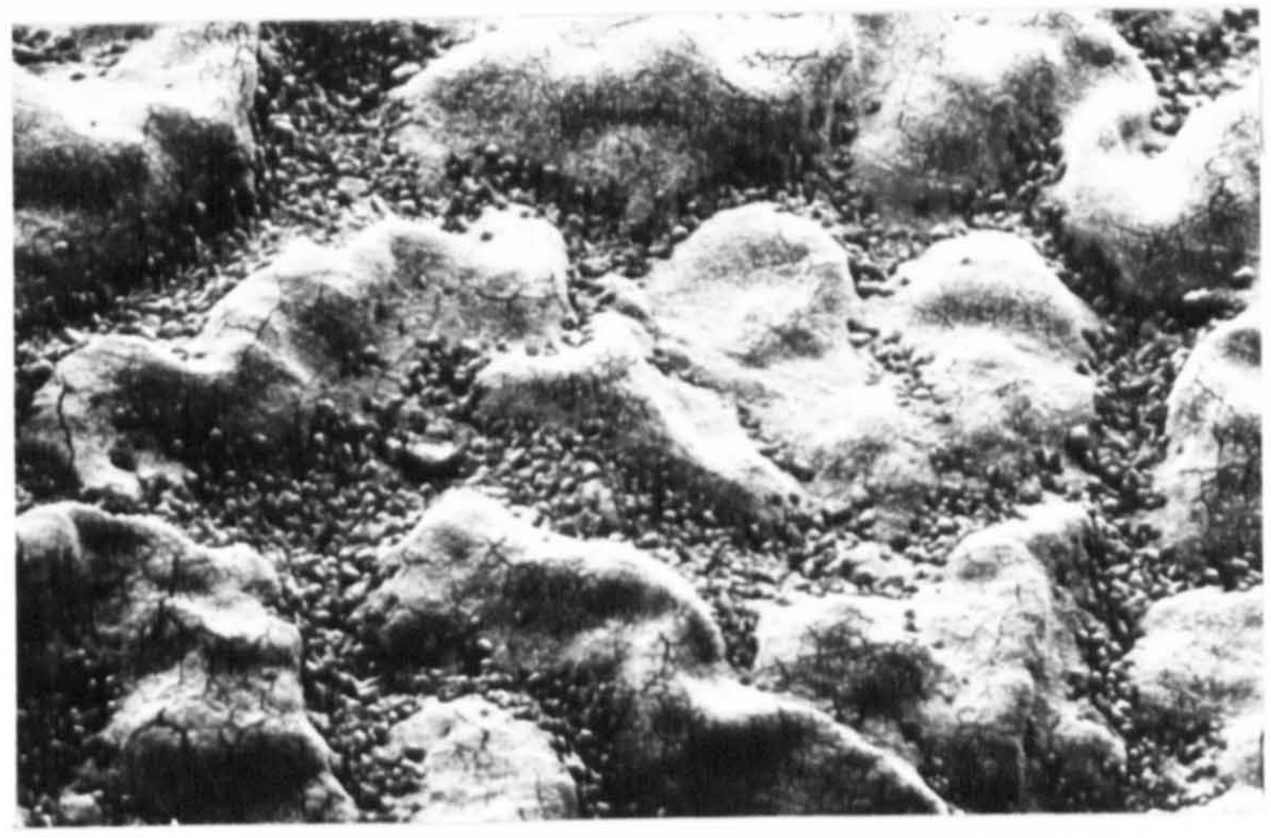

200 μm

(c)

200 μm

Figure VI.18

Scanning electron micrographs of oxide spalled from mild steel nitrided in $5NH_3:95H_2$ at 700°C; oxidised at 600°C for 650h in air,

(a) underside of "valley" area,

(b) underside of "ridge" area,

(c) edge of "valley" area,

(d) edge of "ridge" area.

(a)

20 μm

(b)

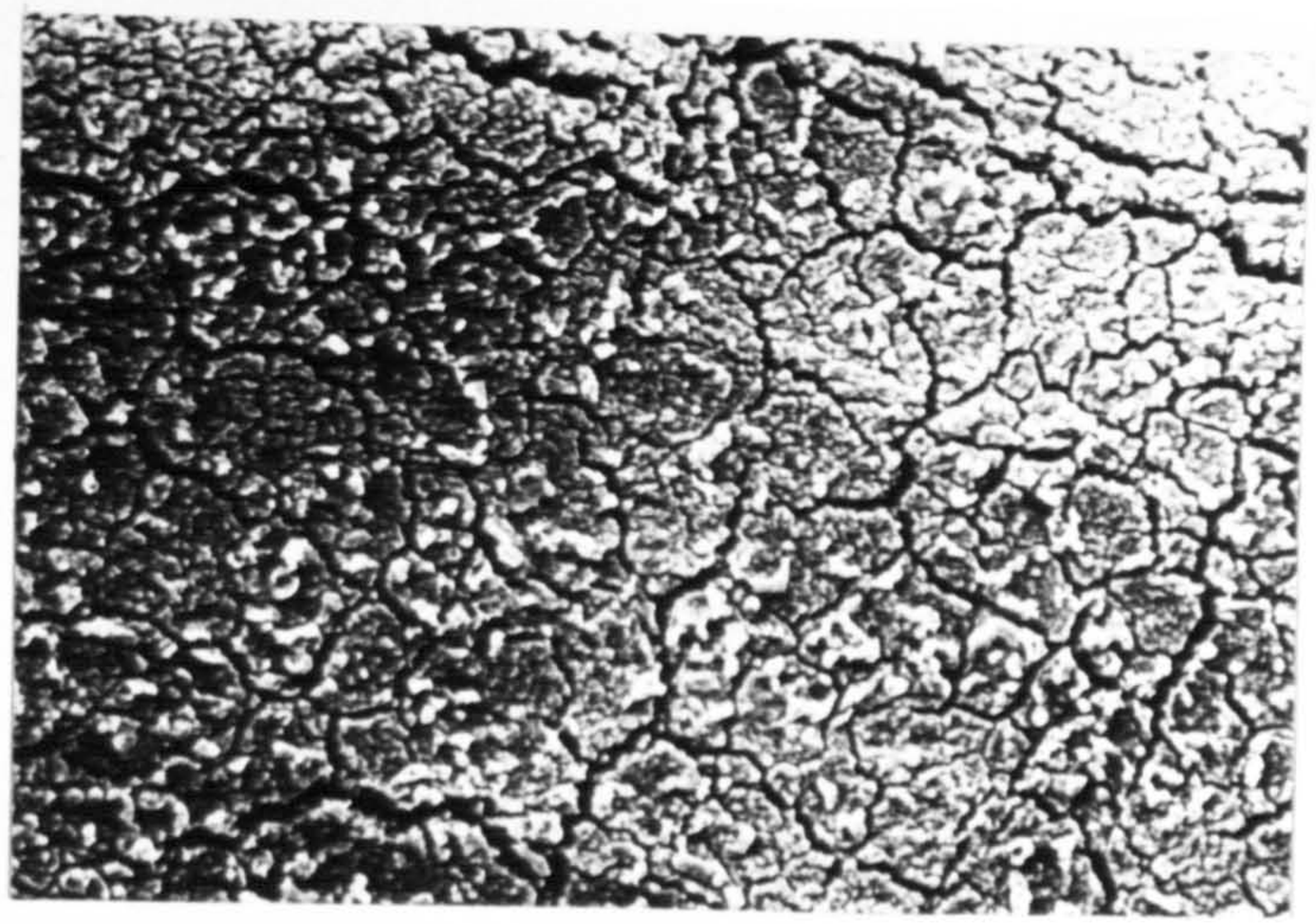

20 μm

(c)

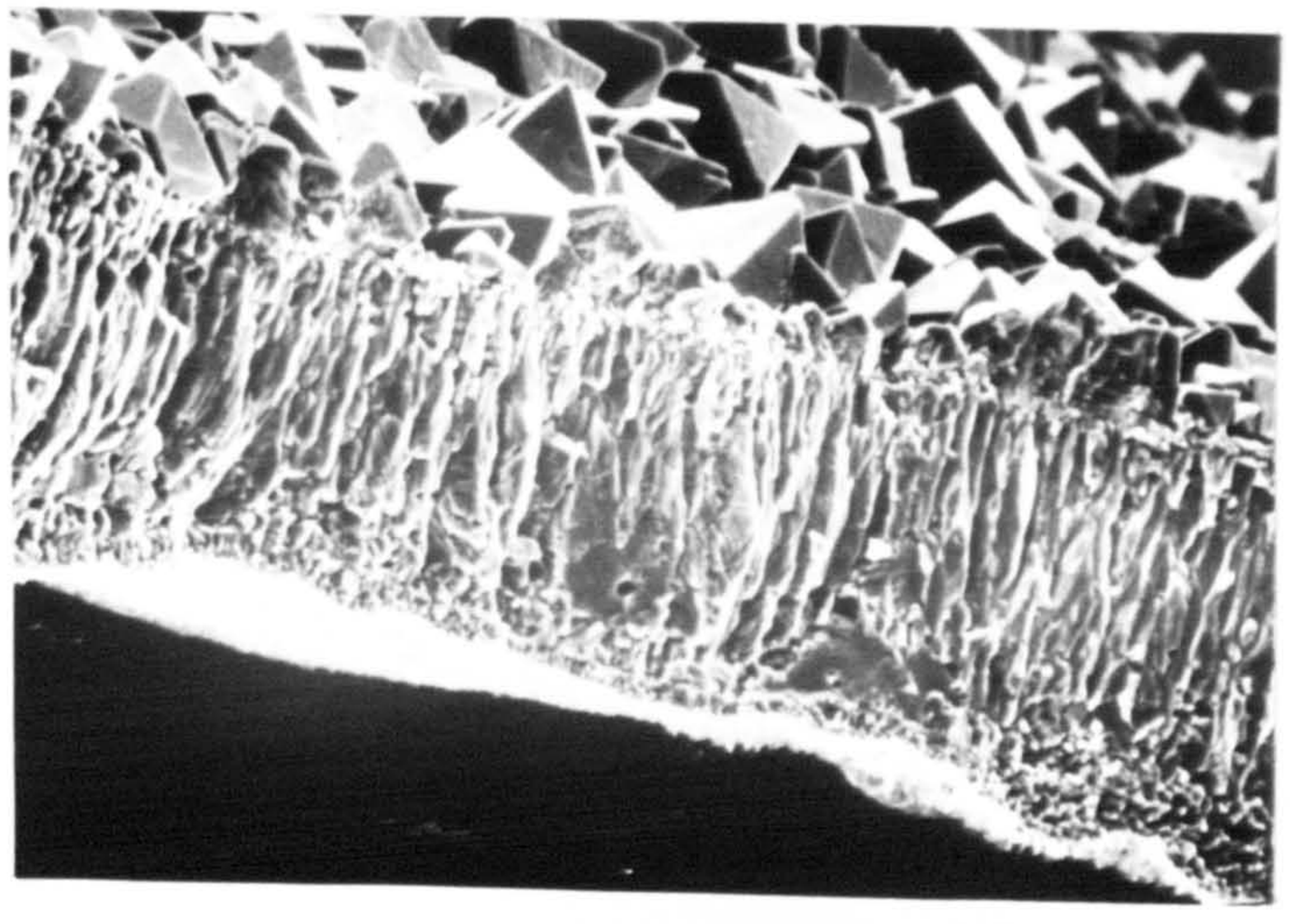

20 μm

(d)

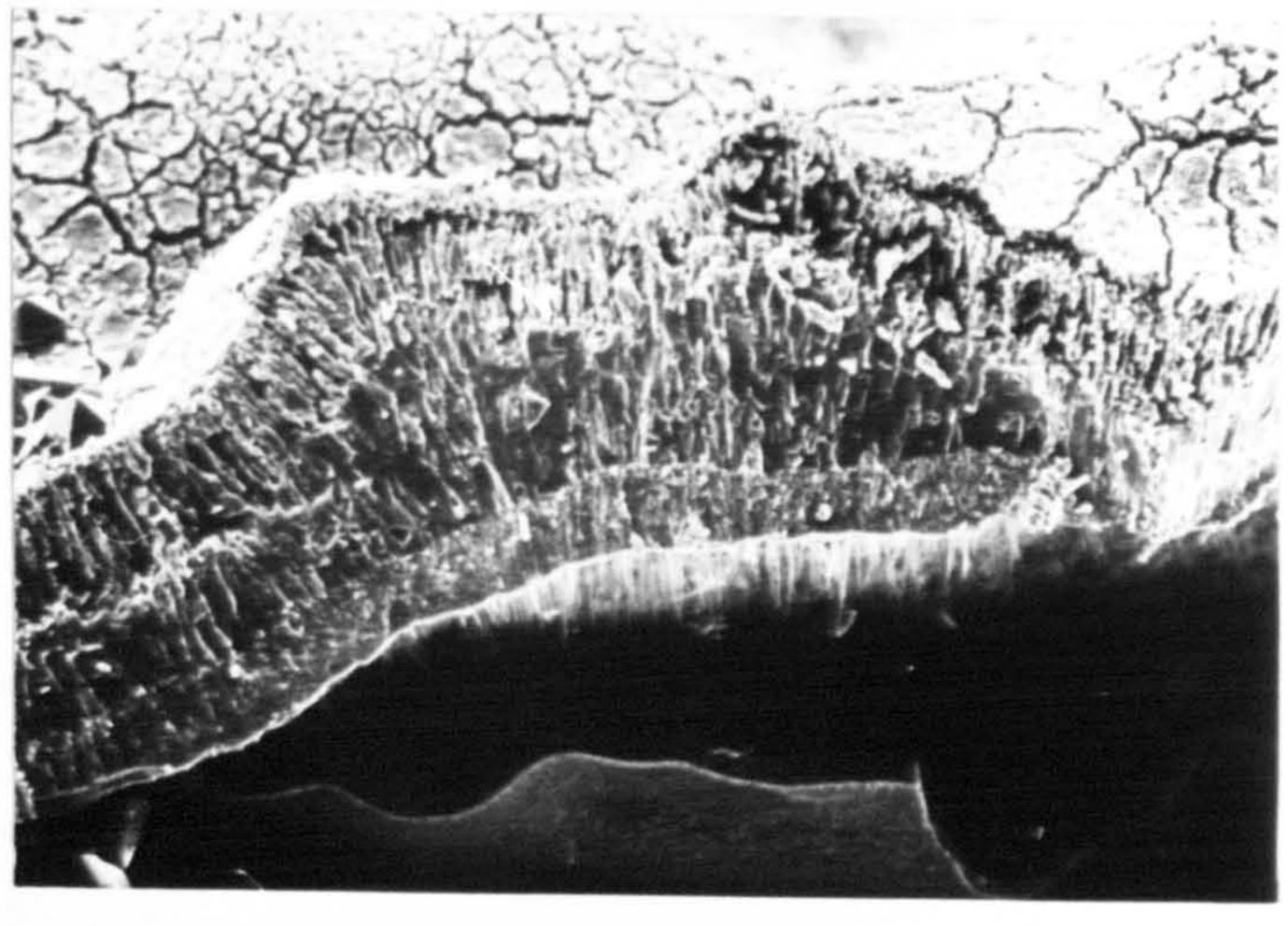

40 μm

is relatively smooth and, unlike the oxide, not convoluted.

Figure VI.18(a) and VI.18(b) show the underside of the inner layer of oxide in Figure VI.17(b) at higher magnification and Figures VI.18(c) and VI.18(d) show the fractured edge of the oxide. The particles in the oxide "valleys" have highly geometric morphologies varying from 5 to 20 μm diameter. Figure VI.19 shows a schematic diagram of the oxide, the morphology of which suggests that buckling of the scale occurs during oxidation.

The tendency for oxide buckling during oxidation is noted by several workers (e.g. Howes, 1968; Howes, 1969; Tien & Pettit, 1972) and is associated with thermal strain gradients (Tien & Davidson, 1975). In the present work, buckling is thought to occur isothermally so differences in the expansion coefficients of the oxide layers will not be relevant. However, since wustite and magnetite grow by outward diffusion of cations and haematite grows by inward diffusion of anions, new oxide will be formed at the interfaces between the oxides rather than at the free surface and so growth stresses are set up. It is thought that these are great enough within the oxide scale to cause buckling. The presence of the three oxides, wustite, magnetite and haematite in the scales of both nitrided and un-nitrided mild steel is confirmed by X-ray diffraction.

The crystalline morphology of the angular particles formed within the voids can be produced only by (a) vapour phase transport of the reactants (Fe and O), or (b) reaction of wustite with

Figure VI.19

Schematic diagram of oxide formed on mild steel nitrided in $5NH_3:95H_2$ at 700°C, oxidised at 600°C in air.

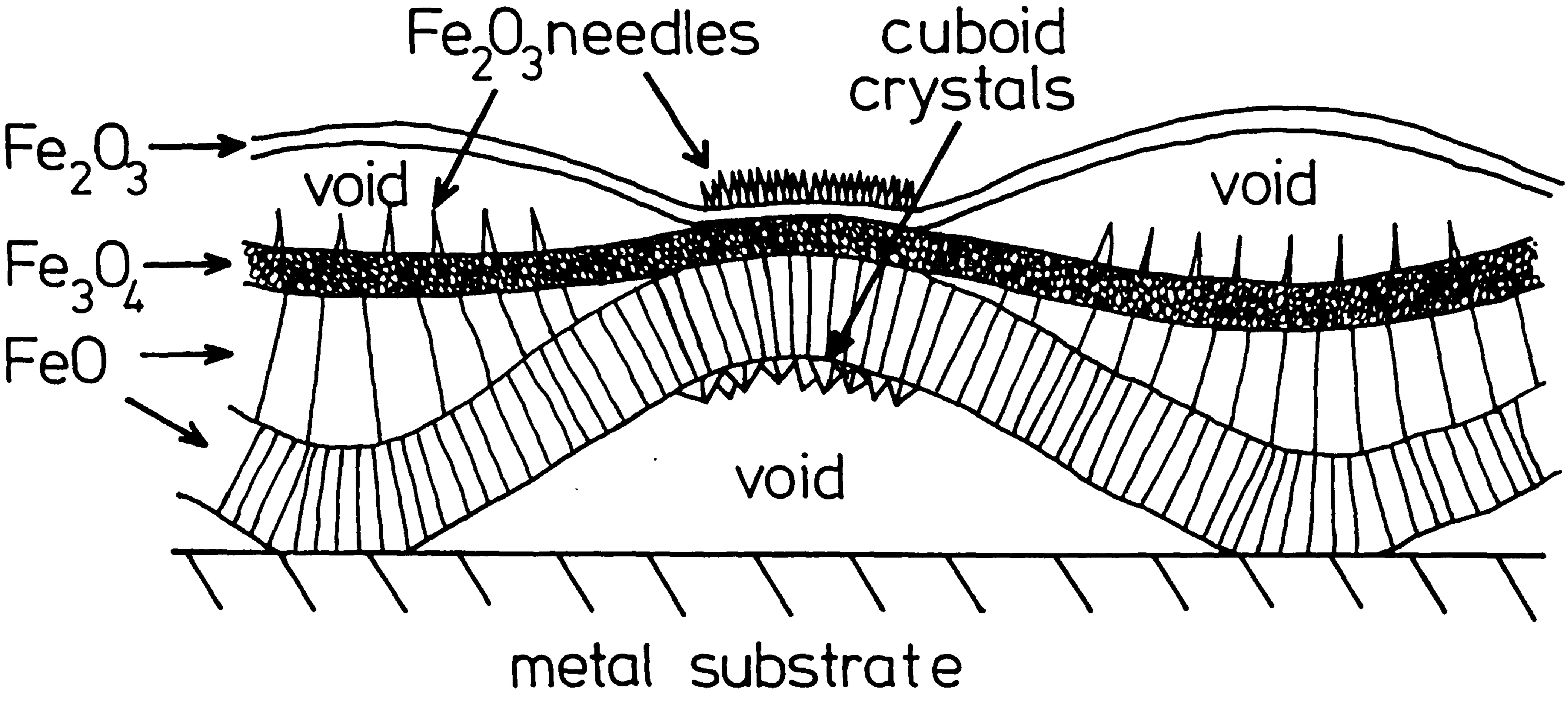
Fe_2O_3needles
cuboid crystals
Fe_2O_3
void
void
Fe_3O_4
FeO
void
metal substrate

inwardly diffusing oxygen to form a higher oxide at the free surface. The vapour pressure of iron at $600^{o}C$ is only about $2x10^{-12}Pa$ ($2x10^{-17}atm$); (Kubaschewski & Alcock, 1979) which is considered to be too low to provide adequate vapour phase transport of iron for (a) to be feasible. The oxygen pressure in the void above the metal surface (see Figure VI.19) will initially be that in equilibrium with Fe and FeO ($1.3x10^{-20}Pa$ ($1.3x10^{-25}atm$) at $600^{o}C$) and so an oxygen concentration gradient exists across the oxide and oxygen will diffuse inwards. The p_{O_2} within the wustite layer will increase and only needs to rise by a factor of 4 to be in equilibrium with FeO and Fe_3O_4 at $600^{o}C$ ($5x10^{-20}Pa$ ($5x10^{-25}atm$)). When the local p_{O_2} close to the oxide/void interface reaches this value wustite will oxidise to magnetite and grow with a geometric morphology as it forms at a free surface. Similar arguments hold if the wustite oxidises to the higher oxide haematite. The crystallites formed on the underside of the wustite have not, however, been positively identified. The presence of the crystallites and the relatively oxide-free metal surface below the voids, indicate that the oxygen pressure within the voids remains very low during oxidation. If cracking of the oxide occurs, with subsequent gas penetration at atmospheric pressure, the metal surface would be expected to oxidise rapidly and fill the void with oxide. This is not observed, implying that the oxide layer does not crack.

Such observations show that the effect of nitriding on the oxidation of mild steel at $600^{o}C$ in air is to produce a very compact oxide scale which has a comparatively small oxide/metal interface contact

area due to buckling. The oxide scale thickness is generally less than that found on un-nitrided mild steel under similar conditions. Thus, the rate of oxidation of mild steel at 600°C is reduced by nitriding, but the extensive spalling during cooling implies that oxidation during thermal cycling will be adversely affected.

VI.11. Oxidation of Nitrided Iron

Figure VI.20 shows the oxidation curves obtained for un-nitrided and nitrided ($7NH_3:93H_2$ at 700°C) pure iron specimens oxidised (i) isothermally in air at 480°C and (ii) with thermal cycling where the specimen is removed from the furnace (at 480°C) every 24 hours, see section V.5(b). Table VI.5 shows the parabolic rate constants and r-coefficients obtained. There is little difference between the rate of oxidation of the pure iron specimens, whether nitrided or un-nitrided, and whether oxidised isothermally or cyclically, although there are minor deviations at longer times. Figure VI.21 shows the rate of oxidation for prolonged times obtained for un-nitrided and nitrided ($7NH_3:93H_2$ at 700°C) pure iron specimens oxidised by thermal cycling between 480°C and room temperature. The difference is hardly of practical significance but does show that nitrided iron oxidises slightly more slowly than un-nitrided iron. The improved adherence of the oxide on nitrided iron specimens is confirmed by metallographic examination.

Figure VI.20

Oxidation curves of un-nitrided and nitrided (in $7NH_3:93H_2$ at $700^{\circ}C$) iron oxidised in air.

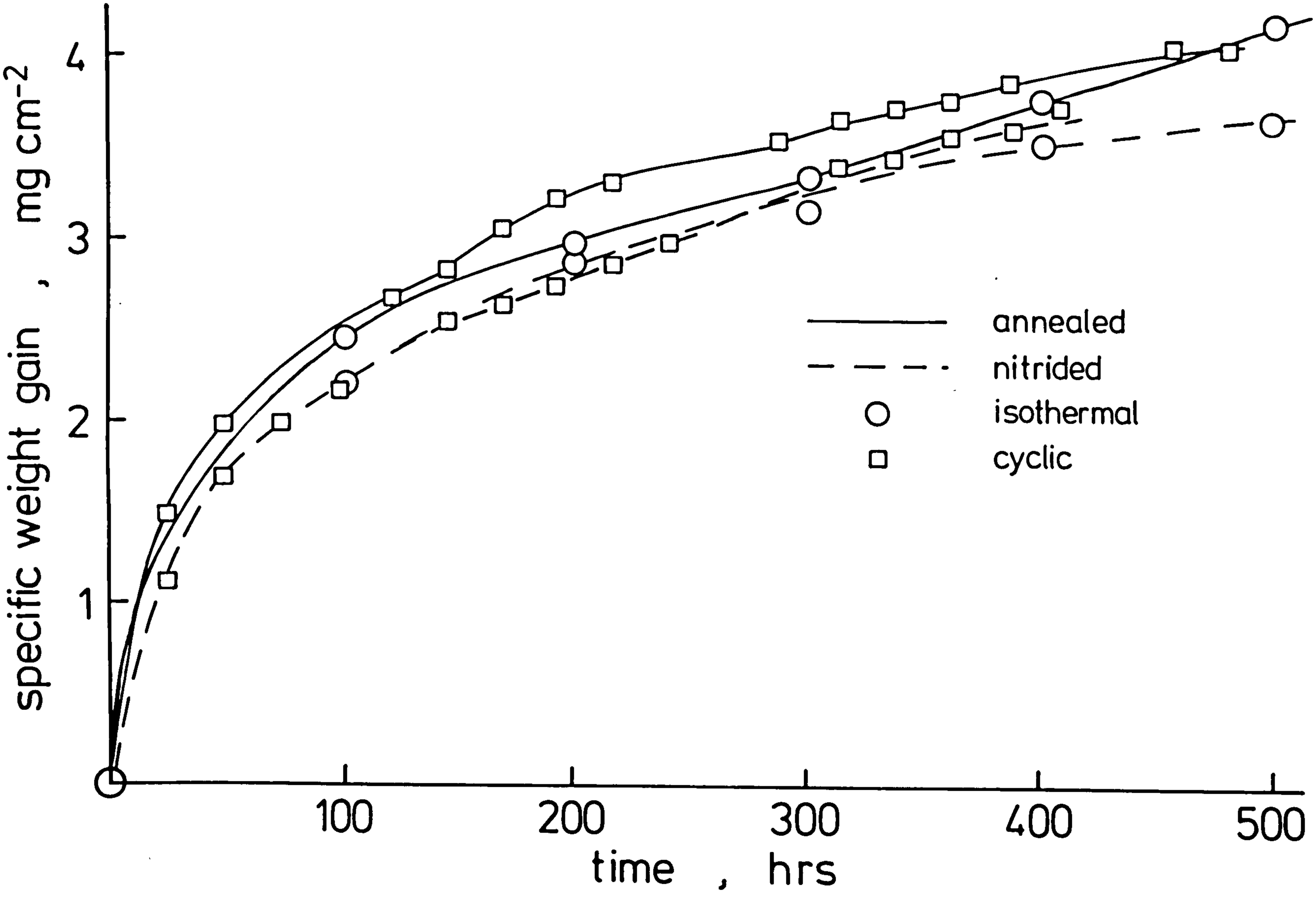
specific weight gain , mg cm-2
4
3
2
1
100
200
300
400
500
time , hrs
annealed
nitrided
isothermal
cyclic

Figure VI.21

Long term oxidation curves of un-nitrided and nitrided (in $7NH_3:93H_2$ at $700^{\circ}C$) iron at $480^{\circ}C$ in air.

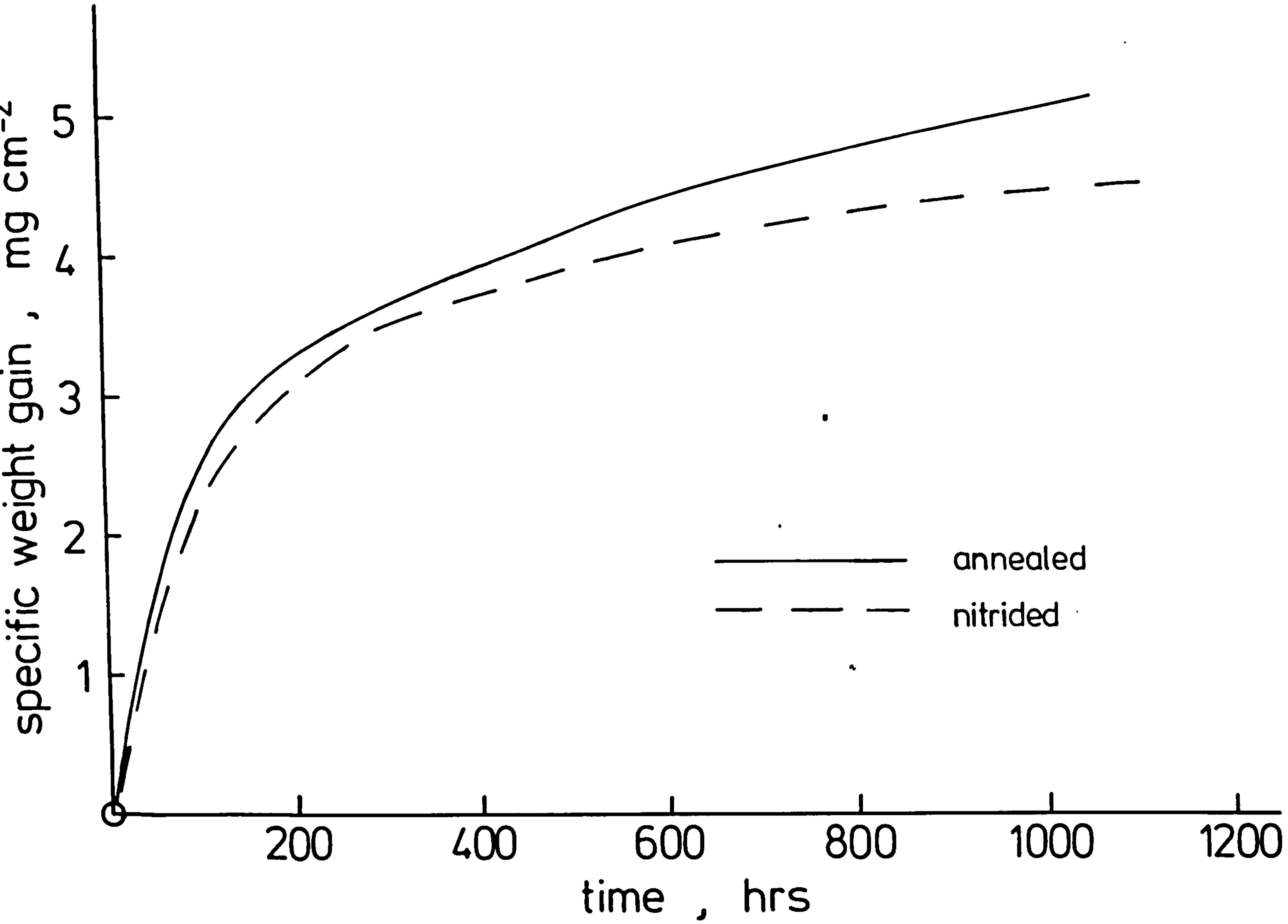
specific weight gain , mg cm^{-2}
5
4
3
2
1
200
400
600
800
1000
1200
time , hrs
annealed
nitrided

Table VI.5

Parabolic rate constants and linear regression coefficients (r) for iron specimens oxidised isothermally at 480°C and cyclically at 480°C-room temperature.

Specimen	Temperature °C	Time h	Parabolic rate constant, k_p $g^2\ cm^{-4}\ s^{-1}$	r
Un-nitrided	480	500	8.33×10^{-12}	0.99
Nitrided	480	500	7.50×10^{-12}	0.98
Un-nitrided	r.t.-480	530	8.39×10^{-12}	0.99
Nitrided	r.t.-480	400	8.97×10^{-12}	0.99

VI.12. Discussion

The effects of nitriding on the subsequent oxidation of mild steel in air is summarised as:

(a) the oxidation rate during isothermal oxidation is unchanged;

(b) the rate of oxidation during thermal cycling is increased;

(c) the nucleation of the initial oxide occurs on dispersed nitrides;

(d) the oxide layer shows a duplex morphology with a fine-grained inner layer and a coarse-grained outer layer;

(e) the transport mechanism in the oxide is altered so that oxide formation occurs at the metal/magnetite interface as well as at the magnetite/haematite interface;

(f) the adhesion at the metal/oxide interface is enhanced, but voidage appears at the interface between the two magnetite layers.

Duplex oxide layers have been observed in a number of conditions (Scott, 1977) and are often characterised by an outer porous layer of large columnar crystals, developed by unconstrained growth away from the substrate, and a fine-grained inner layer. On some alloys the crystal structures or chemical compositions of the layers are different as well as their morphologies. In many other examples the crystal structures of the layers are the same, as in the present case. The observations have been related to the outward movement of metal cations through the scale via a solid-state diffusion process, which

remains rate-controlling, together with simultaneous inward transport of oxidant to the metal/oxide interface. Thus, oxide is formed at both the oxide/gas interface and the oxide/metal interface.

There are two possible mechanisms to explain the formation of the inner oxide. The first assumes that the oxidant passes through the oxide via pores or cracks to reach the metal (Gibbs & Hales, 1977a) while the other suggests that the oxidant gains access to the metal by continual dissociation of the oxide (Dravnieks & McDonald, 1948). It is unlikely that oxide dissociation could account for the observed growth rate of the inner oxide on ferrous alloys and the present evidence is consistent with the passage of oxidant gas through the oxide to form the inner layer.

Enhanced adherence of the oxide to the substrate on nitrided mild steel oxidised in air has not been as beneficial as anticipated. Indeed, the effect of nitriding on subsequent thermal cycling is to increase the rate of oxidation. These results are at variance with those obtained in simulated flue gas (Hendry, 1978). The morphology of the oxides suggests that those formed on nitrided mild steel in air will be resistant to spalling under more aggressive conditions and it is likely that the advantages of nitriding on the subsequent oxidation of mild steel in simulated flue gas are a consequence of the increased aggressiveness of the oxidants.

Many of the features of the oxidation of nitrided mild steel are analogous to those found in the oxidation of dispersion-strengthened superalloys; see section

III.8. The adherent fine-grained inner layer is expected to have an increased fracture strength and this, combined with the elimination of vacancy condensation at the oxide/metal interface, should increase spalling resistance.

Two of the mechanisms attributed to the effects of dispersoids in superalloys are relevant to the oxidation of nitrided mild steel. The first is the "vacancy sink" mechanism (Stringer, 1966) and the second is the mechanism whereby the oxide forming reaction is changed so that growth occurs at the metal/oxide interface and not at the gas/oxide interface (Stringer et al., 1972). The first mechanism implies that outwardly growing oxide would continue to form, whereas the second mechanism would result in an inwardly growing oxide. In nitrided mild steel both inward-growing and outward-growing magnetite layers continue to form during oxidation and a combination of the two mechanisms is therefore thought to apply.

It has been noted (Gibbs & Hales, 1977b) that a disadvantage of duplex oxide scales is that the boundary between inner and outer layers often contains clearly defined remnants of the initial interfacial voidage, as found in the present work, and is therefore a plane of weakness. The outer layer may spall off under thermal-cycling or mechanical loading. However, if metal cation diffusion is rate controlling the metal attack rate will remain unchanged.

Chapter VII

THE OXIDATION OF IRON-CHROMIUM-NITROGEN ALLOYS

VII.1. Introduction

There is a strong tendency for chromium-containing scales to spall on cooling and this renders them less protective under thermal cycling. Hence, binary Fe-Cr alloys with low Cr contents are not used extensively for their corrosion resistance. The present results for the oxidation of mild steel (Chapter VI) indicate that nitriding improves the metal-oxide adherence and dispersed particles also confer improved metal-oxide adherence to super-alloy materials (see section III.8). It was considered, therefore, that nitriding and heat treating a low chromium Fe-Cr alloy to give a dispersion of incoherent nitride particles would give an alloy with improved oxidation resistance.

The 2.32w/oCr alloy (N.P.L. cast 38AF2; see Table VII.1) was cold-rolled to strip about 200 μm thick, cut into coupons about 15x15mm, and annealed in hydrogen at 840^{o}C for 17h.

VII.2. Nitriding Procedure

The kinetics of nitriding iron-chromium

Table VII.1

Chemical analysis of iron-chromium alloy, w/o

Cast No.	Cr	C	Si	S	O	N
38AF2	2.32	0.0038	0.003	0.0045	0.0024	0.0014

alloys with greater than 2w/oCr follow the internal nitriding equation (Mortimer, 1971); see section II.5. Two sets of nitrided specimens were prepared containing (i) coherent Cr-N clusters and (ii) incoherent CrN precipitates. Nitriding in $10NH_3:90H_2$ at $575^{o}C$ produces a structure consisting mainly of coherent clusters with some CrN precipitation (Pipkin & Middleton, 1973). The minimum time for through-nitriding 200 μm foil under the above conditions is 5h.

Table VII.2 shows the weight gain and lattice parameter of specimens nitrided in $10NH_3:90H_2$ at $575^{o}C$ for 5h and the expected weight gain, assuming that nitrogen associates with chromium in the atomic ratio 1Cr:1N . The difference between the weight gain and the w/o nitrogen calculated from lattice parameter measurements represents the amount of nitrogen precipitated as CrN . To produce specimens containing only incoherent CrN , nitrided samples were aged at $650^{o}C$ for 6h in a $NH_3:H_2$ gas mixture having the same nitriding potential as the original nitriding conditions. Weighing confirmed there was no nitrogen loss, or gain, during aging. X-ray powder photography of the aged specimens showed very diffuse high-angle lines which prevented precise measurement of lattice parameters, but visual comparison with the un-nitrided alloy showed that nitrogen had precipitated from solid solution.

In the microstructures of Figure VII.1, (a) is a bright field micrograph of the [001] zone of the as-nitrided alloy and shows a fine distribution of clusters, about 120 Å in diameter, lying parallel to the $\{100\}$ matrix planes. Electron diffraction

Figure VII.1

Transmission electron micrographs of

Fe-2.32w/oCr:

(a) nitrided in $10NH_3:90H_2$ at 575°C.

(b) nitrided in $10NH_3:90H_2$ at 575°C;

aged at 650°C for 6h.

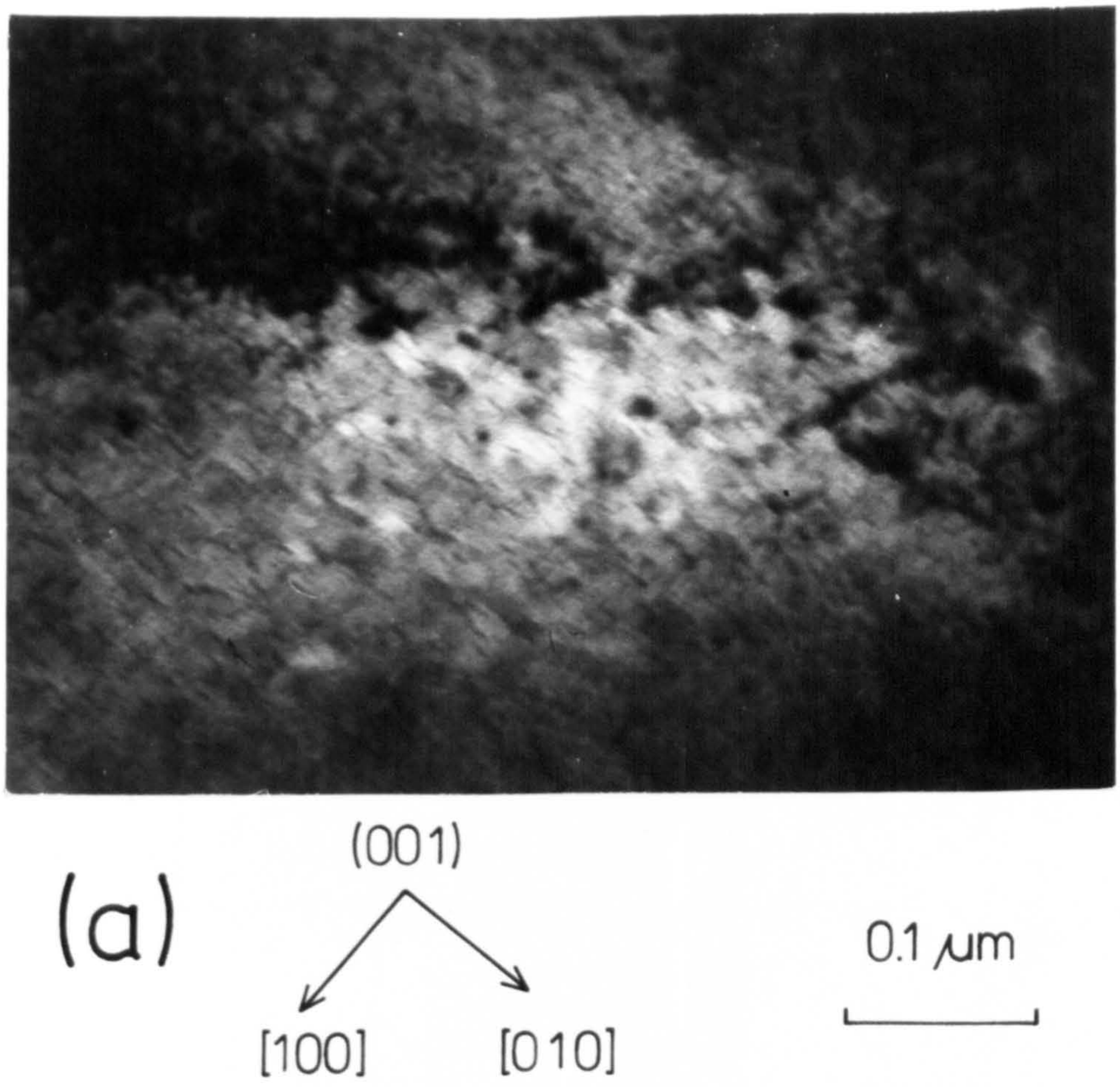

(a)

(b)

Table VII.2

Weight gains and lattice parameters of nitrided Fe-2.32 w/o Cr

Specimen	Time h	Calculated weight gain (w/o)	Actual weight gain (w/o)	Lattice parameter Å	N content from lattice parameter (w/o)	w/o N precipitated as CrN
Annealed	-	-	-	2.8671	-	-
Nitrided, $10NH_3:90H_2$ at 575°C	5	0.694	0.673	2.8784	0.403	0.270
Nitrided as above (Pipkin & Middleton, 1973)	7	0.694	0.60	2.8785	0.410[+]	0.190

[+] assuming a for the un-nitrided alloy is 2.8670 Å (Pipkin & Middleton, 1973)

patterns show continuous streaking in the ⟨100⟩ directions. (b) is a bright field micrograph of the over-aged alloy, taken under similar conditions. The disc-shaped precipitates are about 300 Å in diameter and were identified from electron diffraction patterns as f.c.c. CrN with the Baker-Nutting orientation relationship (Baker & Nutting, 1959) :

$$(001) \;//\; (001)_{CrN} \;;\quad [100] \;//\; [1\bar{1}0]_{CrN} .$$

Metallography showed significant amounts of grain boundary precipitation in both the as-nitrided and over-aged alloys.

VII.3. Oxidation at 500°C

Figure VII.2 shows the specific weight gain curves of Fe-2.32w/oCr alloys oxidised in air at 500°C following the procedure described in section V.5(b) and Table VII.3 gives rate constants determined at each weighing point, assuming parabolic kinetics. The values of k_p, for each specimen, do not vary greatly with time showing that the curves do approximate to a parabolic form. The rate constant for pure iron at 500°C, taken from Figure III.2, is $1\times10^{-11} g^2\ cm^{-4} s^{-1}$. However, Caplan & Cohen (1966) show that the oxidation rate increases to about $2\times10^{-10} g^2\ cm^{-4} s^{-1}$ at 500°C if the iron is cold-worked prior to oxidation; see section III.6. The rates of oxidation of the nitrided and un-nitrided Fe-2.32w/oCr are higher than that of annealed iron, but are less than that of cold-worked iron. Thus,

Figure VII.2

Oxidation curves for Fe-2.32w/oCr alloys, cyclically oxidised in air at 500°C to room temperature.

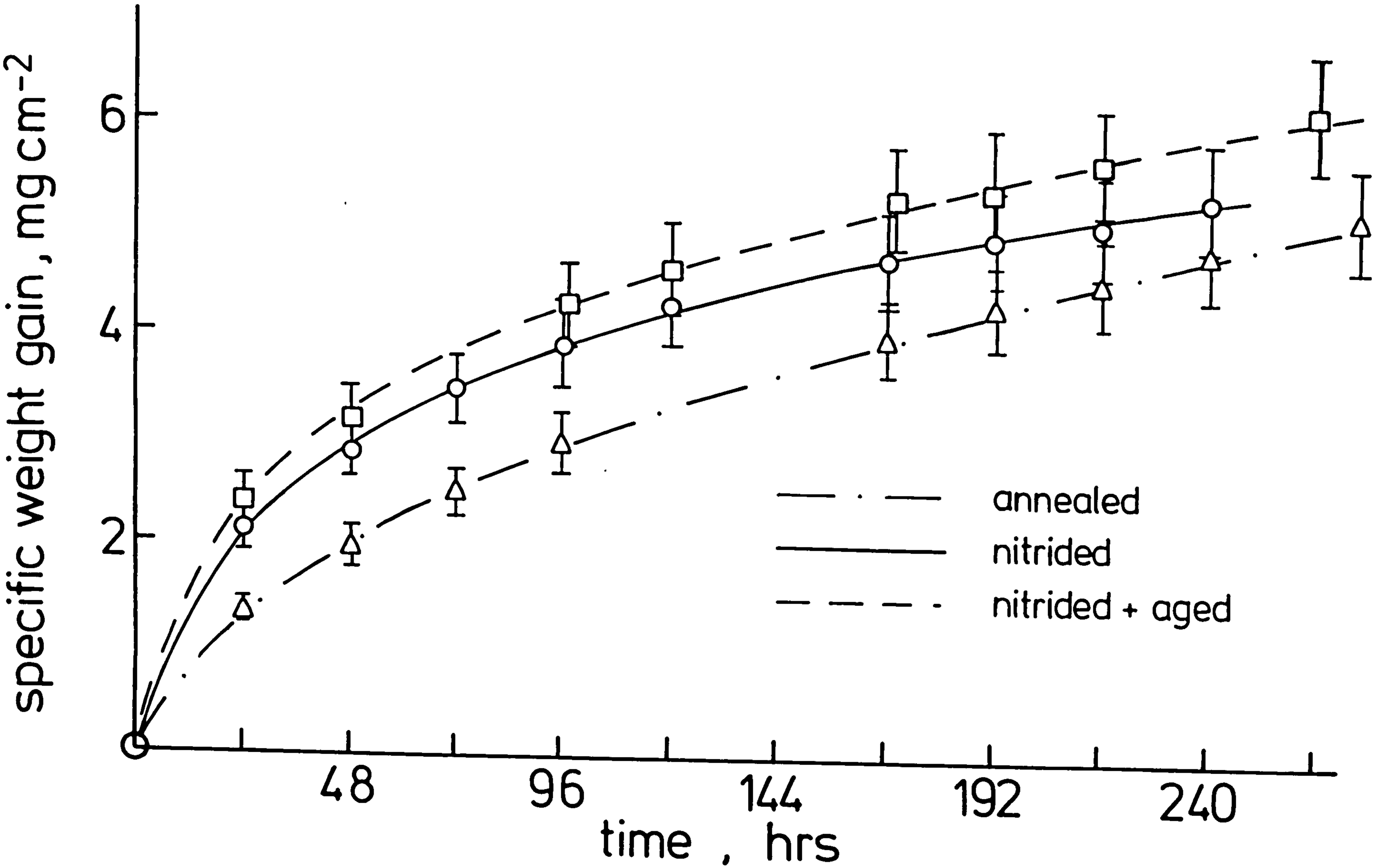
specific weight gain, mg cm-2
6
4
2
48
96
144
192
240
time , hrs
annealed
nitrided
nitrided + aged

Table VII.3

Parabolic rate constants for Fe-2.32w/oCr alloys, cyclically oxidised in air at 500°C to room temperature.

Time h	Parabolic rate constants (k_p), $g^2\ cm^{-4}\ s^{-1} \times 10^{11}$		
	Annealed alloy	Nitrided alloy*	Nitrided and aged alloy**
24	2.1	5.2	6.6
48	2.2	4.8	5.8
72	2.3	4.6	-
96	2.5	4.3	5.2
120	-	4.2	4.9
144	-	-	-
168	2.6	3.6	4.6
192	2.6	3.5	4.3
216	2.6	3.3	4.1
240	2.6	3.3	-
264	2.7	-	4.0

* Nitrided in $10NH_3 90H_2$ at 575°C for 5h.

** Nitrided in $10NH_3 : 90H_2$ at 575°C for 5h; aged at 650°C for 6h.

nitriding with or without subsequent aging seems slightly to increase the rate of oxidation, but the error bars of the oxidation curves, calculated from the estimated errors in weight and surface area measurements, show that any differences are hardly significant.

Scanning electron micrographs of the nickel plated oxide scales on all three specimens are shown by Figure VII.3 to have a duplex structure with a relatively porous outer layer and a compact inner layer. On the annealed alloy some voidage is present at the interface of the two oxide layers (Figure VII.3(a)) and cracking of the oxide occurs perpendicular to the metal surface. On the nitrided alloy voidage is apparent at the metal/oxide interface (Figure VII.3(b)). Grain boundary chromium nitride in the metal substrate appears as a band of darker material perpendicular to the surface and this extends into the inner oxide layer, where it is thinner than in the metal substrate. The oxide on the nitrided and aged alloy is coherent with the substrate (Figure VII.3(c)) and again grain boundary CrN within the substrate extends into the inner oxide layer. A band of CrN also exists at the metal/oxide interface in one of the substrate grains arrowed in Figure VII.3(c). The compact oxide is much narrower above the CrN at the interface than elsewhere.

Oxide scales were chemically stripped from isothermally oxidised Fe-Cr alloys (500^{o}C for 300h) and Figure VII.4 shows the underside of such oxide specimens from annealed material. (a) shows that the oxide clearly replicates the grain size of the substrate. The oxidation rate is influenced by the

Figure VII.3

Scanning electron micrographs of Fe-2.32w/oCr, cyclically oxidised at 500°C-room temperature in air,

(a) annealed alloy oxidised for 264h,

(b) nitrided in $10NH_3:90H_2$ at 575°C; oxidised 240h,

(c) nitrided 575°C in $10NH_3:90H_2$ at 575°C; aged at 650°C for 6h; oxidised 264h.

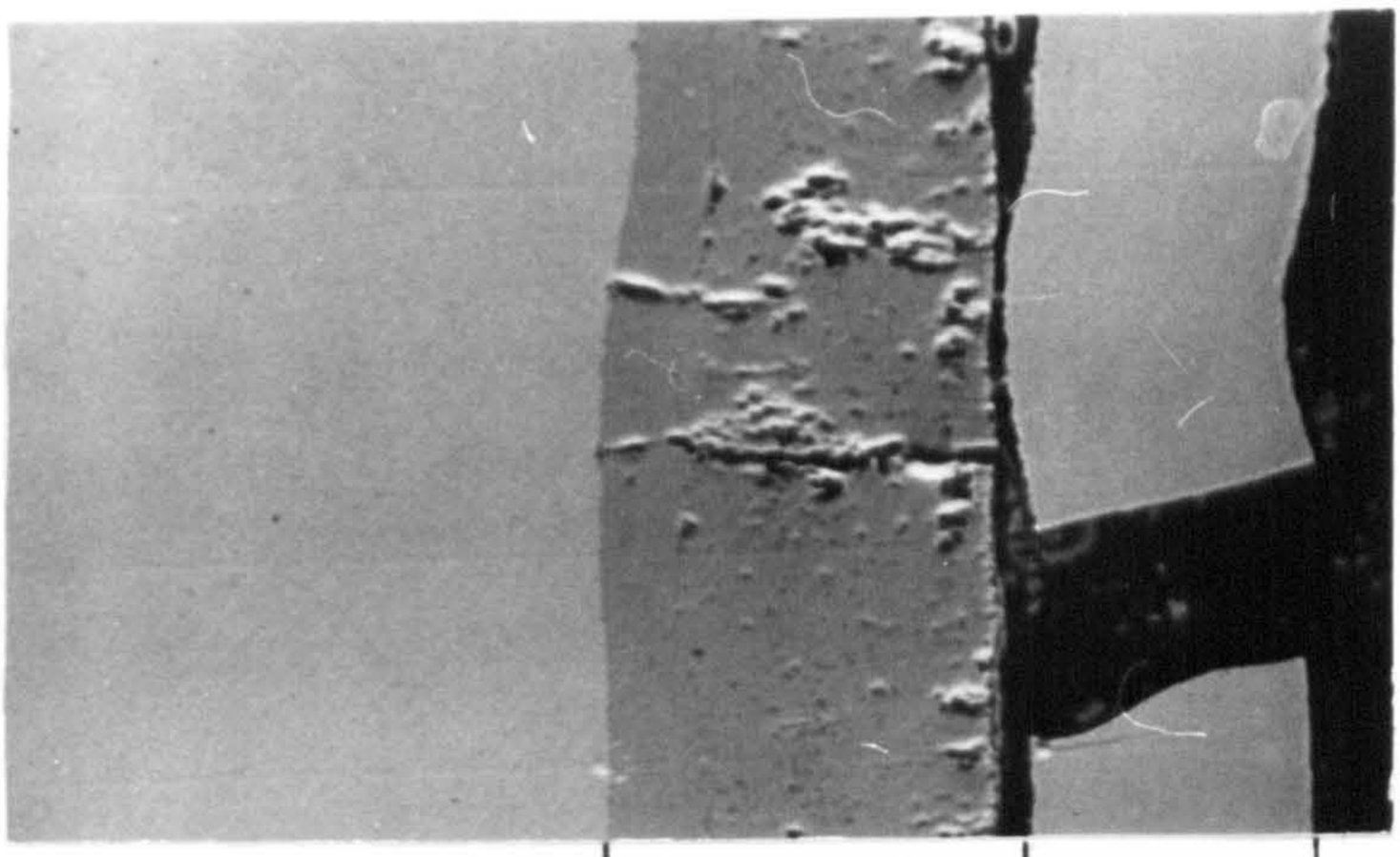

(a)

20 μm

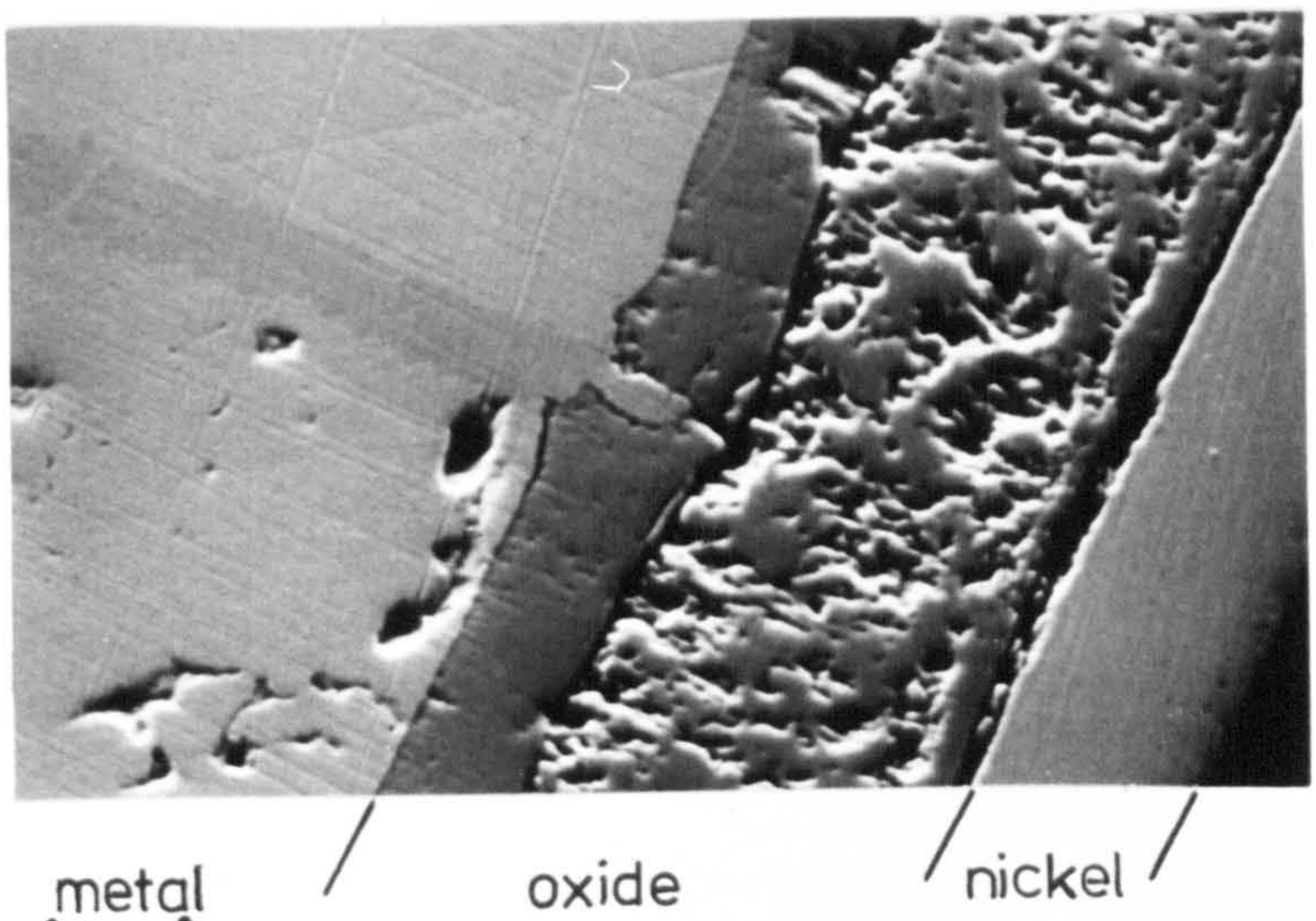

(b)

20 μm

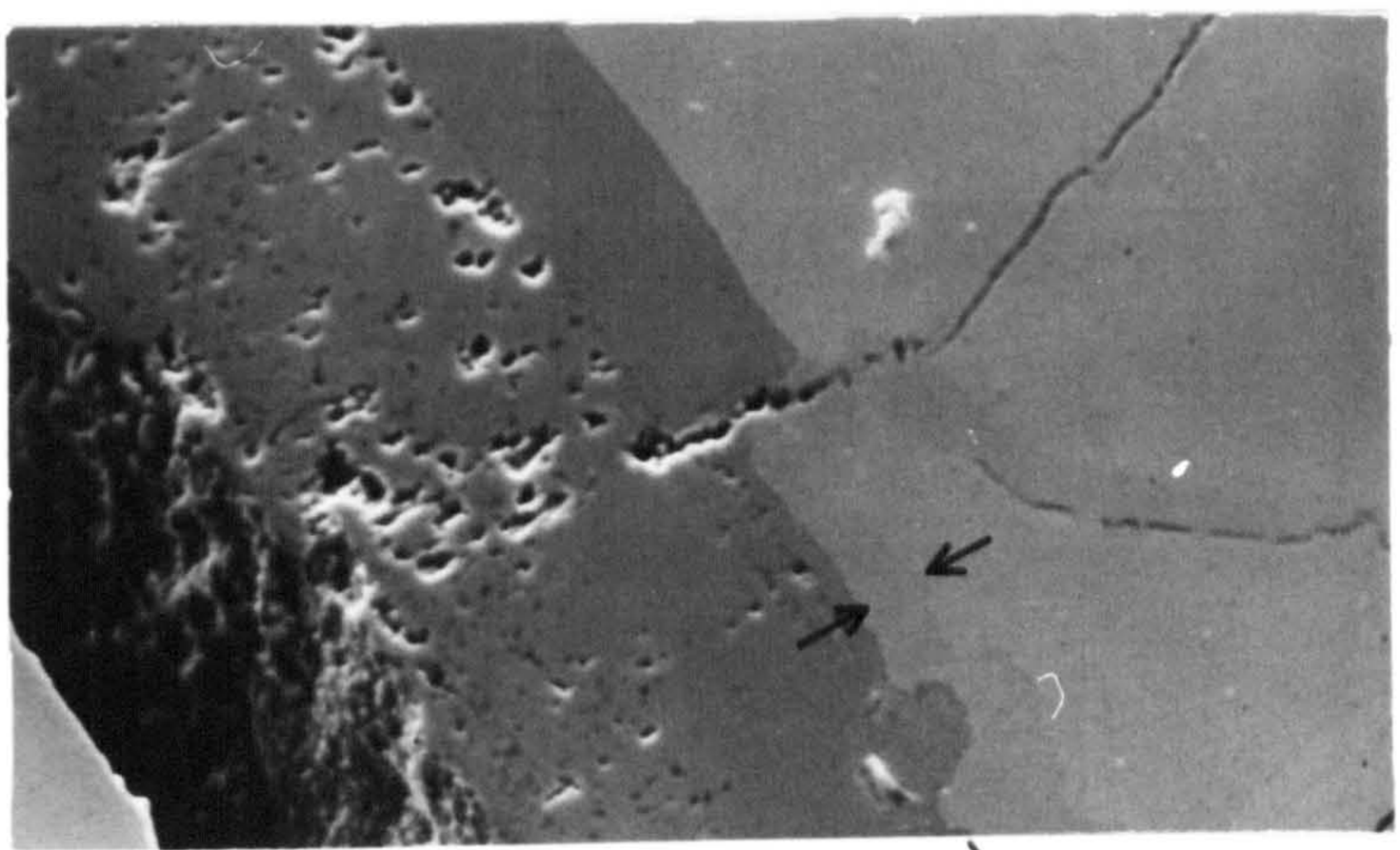

(c)

20 μm

Figure VII.4

Scanning electron micrographs of oxide stripped from Fe-2.32w/oCr; oxidised at 500°C for 300h in air.

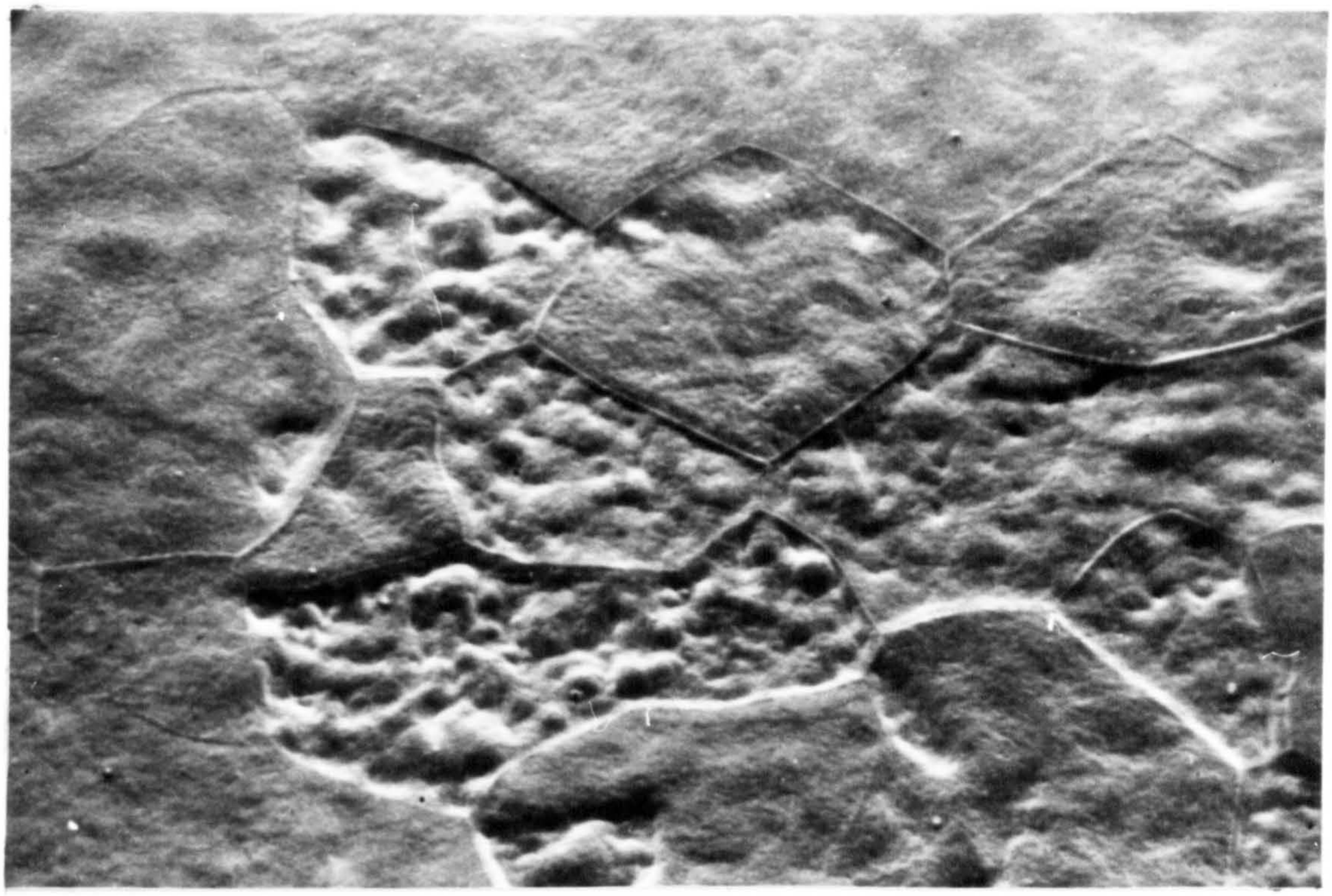

(a)

100 μm

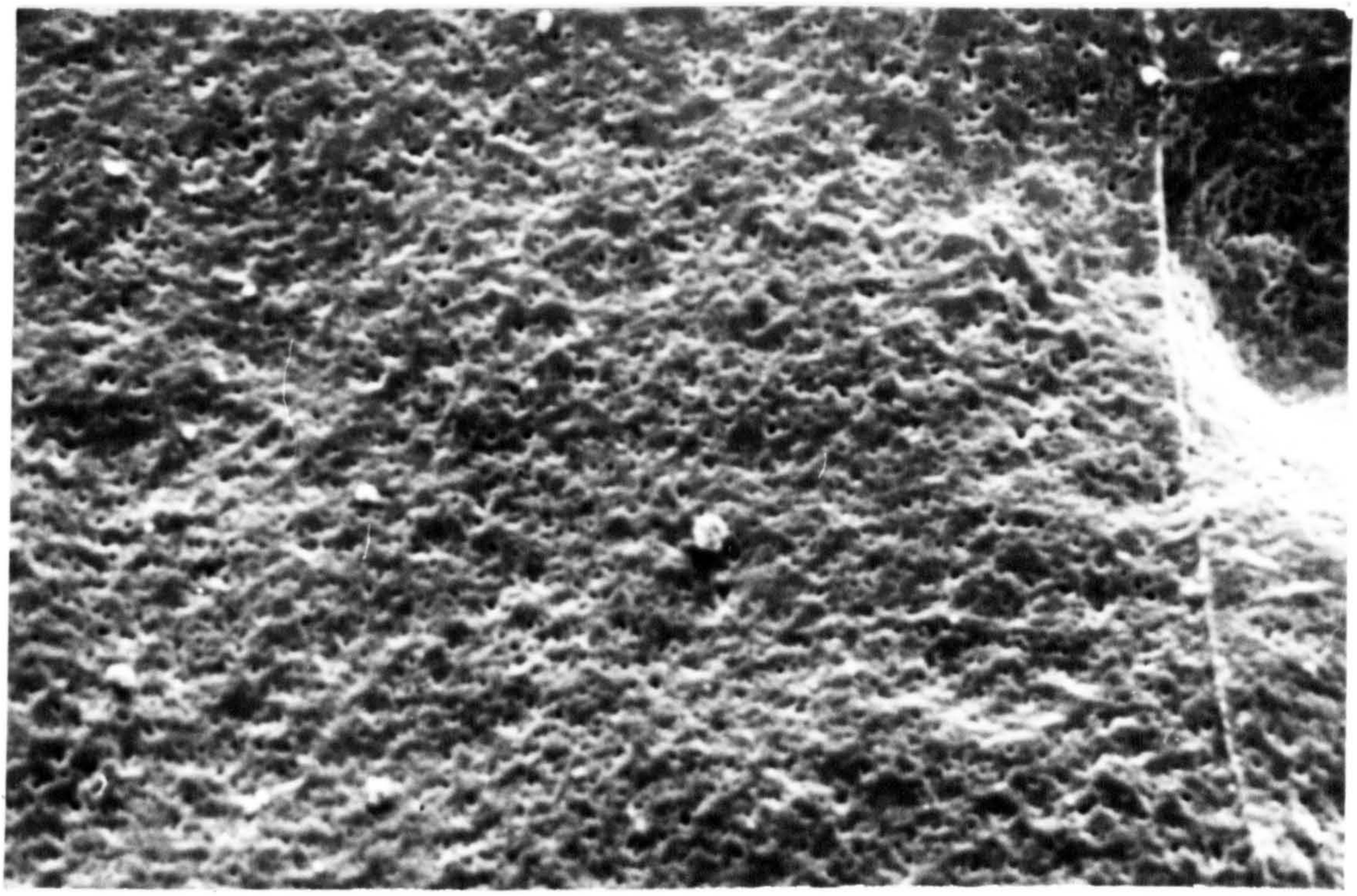

(b)

10 μm

orientation of the matrix, as illustrated by the varying depths of the oxide surface in different grains. The oxide is covered in small voids as seen at higher magnification (b). The areas corresponding to the grain boundaries of the matrix do not show any evidence of enhanced or suppressed oxidation.
Figure VII.5 shows the underside of oxide stripped from the metal after nitriding to give a clustered matrix and (a) again shows that it replicates the substrate grain size; (b) is the same at higher magnification. The voidage of the surface is even more pronounced than on the annealed specimen. The matrix grain-boundary region shows extensive outgrowths which are the remnants of CrN precipitated in the substrate grain boundaries that have not been dissolved during the stripping process. The presence of the CrN indicates that stripping has occurred at the oxide/metal interface and not at the interface between the two oxide layers. Relatively large dimples, about 30μm diameter, occur in the oxide both within the matrix grains and at the grain boundaries, probably a result of blistering at the metal/oxide interface. In Figure VII.6, which shows the oxide from the nitrided and aged alloy, the grain size of the matrix is again clearly reflected in the morphology of the oxide (a) and at higher magnification (b) the surface of the oxide appears much smoother than in the previous specimens with little evidence of voidage. The grain-boundary regions again contain CrN. Dispersed incoherent CrN precipitates thus act as vacancy sinks eliminating metal/oxide interfacial voidage, whereas coherent Cr-N clusters do not.

X-ray powder photographs of the stripped oxides are shown in Figure VII.7. Three phases are present

Figure VII.5

Scanning electron micrographs of oxide stripped from Fe-2.32w/oCr, nitrided in $10NH_3{:}90H_2$ at 575°C; oxidised at 500°C for 300h in air.

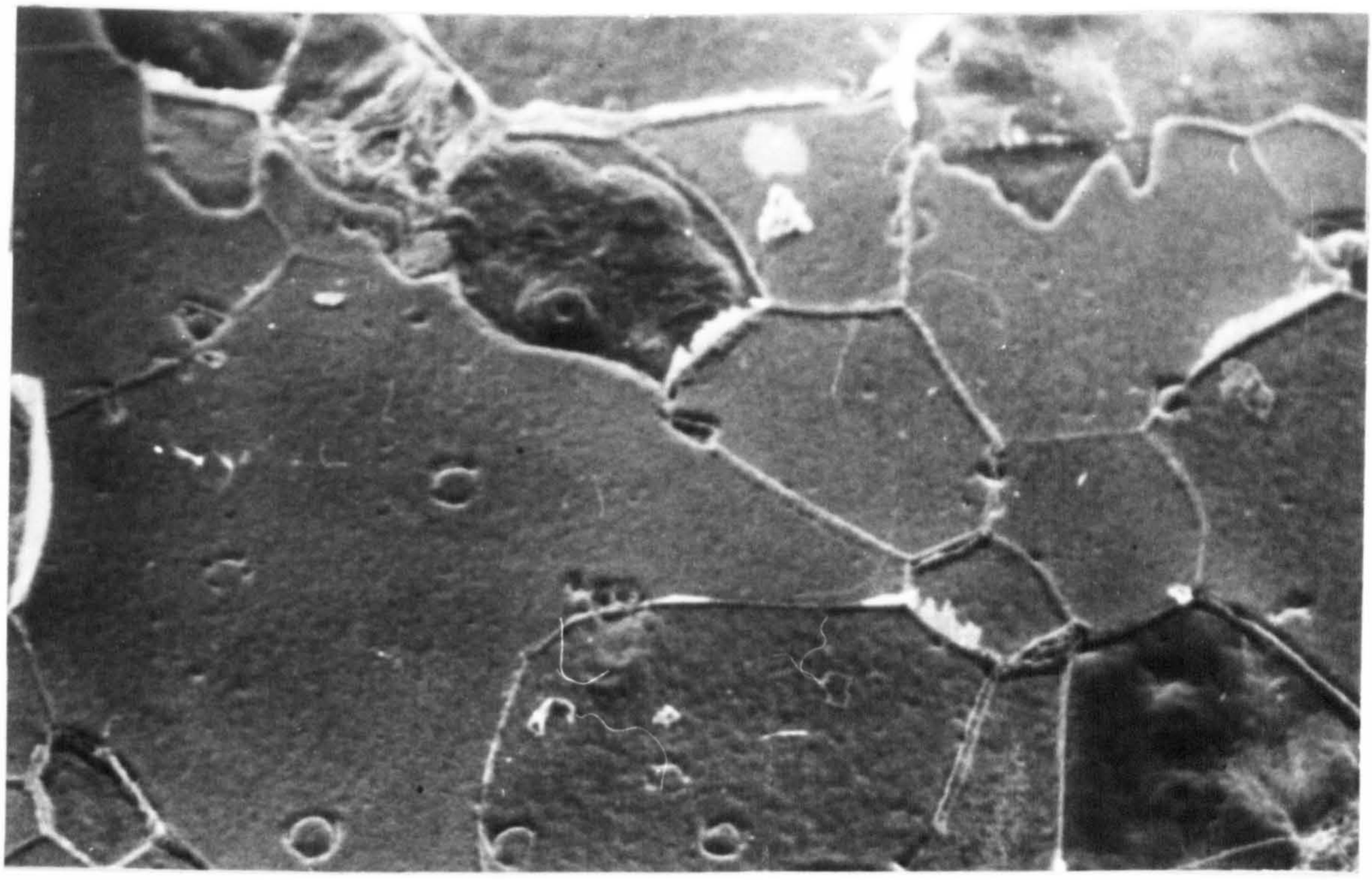

(a)

100 μm

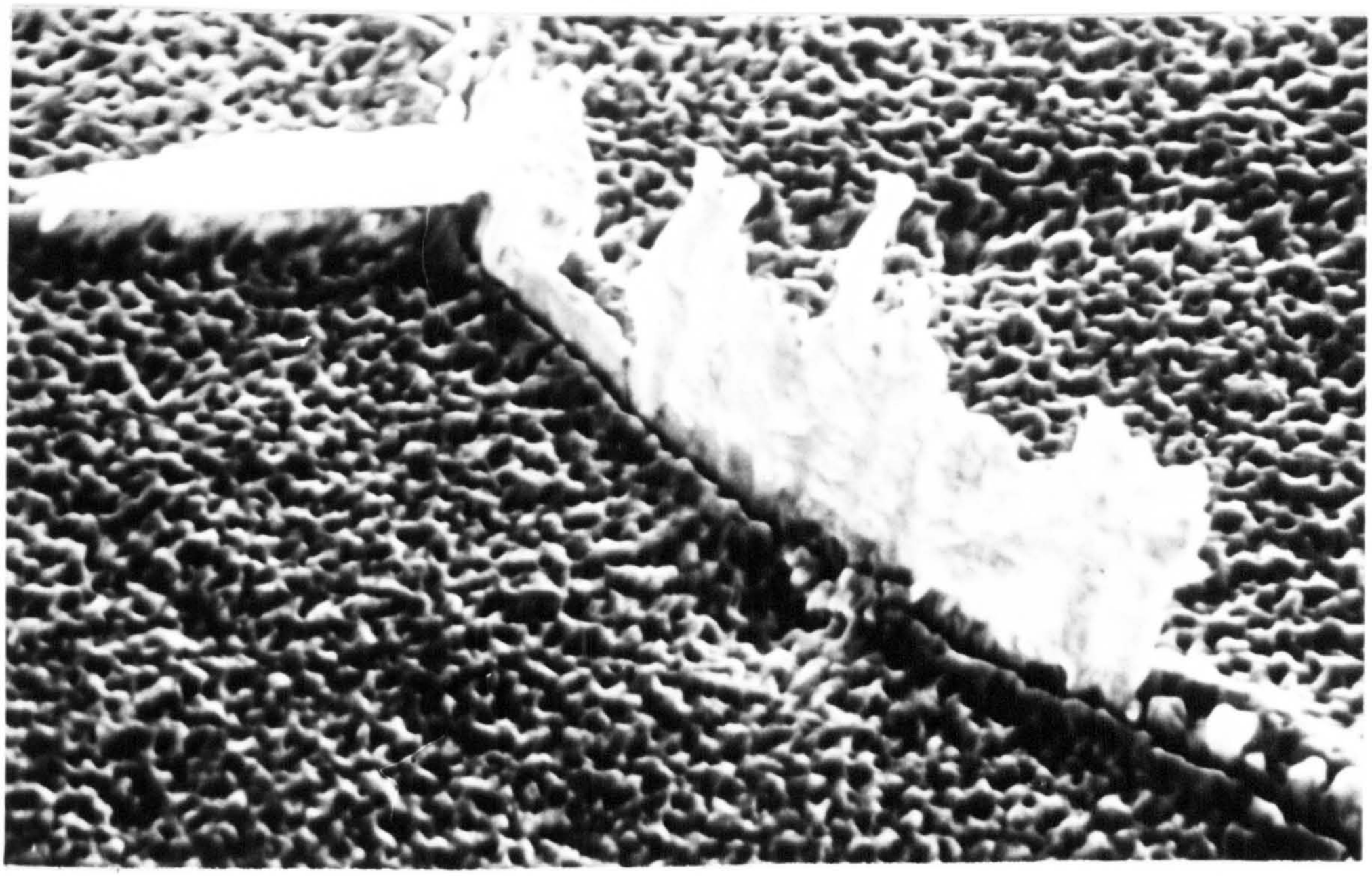

(b)

10 μm

Figure VII.6

Scanning electron micrographs of oxide stripped from Fe-2.32w/oCr; nitrided in $10NH_3:90H_2$ at 575°C, aged at 650°C for 6h; oxidised at 500°C for 300h in air.

(a)

100 μm

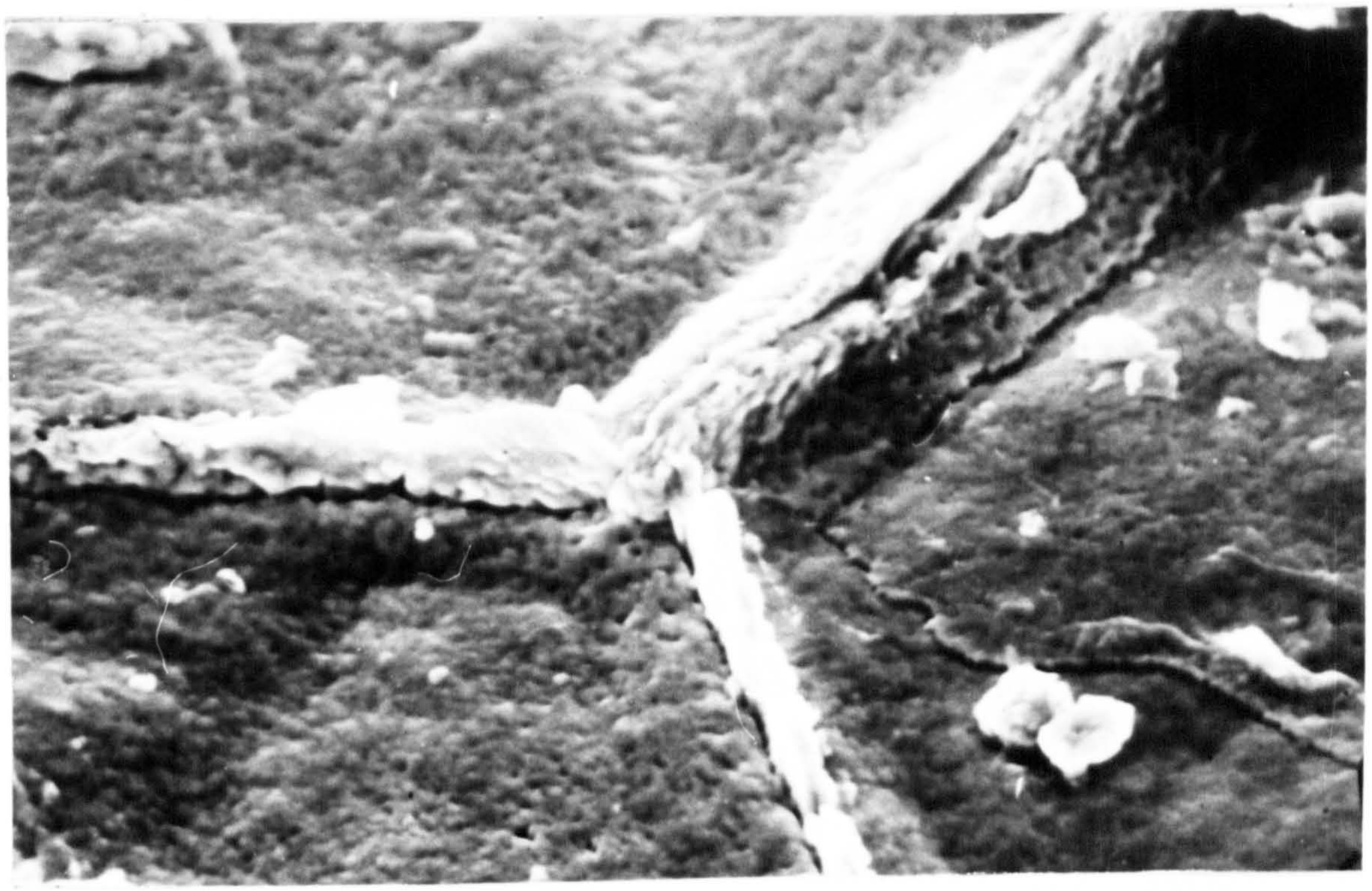

(b)

10 μm

Figure VII.7

X-ray photographs of oxides from Fe-2.32w/oCr specimens; oxidised at 500°C for 300h, in air,

(a) annealed,

(b) nitrided in $10NH_3:90H_2$ at 575°C.

(c) nitrided in $10NH_3:90H_2$ at 575°C; aged 650°C for 6h.

(a)

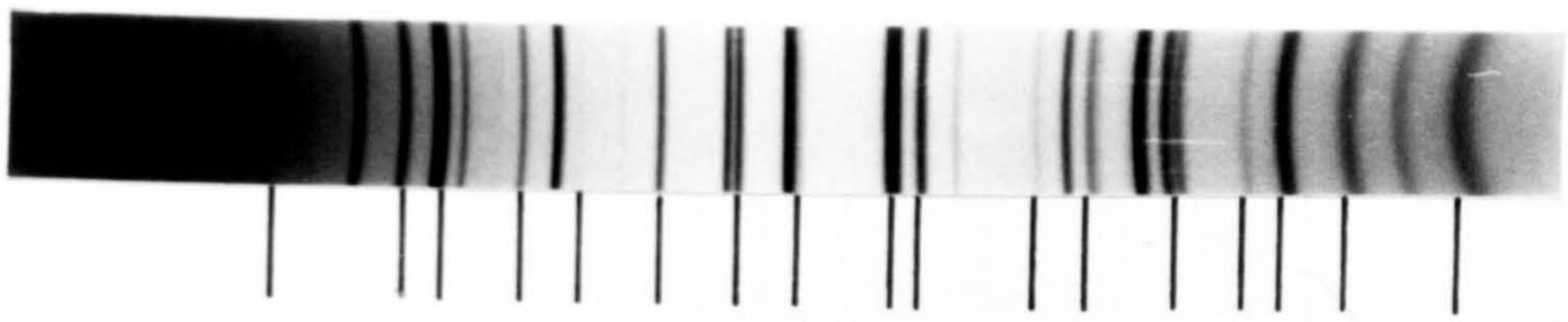

(b)

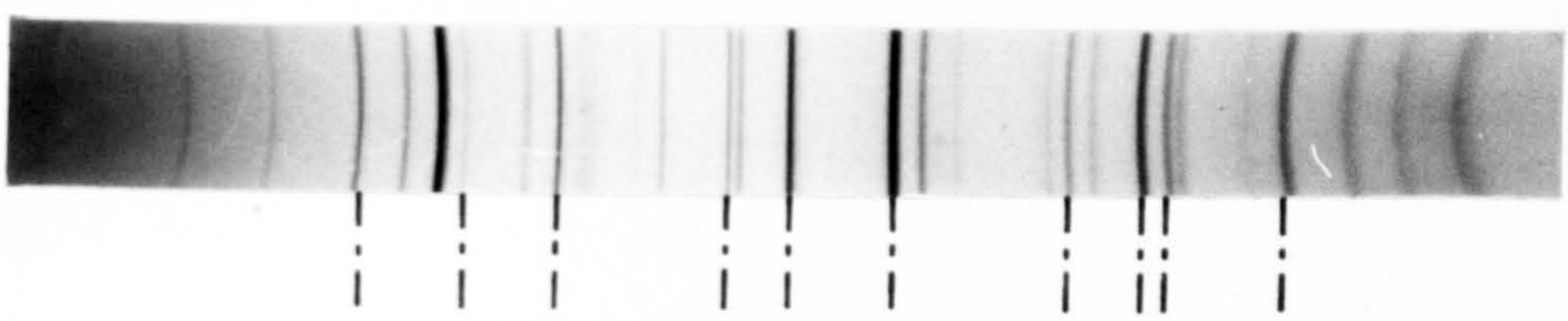

(c)

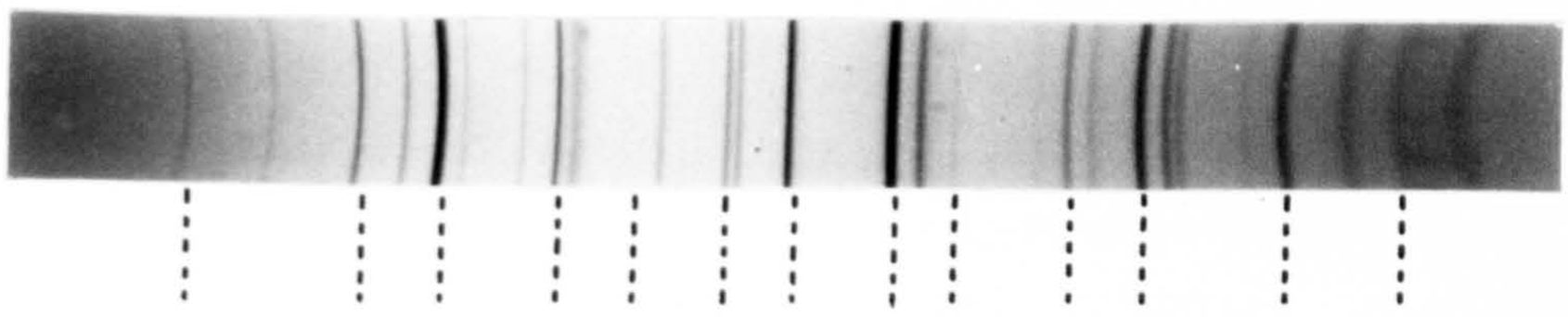

| – Fe_2O_3

¦ – Fe_3O_4

⋮ – $FeCr_2O_4$

in all specimens: haematite (Fe_2O_3), magnetite (Fe_3O_4) and an iron-chromium spinel ($FeCr_2O_4$). The photograph of the oxide from the annealed specimen has had a longer exposure than the other two but the relative intensities of the lines from the three oxide phases are similar in all three photographs indicating that the relative amounts of the three phases are the same. X-ray energy dispersive analysis of metallographic specimens shows the chromium in the oxide to be predominantly in the inner compact scale layer; see Figure VII.8. Similar results were obtained for the annealed and the as-nitrided specimens. The inner compact scale therefore consists of iron-chromium spinel, $FeCr_2O_4$.

VII.4. Oxidation at 650°C

Similar specimens were oxidised at 650°C using the same oxidation and weighing techniques and weight gains are shown in the parabolic plots of Figure VII.9. The results for the annealed alloy lie on a straight line, showing that the alloy has a parabolic oxidation rate and the slope gives a rate constant of 1.75×10^{-10} g^2 cm^{-4} s^{-1}. The as-nitrided and the nitrided and aged specimens follow similar rates for the first 50h, but then the rate increases dramatically. The rate constant of iron at 650°C is about 1×10^{-9} g^2 cm^{-4} s^{-1} (from Figure III.2) and the curve corresponding to this on Figure VII.9 lies approximately parallel to the curves of the nitrided and the nitrided and aged alloys at times greater than 72h. X-ray powder photographs show haematite, magnetite, wustite and iron-chromium spinel in all three specimens.

Figure VII.8

Scanning electron micrographs of Fe-2.32w/oCr; nitrided in $10NH_3:90H_2$ at 575°C, aged at 650°C for 6h; cyclically oxidised in air from 500°C to room temperature,

(a) secondary electron image,

(b) Cr-Kα X-ray image,

(c) Fe-Kα X-ray image.

(a)

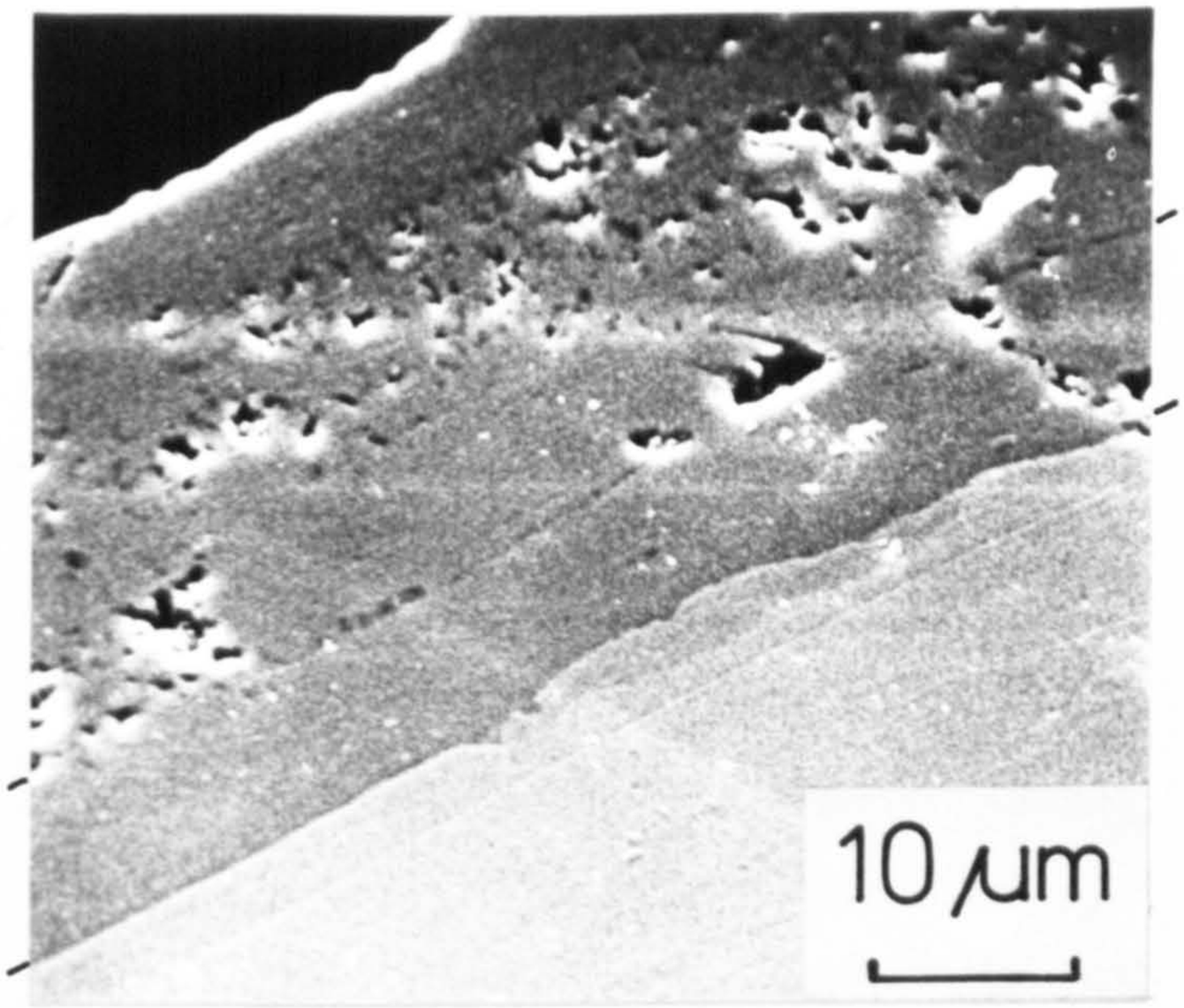

(b)

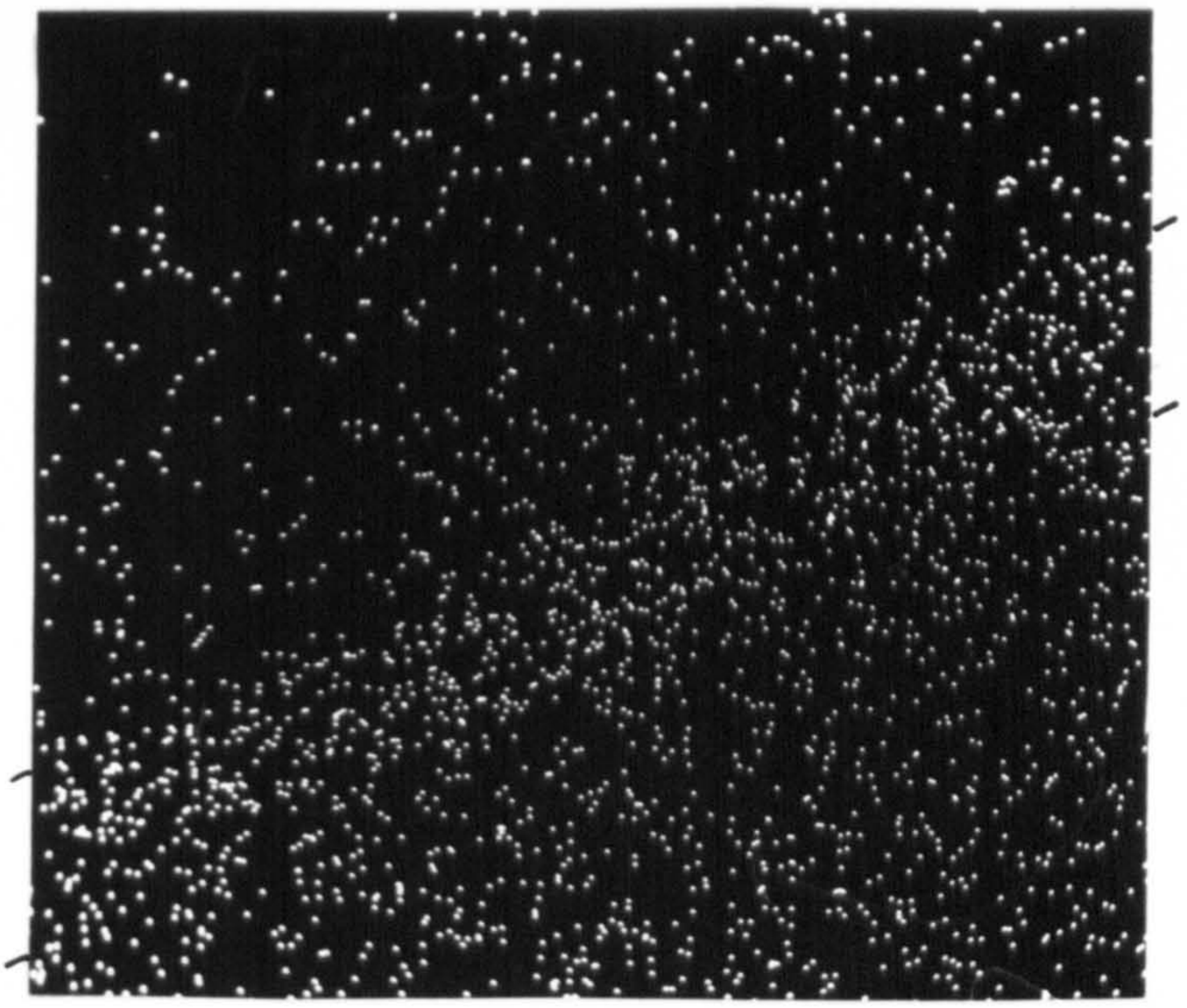

(c)

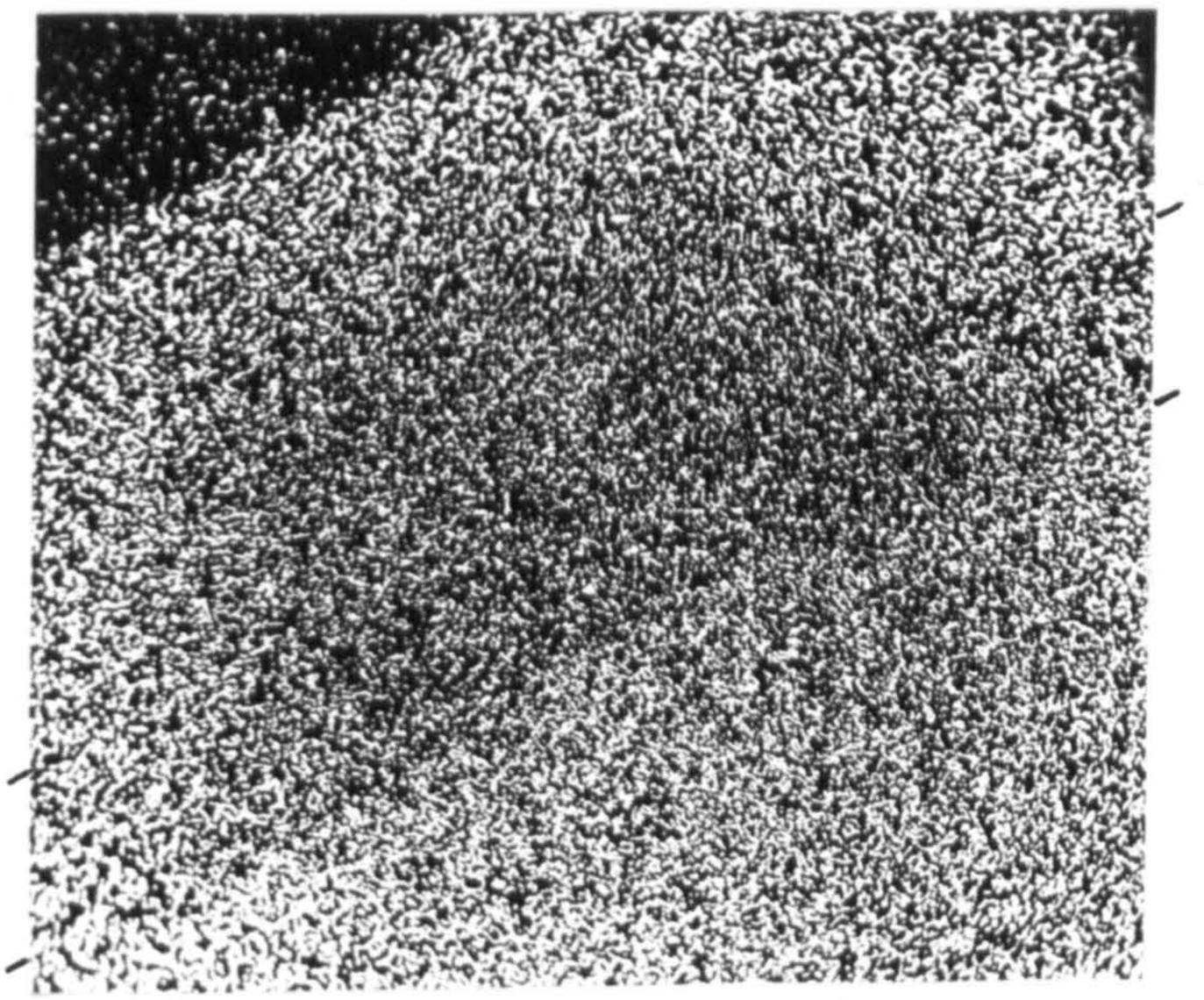

Figure VII.9

Parabolic plots of oxidation curves for Fe-2.32w/oCr alloys, cyclically oxidised from 650°C to room temperature.

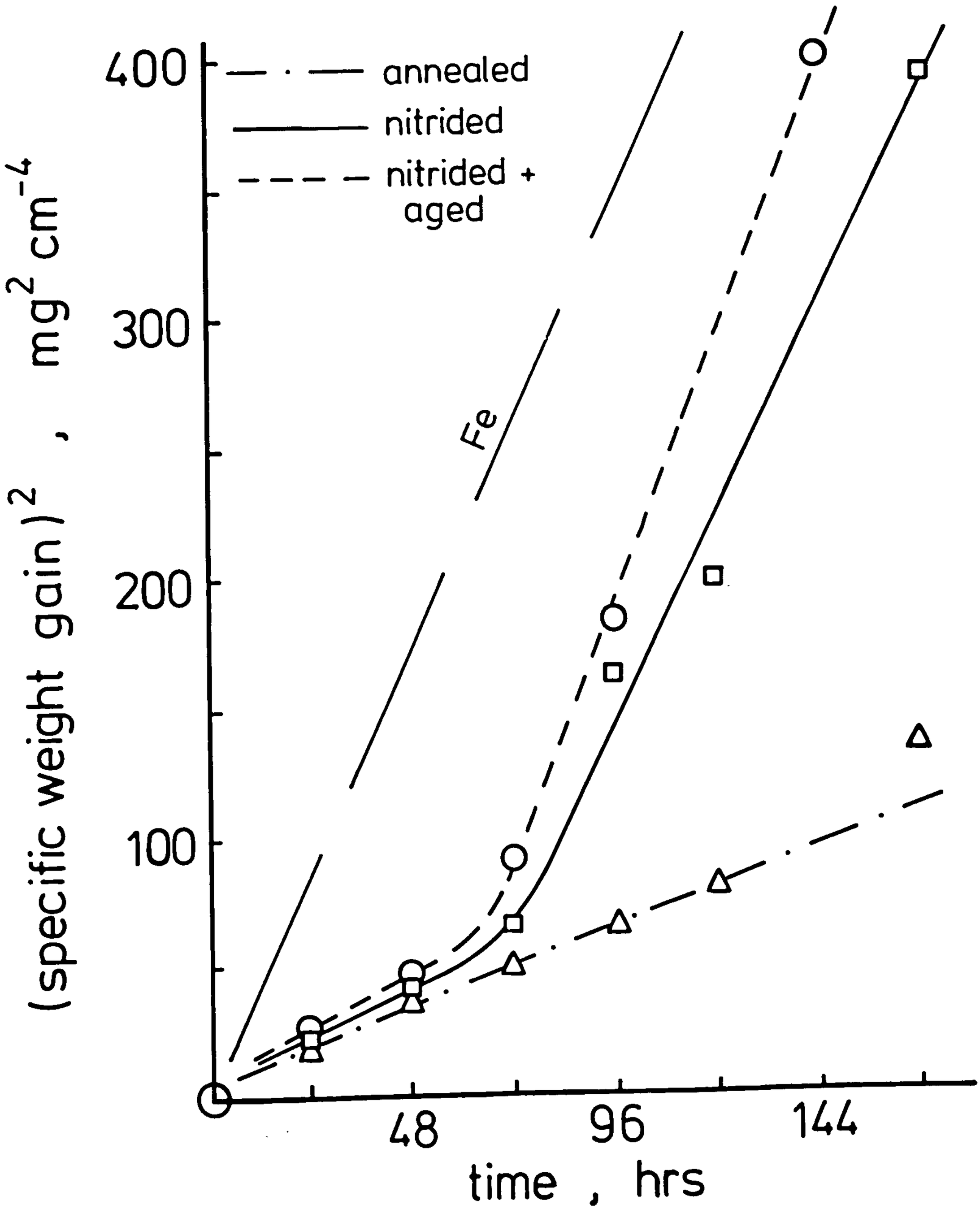
annealed
nitrided
nitrided + aged
Fe
400
300
200
100
48
96
144
(specific weight gain)^2 , mg^2 cm^{-4}
time , hrs

VII.5. Discussion

The rate of oxidation of Fe-2.32w/oCr at 500°C, with periodic cooling to room temperature, is slightly higher than for annealed pure iron. The oxide morphology shows an outer scale consisting of a thin haematite layer on a magnetite layer and an inner, inward-growing, iron-chromium spinel layer. Nitriding, with or without subsequent aging, has little effect on the oxidation rate at 500°C and does not affect the oxide phases formed. However, on nitrided and aged material, voidage at the oxide/metal interface is eliminated. This is thought to result from incoherent CrN particles providing vacancy sinks at the particle/matrix interfaces similar to the effect of oxide dispersions in superalloys; see section III.8. The effects are also similar to those of cold work on the oxidation kinetics of iron (Caplan & Cohen, 1966), see section III.6. Cold work can also increase the oxidation rate of low chromium Fe-Cr alloys (Wood et al., 1970) by providing vacancy sinks in the alloy. This reduces the cation vacancy gradient across the scale and local detachment of the scale from the alloy by vacancy coalescence is delayed. An opposing effect of cold work is to increase the interdiffusion coefficient of chromium along short-circuit paths (dislocations) which leads to a more rapid formation of the rate-limiting chromium-containing oxides at the surface. The overall oxidation kinetics of the cold worked material will thus be influenced by a balance between the two opposing effects. The elimination of porosity at the metal/oxide interface is also a consequence of the change in growth mechanisms - as the inner oxide grows by inward diffusion of oxygen anions and reaction at the metal/oxide interface, cation vacancy diffusion

and condensation will no longer occur.

Published work (Boggs et al., 1965; Boggs et al., 1967; Hussey & Cohen, 1971) indicates that the first-formed oxide on iron substrates at normal atmospheric pressures is Fe_3O_4. Once a compact layer of Fe_3O_4 is formed on the iron substrate, Fe_2O_3 nucleates and grows rapidly to cover this layer. A duplex scale is formed with Fe_3O_4 growing by cation diffusion and reaction at the magnetite/haemetite interface; the haematite is formed mainly by anion diffusion. During oxidation of low chromium Fe-Cr alloys the initial mechanism is the same as for unalloyed iron and only when the magnetite/haematite layers have been established is a $(Cr,Fe)_2O_3$ or $FeCr_2O_4$ layer produced beneath the magnetite (Kubaschewski & Hopkins, 1962).

Dispersed CrN particles in the matrix eliminate metal/oxide interfacial voidage, but do not prevent the formation of chromium-spinel although the thermodynamics of the spinel forming reaction will be changed. Considering the formation of magnetite by the reaction

$$3Fe + 2O_2 = Fe_3O_4 \quad \ldots\ldots \text{VII.1}$$

the free energy of formation, ΔG^o_T, is given by

$$\Delta G^o_T = -RT \ln (1/P_{O_2}^2) \quad \ldots\ldots \text{VII.2}$$

if the solid compounds have unit activities. From equations VII.1 and VII.2, $P_{O_2} = 5\times10^{-26}$ Pa (5×10^{-31} atm) at 773K (data from Kubaschewski and Alcock, 1979).

On an un-nitrided Fe-2.32w/oCr alloy, the formation of iron-chromium spinel, by the reaction

$$Fe_3O_4 + 6Cr + 4O_2 = 3FeCr_2O_4 \quad \ldots\ldots \text{VII.3}$$

has a free energy change

$$\Delta G^o_T = -RT \ln (1/p_{O_2}^4 \cdot a_{Cr}^6) \quad \ldots\ldots \text{VII.4}$$

Putting $a_{Cr} \equiv [Cr]$ = atomic fraction of Cr (0.0249), then $p_{O_2} = 4\times10^{-58}$Pa($4\times10^{-63}$atm) at 773K. This is much lower than the partial pressure of oxygen in equilibrium with magnetite at 773K and so the iron-chromium spinel will be thermodynamically more stable than magnetite under equivalent conditions.

In the case of nitrided Fe-Cr alloys the situation is complicated by the fact that the chromium is combined in the alloy as CrN. The oxidation of nitrided specimens proceeds first by the formation of iron oxides (by reaction with atmospheric oxygen) and then by the reaction

$$Fe_3O_4 + 6CrN + 4O_2 = 3(FeCr_2O_4) + 3N_2 \quad \ldots\ldots \text{VII.5}$$

for which $\Delta G^o_T = -RT \ln (p_{N_2}^3 / p_{O_2}^4)$ VII.6

Assuming p_{N_2} is the partial pressure of nitrogen in equilibrium with CrN its value may be calculated from the reaction

$$2CrN = 2Cr + N_2 \quad \text{.... VII.7}$$

as $P_{N_2} = 7x10^{-2}Pa\ (7x10^{-7}atm)$ at 773K.

Inserting this into equation VII.6 gives

$$P_{O_2} = 6x10^{-16}Pa\ (6x10^{-21}atm)$$

Thus, under the conditions considered, magnetite is thermodynamically more stable than iron-chromium spinel when the chromium is present as CrN. However, the calculation assumes that the outer iron-oxide layers remain protective and no access of gas to the metal/oxide interface occurs. If there is gas penetration to the metal/oxide interface through pores or cracks in the oxide then the partial pressure of nitrogen will be ~ 0.08 MPa (0.8atm). According to equation VII.6, this will increase the oxygen partial pressure in equilibrium with iron-chromium spinel to $9x10^{-13}Pa(9x10^{-18}atm)$ but because oxygen access to the metal/oxide interface will also be possible P_{O_2} will then reach a maximum value of 0.02 MPa(0.2atm) and both magnetite and iron-chromium spinel will be thermodynamically stable.

The presence of an iron-chromium spinel layer next to the metal/oxide interface in the nitrided alloys, as well as in the un-nitrided material, suggests that oxygen penetration of the magnetite and haematite layers occurs. The thinner CrN layer penetrating the spinel layer from the metal substrate shown by Figure VII.3(b) indicates that CrN is oxidised, but at a relatively slow rate.

The oxidation of Fe-Cr alloys nitrided to give incoherent nitride precipitates is influenced by two opposing mechanisms. The elimination of vacancy condensation at the metal/oxide interface by the incoherent particles acting as vacancy sinks will increase the adherence of the oxide and thus give increased resistance to spalling. However, nitriding of Fe-Cr alloys will immobilise the chromium in the Cr-N clusters or CrN precipitates so that its influence on the oxidation kinetics will be reduced and will result in an increased oxidation rate. The improved coherence of the metal/oxide interface will maintain a high cation exchange area tending to increase the oxidation rate of the alloy. The overall kinetics will be influenced by a balance of these factors and, under the conditions investigated, any differences between the nitrided and un-nitrided alloys are not sufficiently large to be observed. The metallographic observations do uphold the idea that a dispersion of incoherent nitride particles in the substrate eliminates interfacial voidage, thus improving metal-oxide adhesion, and also produces a fine-grained, inner oxide layer with higher fracture strength. The outer oxide layer must allow gaseous oxygen penetration to the metal/oxide interface, resulting in spinel formation at the interface. The micrographs of the oxides are very similar to micrographs of oxidised nitrided mild steel (see e.g. Figure VI.14) which also show an outer, porous oxide layer and an inner, compact layer with voidage at the interface of the two layers and an adherent metal/oxide interface. This is further evidence that the mechanism of growth of the oxide on nitrided mild steel is changed so that the inner fine-grained layer grows by oxygen diffusion inwards rather than by iron cation diffusion outwards.

At 650°C the rate of oxidation of Fe-2.32w/oCr is lower by an order of magnitude than that of iron. The oxidation rate of nitrided specimens is comparable with that of the un-nitrided material for the first 50-70h but then exhibits 'breakaway' kinetics with a subsequent oxidation rate comparable with that of un-alloyed iron. Metallographic examination shows that the scale on the annealed alloy has a relatively thin inner oxide layer, thought to be spinel, covered by a thick, porous, wustite layer that is covered in turn by thin magnetite and haematite layers. The oxide is separated from the metal substrate by a regular interface not showing any regions of enhanced oxidation. The oxides on both the nitrided and the nitrided and aged specimens also show a fine-grained inner oxide layer that is very coherent with the metal substrate. The metal/oxide interface is irregularly shaped and the boundary between the inner oxide layer and the wustite has a similar shape with voidage at the inner layer/wustite interface. The thick wustite layers are generally compact, with some porosity similar to the voidage at the inner layer/wustite interface. The wustite is again covered by thin layers of magnetite and haematite and cracking of the oxide perpendicular to the surface is also evident. The ratio of the thermal coefficient of expansion of FeO to that of Fe is 1.25 (Tylecote & Appleby, 1972) and so stresses in the oxide will result from thermal changes. The effect of nitriding on wustite formation may be to form a more adherent, less plastic oxide layer which is less able to deform during thermal cycling, and consequently fractures to allow gaseous penetration to the metal/oxide interface. This is supported by the observation of cracks in the oxide running perpendicular to the metal/oxide interface and by the irregular nature of the metal/oxide interface

indicating accelerated oxidation of the metal substrate at discrete points.

As has been pointed out (Whittle & Wood, 1967) it is extremely difficult to isolate one factor as the cause of the loss of protective scale and a combination of factors such as scale thickness, scale plasticity, alloy ductility, phase changes, adhesion between alloy and oxide, and alloy and/or oxide grain growth are probably effective. Considering the oxidation of nitrided Fe-Cr at 650°C, the presence of iron-chromium spinel and of cracks perpendicular to the metal/oxide interface, as well as the irregular metal/oxide interface, suggest a mechanical rather than a chemical cause of the accelerated oxidation. The cracking probably results in oxygen penetration to the metal/scale interface causing accelerated oxidation at discrete points on the metal surface. The fact that the oxidation rates are similar to that of the un-nitrided material for the first 50h suggests that the stresses developed during thermal cycling are not large enough to cause cracking of the oxide until it has grown to some critical thickness.

Thus, nitriding of Fe-2.32w/oCr to provide a dispersion of incoherent nitrides has conflicting effects on the oxidation behaviour in that whilst the adherence of the metal/oxide interface is improved by the elimination of void formation, the oxidation rates do not show the expected improvements and indeed, are seriously impaired at 650°C in air.

The results of the oxidation at 650°C are not encouraging and it is thought unlikely that prolonged experiments at this temperature would prove fruitful.

However, although the oxidation rates at 500°C show little difference between nitrided and un-nitrided Fe-2.32w/oCr, the obvious increase in adherence at the metal/oxide interface on nitrided specimens suggests that benefits may arise with increased exposure times or more aggressive conditions.

Areas of further research into the oxidation of nitrided iron-chromium alloys that might profitably be explored are (i) the use of higher chromium contents, (ii) partial nitriding of the alloy to obtain a CrN dispersion with some chromium remaining in solid solution and (iii) the use of a fourth element, such as titanium, so that by suitable nitriding a dispersion of titanium nitride is formed leaving all the chromium in solid solution. Using such methods, the benefits of dispersoids on the oxide morphology and of free chromium on oxidation rates might be combined.

Chapter VIII

THE OXIDATION OF IRON-TITANIUM-NITROGEN ALLOYS

VIII.1. Introduction

In view of the generally unimproved oxidation behaviour observed for nitrided iron-chromium alloys (Chapter VII) it was decided to study a binary iron alloy not normally regarded as oxidation resistant, but which would readily form dispersed nitride particles by suitable nitriding heat treatment. It was hoped that the effect of the dispersed nitride would not be obscured by any decrease in oxidation resistance due to the precipitation of an intrinsically oxidation resistant alloying element as in the case of iron-chromium alloys. The oxidation of binary iron-titanium alloys have not been studied extensively, but Scheil et al. (1936) found that titanium slightly increases the oxidation resistance of iron at 800°C. The nitriding of iron-titanium alloys has been studied by Henderson (1976) and the precipitation sequence follows that of other Fe-X-N systems. Titanium-nitrogen metastable clusters form at normal nitriding temperatures and overage at high temperatures to give stable TiN precipitates.

The Fe-0.5w/oTi alloy (B.I.S.R.A. cast K2733) was cold-rolled to about 400 μm strip and annealed at 950°C for 30 min. 'Bulk' specimens (about 2mm

thick) were cut from 12mm diameter bar, cleaned by abrasion and annealed under similar conditions.

VIII.2. Nitriding Procedure

The kinetics of nitriding of Fe-Ti alloys are consistent with the internal nitriding equation (Henderson, 1976); see section II.5. Two nitriding procedures were used to prepare specimens containing (i) coherent Ti-N clusters and (ii) incoherent TiN precipitates. Nitriding in $25NH_3:75H_2$ at $400^{\circ}C$ results in a fine distribution of small substitutional-interstitial clusters. The time required to through-nitride the foil specimens under these conditions is 105h. Specimens were nitrided for 130h giving 0.25 w/o weight gain which exceeds the increase expected for a N:Ti ratio of 1:1 by a factor of 1.8. Increases in the lattice parameter show that the nitrogen is in (non-random) solid solution and not precipitated (see Table VIII.1).

The high nitrogen pick-up of Fe-Ti alloys has been noted by Henderson (1976); see section II.7.

Previously nitrided specimens were hydrogen reduced at $650^{\circ}C$ for 6h and the weight loss of the through-nitrided foils is in close agreement with the calculated weight of "excess" nitrogen; see Table VIII.2. Aging of the nitrided and hydrogen-reduced alloys at $850^{\circ}C$ for 20h results in a reduction of the lattice parameter (Table VIII.1) due to precipitation of incoherent TiN , although the lattice parameter remains much higher than that expected (2.8664 $\mathring{A}$) if

Table VIII.1

Lattice parameters and weight gain of Fe-0.5w/oTi

Specimen	Lattice parameter Å	Weight gain calculated from lattice parameter w/o	Actual weight gain w/o
Annealed	2.8682	-	-
Nitrided in $25NH_3:75H_2$ at 400°C	2.8751	0.256	0.246
Nitrided in $25NH_3:75H_2$ at 400°C; aged at 850°C for 20h	2.8682	-	-

Table VIII.2

Weight gain of Fe-0.5w/oTi; nitrided in $25NH_3 75H_2$ at 400°C and hydrogen-reduced at 650°C

Calculated weight gain from Ti:N = 1:1 w/o	Actual weight gain after nitriding w/o	"Excess" nitrogen w/o	Net weight gain after nitriding and hydrogen reduction w/o
0.138	0.246	0.108	0.140

all the titanium and nitrogen is precipitated; see section II.7.

Figure VIII.1(a) shows the microstructure of Fe-0.5w/oTi nitrided in $25NH_3:75H_2$ at 400^oC. The matrix consists of a dispersion of fine clusters, about 100 Å in diameter. Electron diffraction patterns have pronounced streaking in $\langle 100 \rangle$ directions showing the clusters to be very thin discs lying on $\{100\}$ matrix planes. (b) shows the microstructure of the nitrided and aged alloy, electron diffraction patterns of which show discrete TiN reflections. (c) is a dark field micrograph, taken using a TiN spot that shows the particles to be incoherent TiN precipitates about 200 Å in diameter.

VIII.3. Oxidation of Fe-Ti-N

Oxidation of the 'bulk' specimens was carried out under thermal cycling conditions (240^o-480^oC) following the procedure described in section V.5(c). Figure VIII.2 shows the oxidation weight gain as a function of time at the upper hold temperature. The r-coefficients (Table VIII.3) indicate that a parabolic rate law is more closely followed by nitrided and aged Fe-0.5w/oTi than by the un-nitrided and as-nitrided alloys. The oxide on the un-nitrided alloy was mostly separated from the metal substrate. A line of porosity associated with the Fe_2O_3/Fe_3O_4 interface was observed, with separation of the two phases in some areas, as in Figure VIII.3(a) which was taken from one of the few areas where oxide/substrate coherency was maintained. The oxide on the

Figure VIII.1

Transmission electron micrographs of Fe-0.5w/oTi,

(a) nitrided in $25NH_3:75H_2$ at 400°C,

(b) nitrided in $25NH_3:75H_2$ at 400°C; hydrogen-reduced at 650°C for 6h; aged at 850°C for 20h,

(c) dark field of (b) using TiN reflection.

(a)

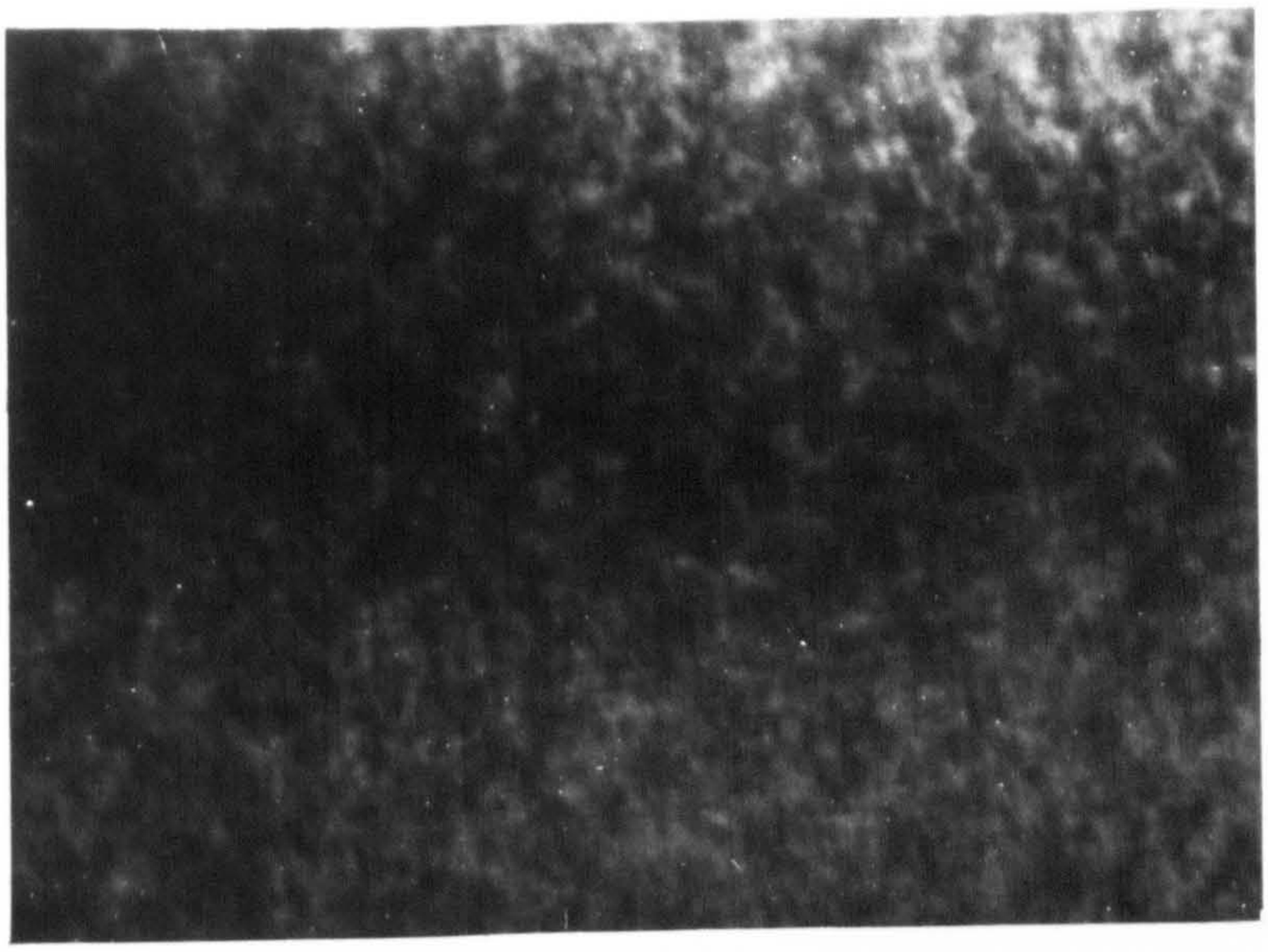

0.1 μm

(b)

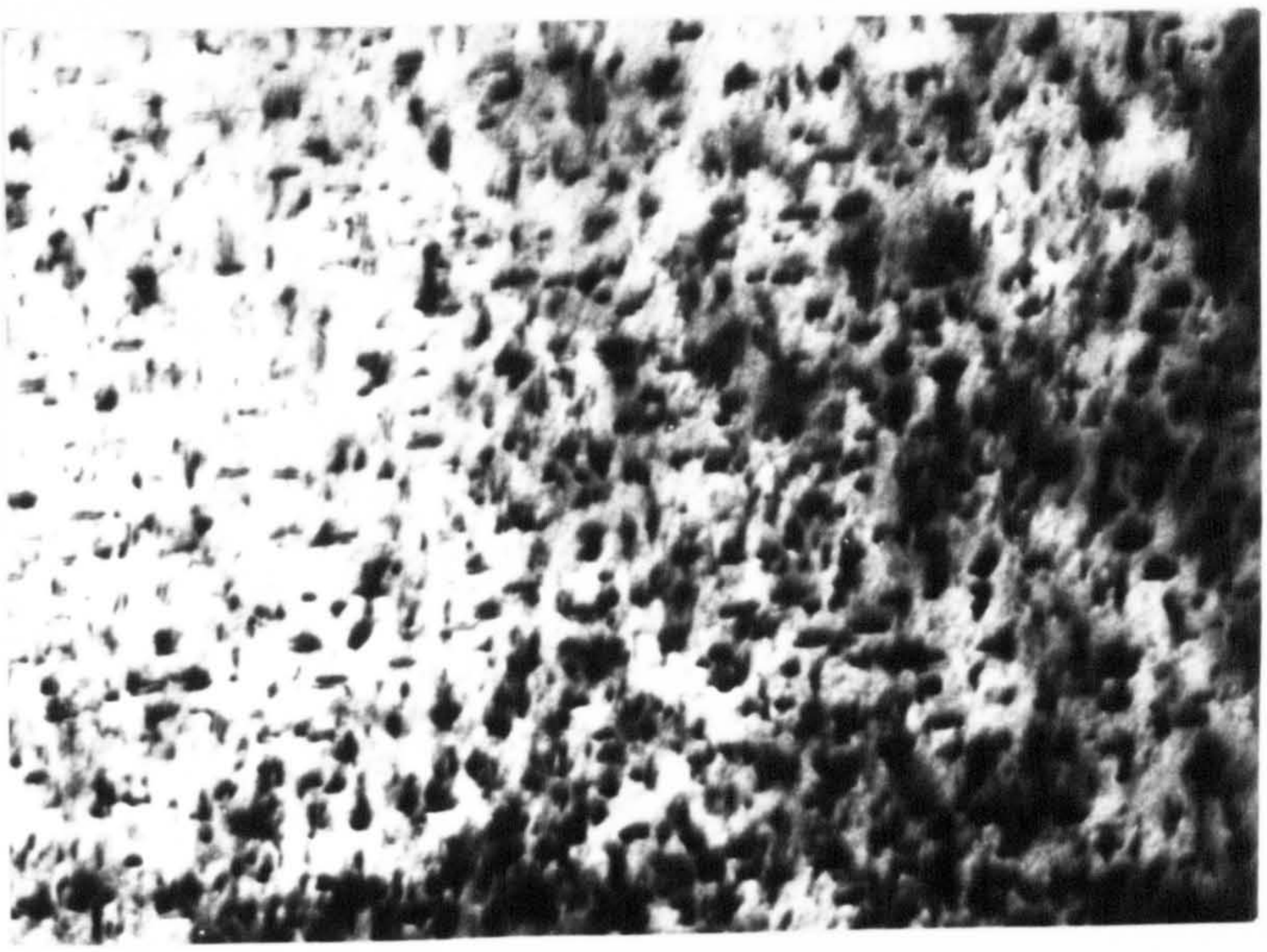

(c)

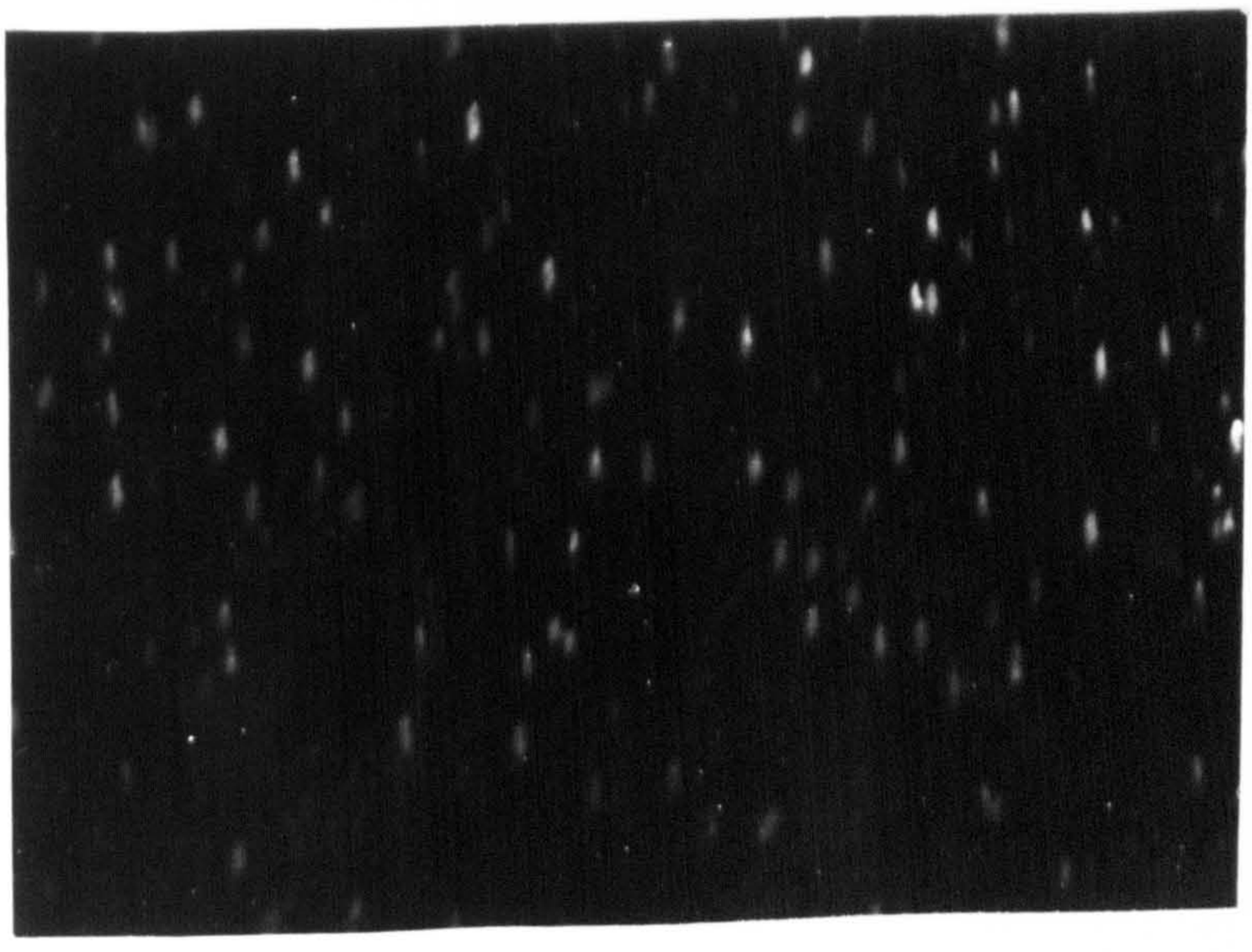

0.2 μm

Figure VIII.2

Oxidation weight gain curves for Fe-0.5w/oTi cyclically oxidised at 240°-480°C in air.

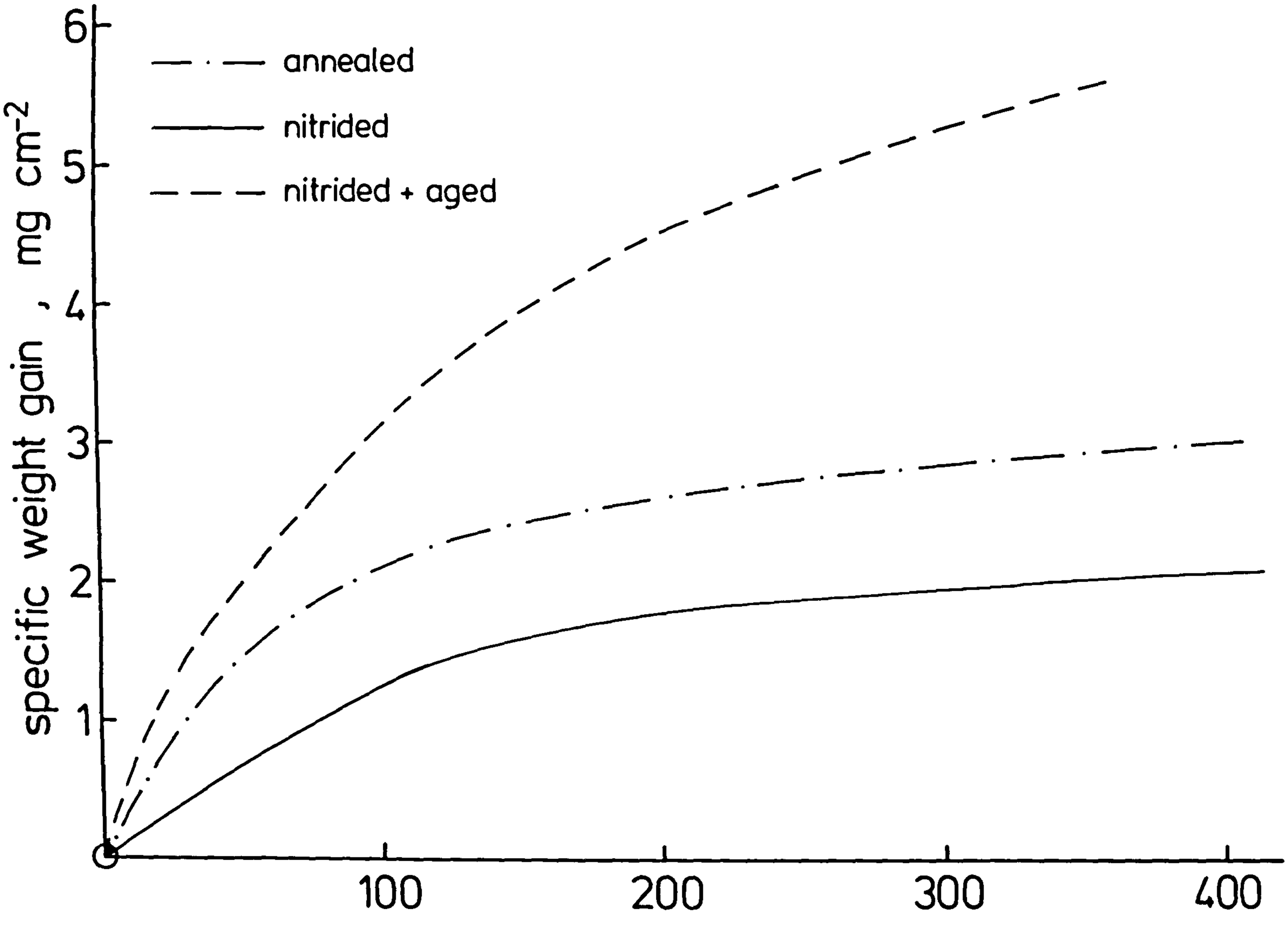
annealed
nitrided
nitrided + aged
specific weight gain , mg cm-2
6
5
4
3
2
1
100
200
300
400
upper hold time , hrs

Figure VIII.3

Optical micrographs of oxide scales on Fe-0.5w/oTi; cyclically oxidised at 240°-480°C in air; etched in HCl,

(a) un-nitrided alloy,

(b) nitrided in $25NH_3:75H_2$ at 400°C,

(c) and (d) nitrided in $25NH_3:75H_2$ at 400°C; hydrogen-reduced at 650°C for 6h; aged at 850°C for 20h.

(a)

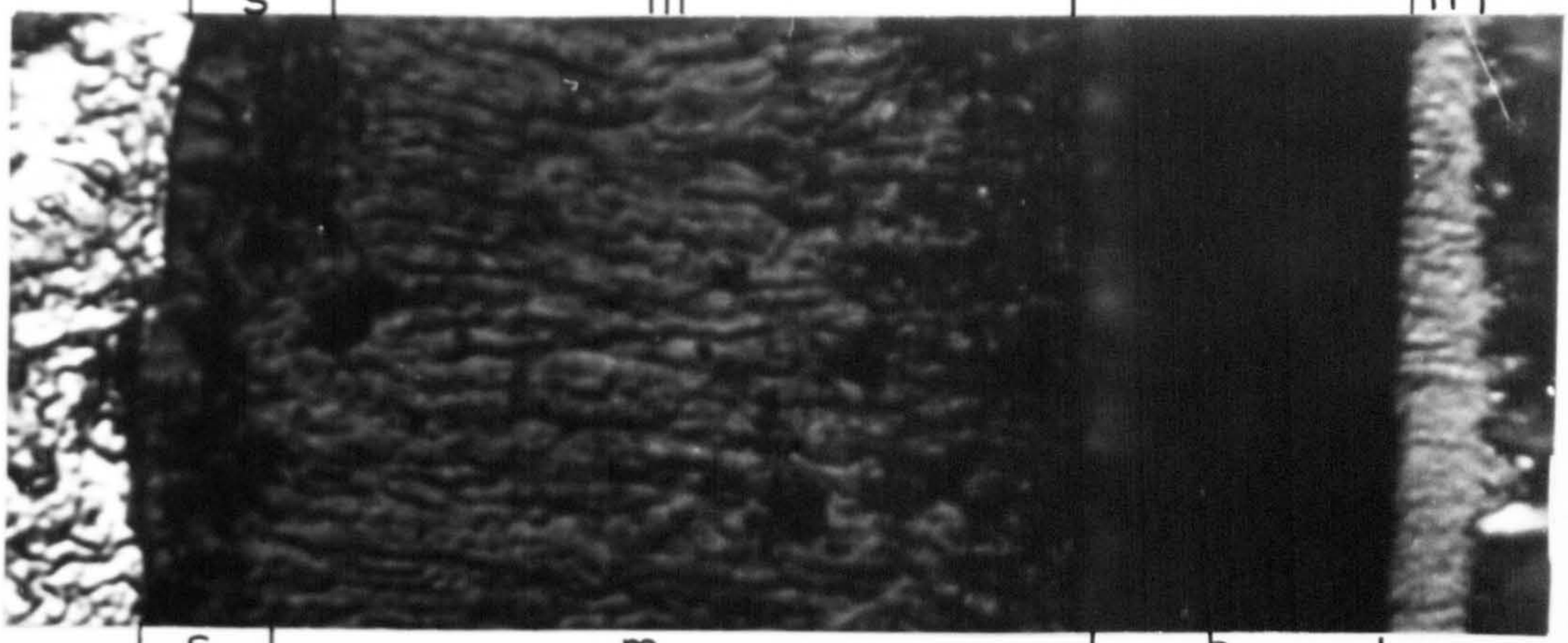

(b)

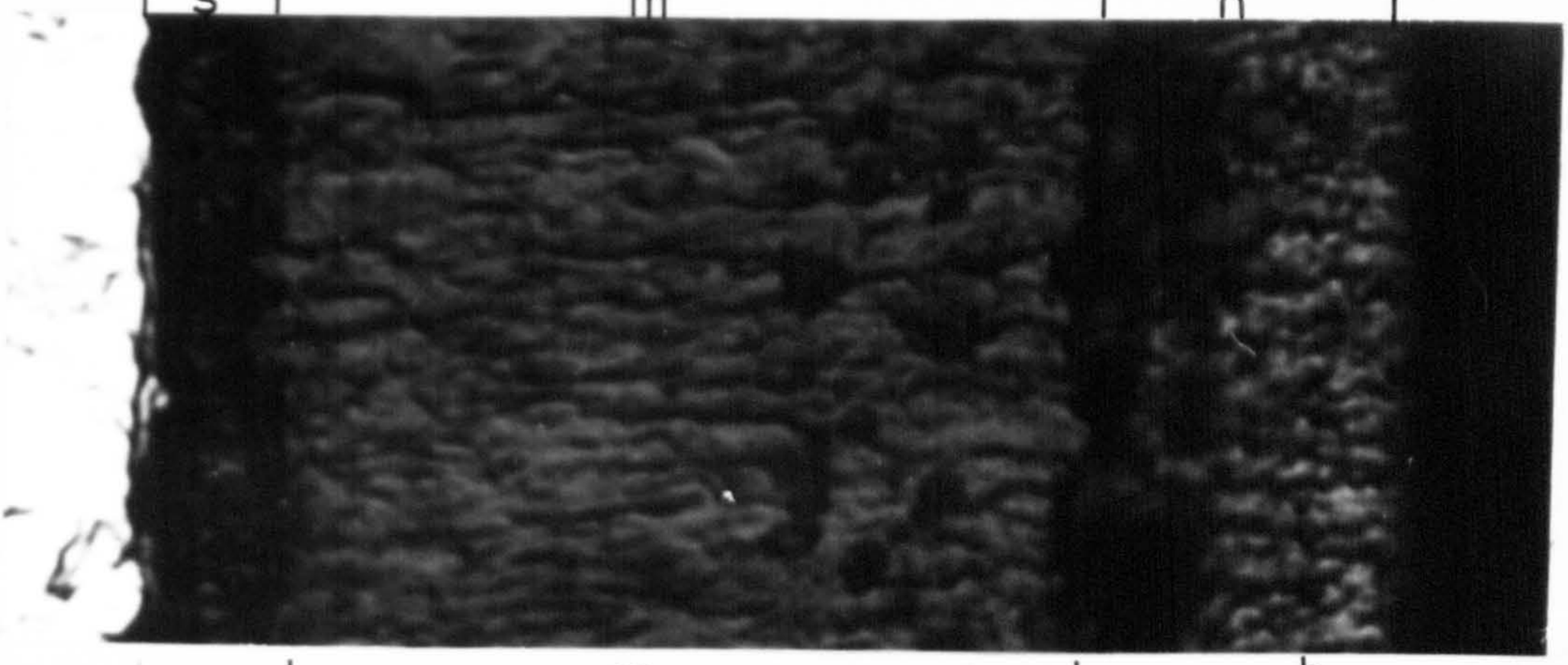

(c)

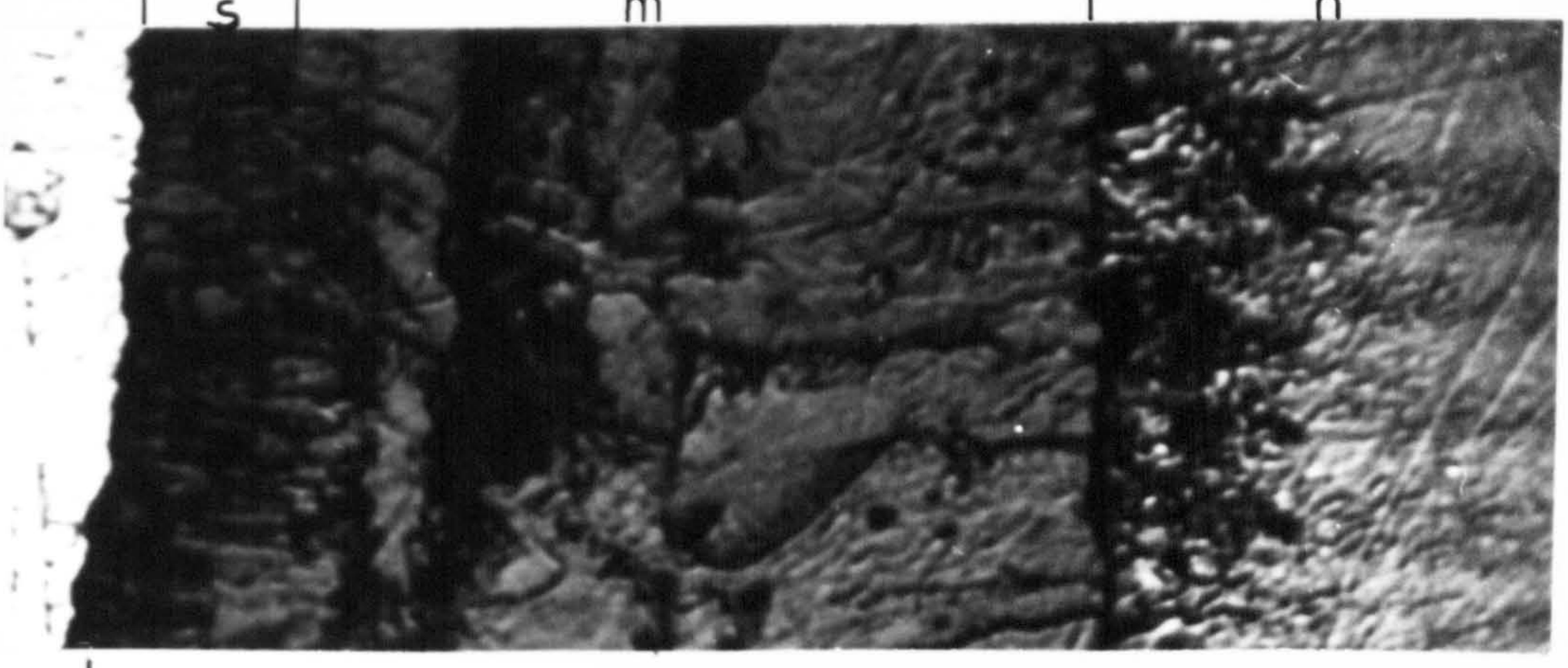

metal

oxide

10 μm

(d)

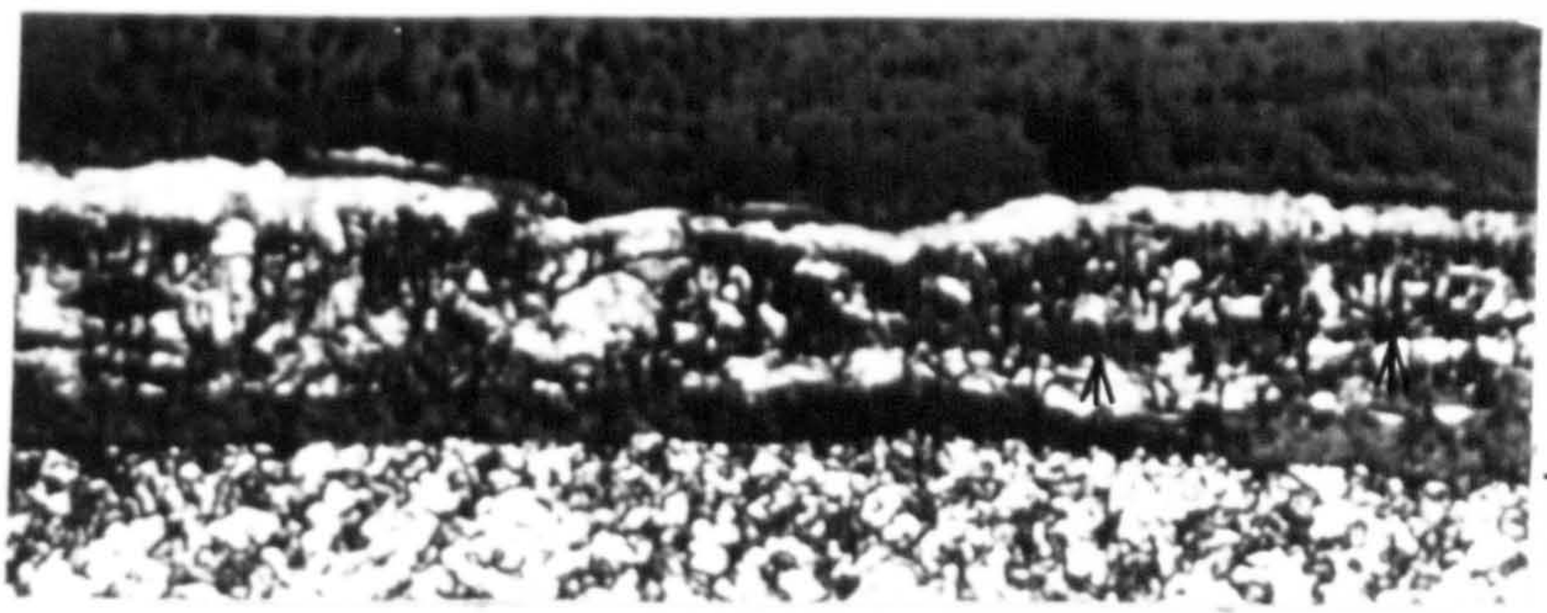

40 μm

Table VIII.3

Parabolic rate constants and linear regression coefficients (r) of Fe-0.5w/oTi alloys, cyclically oxidised at 240°-480°C in air

Specimen	Upper hold time h	Parabolic rate constant (k_p) $g^2\ cm^{-4}\ s^{-1}$	r
Annealed	440	4.46×10^{-12}	0.93
Nitrided in $25NH_3:75H_2$ at 400°C	440	2.92×10^{-12}	0.92
Nitrided in $25NH_3:75H_2$ at 400°C; aged at 850°C for 20h	360	2.50×10^{-11}	0.99

as-nitrided alloy also spalled away from the metal over much of its surface, but Figure VIII.3(b) shows one area where oxide was still coherent with the metal. Porosity is again observed at the magnetite/haematite interface, although no separation of the haematite from the magnetite is observed. The oxide scale on the nitrided and aged specimen is completely adherent and is shown in Figure VIII.3(c). All three specimens show a thin, inner, fine-grained oxide layer, s, beneath a magnetite layer, m, with voidage at their interfaces. The magnetite is equally thick on all three specimens but the haematite layer, h, is much thicker on the nitrided and aged specimen that on the others. Figure VIII.3(d), which is a lower magnification micrograph of (c), shows voidage (arrowed) lying in a line starting at the inner-layer/magnetite interface and extending into the magnetite. This suggests that during thermal cycling separation occurs at the inner-layer/magnetite interface and not at the metal/scale interface.

Figures VIII.4, VIII.5 and VIII.6 are scanning electron micrographs of the etched oxides on the annealed, the nitrided and the nitrided and aged specimens respectively. The titanium and iron distributions as determined by X-ray energy dispersive analysis are shown. All three specimens show a slightly higher titanium concentration in the oxide layer next to the metal/oxide interface corresponding also to a depletion of iron. The grain-size of the magnetite on annealed and as-nitrided specimens is uniform across the scale, whereas that on the nitrided and aged specimens is relatively fine-grained next to the inner oxide layer and is coarser further away from the interface.

Figure VIII.4

Scanning electron micrographs of Fe-0.5w/oTi; cyclically oxidised at 240°-480°C,

(a) secondary electron image,

(b) Ti-Kα X-ray image,

(c) Fe-Kα X-ray image.

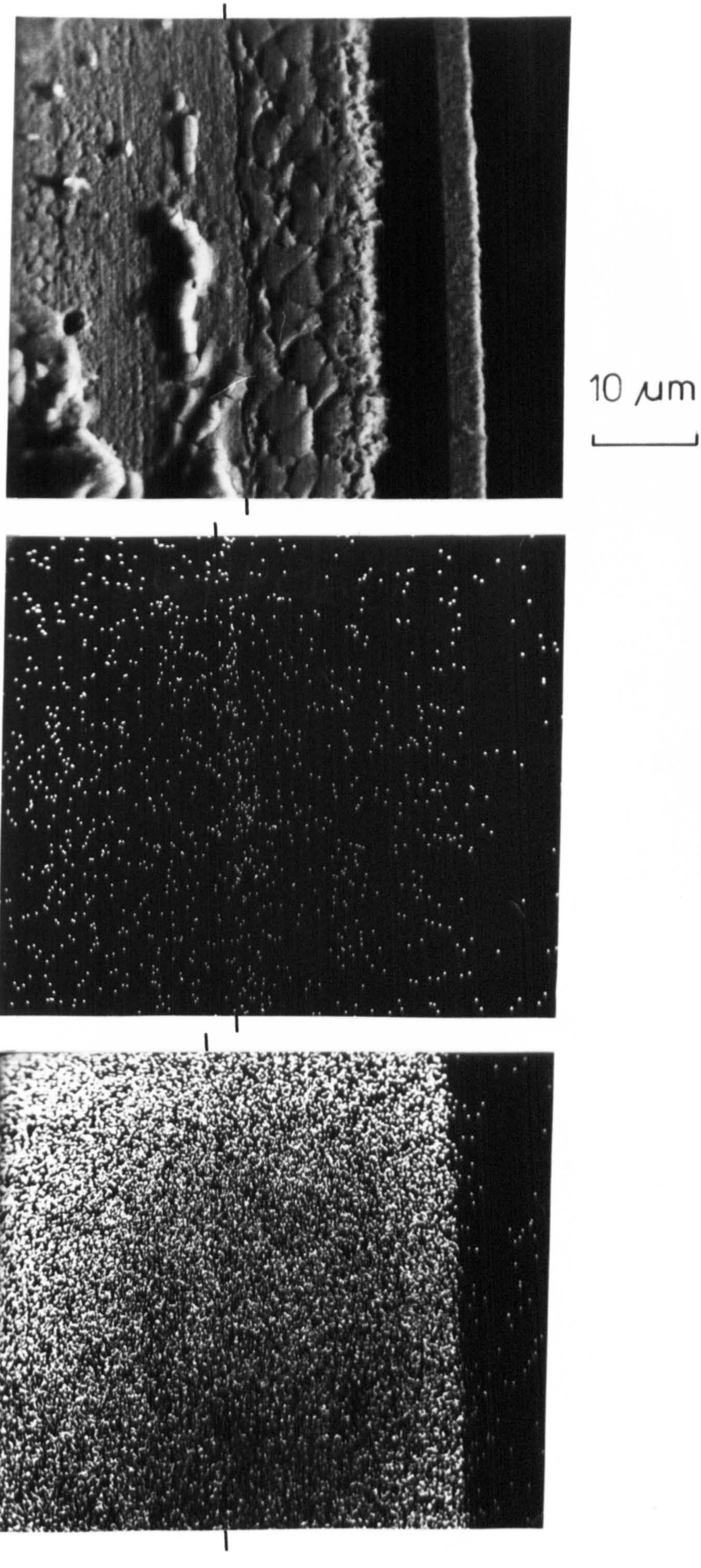
10 μm
(a)
(b)
(c)

Figure VIII.5

Scanning electron micrographs of Fe-0.5w/oTi; nitrided in $25NH_3:75H_2$ at 400°C; cyclically oxidised at 240°-480°C,

(a) secondary electron image,

(b) Ti-Kα X-ray image,

(c) Fe-Kα X-ray image.

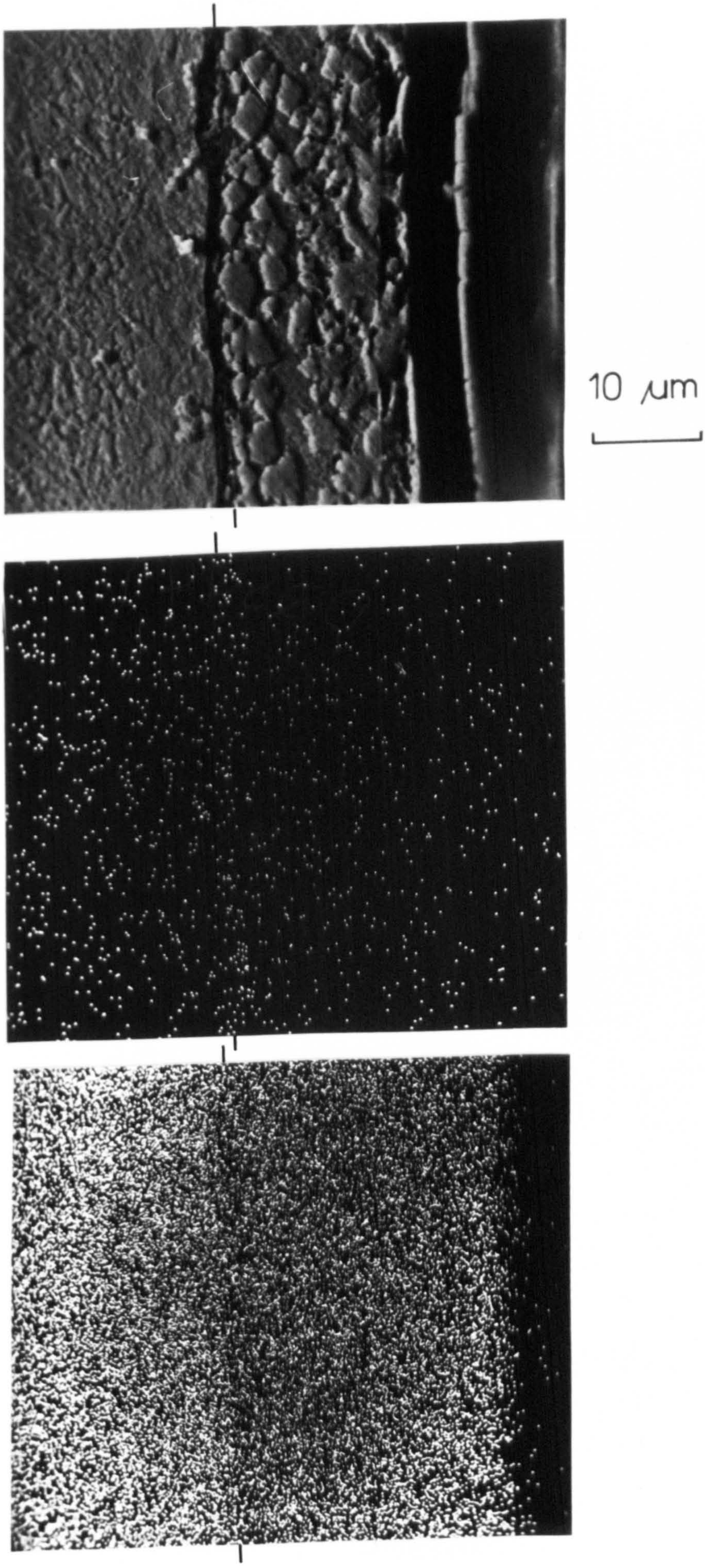
10 μm
(a)
(b)
(c)

Figure VIII.6

Scanning electron micrographs of Fe-0.5w/oTi; nitrided in $25NH_3:75H_2$ at 400°C; cyclically oxidised at 240°-480°C,

(a) secondary electron image,

(b) Ti-Kα X-ray image,

(c) Fe-Kα X-ray image.

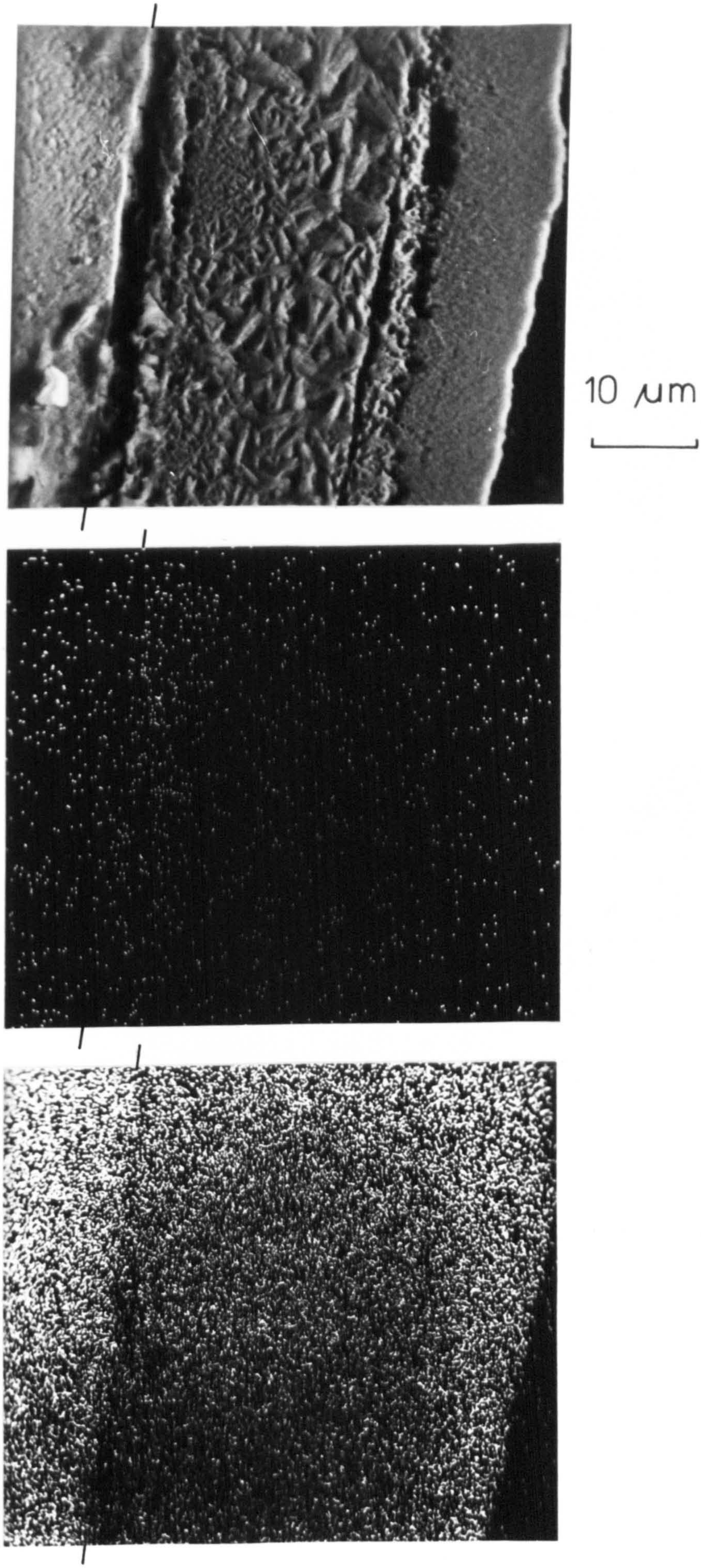
10 μm
(a)
(b)
(c)

X-ray photographs of the oxide scales show only Fe_3O_4 and Fe_2O_3. However, if the thin, inner titanium-containing oxide layer is a spinel, it would be indistinguishable from Fe_3O_4 by X-ray diffraction.

VIII.4. Transmission Electron Microscopy of Oxidised Specimens

(a) In-situ (H.V.E.M.) oxidation

In-situ oxidation experiments were carried out on thin foils in a high voltage electron microscope as described in section V.9. Initial experiments indicated that the electron beam could affect the development of oxide on the foil surface with the result that little oxidation occurred after one hour, although away from the beam incidence area the foil was extensively oxidised after similar exposure times. It was established that periodic observation of the foil with removal of the beam from the area of interest between observations eliminated any beam effects.

Figure VIII.7 shows transmission electron micrographs of Fe-0.5w/oTi foils from in-situ oxidation experiments. (a) shows a foil from a nitrided and aged specimen at $450^{o}C$ before oxygen injection into the column and (b) shows the foil after 15 min oxidation at $p_{O_2} = 10^{-4}Pa(10^{-9}atm)$. The initial oxide grains are very similar in size and shape to the TiN precipitates (see arrowed oxide grains in (b)) showing that the oxide which

Figure VIII.7

Transmission electron micrographs of Fe-0.5w/oTi oxidised at 450°C, in-situ H.V.E.M.,

(a) nitrided in $25NH_3:75H_2$ at 400°C; aged at 850°C for 20h; 0 min oxidation,

(b) as (a) 15 min oxidation,

(c) un-nitrided; oxidised 45 min.

(a)

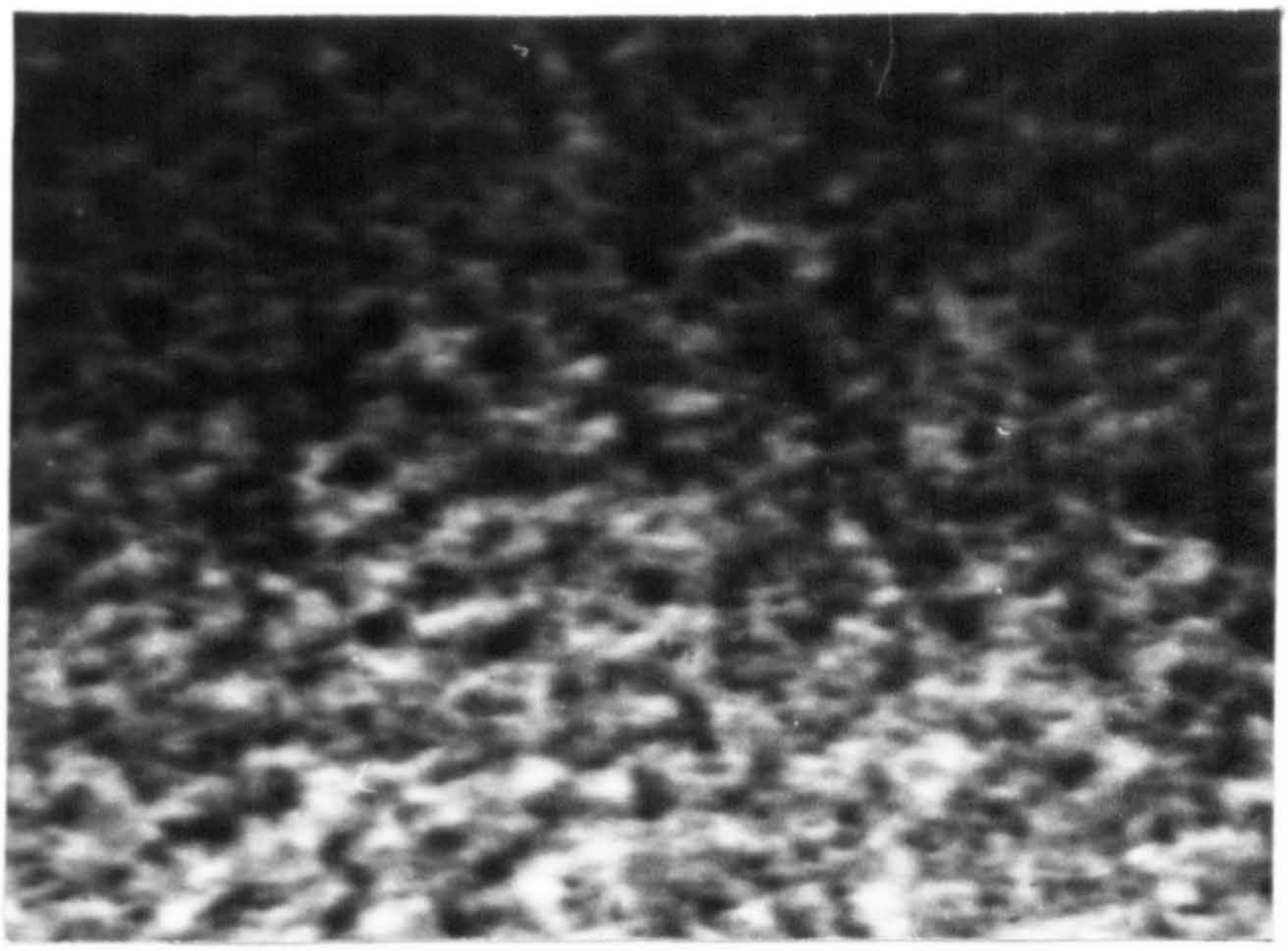

g[200]

(b)

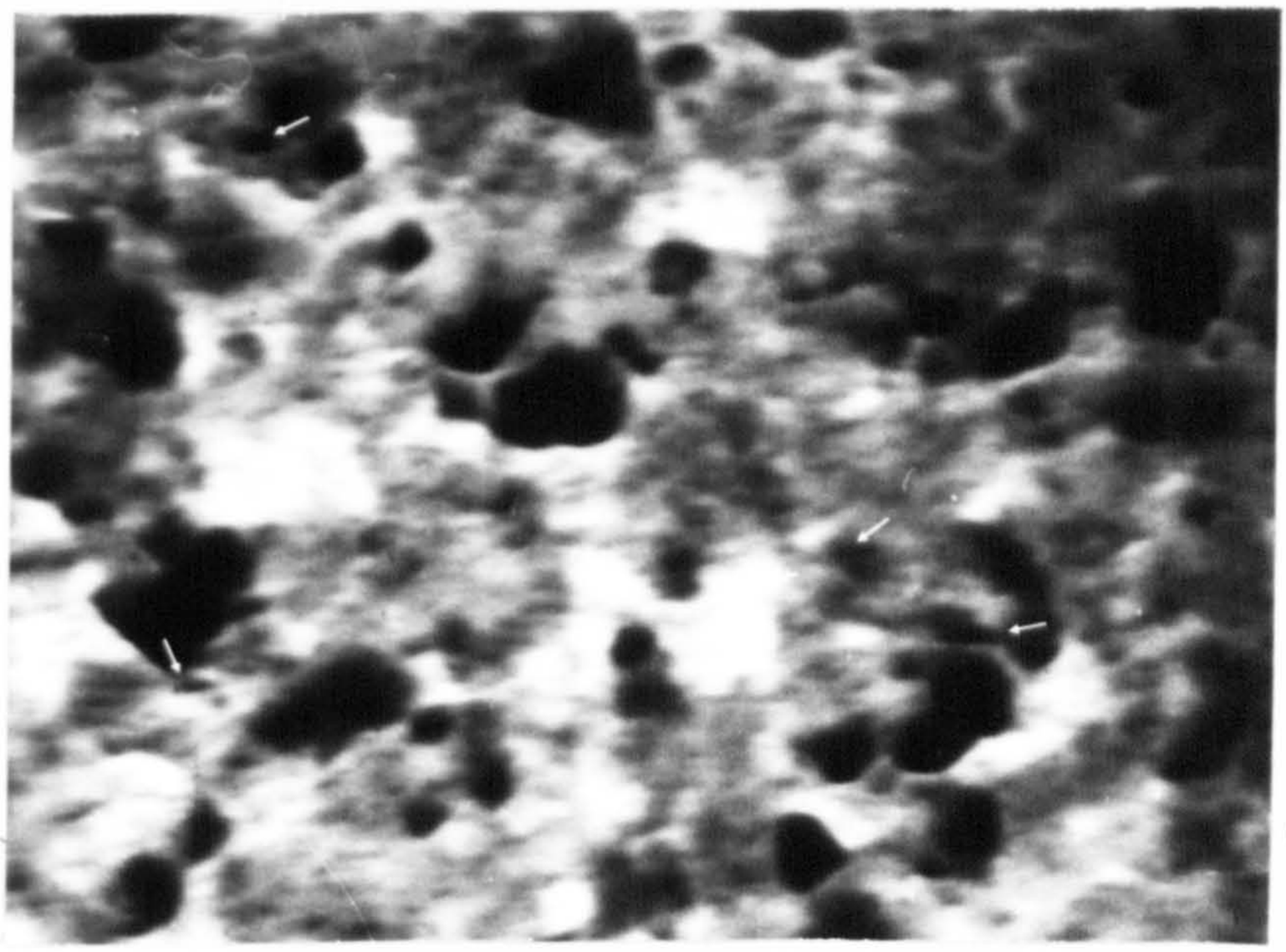

0.2 μm

(c)

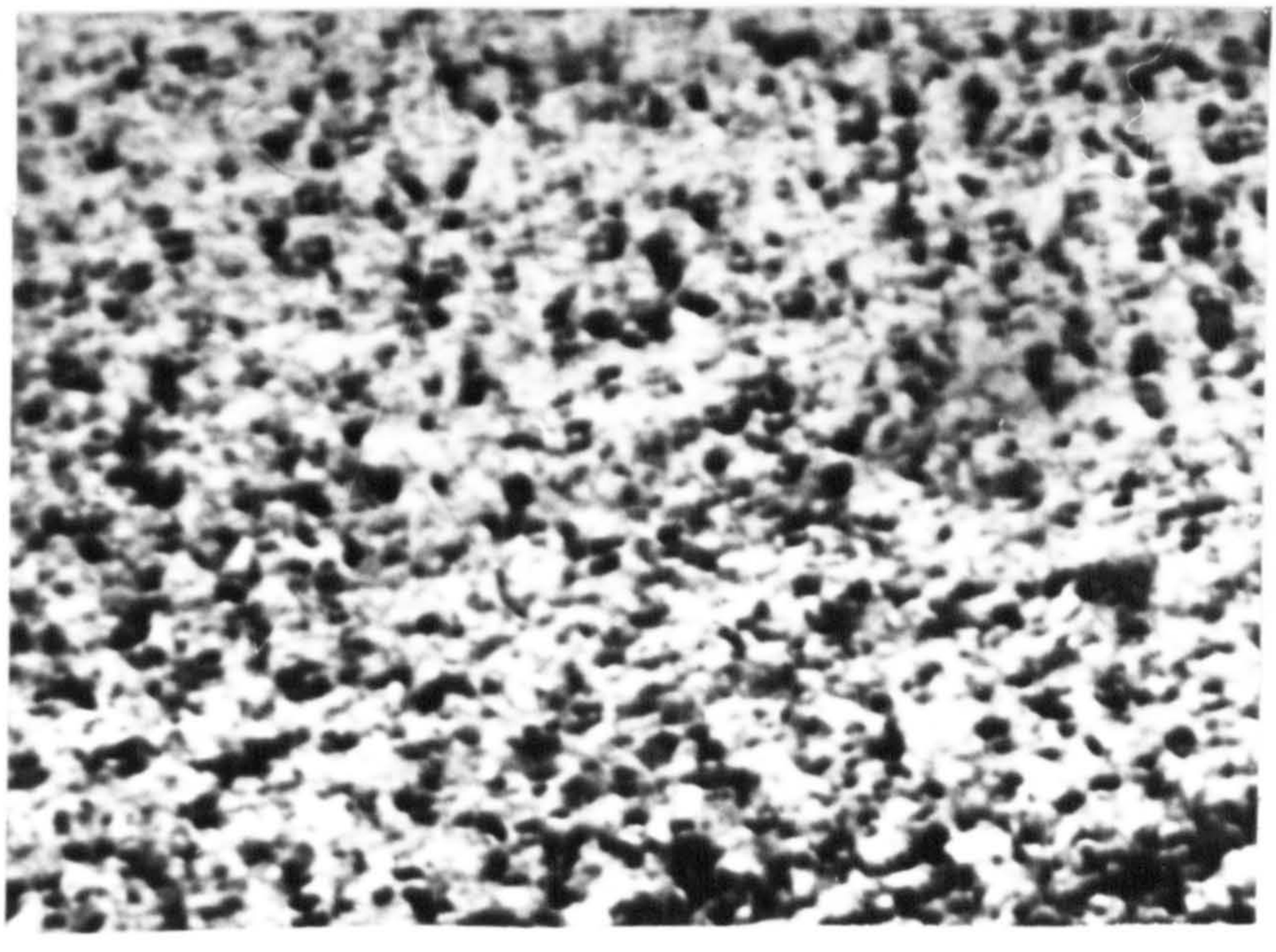

g [200]

forms on the nitrided and aged foil surface under reduced oxygen pressures does in fact nucleate on the incoherent nitride particles. An un-nitrided foil was oxidised under similar conditions to the nitrided and aged foil. No surface oxide developed, even after oxidation for 1h at 450°C but particles did develop within the foil and Figure VIII.7(c) shows the microstructure after 45min. The particles are finely distributed and have large strain fields associated with them (shown by the dark contrast lobes on either side of the particles lying perpendicular to the [200] $\underline{g}$ vector in Figure VIII.7(c)). The observations are interpreted as being due to internally oxidised titanium particles. Internal oxidation is commonly observed (see Hauffe, 1965) when oxygen dissolved in a relatively noble matrix reacts with less noble alloying elements (Class I(a)(1) of Wood's classification; see section III.4).

The absence of surface oxidation of the un-nitrided foil during the in-situ oxidation experiments is a consequence of the reduced oxygen pressure such that all the oxygen present is consumed by internal oxidation. Prolonged exposure under the same conditions will result in complete oxidation of the titanium within the iron matrix, and only then will oxygen react with the iron to cause surface oxidation. Indeed, the nucleation and growth of surface oxide may then be influenced by the internally oxidised Ti-O particles in a similar way to that observed with internally nitrided alloys.

(b) Ex-situ conventional TEM

Ex-situ experiments on the oxidation of

nitrided and aged Fe-Ti specimens indicate that an oxide nucleation mechanism similar to that observed in the H.V.E.M. experiments occurs during atmospheric air oxidation; see Appendix (Coates & Hendry, 1979). A foil of Fe-0.15w/oTi, nitrided and aged to produce a stable distribution of TiN particles in ferrite, was oxidised and then electrochemically polished from one side to produce a thin foil with the oxide still intact. Figure VIII.8 is a dark-field micrograph from an oxide reflection showing small oxide particles in light contrast (about 250 Å in size) and an adjacent area of metal containing nitride particles out of contrast. The inset is a bright-field micrograph of the area containing the TiN particles which have a similar size and shape to the oxide particles.

VIII.5 Discussion

The metallographic evidence from thermally cycled specimens shows that the adherence of the oxide to the substrate on the un-nitrided material is poor due to voidage within the inner oxide layer. On the as-nitrided specimen the scale is unable to resist the stresses caused during final cooling to ambient temperature and spalls extensively, but the oxide on the nitrided and aged specimen is very adherent and is resistant to similar stresses.

The oxidation kinetics are at variance with the metallographic observations. The oxidation rates for the annealed and the as-nitrided specimens during thermal cycling between 240^{o} and 480^{o}C are relatively slow while that for the nitrided and aged alloy remains high and closely follows a parabolic law

Figure VIII.8

Dark field micrograph (TEM) of oxide on nitrided Fe-0.15Ti oxidised 1h at 420°C in air with inset bright-field micrograph of nitride particles.

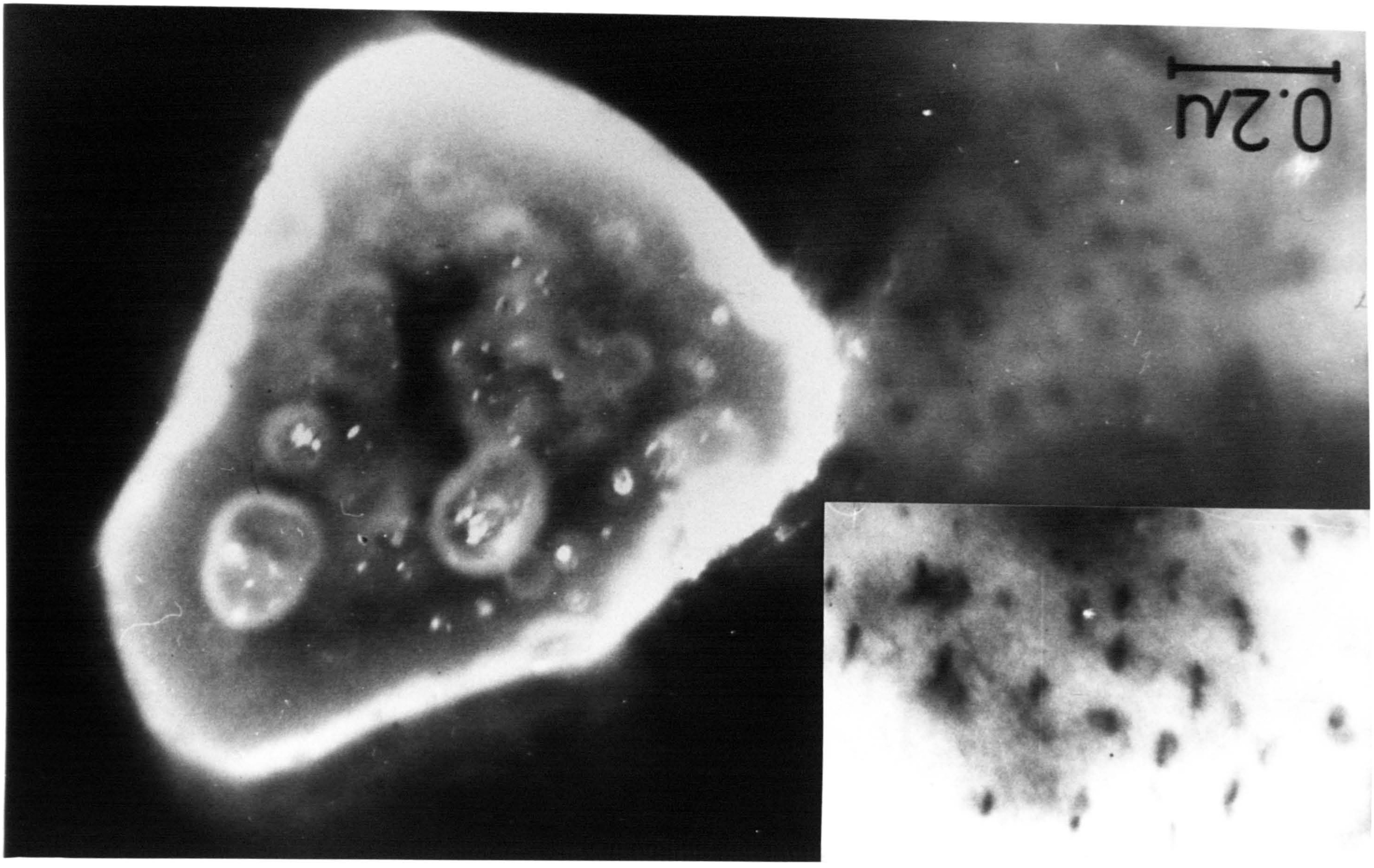
0.2μ

(as shown by the high r-coefficient of the parabolic rate constant). This is probably due to the development of voidage at the metal/oxide interface on the annealed and the as-nitrided specimens which, whilst not causing spalling, does cause a reduction in the interface contact area and thus a reduction in the metal cation flux. This also results in levelling off of the oxidation curves at long times and the relatively low r-coefficients of the parabolic rate constants. The behaviour of the nitrided and aged alloy is a consequence of the coherent metal/oxide interface (resulting from the TiN precipitates acting as vacancy sinks and thus inhibiting interfacial voidage) allowing unhindered metal-cation transfer into the oxide. The effect is similar to that found on nitrided mild steel (Chapter VI) and on nitrided iron-chromium (Chapter VII). No direct evidence of a change in the mechanism of oxide growth on nitrided Fe-Ti alloys to form an inwardly growing inner oxide layer has been found. However, the results are similar to those of nitrided mild steel and Fe-Cr and, by analogy, it is possible that a change in the mechanism also occurs in nitrided Fe-Ti alloys.

The in-situ oxidation experiments show that the first formed oxide does nucleate and grow on incoherent precipitates in the nitrided and aged alloy. As Fe_3O_4 grows by outward diffusion of metal cations, this fine-grained oxide will remain next to the original metal/oxide interface and is expected to have a relatively high fracture strength; see section III.6. Metallography shows that the oxide grain size is finest at its inner edge and coarsens away from the metal/oxide interface. The observation of porosity in

the magnetite on the nitrided and aged alloy (Figure VIII.3(d)) shows that although scale separation does occur during thermal cycling the scale is strong enough to withstand fracture and remains protective. The observation of internal oxidation of the Fe-0.5w/oTi foil during low pressure oxidation raises the question of whether this mechanism occurs during oxidation at normal pressures but metallographic examination of oxidised Fe-0.5w/oTi, using a variety of etchants, and also micro-hardness measurements, have not revealed any evidence of an internal oxidation zone ahead of the external oxide scale.

Chapter IX

THE OXIDATION OF IRON-MOLYBDENUM-NITROGEN ALLOYS

IX.1. Introduction

The oxidation of nitrided Fe-Mo was investigated concurrently with the work on Fe-Ti alloys (Chapter VIII). It is known (see section III.2) that small concentrations of Mo improve the oxidation resistance of iron at 600°-1000°C by the formation of Fe-Mo spinel phases near the metal/oxide interface. Nitriding of Fe-Mo has been extensively investigated at Newcastle (e.g. Speirs, 1969; Driver et al., 1972) and shows features similar to those of other Fe-X-N systems.

The Fe-5w/oMo (N.P.L. cast 39AF2) was cold rolled to about 500 μm and cut into 15x20mm coupons. Some material was rolled further to 150 μm foil and the coupons and foil were annealed in argon at 850°C for 6h.

IX.2. Nitriding Procedure

The kinetics of nitriding Fe-5w/oMo in $7NH_3:93H_2$ at 580°C are consistent with the internal nitriding equation (Hayes & Grieveson, 1975); see section II.5. Two nitriding procedures were used to

prepare (i) coherent Mo-N clusters and (ii) incoherent Fe_3Mo_3N precipitates. Nitriding in $7NH_3:93H_2$ at 580^oC produced a distribution of substitutional-interstitial clusters lying on $\{100\}$ matrix lattice planes. Specimens were nitrided for 18h and 150μm foil specimens showed a weight increase of 0.61w/o(= 2.44a/oN). The nitrided material thus had a Mo:N ratio of 1:0.9, which agrees with the value obtained for similar alloys nitrided at 580^oC in $10NH_3:90H_2$ (Hayes & Grieveson, 1975).

Aging of some coupons and foils was carried out at 720^oC in vacuum for 1h and subsequent X-ray powder diffraction showed that precipitation of the stable η -Fe_3Mo_3N phase had occurred. Figure IX.1 shows X-ray photographs of annealed, nitrided and nitrided and aged specimens. The diffuseness of the matrix lines of the nitrided, and the nitrided and aged specimens compared to the annealed specimen is clear and the presence of η -phase in the aged specimen is also apparent.

IX.3. Oxidation of Fe-Mo-N

Oxidation was carried out isothermally at 480^oC for 500h following the procedure described in section V.5(a). Repeat runs of up to 200h were made to check on the reproducibility of the curves and the results are shown in Figure IX.2. The curves for the annealed and the nitrided and aged specimens are very similar but those for the as-nitrided specimens are anomalous. In one run the oxidation rate was very similar to those of the un-nitrided and the nitrided and aged specimens,

Figure IX.1

X-ray powder photographs, Fe-5w/oMo, Co-Kα radiation,

(a) annealed

(b) nitrided in $7NH_3:93H_2$ at $580^{o}C$,

(c) nitrided in $7NH_3:93H_2$ at $580^{o}C$;
aged at $720^{o}C$ for 1h.

(a)

(b)

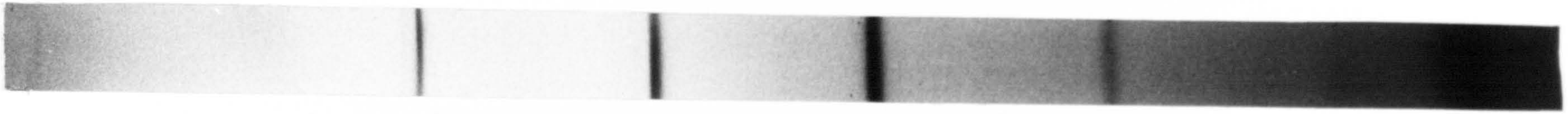

(c)

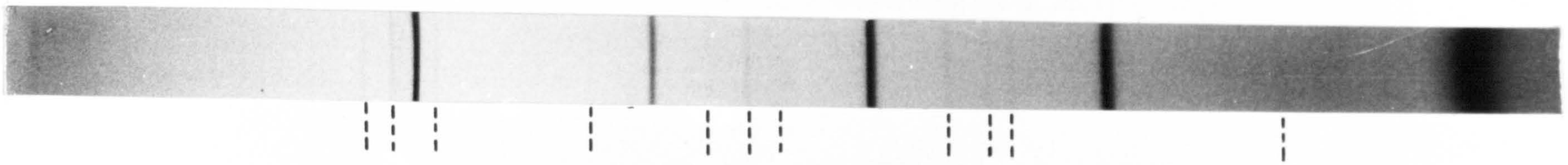

—— α-Fe

----- η-Fe_3Mo_3N

Figure IX.2

Oxidation curves of Fe-5w/oMo alloys oxidised isothermally at 480°C in air.

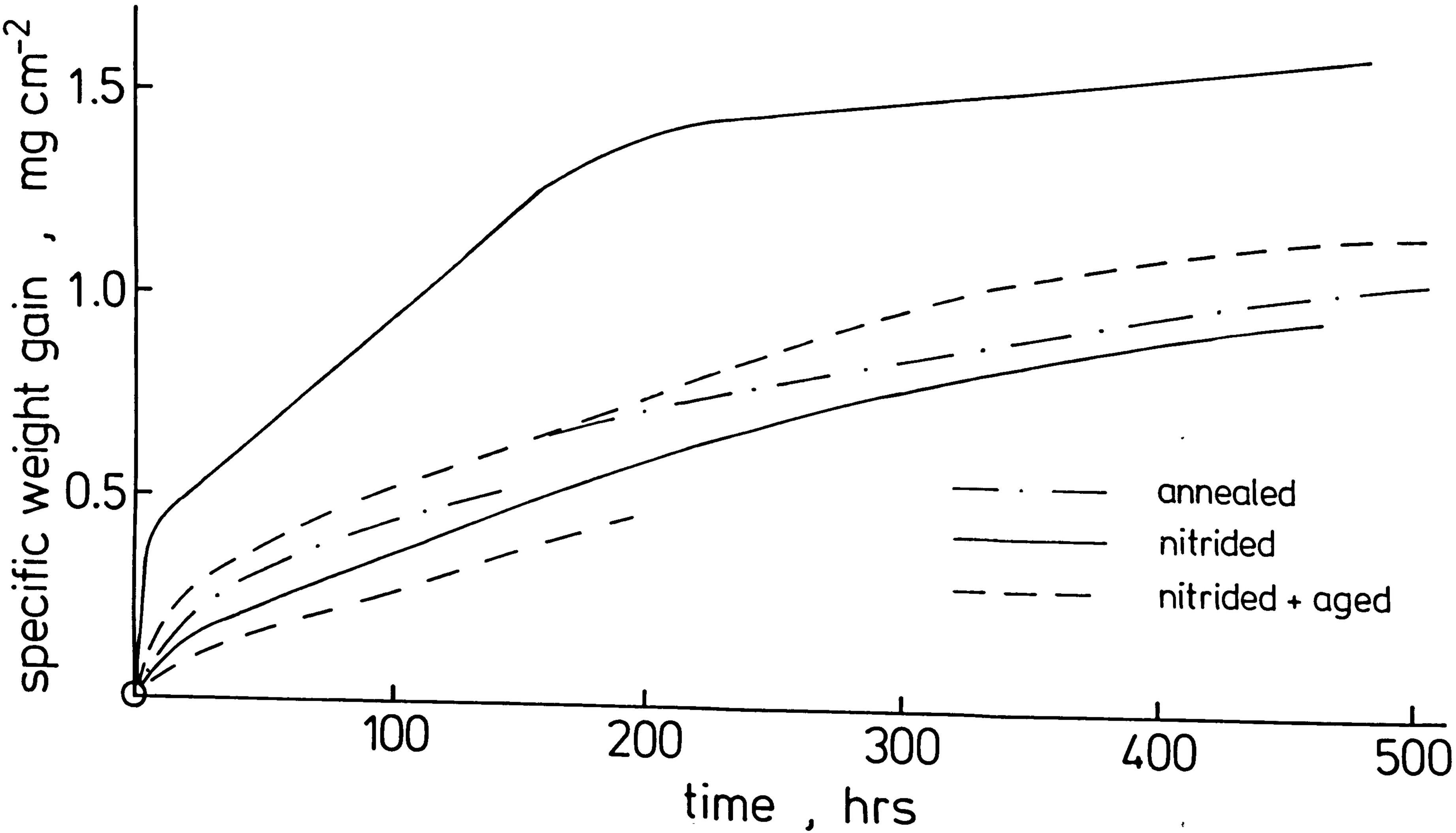
specific weight gain , mg cm^{-2}
1.5
1.0
0.5
100
200
300
400
500
time , hrs
annealed
nitrided
nitrided + aged

but in another run the rate was very rapid for the first 20h followed by a slower rate that nevertheless was still faster than that of the other specimens. The rate eventually slowed to one comparable with the other treatments after about 200h. The cause of the anomalous behaviour is not known.

When the specimens from all three treatments were removed from the thermobalance and allowed to cool in air, there was extensive spalling of the oxide. Figure IX.3 shows scanning electron micrographs of the edges of the spalled scales; the outer surface of the scale is uppermost in all of the micrographs. The scales from the as-nitrided alloy (b) and from the nitrided and aged alloy (c) are more compact than that from the un-nitrided alloy (a), although the scale in (b) shows porosity in a line parallel to its outer surface. It is possible that the oxide in (c) has spalled at the void-containing interface between an inner compact oxide layer and an outer porous layer if the mechanism of formation is the same as that with nitrided mild steel and Fe-Cr and Fe-Ti alloys.

Furnace-cooled specimens retained the oxide on their surfaces, although it could easily be removed mechanically. Figure IX.4 shows scanning electron micrographs of a nitrided Fe-5w/oMo specimen oxidised at 480°C. The X-ray dispersion micrographs (b) and (c) show a thin Mo-enriched band in the oxide next to the metal/oxide interface which is more clearly seen as a depletion of Fe in (c). Similar results were found with the un-nitrided and the nitrided and aged specimens. By X-rays the spalled oxide scale consists of haematite and magnetite, but some

Figure IX.3

Scanning electron micrographs of spalled oxides from Fe-5w/oMo oxidised isothermally at 480°C in air,

(a) annealed alloy,

(b) nitrided in $7NH_3:93H_2$ at 580°C,

(c) nitrided in $7NH_3:93H_2$ at 580°C; aged at 720°C for 1h.

(a)

10 μm

(b)

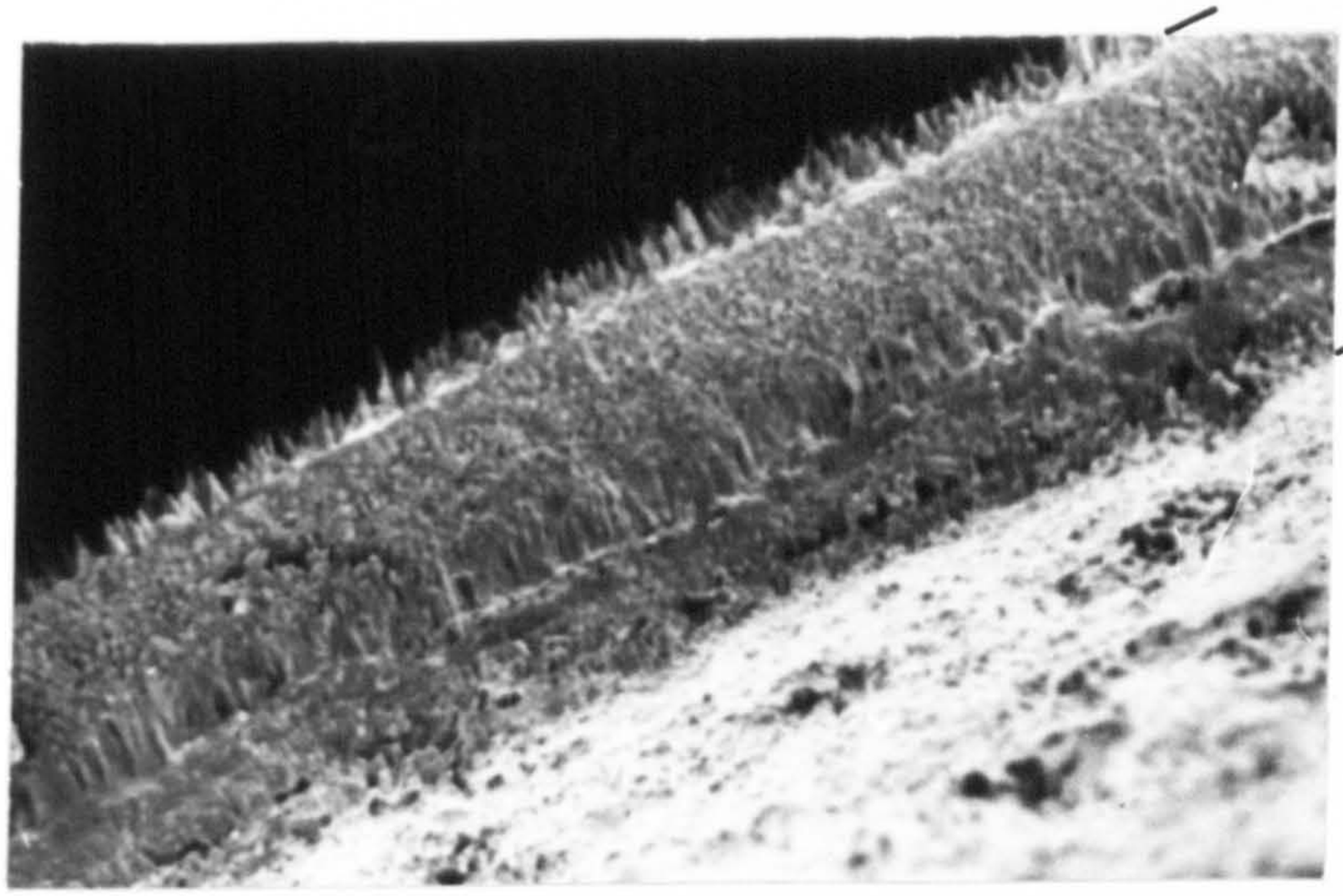

10 μm

(c)

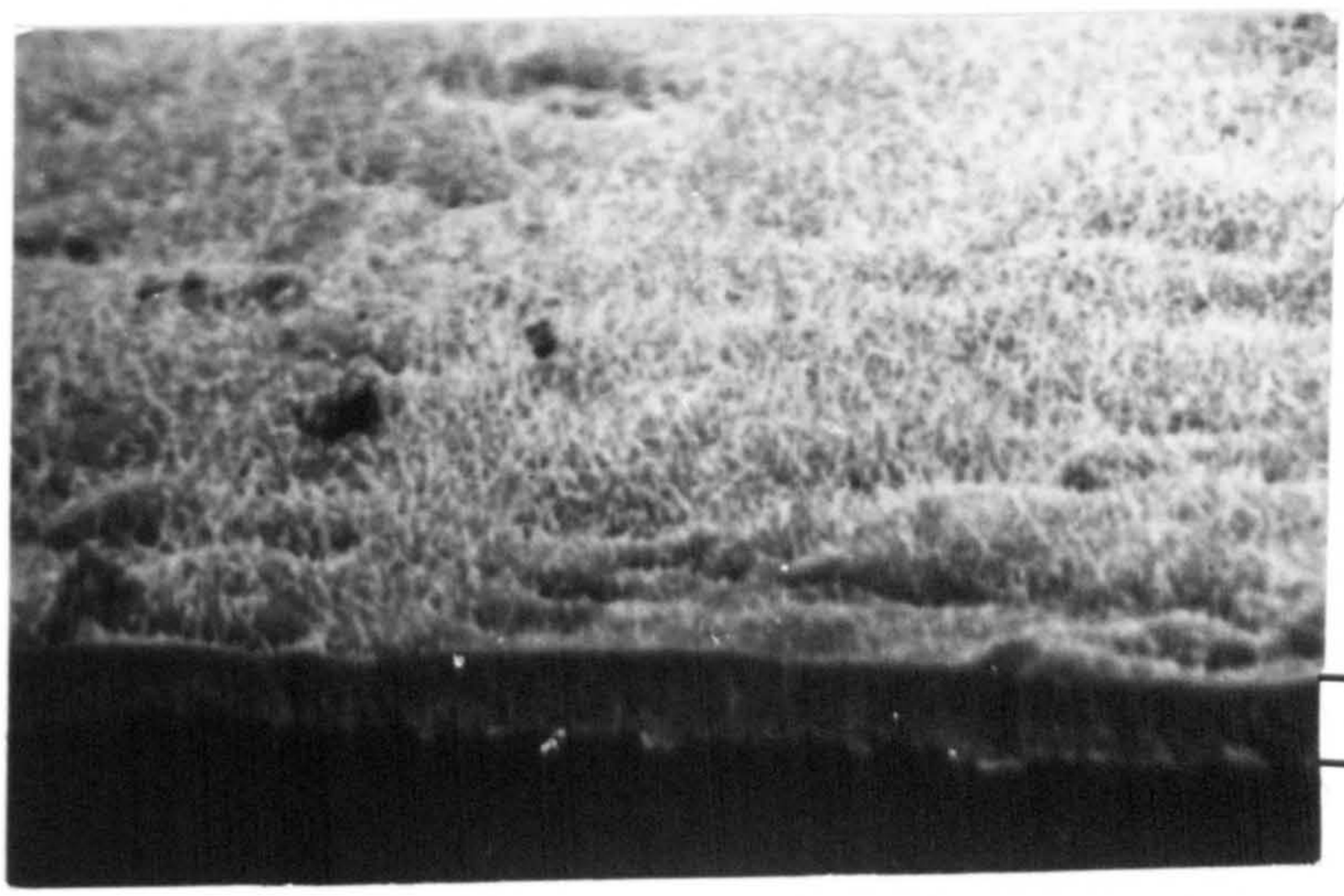

10 μm

Figure IX.4

Scanning electron micrographs of Fe-5w/oMo; nitrided in $7NH_3:93H_2$ at 580°C oxidised at 480°C for 500h in air,

(a) secondary electron image,

(b) Mo-Kα X-ray image,

(c) Fe-Kα X-ray image.

(a)

10 μm

(b)

(c)

reflections remain unidentified.

IX.4. In-situ (H.V.E.M.) Oxidation

In-situ oxidation experiments were carried out on thin foils in a high voltage electron microscope; see section V.9. Figure IX.5 shows transmission electron micrographs obtained from a nitrided and aged Fe-5w/oMo specimen oxidised at 480°C with $p_{O_2} \sim 10^{-4}$Pa(10^{-9}atm). (a) shows the structure at the oxidation temperature before injection of oxygen. The η-Fe_3Mo_3N precipitates take the form of discs, about 200 Å diameter, lying on the {100} planes of the ferrite matrix. (b) and (c) show the foil after 9 and 17 min oxidation, respectively. The initially formed oxide grains are elongated along the {100} ferrite planes, are about 200 Å in length (see arrowed grains), and are formed on η-Fe_3Mo_3N precipitates. As the grains grow they tend to lose their elongated form, but remain relatively small and result in a fine-grained oxide layer. Figure IX.6 shows similar transmission electron micrographs of in-situ oxidised iron foils. (a) is after 15 min oxidation and shows a few dislocations (the elongated features) which were also present before oxidation. The oxide grains on the surface of the foil are initially relatively small (about 300 Å diameter) and are generally equiaxed, but after only 45 min the foil is completely covered in oxide, with much larger grain sizes(up to 1000 Å diameter) as shown in (b).

Figure IX.5

Transmission electron micrographs (H.V.E.M.) of Fe-5w/oMo nitrided in $7NH_3:93H_2$ at 580°C; aged at 720°C for 1h; oxidised in-situ at 480°C,

(a) 0 min oxidation

(b) 9 min oxidation

(c) 17 min oxidation.

(a)

[010]

[100]

(001)

(b)

(c)

0.2 μm

Figure IX.6

Transmission electron micrographs (H.V.E.M.) of iron oxidised in-situ at 480°C,

(a) 15 min oxidation,

(b) 45 min oxidation.

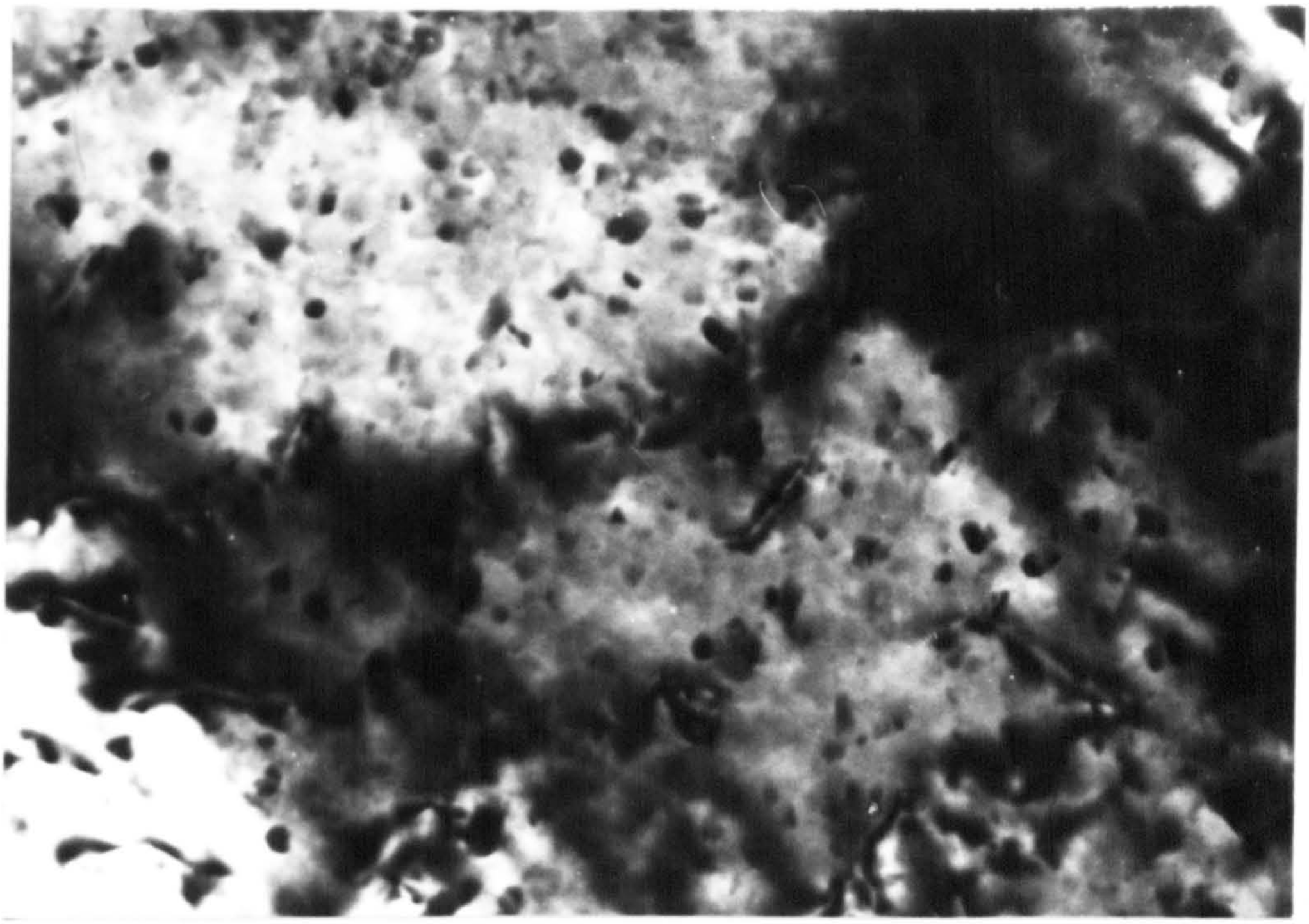

(a)

0.2 μm

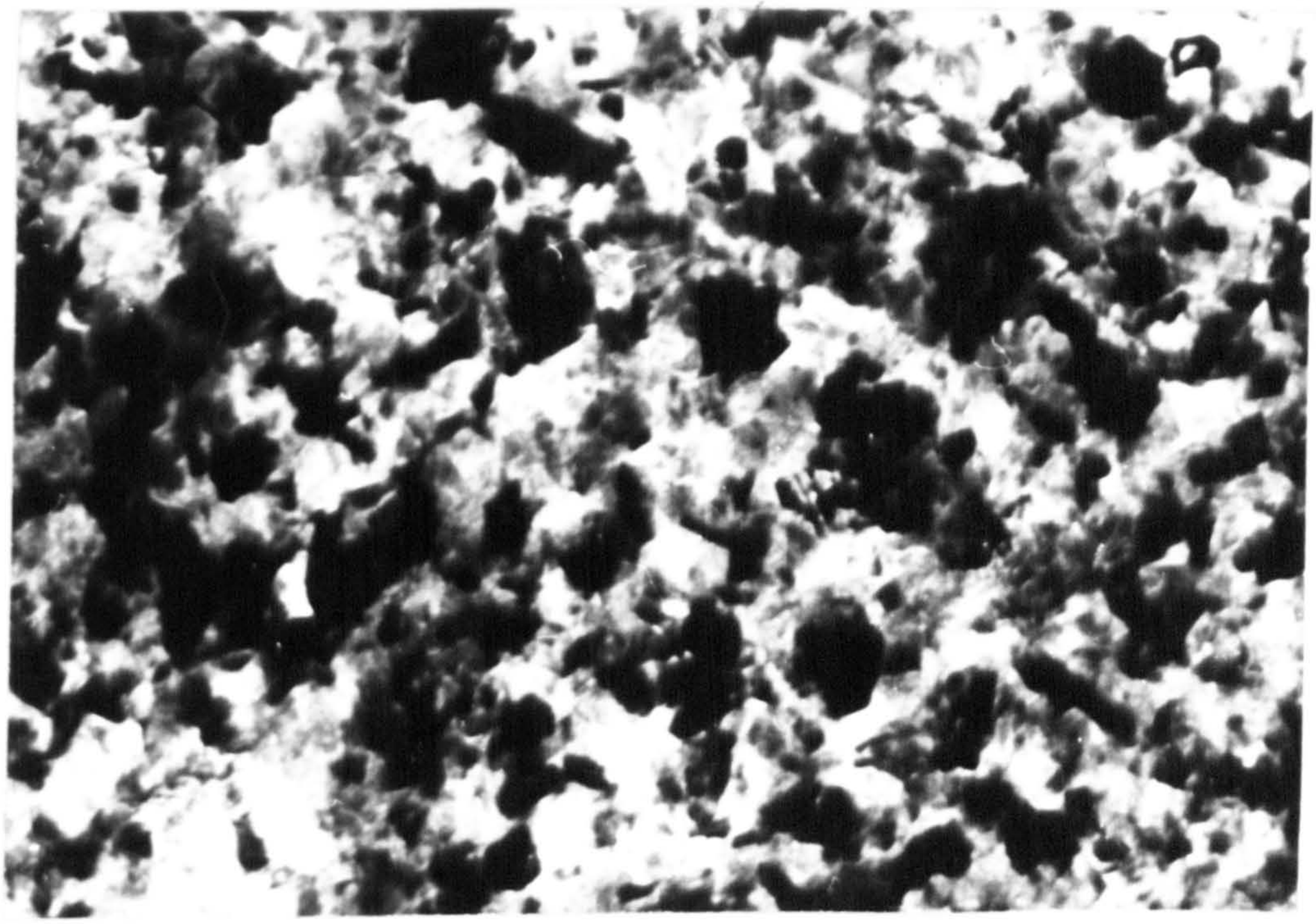

(b)

IX.5. Discussion

The oxidation rates show that the nitriding of Fe-5w/oMo has little effect on the weight gain during isothermal oxidation at 480°C, although the anomalous behaviour during one oxidation run emphasises the care that must be taken with the interpretation of kinetics results. The effects of nitriding and aging, although not showing any increase in the adherence of the oxide, are similar to those on nitrided mild steel (Chapter VI), on nitrided Fe-Cr (Chapter VII) and on nitrided Fe-Ti (Chapter VIII). In particular, the morphology of the oxide from nitrided Fe-5w/oMo shows a duplex structure with a porous outer layer and a compact inner layer, with a row of porosity at their interface; see Figure IX.3(b). The in-situ H.V.E.M. oxidation shows that oxidation of iron with dispersed Fe-Mo nitrides does involve nucleation and growth of the oxide grains on the nitride particles. It thus seems likely that the oxidation mechanisms of nitrided Fe-Mo at 500°C are similar to those found on other nitrided alloys, i.e. the formation of outer magnetite and haematite layers with an inner, fine-grained, inward-growing layer.

Chapter X

OXIDATION OF MILD STEEL IN $0.5SO_2:99.5N_2$

X.1. Introduction

The oxidation kinetics of nitrided and un-nitrided mild steel (Chapter VI) show that nitriding has little effect on the oxidation of mild steel under isothermal conditions, but causes more rapid oxidation under thermal cycling. These results are at variance with the work of Hendry (1978) who found that nitriding gave a much reduced rate of oxidation, especially with thermal cycling. However, the present investigations use laboratory air as the oxidant, whereas Hendry used a simulated flue gas ($N_2:15CO_2:0.3SO_2:10_2$).

The effect of sulphur dioxide is to produce iron sulphide, FeS, as well as the iron oxides found during oxidation in air (Flatley & Birks, 1971) and weight gains on iron specimens are greatly increased as a result of the enhanced diffusivity of iron through the FeS network. Flatley & Birks found that at temperatures below that at which wustite becomes stable (570°C) oxide and sulphide form simultaneously, initially as a fine spheroidal distribution of iron sulphide in a matrix of magnetite. At a later stage, scale cracking occurs and massive sulphides form within the magnetite. The presence of a massive sulphide inclusion increases the ionic transport properties of the scale in that region and further

enhanced growth occurs producing a columnar outgrowth of an oxide-sulphide massive duplex structure on the surface of the scale. Eventually the outgrowths occur all over the scale surface and merge to form a complex scale.

X.2. Oxidation Procedure and Results

Coupons measuring about 10x10x1mm were prepared from annealed mild steel. Some of the coupons were nitrided in $5NH_3:95H_2$ at 700^oC to form an α'-martensite plus γ-austenite structure. The $0.5SO_2:99.5N_2$ gas mixture (from B.O.C.) was used direct from the cylinder at a flow rate of 6 l h^{-1} as used by Flatley & Birks (1971).

Isothermal runs on annealed and on nitrided specimens were carried out at 500^oC for 150h. The total weight gain of the un-nitrided specimen was 8.4mg cm^{-2} and the scale spalled completely from the metal when the specimen was removed from the furnace. The total weight gain of the nitrided specimen was 9.4mg cm^{-2}. The scale remained adherent on cooling, but was not very tenacious and was easily removed mechanically.

Thermal cycling runs on similar specimens were carried out as in section V.5(b). The oxidation weight gain curves are plotted in Figure X.1 and compared with results for the similar oxidation of mild steel (Robinson & Flatley, 1976). All three curves are similar, considering the wide range of scatter noted by Robinson & Flatley. Figures X.2

Figure X.1

Oxidation of annealed and nitrided (in $5NH_3:95H_2$ at $700^{\circ}C$) mild steel in $0.5SO_2:99.5N_2$ cyclically from $500^{\circ}C$ to room temperature.

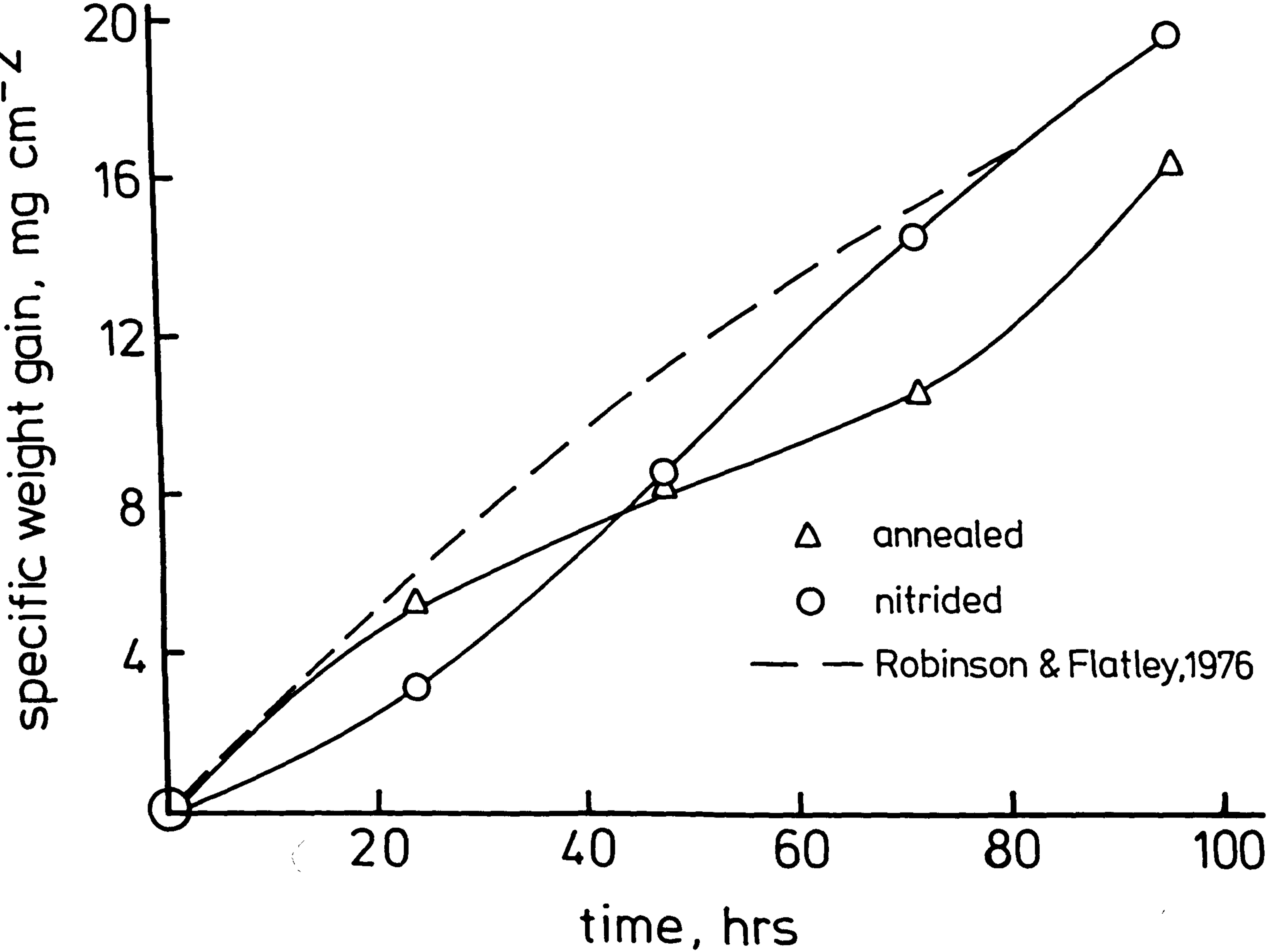
specific weight gain, mg cm^{-2}
20
16
12
8
4
20
40
60
80
100
time, hrs
annealed
nitrided
Robinson & Flatley, 1976

and X.3 show scanning electron micrographs of the annealed and the nitrided specimens respectively. The scale on the annealed material is in layers with an inner,porous layer about 20μm thick next to, but detached from, the metal substrate (Figure X.2). Above this is an 80μm thick columnar layer which is similar to that formed by the outgrowths of duplex sulphide-oxide reported by Flatley & Birks (1971). Separated from this is another stratum showing a similar morphology to the columnar layer. The number of separated scale strata corresponds to the number of thermal cycles which the sample has experienced (4) and the sulphur distribution in the scales is uniform; see Figure X.2(b). The morphology of the scale on the nitrided specimens (Figure X.3) is similar to that on the un-nitrided steel, except that the inner (25 μm thick) layer is very compact. The scale again shows separated strata corresponding to each thermal cycle and the sulphur content is again uniform through the scale (Figure X.3(b)).

X.3. Discussion

The results of thermal cycling of nitrided and un-nitrided mild steel in gases containing sulphur dioxide again show differences between the weight gains and the metallographic observations in that whilst the inner oxide-sulphide layer on the nitrided specimen appears very compact (in contrast to the porous inner layer on the un-nitrided steel) there is apparently no reduction in the scaling rate. The scale spalls from the metal surface during each thermal cycle on both the nitrided and the un-nitrided mild steel and

Figure X.2

Scanning electron micrographs of mild steel thermally cycled from 500°C to room temperature in $0.5SO_2:99.5N_2$,

(a) secondary electron image,

(b) S-Kα X-ray image,

(c) Fe-Kα X-ray image.

(a)

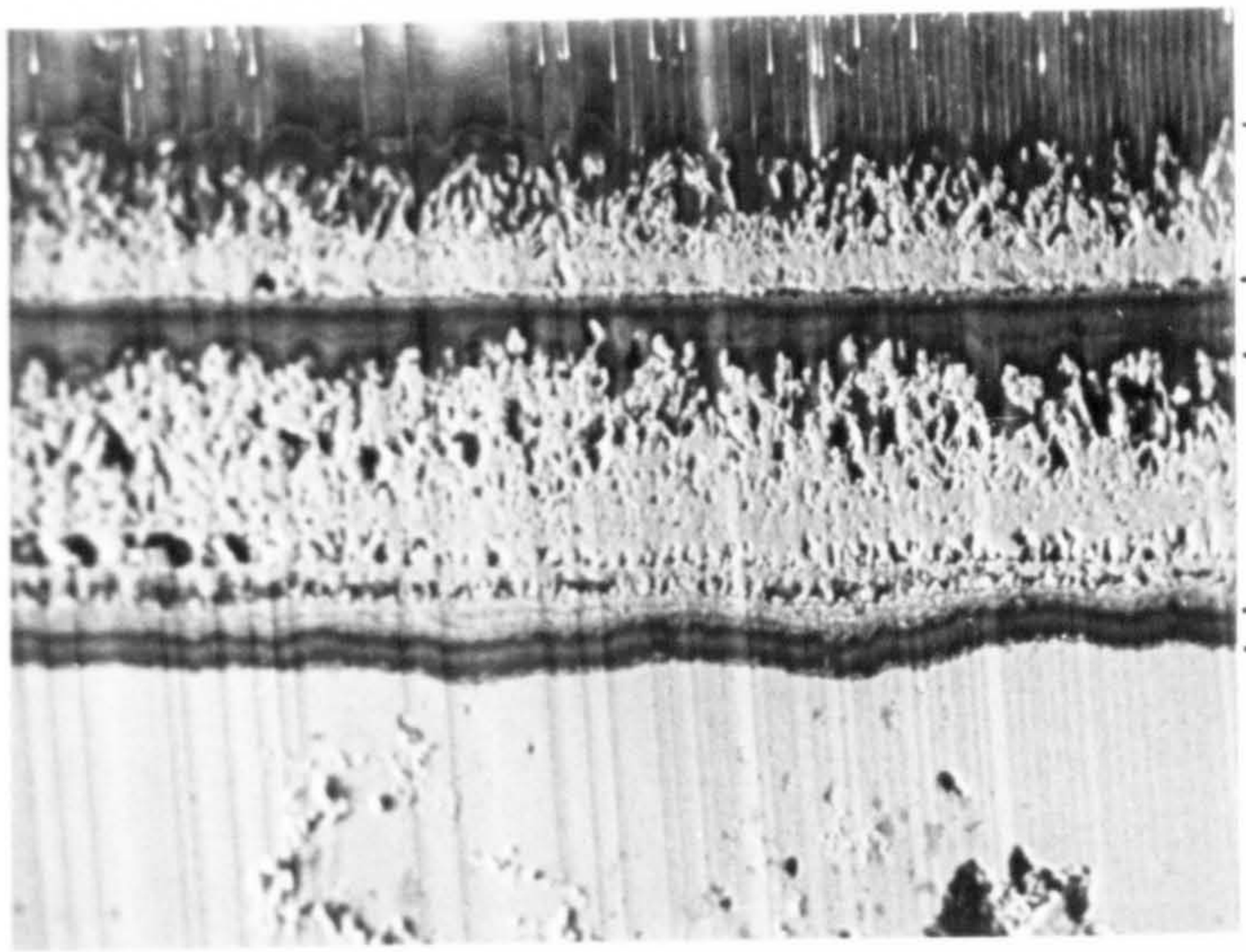

(b)

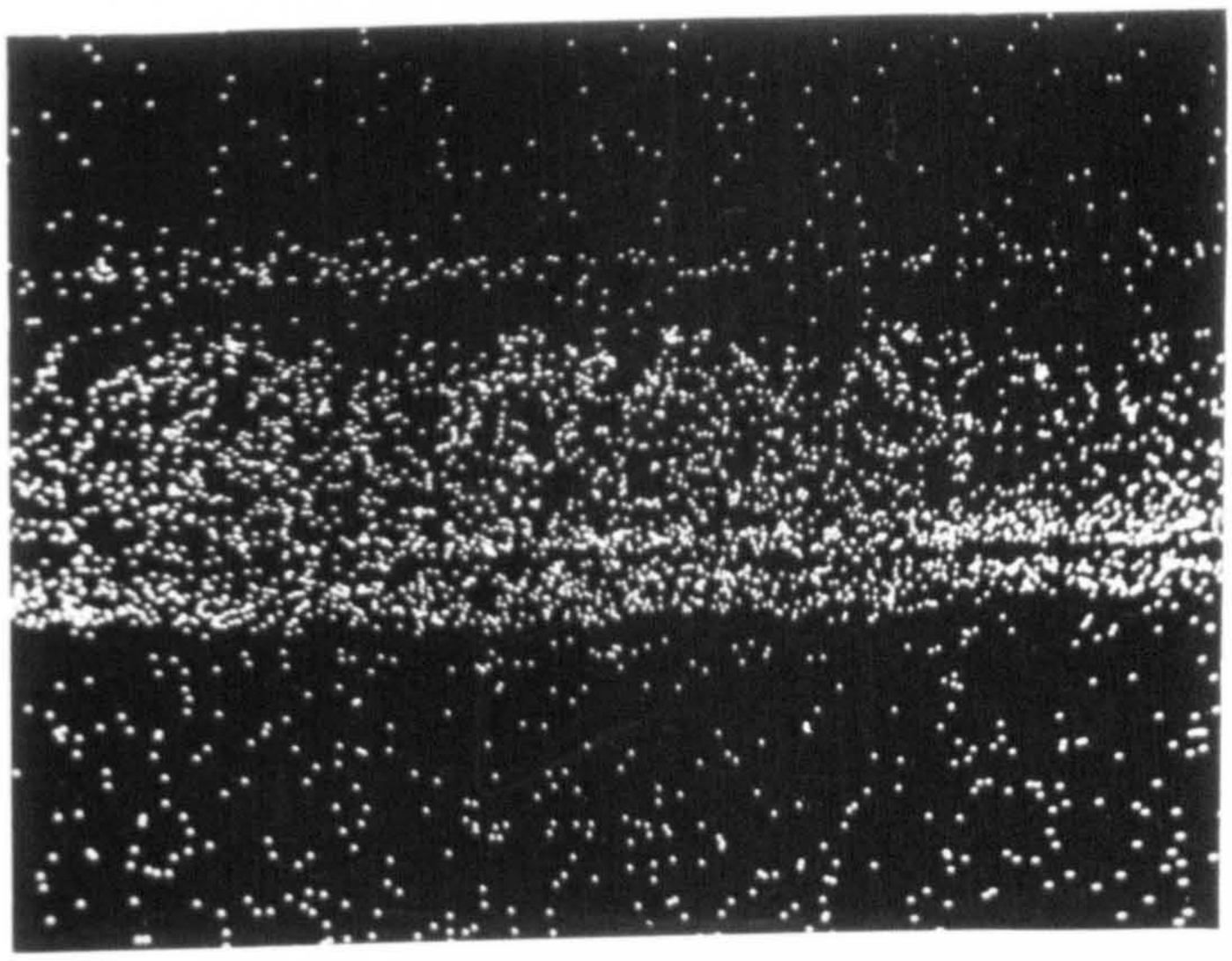

(c)

Figure X.3

Scanning electron micrographs of nitrided mild steel (in $5NH_3$:$95H_2$ at 700°C) thermally cycled from 500°C to room temperature in $0.5SO_2$:$99.5N_2$.

(a) secondary electron image,

(b) S-Kα electron image,

(c) Fe-Kα electron image.

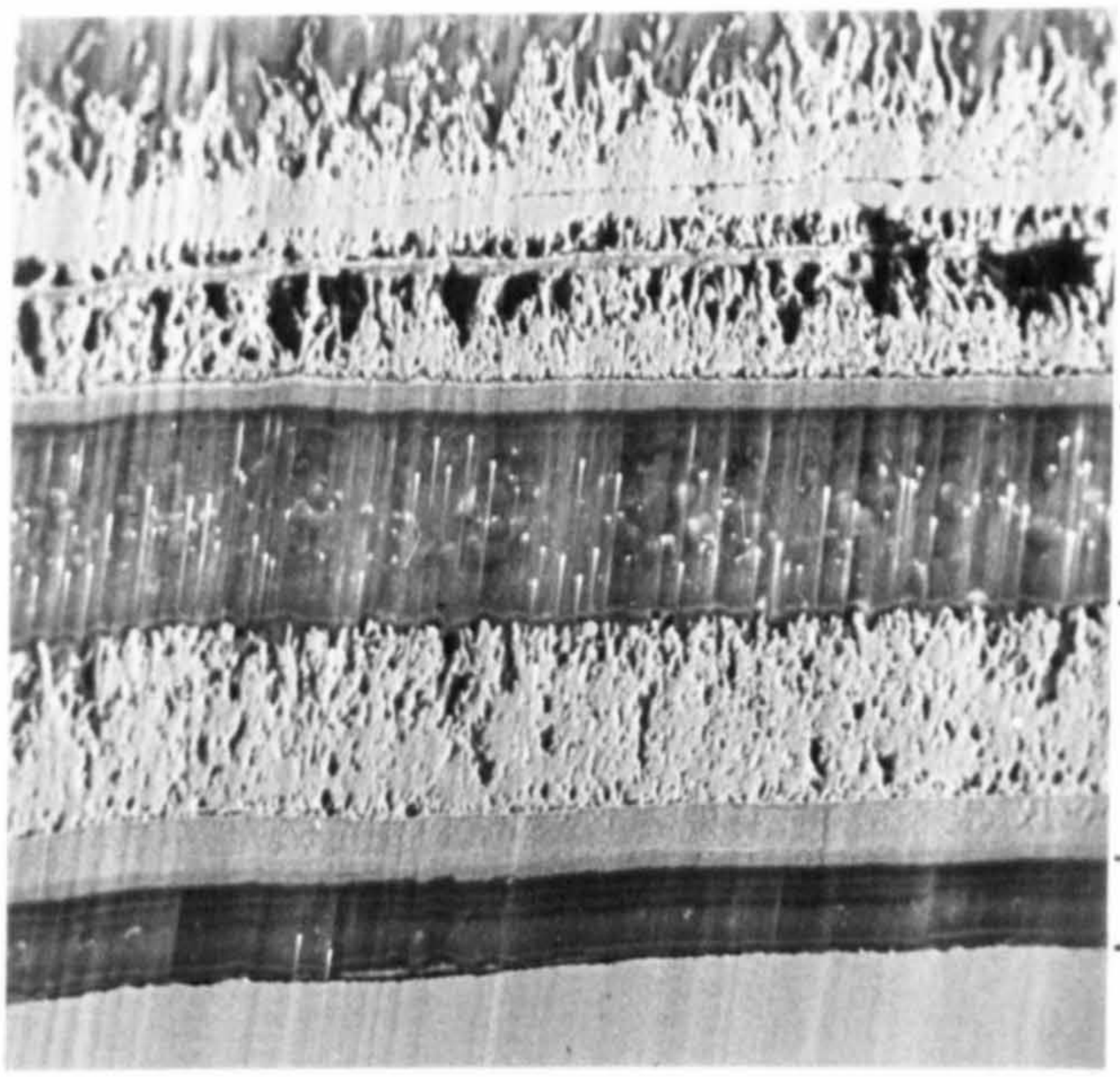

(a)

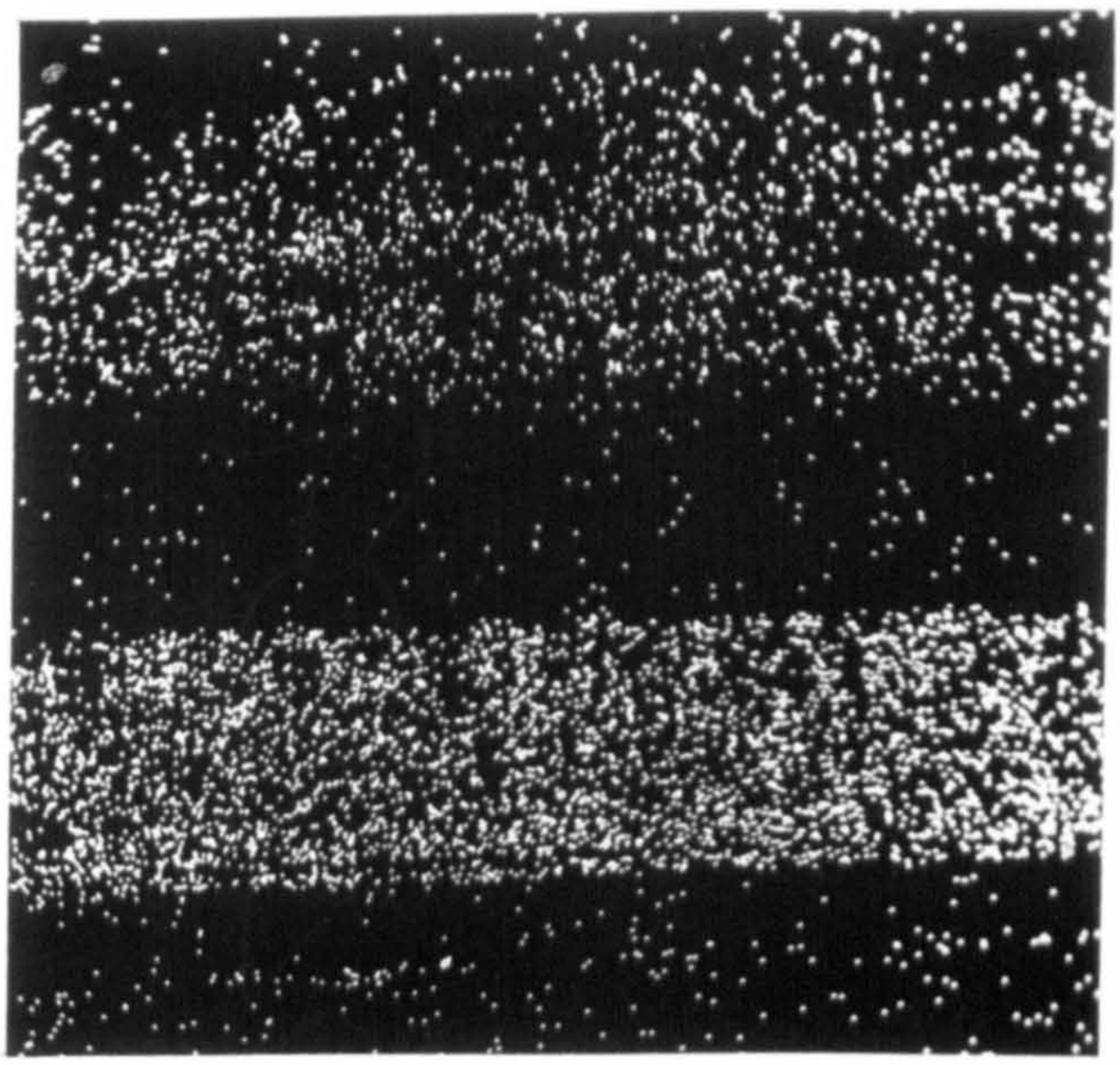

(b)

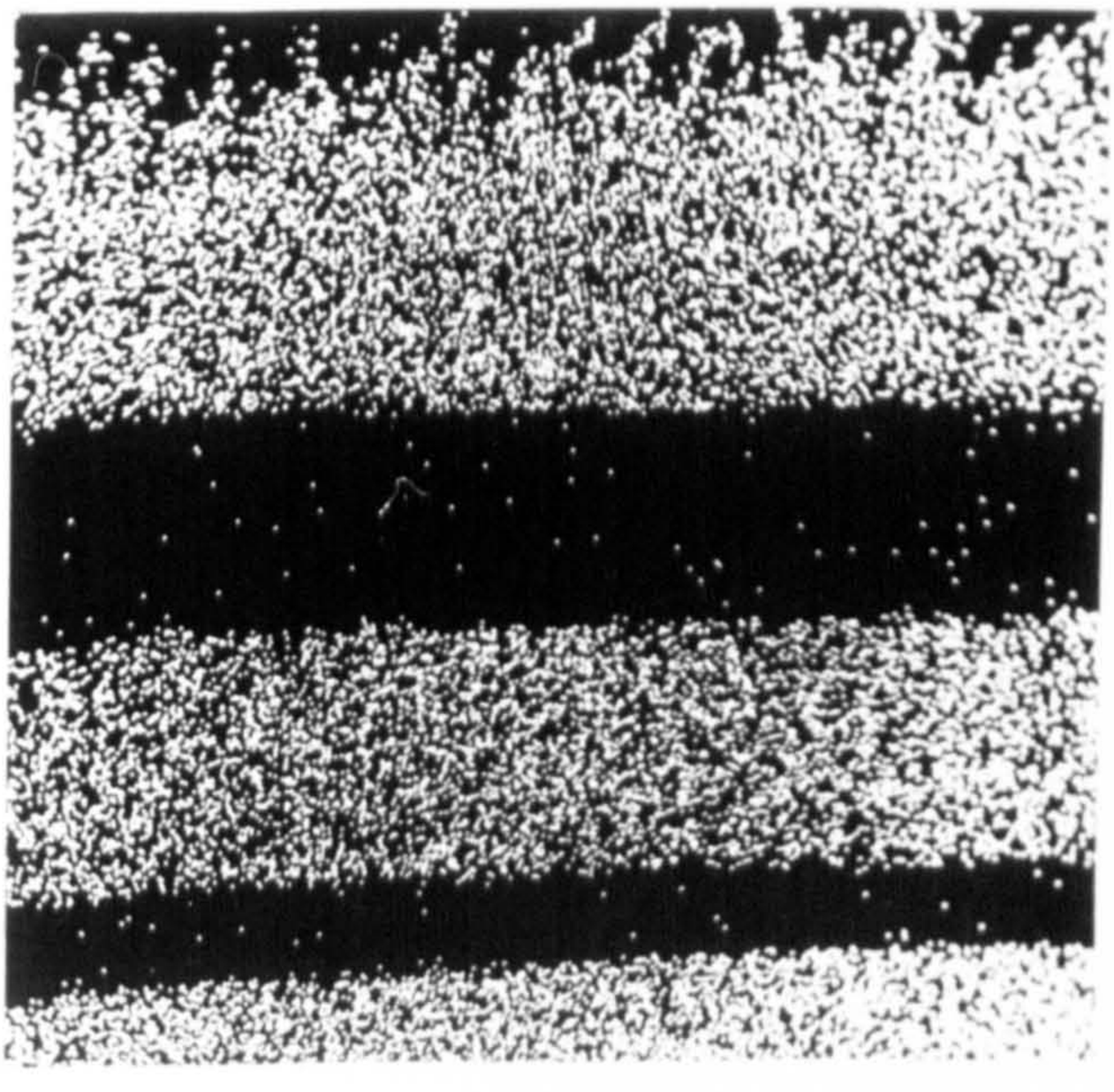

100 μm

(c)

allows oxidant to reach the metal surface, resulting in the high oxidation rates observed. This is in contrast to the results of Hendry (1978) who found that nitriding reduced the scaling rates on mild steel during thermal cycling between 240^{o} and 480^{o}C. He also found that there was a higher concentration of sulphur in the scale next to the metal/scale interface than in the outer scale but this is not confirmed by the present investigation.

The results of the present work are not directly comparable with Hendry's for a number of reasons. Holmes & Pascoe (1972) have listed those parameters important for spalling resistance during thermal cycling (see section III.5) and the following are thought to be relevant to the differences between the two investigations:

(i) the magnitude of the thermal cycle.

The temperature difference used in the present investigation was about 470^{o}C whereas that used by Hendry was 230^{o}C. Also, the present upper hold temperature was 500^{o}C whereas Hendry's was 430^{o}C.

(ii) the rate of change of temperature.

Hendry used 8^{o}C min^{-1} for heating and cooling whereas that of the present investigation, although not recorded, is likely to have been greater. Furthermore, the total cycle time may be important. Hendry used a 1h upper hold time with a 2h cooling and heating cycle whereas in the present investigation the upper hold time was 22h with a cycle time of 2h.

One other parameter relevant to the present work is the partial pressures of the reactive

constituents of the gas (sulphur and oxygen). The equilibrium in the gas phase may be regarded as

$$SO_2 = 1/2\ S_2 + O_2 \quad \ldots\ X.1$$

for which $\Delta G^{\circ}_T = -RT \ln (p_{S_2}^{\frac{1}{2}} \cdot p_{O_2} / p_{SO_2})$ X.2

Under the conditions of the present investigations, $p_{SO_2} = 5x10^{-3}$atm ($5x10^2$Pa) and T = 773K, substituting the value of free energy change (Kubaschewski & Alcock, 1979) in equation X.2 gives $p_{S_2} = 2.9x10^{-16}$atm ($2.9x10^{-11}$Pa) and $p_{O_2} = 5.7 x 10^{-16}$atm ($5.7x10^{-11}$Pa). Hendry (1978) used a gas mixture of $N_2:15CO_2:0.3SO_2:1O_2$, i.e. $p_{SO_2} = 3x10^{-3}$atm ($3x10^2$Pa) and $p_{O_2} = 1x10^{-2}$atm ($1x10^3$Pa), at 430°C (703K). Substituting these values in equation X.2 gives a partial pressure of sulphur, $p_{S_2} = 2.6x10^{-48}$atm ($2.6x10^{-43}$Pa). Thus the partial pressure of sulphur is much greater, and that of the oxygen much less, in the gas used in the present investigation than in that used by Hendry. The differences between the partial pressures of the reactants may influence the rate of the oxidation-sulphidation reactions, although the presence of FeS in the scales on both un-nitrided and nitrided mild steel in the present investigation and that of Hendry (1978) indicates that the actual reactions remain unchanged.

The discrepancy between the two investigations is thought to be a consequence of one or more of the factors outlined above but the exact reason is not known.

Chapter XI

GENERAL DISCUSSION

The effects of nitriding on the oxidation of nitrided iron and iron alloys can be summarised as:

(i) elimination of voidage at the metal/scale interface, increasing the metal/scale adherence;

(ii) nucleation of fine grained oxide on dispersed nitrides;

(iii) formation of an inner oxide layer which grows by inward diffusion of oxygen;

and, (iv) an increase in thermal cycling oxidation rates.

The N-martensite case formed on nitrided mild steel ages rapidly at oxidation temperatures giving a fine distribution of δ'-Fe_4N in a ferrite matrix and low pressure oxidation shows that oxide nucleates and grows on the nitride particles (section VI.6). The subsequent growth of oxide gives an adherent, inner and inward-growing, compact magnetite layer and an outer, porous, outward-growing magnetite layer with voidage at their interface; an outer haematite layer is also formed. The effects of dispersed incoherent nitrides in the substrate are analogous to those of Ni-Cr alloy containing dispersed rare earth oxides (Stringer et al., 1972) and in other dispersoid-containing alloys;

see section III.8. The explanation is thought to be that the increased number of oxide nuclei on the nitrided substrate gives oxide with a finer grain size and this reduces the number of short circuit diffusion paths for iron cations (e.g. dislocations) and increases those for oxygen transport (e.g. oxide grain boundaries). Thus, a scale-forming reaction occurs at the alloy/scale interface, reducing the amount of voidage due to cation vacancy condensation. As the outer, outward-growing oxide continues to grow with time, cation diffusion outwards and reaction at the magnetite/haematite interface must continue, so that an inwards flux of vacancies must still occur. The dispersed incoherent particles are thought to allow the inwardly flowing vacancies to condense at the particle/matrix interface, rather than at the metal/scale interface, further reducing the tendency for vacancy condensation and void formation at the metal/scale interface.

The nitriding of binary Fe-X alloys to produce a dispersion of incoherent nitrides in a ferritic matrix produces similar effects on the oxidation of the alloys to those obtained by nitriding of mild steel. The voidage at the oxide/metal interface on Fe-Cr alloys oxidised at 500°C in air is eliminated on alloys nitrided to give dispersed CrN precipitates (see Chapter VII) and an inner, inward-growing iron-chromium spinel layer is formed. However, a similar layer is also found on the un-nitrided alloy. The adherence of the scale layers on Fe-Ti alloys is also improved by nitriding to give incoherent nitride dispersions (Chapter VIII). In-situ oxidation in a high-voltage electron microscope shows that the oxide nucleates on the titanium nitride

precipitates. At normal oxidation pressures this gives a fine-grained inner oxide layer which is adherent to the substrate. In nitrided Fe-Mo alloys, incoherent nitrides in the substrate also result in the nucleation and growth of fine-grained oxide layers (Chapter IX). It is proposed that the mechanisms of nucleation and growth of the fine-grained, inwardly-growing oxide layer formed on nitrided binary Fe-X alloys are analogous with the mechanisms described for the oxidation of nitrided mild steel.

Other consequences of nitriding on the subsequent oxidation behaviour of the alloys may be relevant, one being an influence on the plastic deformation of the scale. If plastic deformation of the oxide is controlled by Herring-Nabarro creep or Coble creep, then the strain rate in the oxide, and hence the ability of the oxide to accommodate stress, is proportional to the reciprocal of the square of the grain diameter (equation III.5) or the reciprocal of the cube of the grain diameter (equation III.6) respectively. Thus, a fine-grained oxide layer will be better able to accommodate growth or thermal stresses than an oxide of coarser grain size. The "key-on" effect considered for some dispersoid-containing alloys (section III.8) may apply to nitrided Fe-Cr alloys where CrN precipitated at the substrate grain boundaries may physically peg the oxide to the metal, thus improving the spalling resistance. However, the dispersed nitrides in the alloys considered are probably too small to give keying effects. The "blocking" mechanism proposed by Giggins & Pettit (1971; see section III.8) is not thought to be applicable in the present work because the nitrides

are oxidised during the oxidation of the alloys and do not accumulate at the metal/oxide interface. Also, this mechanism does not explain inhibition of voidage at the metal/oxide interface as found in the present work.

The improved adherence of the oxides to the nitrided substrates is at variance with the observed oxidation rates of the alloys. During thermal cycling of mild steel and of Fe-Cr and Fe-Ti alloys, the weight gains are greater for the dispersed-nitride-containing substrates than for the un-nitrided and the clustered alloys. This is thought to be a consequence of the reduction in interfacial voidage on the dispersoid-containing alloys allowing un-restricted cation transfer from the metal to the oxide. Although the interfacial adhesion is improved, the oxidation conditions are not sufficiently aggressive to cause spalling of the scales on the un-nitrided alloys and consequently no benefits of the improved adhesion are noted. The oxidation runs were short compared to the expected exposure times in commercial practice and the improved adherence of the oxide to the substrates may be increasingly beneficial under long-term oxidation or in more aggressive environments. Further investigations are needed to establish the relative merits of nitriding on the in-service oxidation resistance of mild steel and iron alloys.

The oxidation rates in the present work have not shown the improvements that were anticipated but the increased oxide adherence suggests that the effects of incoherent nitrides in the substrate on oxide properties may lead to improved oxidation resistance under specific conditions.

APPENDIX

Influence of nitrogen on oxidation resistance of low-alloy steels

by

D.J. Coates and A. Hendry

Reprinted from

Metal Science, 1979, 13, 315-319.

Influence of nitrogen on oxidation resistance of low-alloy steels

D. J. Coates and A. Hendry

The oxidation resistance of mild steel is shown to be considerably enhanced by additions of nitrogen which result in the formation of an adherent fine-grain-size oxide scale. A mechanism is proposed by which improved protection results from enhanced nucleation of oxide at incoherent nitride particles in the surface metal layer. A suitable nitrided surface is formed by constant activity ageing in an $NH_3 : H_2$ gas mixture to form austenite at nitriding temperature. The resulting austenite + martensite microstructure tempers rapidly during oxidation at 420°C forming incoherent Fe_4N precipitates which act as oxide nucleation sites. Similar results have been obtained from studies of iron alloys containing small additions of titanium. Formation of a surface layer containing a fine dispersion of titanium nitride particles in a ferrite matrix is shown to enhance oxidation resistance.

The proposed mechanism is similar to that of the development of improved oxidation resistance in superalloys by subsurface dispersion of incoherent stable oxide particles.

Contribution to a conference on 'Residuals, Additives, and Material Properties' held at The Royal Society, London, on 15–17 May 1978. D. J. Coates, BSc, and A. Hendry, BSc, PhD, MInstP, are in the Crystallography Laboratory, The University, Newcastle upon Tyne, Mr Coates was awarded the Galloway Medal of the Institution of Corrosion Science and Technology for his contribution to this paper.

Fireside corrosion of mild steel boiler tubes in coal-fired power generating plant can result in premature tube failure with a consequent costly loss of generating time. Solutions to this problem have been sought through the use of replacement steels of higher alloy content (for example, $2\frac{1}{4}$Cr–Mo and 9Cr–Mo) or by coating mild steel tubes with an oxidation-resistant material. Metallic coatings in the form of flame-sprayed alloys or co-extruded tubing are generally expensive, and ceramic coatings such as silica or silicon carbide have proved unsuccessful because they are not sufficiently adherent to withstand the stresses imposed during fabrication and service.

The problems of cost and integrity of the metal surface may be solved simultaneously by application of the principles of internal nitriding, Hendry[1] and Lehrer,[2] Fig. 1. By suitable choice of temperature and nitriding potential ($NH_3 : H_2$ ratio) it is possible to nitride iron to form a surface layer which is completely austenitic (γ) at nitriding temperature without forming iron nitride (γ' or ε) on the surface. On cooling to room temperature the austenite transforms to a surface layer of nitrogen martensite (α') and retained austenite. Nitrided mild steel combines the strength of martensite, within an integral surface layer of metal, with enhanced corrosion resistance and can be formed using existing heat treatment technology at very low cost.

The results[1] of laboratory oxidation tests on nitrided mild steel in simulated flue gas* ($N_2 + 15CO_2 + 0{\cdot}3SO_2 + 1O_2$) are summarized in Fig. 2. The results were obtained during isothermal oxidation at 420°C, Fig. 2(*a*), under thermal cycling conditions from 200–420°C, with one hour at upper and lower temperatures and heating and cooling rates of 8°C min^{-1}, Fig. 2(*b*), and under cyclic variations of oxygen potential which was achieved by alternating discontinuously between 1 vol.-%O_2 and 1 vol.-%CO in the gas mixture in 24 h periods, Fig. 2(*c*). The results are compared with mild steel and 9Cr–1Mo steel. It was shown by Hendry[1] that the oxide grain size on nitrided mild steel was considerably smaller than that on un-nitrided control samples. A model was proposed which attributed the improvement of oxidation resistance by nitriding to refinement of oxide grain size and modification of the condensation process for cation vacancies which result in improved oxide adhesion on the metal surface. The present work presents the results of an X-ray diffraction and electron microscopy investigation of the mechanism by which the fine-grained adherent oxide layer is formed.

EXPERIMENTAL

The procedure for nitriding mild steel and iron-titanium alloys has been reported previously.[1,3] Oxidation was carried out at 420°C in static air on bulk specimens for optical and scanning electron microscopy (SEM) and on 200 μm thick foil for transmission electron microscopy (TEM). Thin oxide films for TEM were stripped from the metal surface using a solution of 12 wt-% iodine in methanol, and electropolished foils were prepared using a solution of 16 vol.-% perchloride acid : 16 vol.-% *n*-butoxyethanol : 64 vol.-% acetic acid at 0°C and 20 V. TEM specimens of oxide adhering to the metal substrate were prepared by covering the oxidized surface with a protective lacquer and electropolishing the exposed metal surface to penetration. The lacquer was then removed and both oxide and metal surfaces electropolished to the final thickness.

RESULTS AND DISCUSSION

The fine grain size of the oxide layer on nitrided mild steel and the increased coherency between oxide and metal

* Compositions of gases in vol.-%.
Compositions of steels in wt-%.

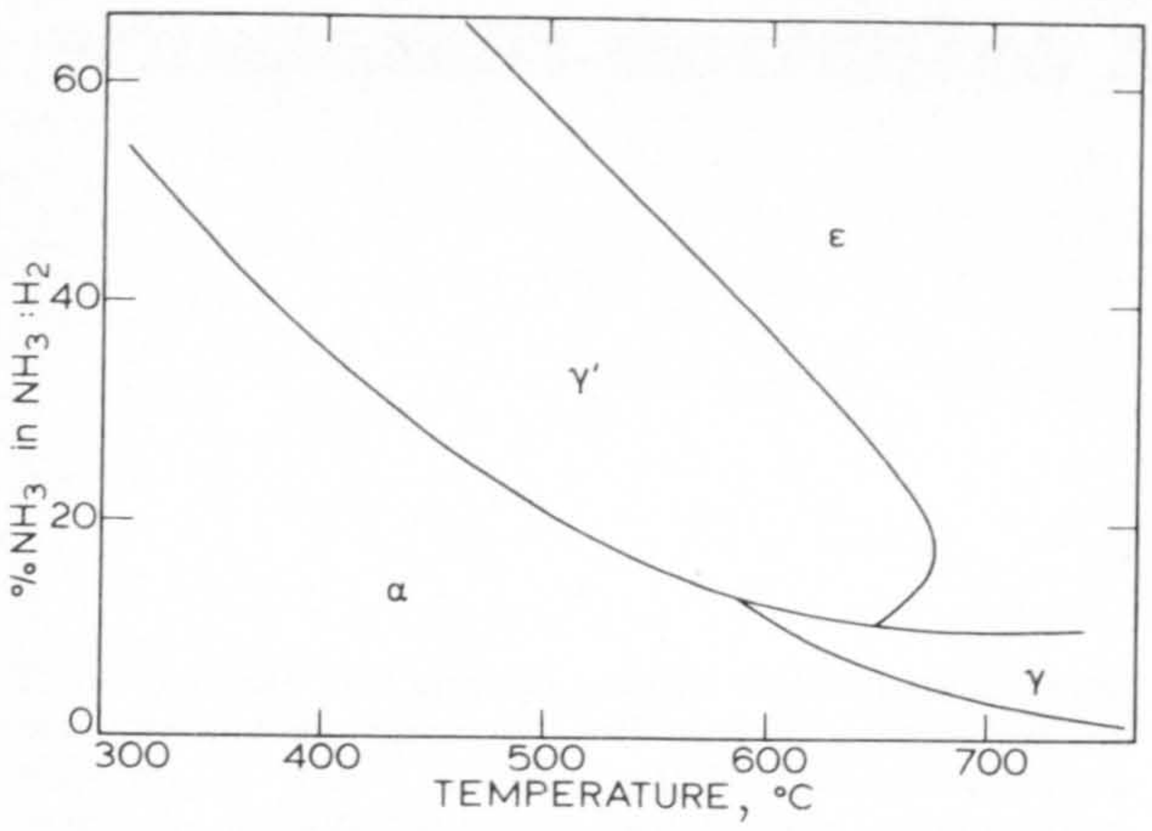

1 Equilibration of iron with $NH_3 : H_2$ gas mixtures at different temperatures. After Lehrer.[2]

relative to the un-nitrided steel have previously been established,[1] Fig. 3. It was also shown that the condensation of cation vacancies into voids at the metal/oxide interface, which is a characteristic feature of the oxidation of iron, is completely eliminated on nitrided steel. It was proposed, therefore, that the improved oxidation resistance of nitrided mild steel results from the increased oxide

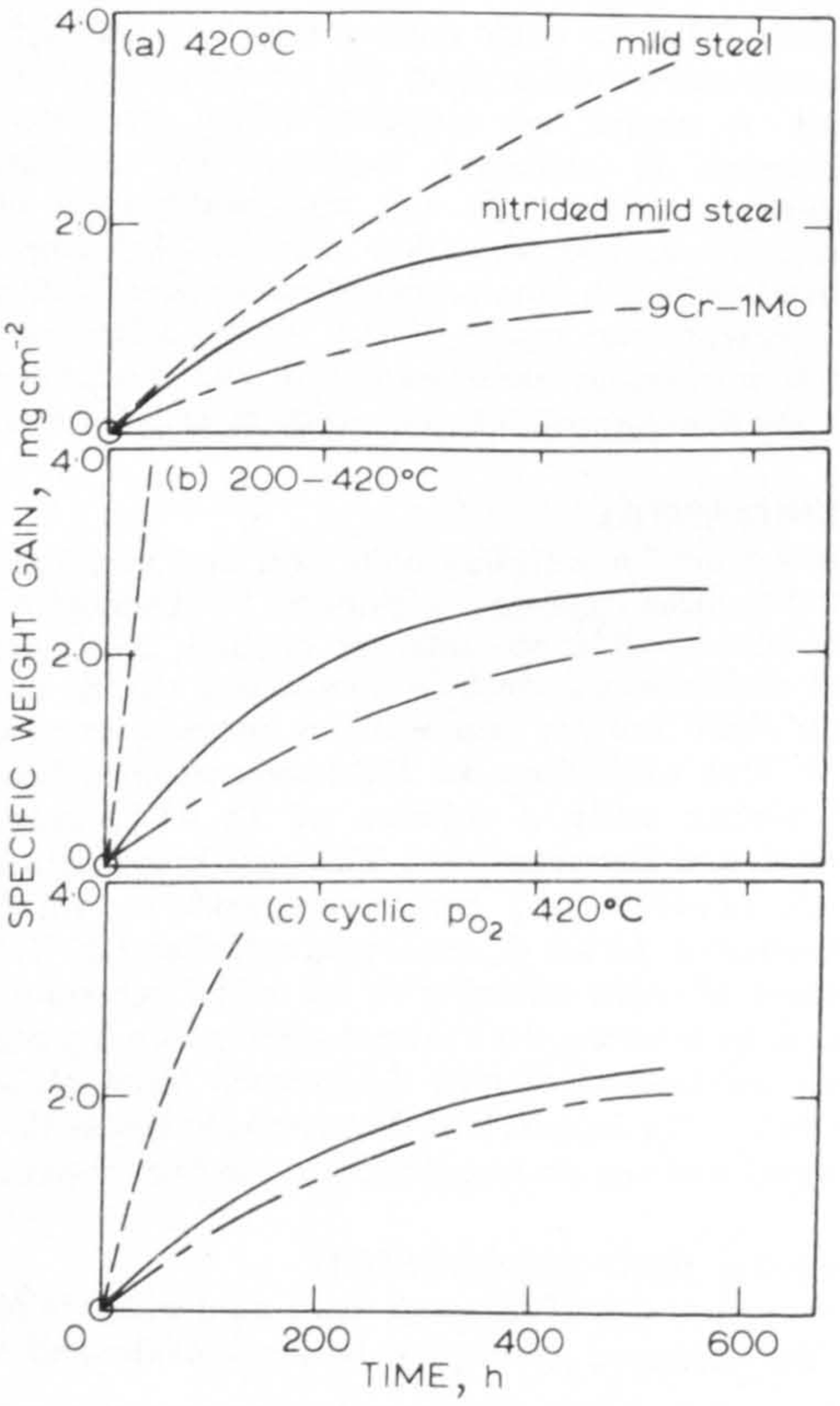

2 Oxidation of nitrided mild steel in (N_2 + 15CO_2 + 0·3SO_2 + 1O_2).

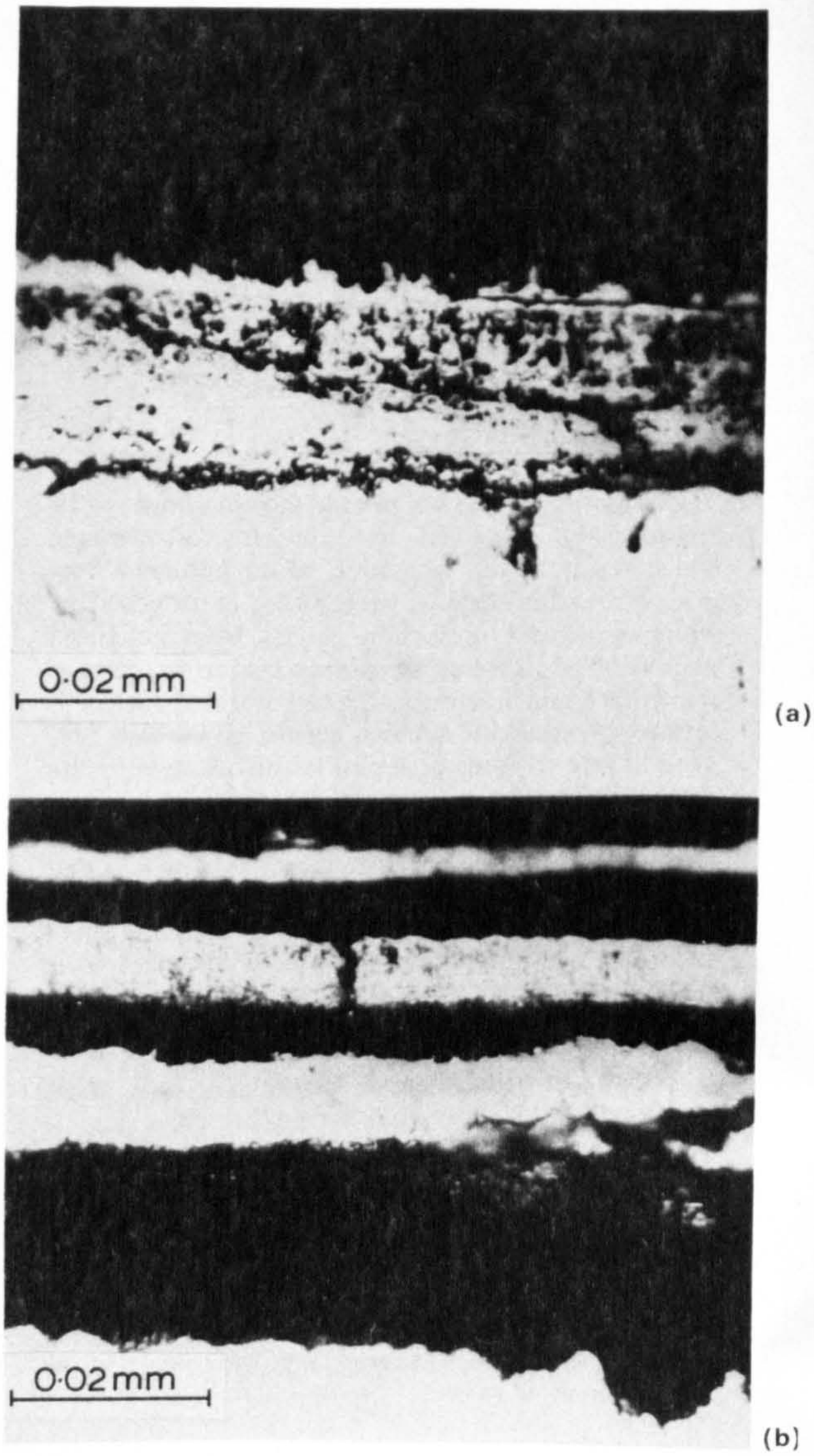

3 Optical micrographs of scale layers on (a) nitrided and (b) un-nitrided mild steel oxidized in simulated flue gas at 600°C for 500 h.

fracture strain consistent with a fine oxide grain size and from enhanced nucleation of oxide on the metal surface. The nitrided metal surface consists of a duplex microstructure of austenite (γ) and martensite (α') (see Hendry[1]) in which the martensite packets are typically 1 μm wide and contain microtwins with a lath width of approximately 15 nm. On the basis of these observations it was proposed that enhanced oxide nucleation occurred on the fine grain ($\alpha' + \gamma$) surface.

A series of experiments were performed to determine the nature of oxide growth. Nitrided mild steel samples were oxidized in air at 420°C for short times and the surface examined in an X-ray diffractometer using monochromated Cu K_α radiation. The results are shown in Fig. 4. After less than 5 min the ($\alpha' + \gamma$) surface layer is completely tempered to ferrite (α) with simultaneous precipitation of γ'-Fe_4N in the ferrite matrix and nucleation of Fe_3O_4 on the metal

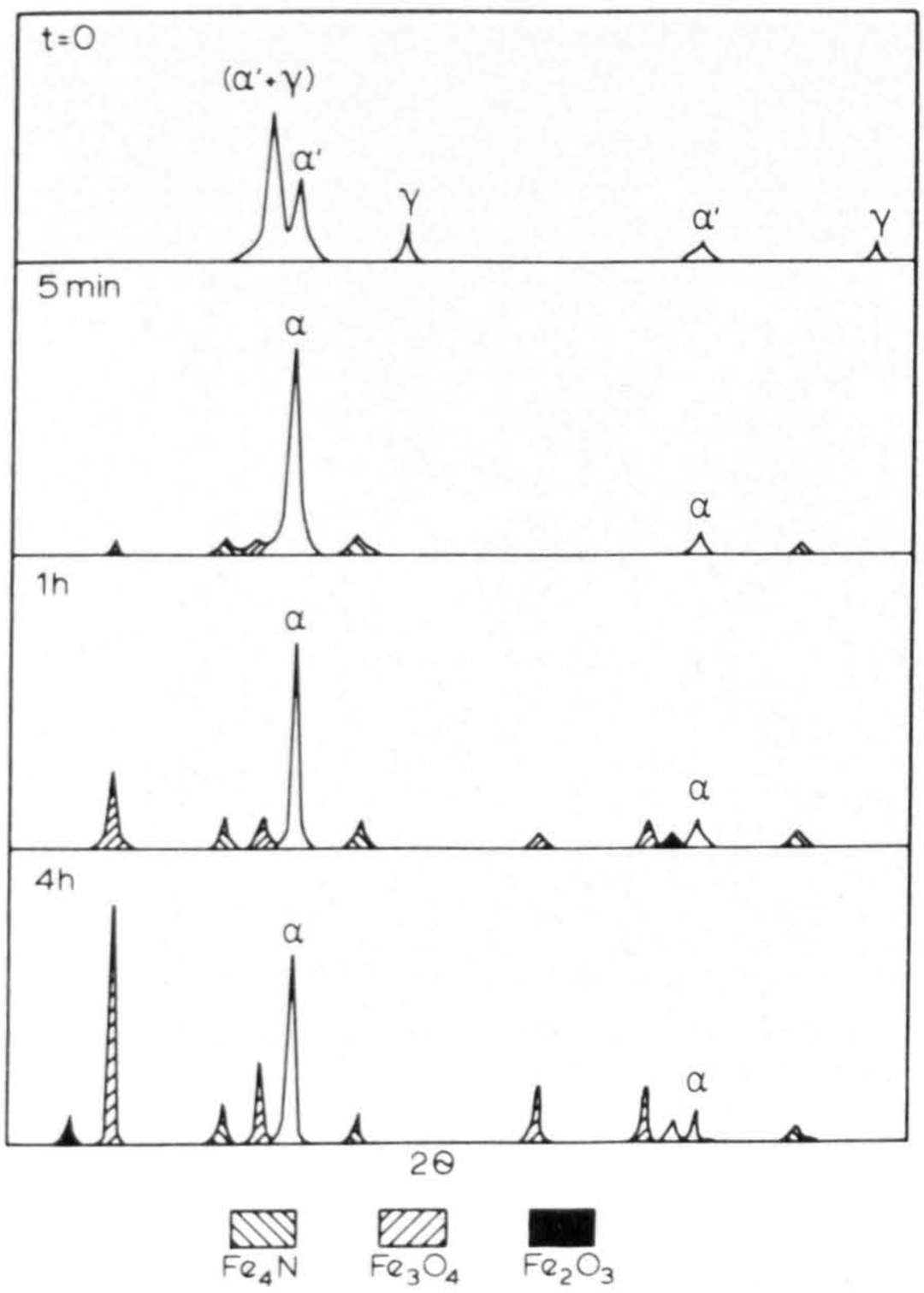

4 X-ray diffractometer traces of surface of nitrided mild steel oxidized in air at 420°C.

surface. X-ray line broadening calculations indicate that both precipitate and oxide nuclei are approximately 500 Å in diameter. The size of the γ'-Fe_4N particles has been confirmed by TEM[1] and shown to be stable over prolonged exposure at 420°C. The oxide grain size was directly determined on oxide replicas stripped from the metal surface after 5 min oxidation at 420°C. Figure 5 shows the oxide structure with individual oxide grains ringed.

The rapid rate of tempering of the nitrided surface is at variance with measurements performed on bulk samples of nitrogen martensite. The residual stress within the nitrided layer will however be relaxed preferentially at the free surface resulting in a more rapid tempering rate and this is shown in Fig. 6 where the relative intensities of the {111} reflections of γ-austenite and γ'-Fe_4N, measured from X-ray diffractometer traces of the specimen surface, are plotted as a function of depth below the surface. Precipitation of γ'-Fe_4N is enhanced within 25 μm of the surface but at greater depth a high proportion of austenite—and martensite—remains in the structure.

The microstructural observations provide circumstantial evidence of a direct correlation between the distribution of nitride particles in the surface layer of metal and the nucleation of small oxide grains on that surface. It is proposed that the observed fine-grained oxide on nitrided mild steel results from enhanced nucleation on nitride particles, and is not caused by the properties of the martensitic surface layer produced by nitriding as was previously suggested,[1] since the surface transforms within a few minutes at the oxidation temperature. The evidence is not unequivocal, however, and the possible influence of the martensitic structure cannot be eliminated.

If a stable nitride forming element is present in the steel then internal nitriding can be carried out in the ferritic state,

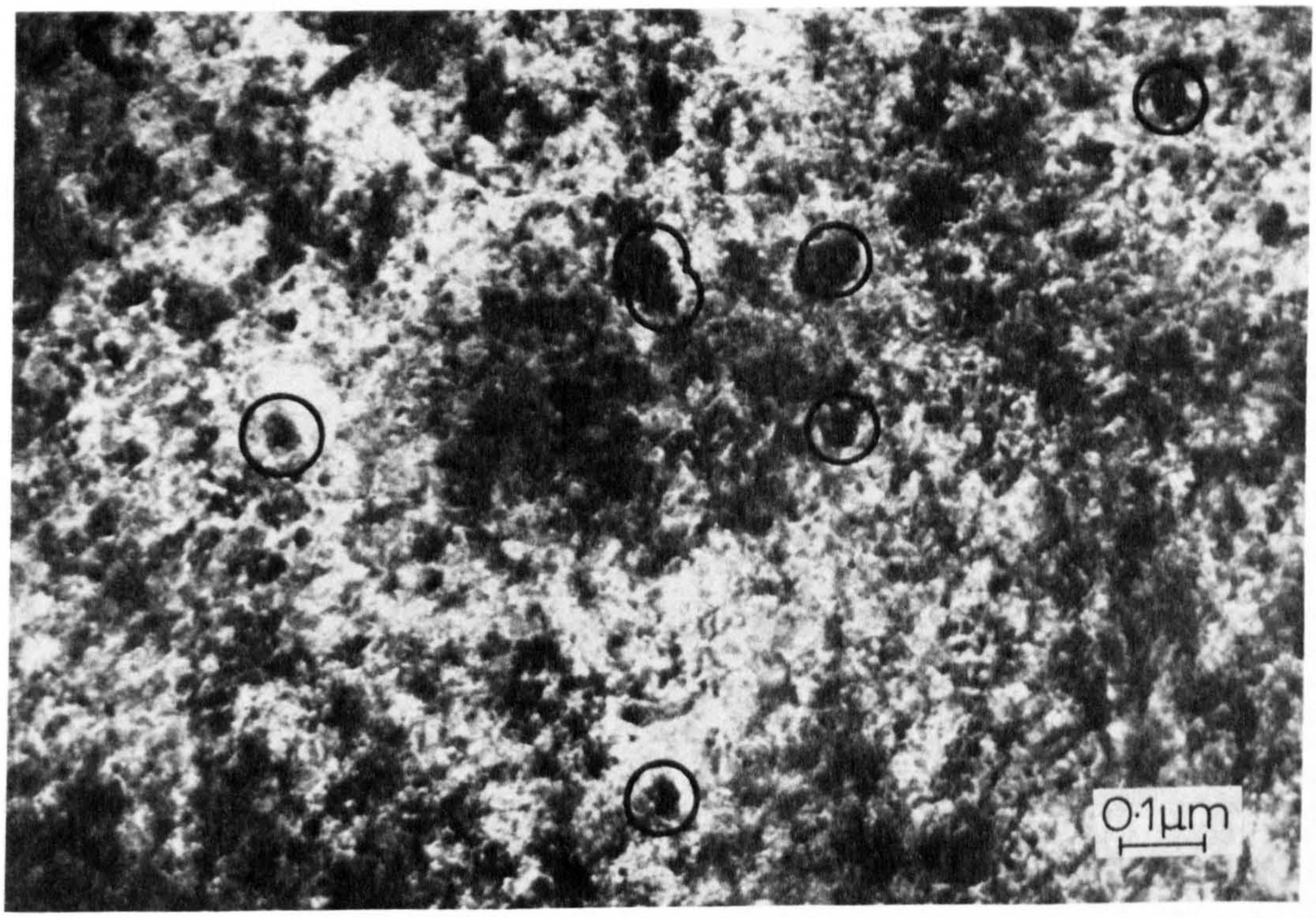

5 Oxide replica from nitrided mild steel oxidized for 5 min in air at 420°C.

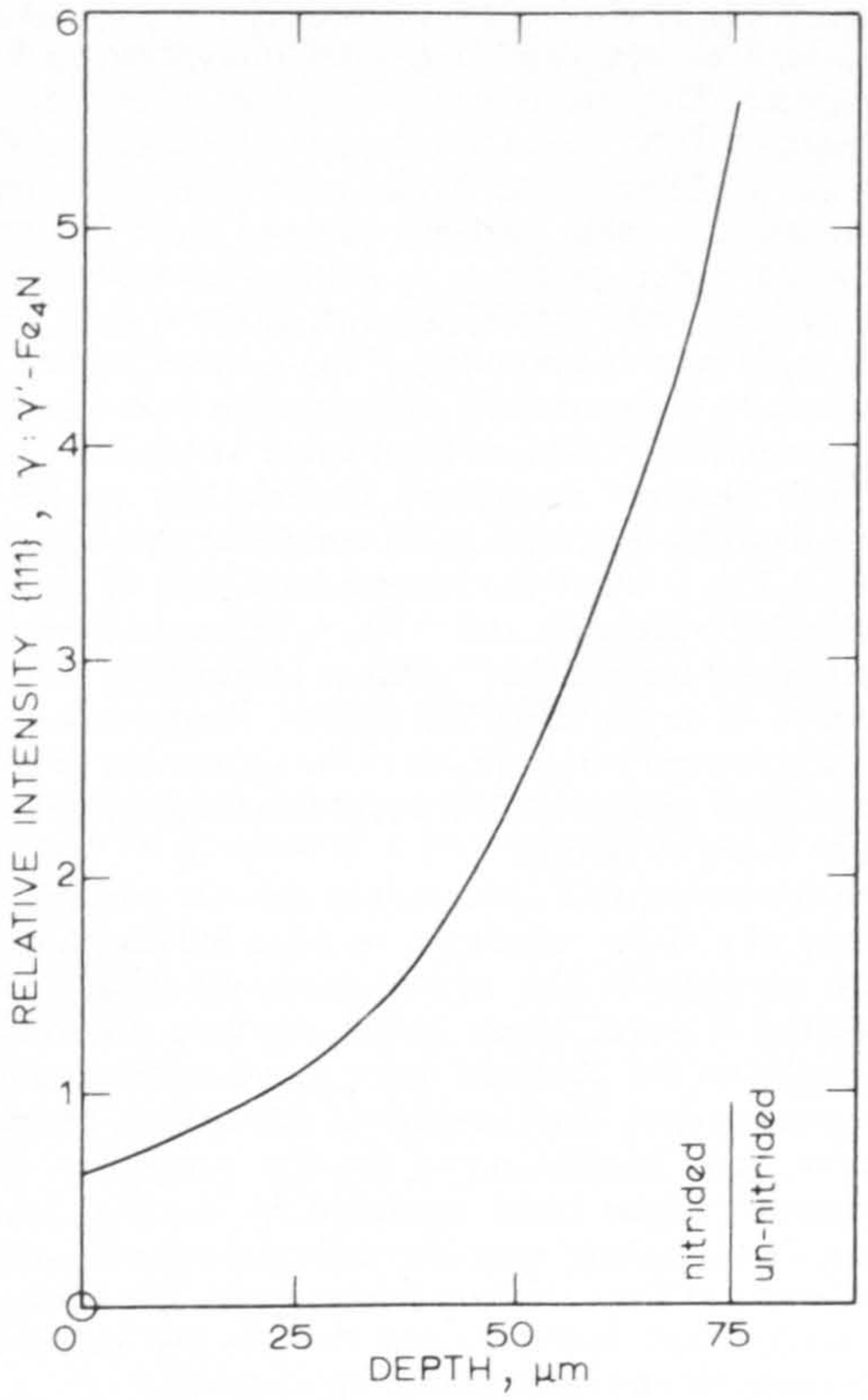

6 Variation of proportions of γ-austenite to γ′-Fe_4N with depth in surface layer of nitrided mild steel oxidized for 1 h in air at 420°C.

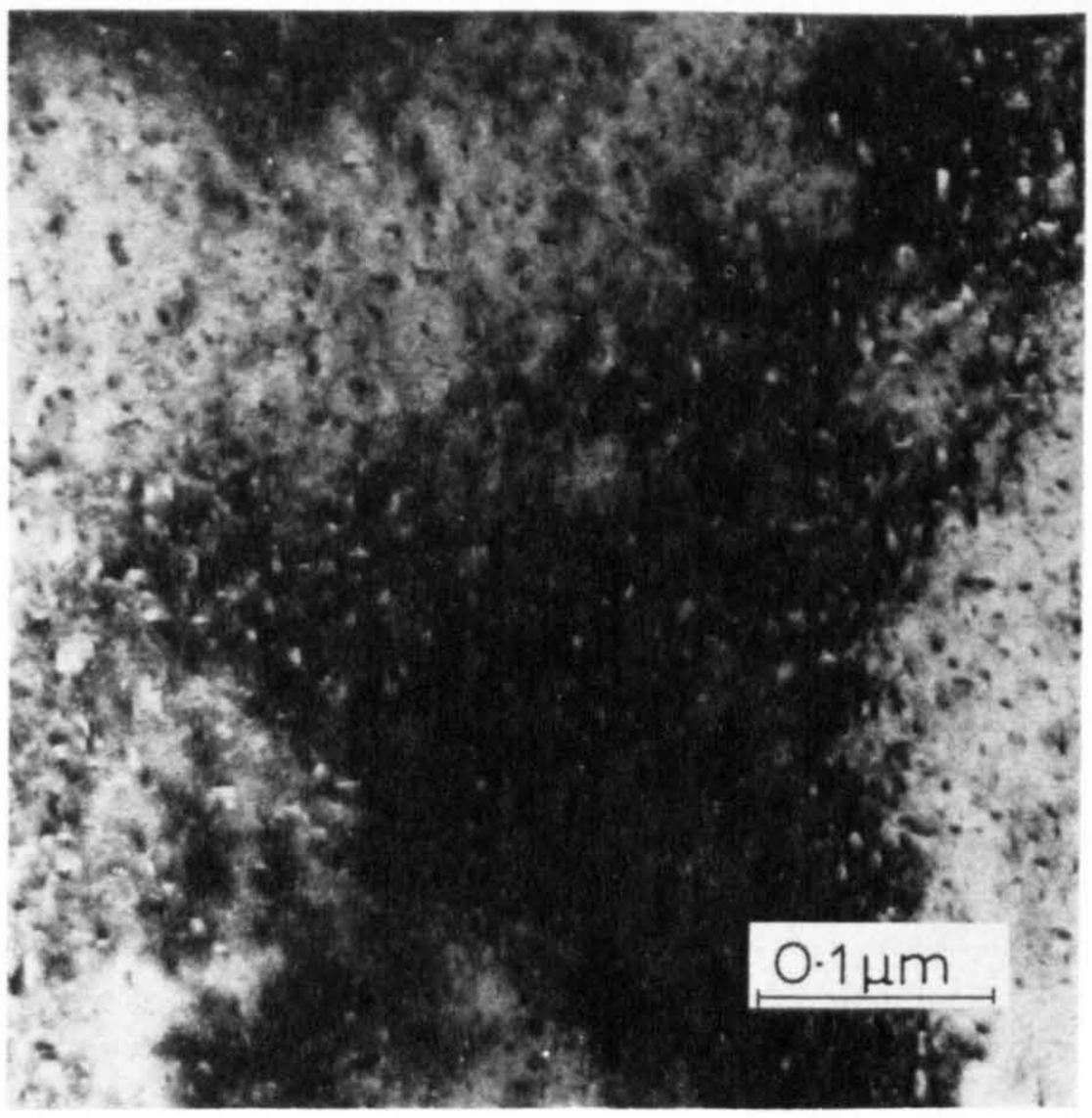

7 Transmission electron micrograph of nitrided Fe–0·15Ti. $4NH_3 : 96H_2$ at 580°C.

and alloy-nitride particles or substitutional-interstitial GP zones are precipitated in preference to γ′-Fe_4N and no martensite is formed (see Jack[3]). An alloy of Fe–0·15Ti was nitrided to produce a stable distribution of TiN particles in ferrite in the surface layer, Fig. 7, and tests in air at 420°C confirmed that oxidation resistance was superior to the un-nitrided alloy. A fine-grain-size oxide is formed which adheres strongly to the metal surface (Fig. 8). Using the technique of polishing from one side to prepare surface specimens of metal foil with the oxide intact, it is possible to obtain images in TEM of oxide nuclei and the nitride particles on which nucleation occurs. Figure 9 is a dark-field micrograph from an oxide reflection showing small oxide particles adjacent to the metal surface in contrast and about 250 Å in size, and an adjacent area of metal containing nitride particles out of contrast. The inset is a bright-field micrograph of the area containing the TiN particles.

The development of improved oxidation resistance in superalloys by the subsurface dispersion of oxide particles is well established[4,5] and a number of mechanisms have been proposed (see Whittle[5]). These include (i) changes in the mechanism of oxidation, (ii) keying or pegging of the oxide to the metal, (iii) modification of vacancy condensation at the oxide/metal interface, and (iv) refinement of oxide grain size. The present work is the first example of the extension of these principles to low-alloy steels and the use of nitride dispersions to give improved oxidation resistance. It has been shown[1] that there is no change in oxidation mechanism, that scale growth proceeds by the outward

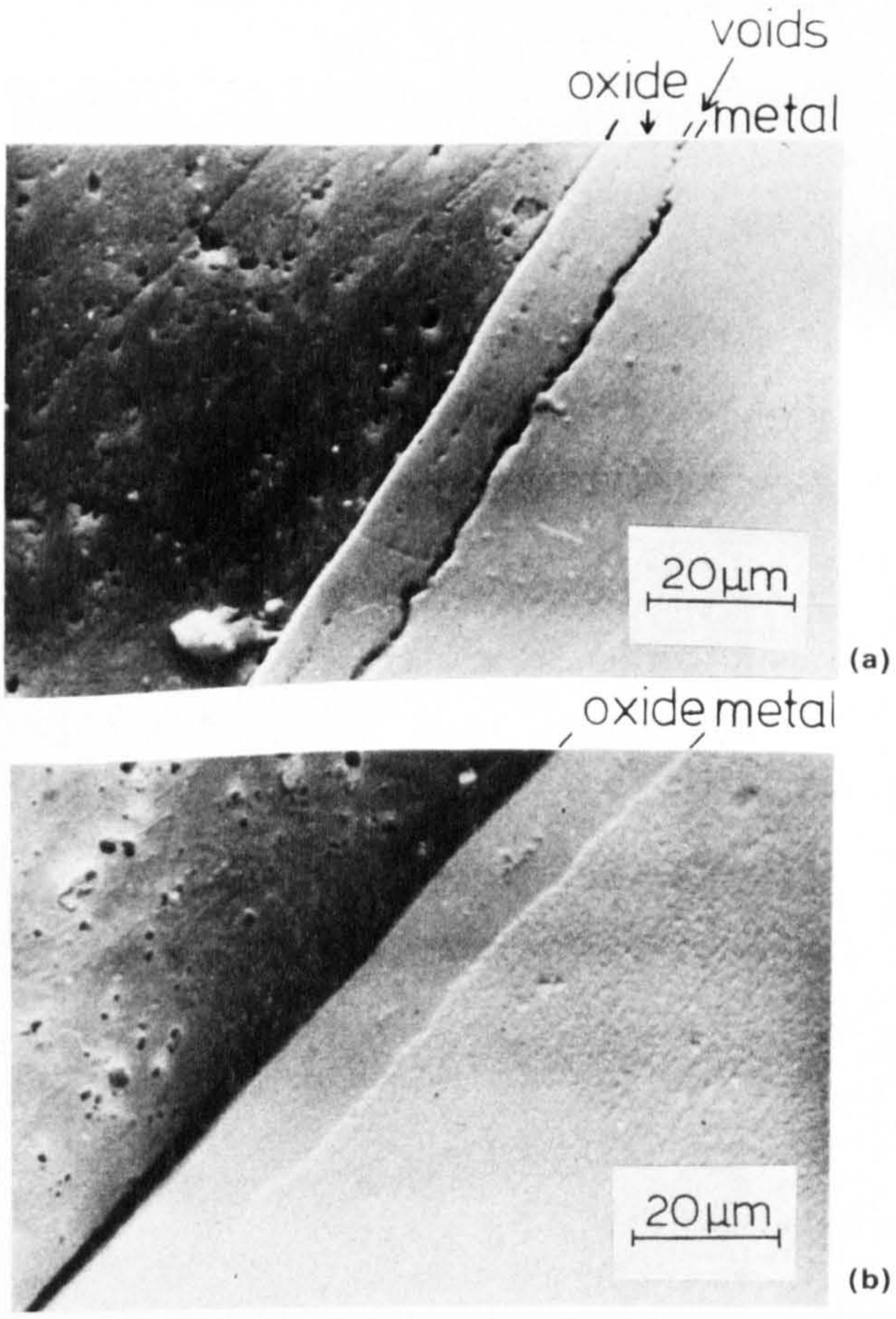

8 Scanning electron micro … oxide on Fe–0·15Ti (a) un-nitrided and (b) nitrided. Oxidized for 500 h at 420°C in air.

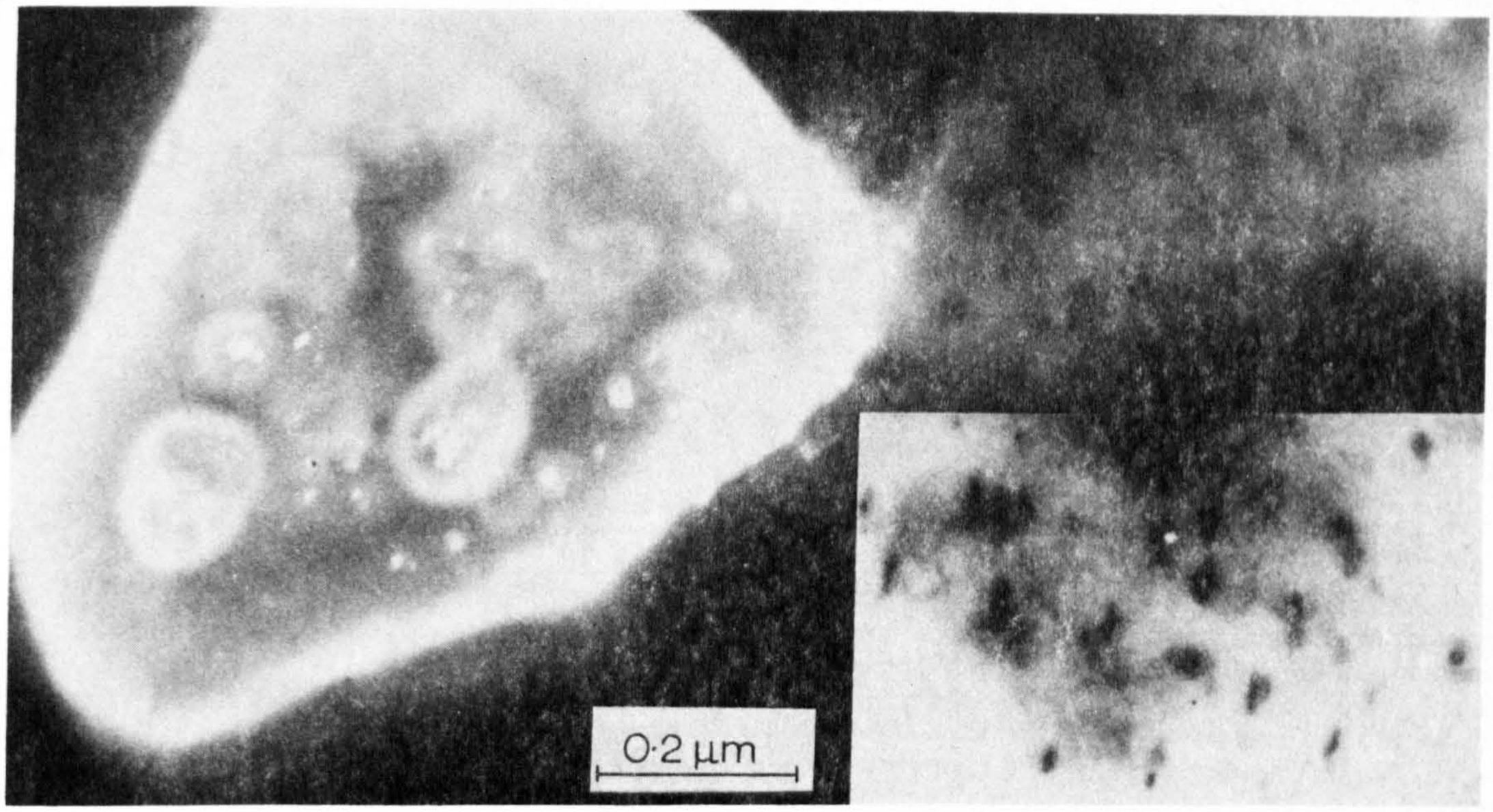

9 Transmission electron micrograph of oxide on nitrided Fe–0·15Ti oxidized 1 h at 420°C in air. Dark-field micrograph of oxide with inset bright-field micrograph of nitride particles.

diffusion of iron cations, and that there is no evidence of oxide pegging. There is however evidence to suggest that the mechanism by which vacancies are eliminated is changed (Hendry[1] and Fig. 7). It is not certain how this occurs but the effect is clearly important since vacancy condensation into voids at the oxide/metal interface is a prime cause of oxide spalling and is eliminated in nitrided steels. It is possible that the nitride/metal interface acts as a vacancy sink. The major contribution to improved oxidation resistance, however, is the effect of a fine dispersion of nitride particles on oxide nucleation. An extremely fine grained oxide is produced with a consequent increase in oxide fracture strain.[6,7] The oxide is therefore capable of withstanding the stresses which arise during growth in an aggressive environment, and the results in Fig. 2 show that the oxide formed on nitrided mild steel is capable of withstanding the stresses generated by thermal cycling and changes in oxygen potential typical of the operating conditions in a coal-fired power-station boiler.

CONCLUSIONS

Improved oxidation resistance of nitrided low-alloy steels is attributed to the effect on oxide fracture strain of oxide grain size resulting from a fine distribution of nucleation sites on nitride particles. The nitride interparticle spacing is small and an extremely fine grain size oxide is formed. The mechanical strength of an oxide layer increases with decreasing grain size and the present results show that the fracture strain of the oxide on nitrided alloys is not exceeded under the experimental conditions investigated. The oxide is therefore coherent and protective. Condensation of vacancies into voids at the oxide/metal interface, which is characteristic of the oxidation of iron alloys, does not occur during oxidation of nitrided low-alloy steels.

ACKNOWLEDGEMENTS

We acknowledge the interest and support given by Professor K. H. Jack in the Wolfson Research Group for High Strength Materials, Crystallography Laboratory. We are also grateful to the CEGB (Research Division) for provision of a research support grant for one of us (DJC).

REFERENCES

1. A. HENDRY: *Corros. Sci.*, 1978, **18,** 555.
2. F. LEHRER: *Z. Elektrochem.*, 1930, **36,** 383.
3. K. H. JACK: 'Heat Treatment '73', p. 39. **1974:** London (Metals Society).
4. J. STRINGER, B. A. WILCOX, and R. I. JAFFEE: *Oxid. Met.*, 1972, **5,** 11.
5. D. P. WHITTLE and J. STRINGER: Proc. Conf. 'Residuals, Additives, and Materials Properties', to be published in *Phil. Trans. R. Soc.*
6. D. L. DOUGLASS: 'Oxidation of metals and alloys', p. 137. **1971:** New York (ASME).
7. J. STRINGER: *Corros. Sci.*, 1970, **10,** 513.

Short communication

Structure and magnetic properties of Fe–Cr–Co–Mo alloy melted in open induction furnace

S. Szymura and L. Sojka

Permanent magnets based on the Fe–Cr–Co system were suggested by Kaneko *et al.*[1] in 1972. The magnetic properties in such an alloy are produced as the result of spinodal decomposition of the α-phase (stable above 1520 K) into two phases, i.e. iron-rich α_1 and chromium-rich α_2. At high temperatures (1420 K) another transformation is possible, namely precipitation of γ-phase from the α-phase. The α-phase region can be extended by the addition of such α-forming elements as Nb, Al, Ti, Si, Mo, and W.[2–4]

The energy products of Fe–Cr–Co permanent magnets are similar to those of Alnico 5 but the ductility of the former is better.[1,2] However, it should be noted that the properties cited in previously published papers[1–4] were obtained on alloys melted in vacuum induction furnaces or in an argon atmosphere.

The aim of the present work was to determine the microstructure and magnetic properties of an Fe–Cr–Co–Mo alloy melted in an open induction furnace, as is the case for the Alnico-type alloys.

EXPERIMENTAL DETAILS

An Fe–Cr–Co–Mo alloy with the chemical composition shown in Table I was melted in an open induction furnace with a magnesite crucible. Pure (better than 99·9%) raw materials were used. The heat-treatment procedure is shown in Fig. 1. The specimens were homogenized at 1570 K, quenched in water and annealed for 40 min at 910 K in a 300 kA m^{-1} magnetic field. Multistage tempering was carried out between 873 and 833 K.

The microstructure of the alloy was examined under an optical microscope using transverse polished sections etched in a reagent containing 5 g $CuCl_2$, 40 cm^3 HCl (36%), 5 cm^3 HNO_3 (75%), and 50 cm^3 H_2O. Etching must be carried out soon after polishing because otherwise the surface of the specimens may become passivated.

The chemical composition of the phases present in the alloy was determined with a microprobe and the phase constitution by X-ray diffraction. The magnetic properties of the material were determined by means of a MY-55 AEG permeameter with an accuracy of the order of 1%.

RESULTS AND DISCUSSION

Metallographic evidence showed that the homogenizing treatment failed to produce a fully homogeneous structure; some very fine particles, 2 to 10 μm, were present. The shape, distribution, and composition of the particles seem to

Table I Chemical composition of alloy, wt-%

Fe	Cr	Co	Mo	C	N	O
42·38	28·69	25·36	2·95	0·019	0·114	0·028

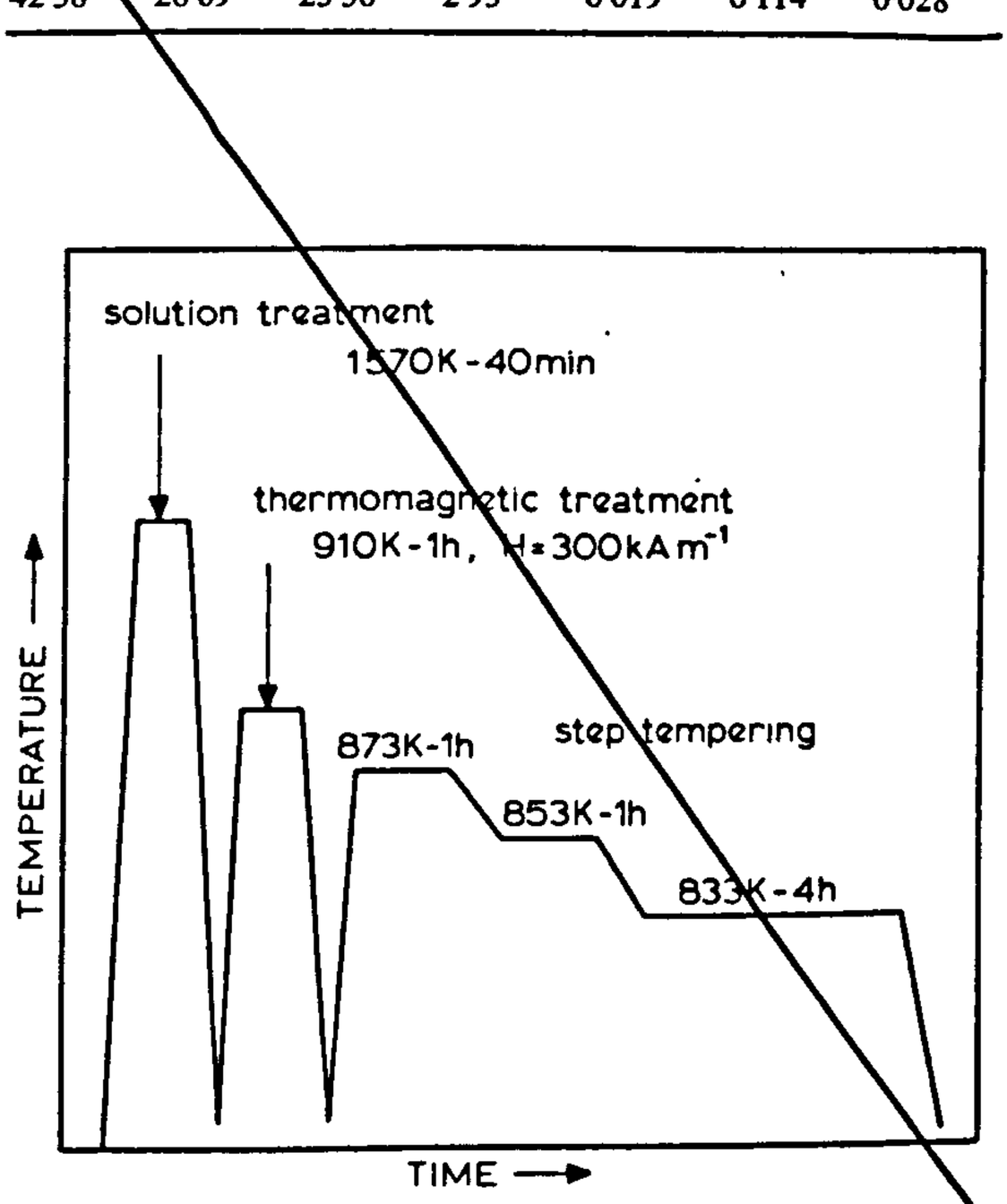

1 Heat-treatment diagram.

Manuscript received 11 July 1978; in final form 7 November 1978.
S. Szymura, DSc, is in the Institute of Physics, Technical University, Częstochowa, and L. Sojka, MSc, is in the Institute of Ferrous Metallurgy, Gliwice, Poland.

REFERENCES

Averbach, B.L. & Cohen, M., 1948, Trans. A.I.M.E., 176, 401.

Baker, R.G. & Nutting, J., 1951, "Precipitation Processes in Steels", I.S.I. Special Report No. 64.

Birchenall, C.E., 1959, Z. Electrochm., 63, 790.

Boggs, W.E., Kachik, R.H. & Pellisier, G.E., 1965, J. Electrochem. Soc., 112, 539.

Boggs, W.E., Kachik, R.H. & Pellisier, G.E., 1967, J. Electrochem. Soc., 114, 32.

Brenner, S.S., 1955, J. Electrochem. Soc., 102, 7.

Caplan, D. & Cohen, M., 1952, J. Metals, 4, 1057.

Caplan, D. & Cohen, M., 1966, Corr. Sci., 6, 321.

Coates, D.J. & Hendry, A., 1979, Met. Sci., 13, 315 (see Appendix).

Coble, R.L., 1963, J. Appl. Phys., 34, 1679.

Darken, L.S. & Gurry, R.W., 1945, J. Am. Chem. Soc., 67, 1398.

Darken, L.S. & Gurry, R.W., 1953, "Physical Chemistry of Metals", New York: McGraw-Hill.

Davies, M.H., Simnad, M.T. & Birchenall, C.E., 1951, J. Metals, 3, 889.

Davis, H.H., Graham, H.C. & Kvernes, I.A., 1971, Oxid. Met., 3, 431.

Douglass, D.L., 1971, "Oxidation of Metals and Alloys", A.S.M.E. pp. 137-156.

Dravnieks, A. & McDonald, H.J., 1948, J. Electrochem. Soc., 94, 139.

Driver, J.H., 1972, Unpublished work, University of Newcastle upon Tyne.

Driver, J.H. & Papazian, J.M., 1973, Acta Met., 2, 1139.

Driver, J.H., Unthank, D.C. & Jack, K.H., 1972, Phil. Mag., 26, 1227.

Dunnington, B.W., Beck, F.H. & Fontana, M.G., 1952, Corrosion, 8, 2t.

Flatley, T. & Birks, N., 1971, J.I.S.I., 209, 523.

Francis, J.M. & Jutson, J.A., 1968, Corr. Sci., 8, 445.

Gibbs, G.B. & Hales, R., 1977a, Corr. Sci., 17, 487.

Gibbs, G.B. & Hales, R., 1977b, "Vacancies '76", London: The Metals Society, pp. 201-207.

Giggins, C.S. & Pettit, F.S., 1971, Met. Trans., 3, 1071.

Grieveson, P. & Turkdogan, E.T., 1964, Trans. A.I.M.E., 230, 407.

Hancock, P. & Hurst, R.C., 1974, "Advances in Corrosion Science and Technology, Vol. 4", Ed. by M.G. Fontana & R.W. Staehle, New York: Plenum Press.

Hauffe, K., 1965, "Oxidation of Metals", New York: Plenum Press.

Hayes, P.C., 1973, Ph.D. Thesis, University of Strathclyde.

Hayes, P.C. & Grieveson, P., 1975, Scripta Met., 9, 39.

Henderson, S., 1976, Ph.D. Thesis, University of Newcastle upon Tyne.

Hendry, A., 1978, Corr. Sci., 18, 555.

Hepworth, M.T., Smith, R.P. & Turkdogan, E.T., 1966, Trans. A.I.M.E., 236, 1278.

Herring, C., 1950, J. Appl. Phys., 21, 437.

Holmes, D.R. & Pascoe, R.T., 1972, Werkst. Korr., 23, 859.

Howes, V.R., 1968, Corr. Sci., 8, 221.

Howes, V.R., 1969, J. Electrochem. Soc., 116, 1286.

Howes, V.R., 1970, Corr. Sci., 10, 99.

Howes, V.R. & Richardson, C.N., 1969, Corr. Sci., 9, 385.

Hussey, R.J. & Cohen, M., 1971, Corr. Sci., 11, 699.

Ilschner, B., Reppich, B. & Riecke, E., 1964, Disc. Faraday Soc., 38, 243.

Jack, D.H., Lidster, P.C., Grieveson, P. & Jack, K.H., 1971, Conference on Metallurgical Thermochemistry, Sheffield.

Jack, K.H., 1951a, Proc. Roy. Soc. A208, 216.

Jack, K.H., 1951b, Proc. Roy. Soc. A208, 200.

Jack, K.H., 1975, "Heat Treatment '73", London: The Metals Society, pp. 39-50.

Kirkwood, D.H., Atasoy, O.E. & Keown, S.R., 1974, Met. Sci., 8, 49.

Kofstad, P., 1966, "High Temperature Oxidation of Metals', New York: Wiley.

Krawitz, A. & Sinclair, R., 1975, Phil. Mag. 31, 617.

Kubaschewski, O. & Alcock, C.B., 1979, "Metallurgical Thermochemistry" 5th Edn., Oxford: Pergamon Press.

Kubaschewski, O. & Hopkins, B.E., 1962, "Oxidation of Metals and Alloys" 2nd Edn., New York: Academic Press.

Kuenzly, J.D. & Douglass, D.L., 1974, Ox. Met., 8, 139.

Kumar, A., Nasrallah, M. & Douglass, D.L., 1974, Oxid. Met., 8, 227.

Kvernes, I.A., 1973, Oxid. Met., 6, 45.

Lai, D., Borg, R.J., Brabers, M.J., MacKenzie, J.D. & Birchenall, C.E., 1961, Corrosion, 17, 357.

Lehrer, E., 1930, Z. Electrochem., 36, 383.

Lloyd, G.O., Saunders, S.R.J., Kent, B. & Fursey, A., 1977, Corr. Sci., 17, 269.

Mortimer, B., 1971, Ph.D. Thesis, University of Newcastle upon Tyne.

Mortimer, B., Grieveson, P. & Jack, K.H., 1972, Scand. J. Met., 1, 203.

Nabarro, F.R.N., 1948, "Report of a Conference on the Strength of Solids", London: Phys. Soc., p. 75.

Nelson, J.B. & Riley, D.P., 1945, Proc. Phys. Soc., 57, 160.

Pehlke, R.D. & Elliot, J.F., 1960, Trans. Met. Soc. A.I.M.E., 218, 1088.

Pfeiffer, H., 1957, Werkst. Korr., 8, 574.

Pilling, N.B. & Bedworth, R.E., 1923, J. Inst. Met., 29, 529.

Pipkin, N.J., 1968, Ph.D. Thesis, University of Newcastle upon Tyne.

Pipkin, N.J. & Middleton, P., 1973, Unpublished work, University of Newcastle upon Tyne.

Pitsch, W., 1961, Arch. Eisenhüttenw., 32, 573.

Pope, M., 1972, Ph.D. Thesis, University of Newcastle upon Tyne.

Pope, M., Jones, D.M. & Jack, K.H., 1975, "Proc. of Fifth Int. Conf. on Internal Friction and Ultrasonic Attenuation in Crystalline Solids", Aachen, 1973, ed. by Lenz & Lücke. Berlin-Heidelberg: Springer-Verlag, pp. 266-275.

Rahmel, A., 1962, Z. Electrochem., 66, 363.

Rahmel, A., Jager, W. & Becker, K., 1959, Arch. Eisenhüttenw., 30, 351.

Roberts, W., 1970, Ph.D. Thesis, University of Newcastle upon Tyne.

Robinson, M.T. & Flatley, T., 1976, C.E.G.B. Internal Report, No. SSD/MID/R26/76.

Scheil, E. & Kiwit, K., 1936, Arch. Eisenhüttenw., 9, 405.

Schenk, H., Frohberg, M. & Graf, H., 1958, Arch. Eisenhüttenw., 29, 683.

Schwerdtfeger, K. ' Turkdogan, E.T., 1970, "Techniques for Metals Research", Vol. 4, pt. 1, New York: Interscience.

Scott, V.D., 1977, "Vacancies '76", London: The Metals Society. p. 208.

Seltzer, M.S., Wilcox, B.A. & Jaffee, R.I., 1972, Met. Trans., 3, 2390.

Silcock, J.M., Heal, T.J. & Hardy, H.K., 1953-54, J. Inst. Metals, 82, 239.

Speirs, D.L., 1969, Ph.D. Thesis, University of Newcastle upon Tyne.

Speirs, D.L., Roberts, W., Grieveson, P. & Jack, K.H., 1970, "Proc. of the 2nd. Int. Conf. on the Strengthening of Metals and Alloys", Asilomar: American Society for Metals, pp. 601-605.

Stanley, J.K., Von Hoene, J. & Huntoon, R.T., 1951, Trans. Amer. Soc. Met., 43, 426.

Stephenson, A., 1973, Ph.D. Thesis, University of Newcastle upon Tyne.

Stott, F.H., Golightly, F.A. & Wood, G.C., 1979, Corr. Sci., 19, 869.

Stringer, J., 1966, Metall. Rev., 11, 113.

Stringer, J., Wilcox, B.A. & Jaffee, R.J., 1972, Ox. Metals, 5, 11.

Stringer, J. & Wright, J.G., 1972, Ox. Metals, 5, 59.

Tamman, G., 1920, Z. Anorg. Chem., 111, 78.

Tien, J.K. & Davidson, J.M., 1975, "Stress Effects and the Oxidation of Metals", Ed. by J.V. Cathcart, New York: A.I.M.E., pp. 200-219.

Tien, J.K. & Pettit, F.S., 1972, Metall. Trans., 3, 1587.

Tylecote, R.F. & Appleby, W.K., 1972, Werks. und Korr., 23, 855.

Tylecote, R.F. & Mitchell, T.E., 1960, J.I.S.I., 196, 445.

Wagner, C., 1933, Z. Physik. Chem. B21; 25.
Wallwork, G.R. & Hed, A.Z., 1971, Oxid. Met., 3, 229.
Whittle, D.P., El-Dahshan, M.E. & Stringer, J., 1977, Corr. Sci., 17, 879.
Whittle, D.P. & Wood, G.C., 1967, J. Electrochem. Soc., 114, 986.
Winterbottom, A.B., 1950, J.I.S.I., 165, 9.
Wood, G.C., 1970, Oxid. Met., 2, 11.
Wood, G.C., Wright, I.G. Hodgkiess, T. & Whittle, D.P., 1970, Werks. und Korr., 21, 900.
Wright, I.G. & Wilcox, B.A., 1974, Oxid. Met., 8, 283.

Yearian, H.J., Randell, E.C. & Longo, T.A., 1956, Corrosion, 12, 515t.